ALMA MATER STUDIORUM
UNIVERSITÀ DI BOLOGNA

DOTTORATO DI RICERCA IN ASTROFISICA

CICLO XXXVIII

Settore Concorsuale: 02/C1 - ASTRONOMIA, ASTROFISICA, FISICA DELLA TERRA E DEI PIANETI

Settore Scientifico Disciplinare: FIS/05 - ASTRONOMIA E ASTROFISICA

Probing the Expansion History of the Universe through Cosmic Time

Presentata da: **Elena Tomasetti**

Coordinatore Dottorato
Prof. Andrea Miglio

Supervisore
Prof. Michele Ennio Maria Moresco

Co-supervisori
Prof.ssa Carmela Lardo
Prof. Andrea Cimatti

Esame finale anno 2026

Abstract

This Thesis explores a new avenue to constrain the expansion history of the Universe, exploiting cosmic time as a cosmological probe rather than the traditional luminosity or distance used in standard candles and standard rulers. This is done studying and improving two alternative and complementary approaches: *cosmic clocks* and *cosmic chronometers*.

The cosmic clocks approach focuses on the absolute ages of the most long-lived structures, which provide a lower bound to the age of the Universe and, consequently, an upper limit to the Hubble constant, H_0. The cosmic chronometers method, on the other hand, is based on a differential approach: by measuring the ageing in redshift of massive and passively evolving galaxies, it provides a direct measurement of the Hubble parameter at high redshift, $H(z)$, with minimal cosmological assumptions.

In the first part, we explore the cosmic clocks approach with different tracers. We start with a sample of old Milky Way (MW) stars, for which ages were obtained via Bayesian isochrone fitting, combining modern stellar evolutionary models with the precise photometric and astrometric data from *Gaia* DR3. We then move to MW globular clusters (GCs), assessing the age-dating potential of the full spectral synthesis methods, benchmarking them against classical isochrone fitting, and identifying current limitations. This provides a crucial step toward applying our method to derive ages from integrated spectra of distant, unresolved populations. Lastly, we push the cosmic clocks approach to higher redshifts, investigating the feasibility of using lensed GCs, now detectable thanks to the James Webb Space Telescope, as tracers of the cosmic time in the younger Universe.

In the second part, we apply the cosmic chronometers approach in two redshift regimes, at $z \sim 0.5$ and $z \sim 1.25$, while addressing several challenges aimed at advancing the method from different perspectives. First, we develop a more robust implementation of the full spectrum fitting technique and explore some of the main sources of systematics affecting it, thereby opening promising avenues for future applications. We then extend the analysis to galaxy clusters, a key environment where other complementary cosmological probes are often employed, to evaluate the potential of this approach in this regime opening the possibility, at the same time, for a first fully-consistent multi-probe analysis. Finally, we present forecasts for the performance of the cosmic chronometers technique in the context of forthcoming large-scale spectroscopic surveys, which are expected to achieve percent-level precision.

A fundamental strength of this work is that all age determinations are fully independent of any cosmological model, relying exclusively on stellar models and population synthesis prescriptions. This approach allows us to provide new, independent constraints on the age of the Universe and on H_0, along with two new determinations of $H(z)$, paving the way toward a time-based reconstruction of the cosmic expansion history.

Contents

Introduction

Nowadays, the expansion of the Universe can be traced across most of cosmic history, from the primordial imprint left on the cosmic microwave background to the formation and growth of the Large-Scale Structure. The prevailing theoretical framework describing this evolution is the ΛCDM model, grounded in General Relativity and the Cosmological Principle. In this paradigm, the cosmic energy budget is dominated by two elusive components: dark energy, responsible for the observed accelerated expansion (Riess et al., 1998; Perlmutter et al., 1999) and contributing about 70% of the total, and dark matter, interacting with ordinary matter primarily through gravity and accounting for roughly 25%. The remaining 5% is the baryonic matter that we can observe directly and describe in detail with known physics.

Within this framework, the expansion history of the Universe, expressed in terms of the Hubble parameter $H(z)$, plays a central role. It connects the growth of structures, the geometry of spacetime, and the microphysics of the early Universe. Observationally, the most powerful constraints have come from probes that infer distances and angular scales: Type Ia supernovae as standard candles, baryon acoustic oscillations as standard rulers, the anisotropies of the cosmic microwave background, gravitational lensing, and large-scale clustering. Their reach and precision are currently unparalleled, yet the thorough investigations carried out during the last decades have revealed unexpected issues. The most striking issue is the discrepancy between "early-time" inferences of the current expansion rate (the Hubble constant; H_0) from the CMB and "late-time" determinations from the local distance ladder (Abdalla et al., 2022; Di Valentino et al., 2021a, 2025). Whether this discrepancy arises from unaccounted-for systematics or hints at new physics beyond ΛCDM, it underscores the need for complementary observables to investigate the Universe with different tracers and sources of uncertainty.

A conceptually novel and distinct alternative to using luminosity and length (in the form of standard candles and rulers) is to use time itself as a tracer of cosmic expansion. This can be realised through two complementary approaches. *Cosmic clocks* refer to the oldest stellar systems, whose absolute ages provide a lower limit to the age of the Universe, while simultaneously constraining cosmological parameters by setting an upper bound on H_0. *Cosmic chronometers* enable direct and cosmology-independent constraints on $H(z)$, measuring how the ages of massive, passively evolving galaxies change with redshift, thus relying on a differential approach.

The primary strength of these time-based cosmological probes is their independence from classical distance and luminosity measurements, making them naturally orthogonal to the classical probes and well suited to test current cosmological tensions. Their main challenges lie in the astrophysical modelling of time evolution: robust stellar evolution models and isochrones, realistic star-formation histories, careful treatment of metallicity, and α-enhancement are among the key factors that must be rigorously addressed.

In this Thesis, we explore this time-based approach through both absolute age measurements of ancient stellar systems (Tomasetti et al., 2025a,c,d) and differential age dating of massive quiescent galaxies (Tomasetti et al., 2023, 2025b). From these analyses, we present new and complementary measurements of the expansion history of the Universe, deriving cosmology-independent constraints on its age and on H_0, and obtaining direct estimates of $H(z)$ up to high redshifts. In the process, we test and validate different age-dating techniques, quantify key systematics, and place these novel probes within a broader, multi-probe cosmological framework.

This Thesis is structured as follows:

- Chapter 1 provides a historical overview of how modern cosmology has been shaped, from the theoretical foundations to the observational pillars and the current tensions. The chapter then introduces the cosmic clocks and cosmic chronometers approaches, and concludes with an outline of the main age-dating techniques employed in this Thesis.

- Chapter 2 presents three applications of the cosmic clocks approach, each based on a different type of cosmic-age tracer: stars, globular clusters, and lensed star clusters. For each application, the chapter discusses the respective strengths and limitations, the novel cosmological constraints they provide on the age of the Universe and the Hubble constant, and the future prospects they open.

- Chapter 3 outlines two applications of the cosmic chronometers approach in different redshift regimes. In both, the first part is dedicated to the survey description and to the selection of a pure sample of massive and passive galaxies. A detailed characterisation of the physical properties of the cosmic chronometers is then followed by the derivation of a new measurement of $H(z)$ at high redshift.

- Chapter 4 summarises the main results of this Thesis, presenting the new constraints on the evolution of the Hubble parameter and on its local value. The Chapter concludes by discussing the current limitations and how they can be overcome with future observational facilities and methodological improvements.

1.1 The history of an expanding Universe

1.1.1 Early 20th century – Theoretical foundations

The modern theory of cosmology has undergone significant developments throughout the 20th century, grounded in Einstein's General Theory of Relativity (GR). The essence of GR lies in its revolutionary view of gravity as a manifestation of the geometry of space-time, rather than as a force acting at a distance. The curvature of space-time is determined by its matter and energy content, as expressed through Einstein's field equations (Einstein, 1915, 1916):

$$R_{\mu\nu} - \frac{1}{2} g_{\mu\nu} R = \frac{8\pi G}{c^4} T_{\mu\nu} \,, \tag{1.1}$$

where $R_{\mu\nu}$ and $g_{\mu\nu}$ are respectively the curvature and the metric tensors, R is the scalar curvature, and $T_{\mu\nu}$ is the energy-momentum tensor. This equation substantially embodies the equivalence between the space-time geometry, on the left-hand side, and the distribution of energy and momentum, on the right-hand side.
The space-time interval between two infinitesimally close events is defined as

$$\mathrm{d}s^2 = g_{\mu\nu}, \mathrm{d}x^\mu \mathrm{d}x^\nu \,, \qquad \mu, \nu = (0, 1, 2, 3) \,, \tag{1.2}$$

where $\mathrm{d}s^2$ remains invariant under inertial coordinate transformations. The coordinates are denoted by $x^\mu = (ct, x_1, x_2, x_3)$, representing one temporal and three spatial dimensions.

These equations admit dynamic solutions only, corresponding to universes that either expand or contract. In 1917, however, in an attempt to obtain a static universe model consistent with the prevailing belief of the time (i.e., that the Universe was eternal and unchanging), Einstein introduced the cosmological constant, Λ, (Einstein, 1917):

$$R_{\mu\nu} - \frac{1}{2} g_{\mu\nu} R - \Lambda g_{\mu\nu} = \frac{8\pi G}{c^4} T_{\mu\nu}. \tag{1.3}$$

Although he later referred to the introduction of Λ as the "biggest blunder" of his life, we are going to see how the cosmological constant made a remarkable comeback and became one of the cornerstones of modern cosmology. Depending on its position in the equation above, the Λ term can be either interpreted as a geometrical modification of the space-time (left), or as an additional energy component with negative pressure (right).

The FLRW metric. Besides General Relativity, the other fundamental pillar of modern cosmology is the Cosmological Principle, which states that the Universe is homogeneous and isotropic on sufficiently large scales. This means that the Universe's properties are both invariant by translation (homogeneity) and by rotation (isotropy). Under this hypothesis, and assuming the validity of GR, the space-time metric can be expressed as:

$$\mathrm{d}s^2 = -c^2 \mathrm{d}t^2 + a^2(t) \left[\frac{\mathrm{d}r^2}{1 - kr^2} + r^2 (\mathrm{d}\theta^2 + \sin^2 \theta \mathrm{d}\phi^2) \right], \tag{1.4}$$

where (r, θ, ϕ) are the comoving polar coordinates adopted, k describes the spatial curvature of the Universe, and $a(t)$ is the scale factor, which relates physical (X) and comoving (x) coordinates through $X(t) = a(t)x$. The scale factor is conventionally normalised such that $a(t_0) = 1$ at the present time. The

curvature parameter k can take values greater than, equal to, or smaller than zero, corresponding to closed (spherical), flat (Euclidean), or open (hyperbolic) geometries, respectively.

This formulation was first introduced in the 1920s by Alexander Friedmann, then Georges Lemaître related it to the expanding-universe solutions of Einstein's equations, while in the mid-1930s Howard P. Robertson and Arthur G. Walker independently demonstrated that this is the most general form of the metric consistent with the assumptions of homogeneity and isotropy. Hence, Eq. 1.4 takes the name of Friedmann–Lemaître–Robertson–Walker (FLRW) metric, and nowadays provides the geometrical framework on which the standard cosmological model is built.

Starting from the FLRW metric, we can define the distance between two objects at different points in space-time. In particular, the *proper distance* is defined as the spatial separation between two points measured at a fixed cosmic time (i.e., for $\mathrm{d}t = 0$). Assuming the FLRW metric and choosing a coordinate system where, without loss of generality, $\mathrm{d}\theta = \mathrm{d}\phi = 0$, the proper distance can be written as

$$d_{\mathrm{PR}} = \int_0^r \frac{a(t)\mathrm{d}r'}{\sqrt{1-kr'^2}} = a(t)F(r), \qquad F(r) = \int_0^r \frac{\mathrm{d}r'}{\sqrt{1-kr'^2}}, \tag{1.5}$$

where the second equality holds because the scale factor $a(t)$ does not depend on r. Since the scale factor varies with cosmic time, the proper distance between two objects also changes as the Universe evolves. The *comoving distance*, on the other hand, is defined as the proper distance between two points evaluated at the present time, t_0, and is related to the proper distance at any epoch by

$$d_{\mathrm{C}} = a(t_0)F(r) = \frac{a(t_0)}{a(t)} d_{\mathrm{PR}}. \tag{1.6}$$

From now on, a subscript zero will be used to denote quantities evaluated at the present time (t_0). When we evaluate the comoving distance at a generic time T_{obs}, we obtain the *comoving horizon*, which represents the size of the region of space that is causally connected at that time.

The Hubble-Lemaître law. In 1927, Georges Lemaître first derived, from the relativistic solutions of Einstein's equations, a linear relation between the recession velocity of galaxies and their distance, providing the theoretical foundation for what later became known as the Hubble–Lemaître law. A few years later, Edwin Hubble observationally confirmed this relation, showing that the recession velocity of galaxies increases with their distance, regardless of the direction in which they are observed.

At first sight, this behaviour could be interpreted as if the Milky Way (MW) occupied a privileged position in the Universe, with all other galaxies moving away from us. However, when interpreted within the framework of the Cosmological Principle, this same law must hold everywhere in the Universe. Therefore, the observed recession of galaxies is not due to their motion through space, but rather to the expansion of space itself, reflected in the increasing scale factor $a(t)$ in the FLRW metric.

We can easily derive this distance-velocity relation by computing the first derivative in time of the proper distance:

$$v = \frac{\mathrm{d}}{\mathrm{d}t} d_{\mathrm{PR}} = \dot{a}(t)F(r), \tag{1.7}$$

which, knowing that $F(r) = d_{\mathrm{PR}}/a(t)$, becomes:

$$v = \frac{\dot{a}(t)}{a(t)} d_{\mathrm{PR}} = H(t) d_{\mathrm{PR}}, \tag{1.8}$$

where $H(t) = \dot{a}(t)/a(t)$ is the Hubble parameter, measured in km s^{-1}Mpc^{-1}. When evaluated at the present time, t_0, H_0 is referred to as the Hubble constant, and Eq. 1.8 takes the original form of the Hubble-Lemaître law (Lemaître, 1927; Hubble, 1929).

The value of the Hubble constant, H_0, is today one of the most debated quantities in cosmology, as will be discussed later on. A commonly adopted reference value is $H_0 \simeq 70$ km s^{-1} Mpc^{-1}. In the nearby Universe, this expansion rate is comparable to or even smaller than the typical peculiar velocities induced by the gravitational attraction of neighbouring galaxies. For instance, the Milky Way and the Andromeda galaxy are moving towards each other at about 120 km s^{-1}. At larger distances, however, the Hubble flow increasingly dominates over peculiar motions, and the recession velocity of galaxies becomes a more direct tracer of the global expansion of the Universe.

Cosmological redshift. In an expanding Universe, cosmological distances can be measured by evaluating the position of well-known spectral lines in galaxy spectra, and comparing them with their rest-frame values, to quantify how much they have been shifted towards redder wavelengths. This shift, known as the cosmological redshift, arises because, as a consequence of the expansion, the light emitted from a distant source undergoes the Doppler effect. If we consider a photon emitted at time t with wavelength $\lambda_{\rm em}$, that we observe today, at t_0, the observed wavelength, $\lambda_{\rm obs}$, will be:

$$\lambda_{\rm obs} = \frac{a(t_0)}{a(t)}\lambda_{\rm em} = \frac{1}{a(t)}\lambda_{\rm em}, \tag{1.9}$$

owing to the expansion of the Universe between t and t_0, and to the usual assumption that $a(t_0) = 1$. The cosmological redshift is then defined as:

$$z = \frac{\lambda_{\rm obs} - \lambda_{\rm rest}}{\lambda_{\rm rest}} = \frac{1}{a(t)} - 1 \qquad \rightarrow \qquad a(t) = \frac{1}{1+z}. \tag{1.10}$$

If $a(t_0) = 1$ and the scale factor is always increasing with time, this means that $a(t) < 1$ at any epoch, and that z is defined as positive as a consequence.

If we consider the definition of the Hubble parameter given in Eq. 1.8, this can be rewritten in terms of redshift as:

$$H(z) = \frac{\dot{a}(t)}{a(t)} = -\frac{1}{1+z}\frac{{\rm d}z}{{\rm d}t}. \tag{1.11}$$

We can observe here how this equation, which is going to be central throughout this Thesis, relies solely on the assumption of an FLRW metric and on the definition of the cosmological redshift. In addition, by integrating the above equation over redshift, we can retrieve the expression of the cosmic time as a function of z:

$$t(z) = \int_z^\infty \frac{1}{H(z')(1+z')} dz'. \tag{1.12}$$

It is also useful to define the *look-back* time, $t_{\rm LB}$, as the difference between the age of the Universe today and at a certain redshift, z:

$$t_{\rm LB}(z) = t_0 - t(z), \tag{1.13}$$

essentially quantifying the time elapsed from a certain redshift up to now.

Luminosity distance and angular diameter distance. In an expanding Universe, the observed flux of a distant source is affected not only by the geometric spread of photons over the solid angle, but also by time dilation and the cosmological redshift induced by the expansion. The *luminosity distance*,

d_L, is defined as the quantity that relates the intrinsic luminosity, L, of an astrophysical source to its observed flux, f, through: $f = L/(4\pi d_{\rm L}^2)$. In a FLRW Universe, the luminosity distance is directly related to the comoving distance, d_C, as

$$d_{\rm L}(z) = (1+z) d_{\rm C}(z). \tag{1.14}$$

Analogously, the *angular diameter distance*, $d_{\rm A}$, is defined as the distance at which a source of known extension D is observed with an angular separation $\delta\theta$, such that $\delta\theta = D/d_{\rm A}$. Angular diameter distance and comoving distance are linked by:

$$d_{\rm A}(z) = \frac{1}{1+z} d_{\rm C}(z). \tag{1.15}$$

Friedmann models. In 1922, years before the discovery of the expansion of the Universe, Alexander Friedmann, starting from GR and assuming the Cosmological Principle, derived two fundamental equations describing how the scale factor, a, and thus the Hubble parameter, varies with time. These are known as the Friedmann equations (Friedmann, 1922), and they can be written as:

$$\left(\frac{\dot{a}}{a}\right)^2 + \frac{kc^2}{a^2} = \frac{8\pi}{3} G\rho, \tag{1.16}$$

$$\frac{\ddot{a}}{a} = -\frac{4\pi G}{3}\left(\rho + \frac{3p}{c^2}\right), \tag{1.17}$$

where ρ and p are, respectively, the density and pressure of the cosmic fluid, a continuous mixture of different components, each with its own properties. The first, Eq. 1.16, shows that the rate of cosmic expansion increases with the density ρ of the Universe, while the second, Eq. 1.17, shows that increasing pressure and energy density tend to slow down the expansion.

In a flat Friedmann universe, $k = 0$, the first equation becomes:

$$H^2 = \frac{8\pi G\rho}{3}, \tag{1.18}$$

from which we can derive the critical density, $\rho_{\rm crit}$, required to have such null curvature:

$$\rho_{\rm crit} = \frac{3H^2}{8\pi G}. \tag{1.19}$$

This quantity also allows us to define useful adimensional density parameters for each component of the fluid, $\Omega_i = \rho_i/\rho_{\rm crit}$. Considering the global density parameter, Ω, and evaluating Eq. 1.16 in t_0, we obtain:

$$H_0^2(1-\Omega_0)a^2 = -kc^2, \tag{1.20}$$

showing the tight connection between the adimensional density parameter and the space geometry. In particular, $\Omega = 1$ produces a flat curvature, $\Omega > 1$ a positive curvature, and $\Omega < 1$ a negative one.

1.1.2 Late 20th century – Observational pillars and the *concordance* paradigm

If the first half of the 20th century was crucial in establishing the theoretical foundations on which modern cosmology is built, the second half was marked by a series of groundbreaking discoveries that transformed it into a precision science and led to what we now refer to as the standard cosmological model.

Cosmic microwave background. In 1965, a serendipitous discovery by Arno Penzias and Robert Wilson revealed a faint, isotropic radiation in the microwave frequency range that could not be attributed to any specific astrophysical source (Penzias & Wilson, 1965). Its spectrum was found to be extremely well described by a blackbody with a temperature of 2.725 K. This cosmic microwave background (CMB) represents the thermal relic of the early Universe, a snapshot of the epoch following recombination, when the temperature had reduced enough to allow electrons and protons to combine into neutral hydrogen, and to photons to stream freely through space. The discovery of the CMB provided one of the most evident confirmations of the Big Bang model, demonstrating the existence of an epoch in the Universe's history in which it was much hotter and, thus, denser. Moreover, its evident isotropy offered a strong observational support to the cosmological principle, turning it from a mere theoretical assumption into a well-established observational fact.

In 1992, the COBE satellite revealed small fluctuations in the CMB temperature of the order of $\delta T/T \sim 10^{-5}$ (Smoot et al., 1992). The presence of these anisotropies does not contradict the cosmological principle, but confirms that the Universe is homogeneous and isotropic only when averaged over sufficiently large scales. These tiny primordial fluctuations represent the seeds of all cosmic structures that, under the influence of gravity and cosmic expansion, eventually grew into the galaxies, clusters, and large-scale structures we observe today.

Dark matter. Discussions about the existence of dark matter can be traced back to the early 1900s, but it was only with Fritz Zwicky's 1933 observation of the large velocity dispersion in the Coma Cluster (Zwicky, 1933), inconsistent with the gravitational pull of the visible matter, that the concept began to gain increasing credibility. In the 1970s, measurements of spiral galaxies' rotation curves (e.g., Rubin & Ford, 1970), traced through neutral hydrogen emission, revealed that instead of declining as the square root of the distance, as expected from the visible mass distribution, they remained remarkably flat out to the outermost regions. This behaviour again required the presence of a massive, non-luminous component interacting solely through gravity, which became known as *dark matter* (DM).

Further evidence later emerged from gravitational lensing, X-ray emission from galaxy clusters, mass-to-light ratios in galaxies, and large-scale galaxy clustering, all reinforcing not only the presence of this component but also its dominance over its baryonic, luminous counterpart. Despite this consistent observational support, the fundamental nature of dark matter remains unknown to this day.

Dark energy. Approaching the end of the last century, another fundamental turning point was reached with the discovery of the accelerated expansion of the Universe. This breakthrough came from observations of Type Ia supernovae (SNIa), which serve as classical standard candles thanks to the nearly universal behaviour of their light curves. Through extensive surveys carried out by two major collaborations, the *Supernova Cosmology Project* and the *High-z Supernova Search Team*, it became possible to reconstruct the Hubble diagram up to redshift $z \sim 0.8$. The results revealed an unexpected finding: all the observed SNIa at that redshift appeared dimmer than what was predicted in a matter-dominated, decelerating universe, implying that the expansion of the Universe is currently accelerating (Riess et al., 1998; Perlmutter et al., 1999). This implied the need for a new, unknown source of energy, called *dark energy* (DE), responsible for driving this late-time acceleration. Within this framework, the cosmological constant, Λ, made its return, now interpreted as a form of vacuum energy counteracting gravity on cosmological scales. It is the simplest DE candidate, but other possibilities are not excluded.

ΛCDM model

For what we have discussed in this Chapter so far, by the end of the past century, a coherent picture of a *concordance* cosmological model was emerging, capable of reproducing the various observational evidence into a single theoretical framework. This model describes a Universe composed of matter (both baryonic and dark), radiation, and dark energy, the latter often represented by the cosmological constant, Λ. To account for the observed formation and growth of large-scale structures, the model also requires that most of the dark matter exists in the form of cold dark matter (CDM). These last two components, Λ and CDM, seem to dominate the total energy density, contributing approximately 70% and 25% of the whole budget. Baryonic matter, instead, contributes only for the remaining 5%, with a minimal contribution from radiation. Owing to their dominance, this framework is commonly known as the ΛCDM model.

Another fundamental feature of the concordance model concerns the geometry of the Universe. Over the past decades, a combination of independent cosmological probes, including the ones mentioned above, has provided increasingly precise estimates of the total density parameter, Ω_0, which is found to be extremely close to unity. For example, the Planck Collaboration (Planck Collaboration et al., 2020) reports $\Omega_0 = 0.999 \pm 0.002$, implying that the total energy density equals the critical density and that the large-scale geometry of the Universe is consistent with spatial flatness ($k = 0$).

Considering the observational evidence discussed above, namely the accelerated expansion and the spatial flatness of the Universe, the Friedmann equations need a slight reformulation. In particular, having included the cosmological constant in the picture, the terms of pressure and density in Eq. 1.16 and Eq. 1.17 need to accommodate a repulsive term, able to reproduce this accelerated expansion. Specifically, when dark energy is parametrised through the cosmological constant, this can be implemented through the following substitutions:

$$p \rightarrow p - \frac{\Lambda c^4}{8\pi G} \qquad \rho \rightarrow \rho + \frac{\Lambda c^2}{8\pi G}. \tag{1.21}$$

The total energy density, then, will take the form:

$$\sum_i \Omega_i(z) = \Omega_m(z) + \ \Omega_r(z) + \Omega_k(z) + \Omega_\Lambda(z), \tag{1.22}$$

where Ω_k is the curvature parameter $\Omega_k = -kc^2/(Ha)^2$, and Ω_Λ is the Λ density parameter $\Omega_\Lambda = \Lambda c^2/3H^2$.

Each component of the cosmic fluid, then, is characterised by its own equation of state (EoS), relating pressure and density as:

$$p = w(z)\rho c^2, \tag{1.23}$$

where $w(z)$ varies for each component and may, in principle, depend on redshift. In a ΛCDM framework, each component has a constant value of w: $w = 1/3$ for radiation (e.g., photons and relativistic neutrinos), $w = 0$ for matter (including CDM, baryonic matter, and non-relativistic neutrinos), and $w = -1$ for Λ. It is worth noting that this assumption on the dark energy EoS represents a particular case, as an accelerated expansion can be achieved for any $w < -1/3$. Starting from the Friedmann equations and assuming momentum conservation, the general expression of the energy density evolution can be obtained:

$$\rho_i(z) = \rho_{i,0} \exp\left[\int_0^z \frac{3(1 + w_i(z'))}{1 + z'} dz'\right], \tag{1.24}$$

which, in the case of constant w_i, simplifies to:

$$\rho_i(z) = \rho_{i,0}(1+z)^{3(1+w_i)}. \tag{1.25}$$

Finally, combining it with Eq. 1.16 and considering Eq. 1.22, the Hubble parameter can be expressed as a function of redshift, separating the contributions from each component of the fluid:

$$H(z) = H_0\sqrt{\Omega_{r,0}(1+z)^4 + \Omega_{m,0}(1+z)^3 + \Omega_{\mathrm{DE},0}(1+z)^{3(1+w)} + \Omega_{k,0}(1+z)^2} = H_0 E(z), \tag{1.26}$$

where we have defined the normalized Hubble parameter, $E(z) = H(z)/H_0$. Given the current constraints on the radiation density parameter, $\Omega_{r,0} \sim 10^{-5}$, its contribution is usually neglected, particularly at late times ($z \lesssim 10$). Combining this approximation with the assumptions of spatial flatness ($\Omega_k = 0$) and of a cosmological constant characterised by $w = -1$, the expression for the Hubble parameter simplifies to:

$$H(z) = H_0\sqrt{\Omega_{m,0}(1+z)^3 + \Omega_\Lambda}, \tag{1.27}$$

where $\Omega_{m,0} + \Omega_\Lambda = 1$ to preserve spatial flatness.

Alternative dark energy assumptions. In a flat ΛCDM, DE is included in its simplest form, a vacuum energy with constant EoS parameter $w = -1$. As Eq. 1.24 anticipated, though, w could in principle evolve with cosmic time. The most common parametrization used to allow for a time-varying DE is the one proposed by Chevallier and Polarski (Chevallier & Polarski, 2001) and later refined by Linder (Linder, 2003), known as the CPL parametrization:

$$w(z) = w_0 + w_a\left(\frac{z}{1+z}\right). \tag{1.28}$$

When this formalism is adopted, the resulting cosmological model is commonly referred to as an open or flat w_0w_aCDM model, depending on the spatial curvature. In the special case where $w_a = 0$, fixing the time evolution of dark energy, the model reduces to a wCDM cosmology, which in turn coincides with ΛCDM for $w_0 = -1$.

1.1.3 21st century – Precision cosmology and its tensions

At the turn of the 21st century, cosmology entered a new era, that of precision cosmology. Following the groundbreaking discoveries of the previous decades, the ΛCDM framework had to be put under extensive testing, adopting many different independent observables. Different classes of cosmological probes were developed and progressively refined, supported by major advances in both observational facilities and large-scale surveys, as well as in data analysis techniques.

Among these, the ones that stand out as the main pillars of modern precision cosmology are the so-called *standard candles* and *standard rulers*. Standard candles are astrophysical objects whose intrinsic luminosity can be estimated with sufficient precision, independently of their distance. Once the intrinsic luminosity is known, the luminosity distance can be directly inferred from the ratio between the intrinsic luminosity and the observed flux of the source. An analogous approach can be adopted for the angular diameter distance by measuring the apparent size of an object whose physical dimensions are known, thus considered standard rulers. The most important standard candles are supernovae Type Ia, while the most relevant standard rulers are provided by the CMB and baryon

acoustic oscillations (BAO). Here, we provide a brief overview of these three approaches and their most recent results.

Standard candles

Since the luminosity distance depends on the cosmological model through its parameters (e.g., H_0, Ω_m, Ω_Λ), standard candles provide a powerful way to trace the expansion history of the Universe.

In particular, the distance modulus, μ, of a standard candle at redshift z, assuming a cosmological model described by the set of parameters $\theta = \{H_0, \Omega_m, \Omega_\Lambda, \Omega_k, ...\}$, can be expressed as:

$$\mu \equiv m - M = 5 \log_{10} \left(\frac{d_L(z, \theta)}{10 \text{ pc}} \right). \tag{1.29}$$

A well-known example of standard candles are Cepheid variables, a class of pulsating stars that exhibit a well-defined period–luminosity relation, which has long served as a benchmark for distance measurements. Cepheids, however, are too faint to be observed beyond the local Universe. As anticipated in the previous section, the class of astrophysical object that has been most widely used as a cosmological standard candle are SNIa.

SNIa are thought to originate from the binary evolution of a carbon–oxygen (C-O) white dwarf that accretes material from a companion star, until it reaches the Chandrasekhar limit of 1.44 $M_\odot$, above which the degenerate electrons become relativistic and the white dwarf unstable. This instability triggers an internal reaction that converts most of the carbon and oxygen into iron, producing a powerful detonation that completely disrupts the star. The resulting explosion shows two key properties making SNIa optimal cosmological standard candles: a very high peak luminosity, allowing this phenomenon to be seen at cosmological distances, and a well-defined correlation between the peak luminosity and the light-curve decay time. Specifically, brighter supernovae tend to decline more slowly, and the distance modulus can be expressed through a parametrisation of the light curve, as follows:

$$\mu = m_B + \alpha s - \beta c - M_B - \Delta_{\text{bias}} + \Delta_{\text{host}}, \tag{1.30}$$

where m_B is the peak magnitude in B-band, s and c are independent properties of the light curve, namely stretch and colour, α and β are correlation coefficients that help standardize the brightness, and M_B is the absolute magnitude in B-band of a simulated SNIa with $s = c = 0$ (see Tripp, 1998; Guy et al., 2005). Finally, Δ_{bias} and Δ_{host} are two correction terms, the first to account for selection effects and biases predicted by simulations, the second due to residual correlations with host galaxy properties. From the comparison of Eq. 1.29 and Eq. 1.30, it is possible to constrain the set of cosmological parameters, θ.

The major effort in exploiting SNIa as cosmological probes has come in the last years from two different projects, the Pantheon (Brout et al., 2022) and the SH0ES (Riess et al., 2022). The Pantheon and its extended release, Pantheon+, have provided the largest and most homogeneous compilation of SNIa to date, 1550 SNIa covering the range $0.001 < z < 2.26$. On the other hand, the SH0ES project (Supernovae and H_0 for the Equation of State) has focused on building a precise local distance ladder, calibrating the SNIa luminosity through Cepheid variables and nearby galaxies, to provide the most accurate direct measurement of the Hubble constant. In Fig. 1.1, the distance ladder reconstruction made by the SH0ES collaboration is reported.

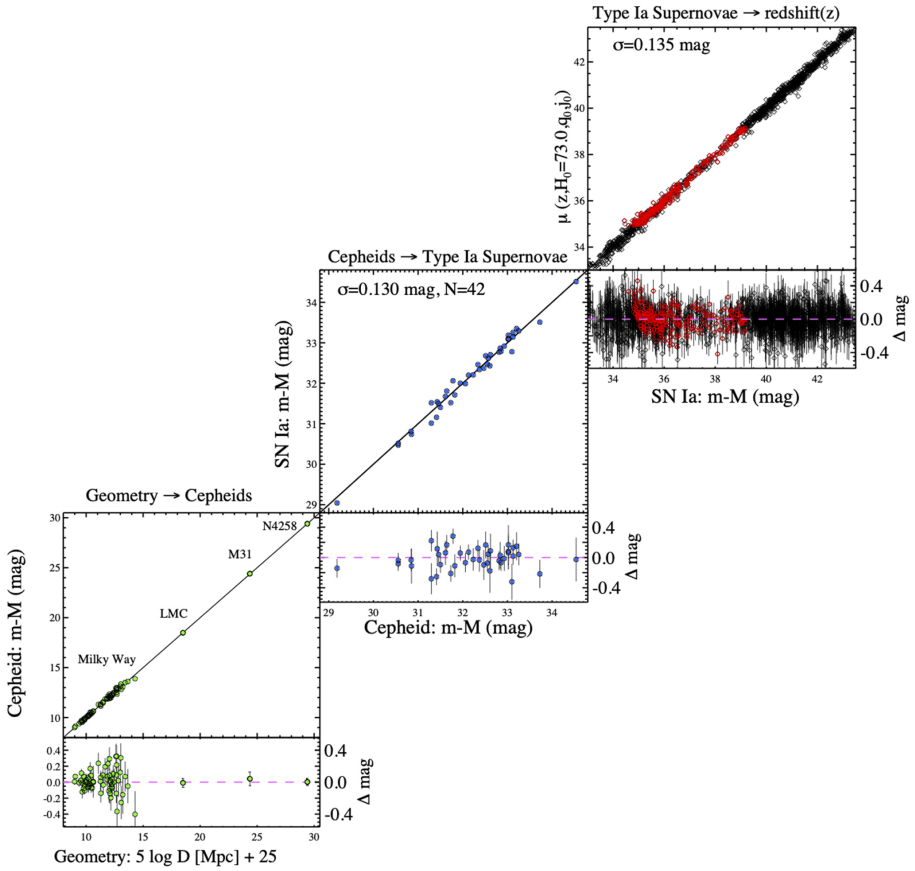

FIGURE 1.1: Reconstruction of the distance ladder from Riess et al. (2022). It shows how SNIa distance measurements are calibrated using Cepheid variable stars, which in turn are anchored to geometric distance measurements, such as those obtained from parallaxes in the Milky Way.

As a result of this extensive effort, the simultaneous fit of these three rungs currently provides the most precise local measurement of the Hubble constant: 73.17 ± 0.86 km s^{-1} Mpc^{-1} (Riess et al., 2022; Breuval et al., 2024).

The cosmic microwave background

As already mentioned in the previous section, the CMB encodes a wealth of information on the early Universe, and has been one of the major focuses of observational cosmology in the past two decades. The goal of subsequent generations of experiments, from *WMAP* to *Planck*, has been to map with increasing precision the temperature anisotropies across the sky. The observed temperature field can be expressed as:

$$\frac{\Delta T}{T}(\theta,\phi) = \frac{T(\theta,\phi) - \langle T \rangle}{\langle T \rangle}, \tag{1.31}$$

where ΔT is the deviation from the mean temperature, $\langle T \rangle$, in the direction identified by the angles (θ, ϕ).

By expanding this temperature perturbation field in spherical harmonics, one obtains:

$$\frac{\Delta T}{T}(\theta,\phi) = \sum_{\ell=0}^{\infty} \sum_{m=-\ell}^{\ell} a_{\ell m} Y_{\ell m}(\theta,\phi), \tag{1.32}$$

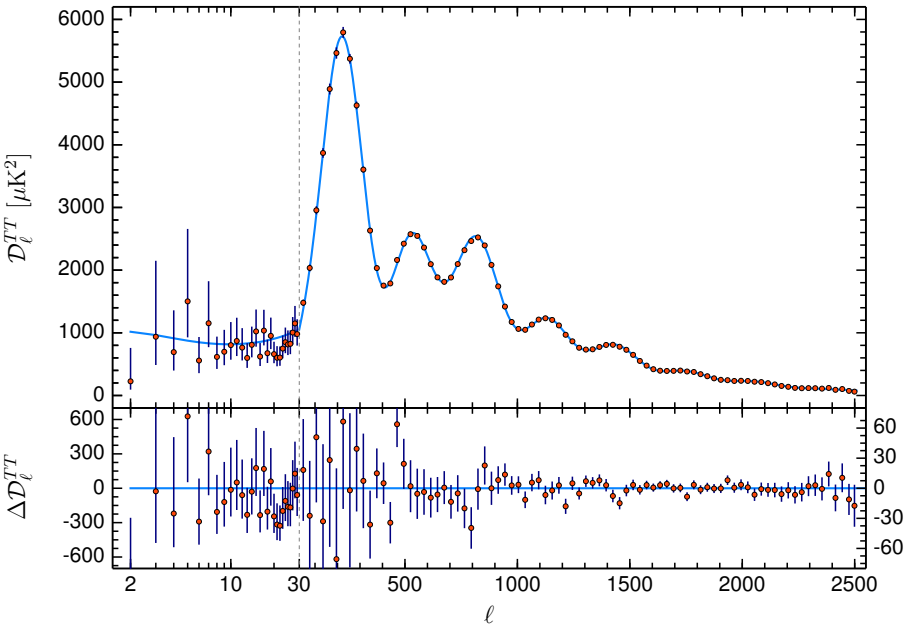

FIGURE 1.2: CMB power spectrum observed by the Planck satellite (red points) in comparison with ΛCDM predictions (blue line) and corresponding residuals. Here $D_\ell^{TT} = \ell(\ell+1)C_\ell/2\pi$. Figure reproduced from Planck Collaboration et al. (2020).

where the coefficients $a_{\ell m}$ represent the amplitude of the temperature fluctuation for a given angular scale, characterized by the multipole moment ℓ. A statistical measure of these fluctuations is given by the correlation function, $C(\theta)$, found by averaging the product of all pairs of values of $\delta T/T$ separated by an angle θ. This correlation function, known as the angular power spectrum of the CMB, takes the expression:

$$C_\ell = \frac{1}{2\ell+1}\sum_{m=-\ell}^{\ell}|a_{\ell m}|^2. \tag{1.33}$$

In general, C_ℓ represents a measure of the temperature fluctuations on the angular scale $\theta \sim 180°/\ell$. The maximum multiple moment that can be probed by a given CMB dataset is limited by the instrument's angular resolution at small scales and by the surveyed sky fraction at large scales.

In Figure 1.2, the shape of the CMB temperature power spectrum observed with the Planck satellite (Planck Collaboration et al., 2020) is reported, showing a well-defined series of acoustic peaks. These arise from oscillations in the tightly coupled photon–baryon fluid that filled the early Universe before recombination. At that epoch, photons and baryons interacted through Thomson and Coulomb scattering, behaving as a single fluid subject to two competing effects: gravitational attraction, mainly due to dark matter overdensities, which tended to compress the fluid, and radiation pressure, which opposed compression. The interplay between these two forces generated standing sound waves, known as acoustic oscillations. Each peak in the power spectrum corresponds to a mode that had reached a different phase of this oscillation by the time of decoupling ($z_{\rm dec} = 1090$), when photons were released and started free streaming through the Universe. The first and most prominent peak, located at an angular scale of $\theta_{\rm hor} \sim 1°$, corresponds to the scale of the sound horizon at recombination. This quantity is directly linked to the size of the sound horizon, $s_{\rm hor}$, through the angular diameter distance ($\theta_{\rm hor} = s_{\rm hor}/d_{\rm A}$), in turn depending on the cosmological parameters Ω_m, Ω_k, and Ω_Λ. Higher-order peaks trace subsequent harmonics, encoding valuable information on the composition and geometry

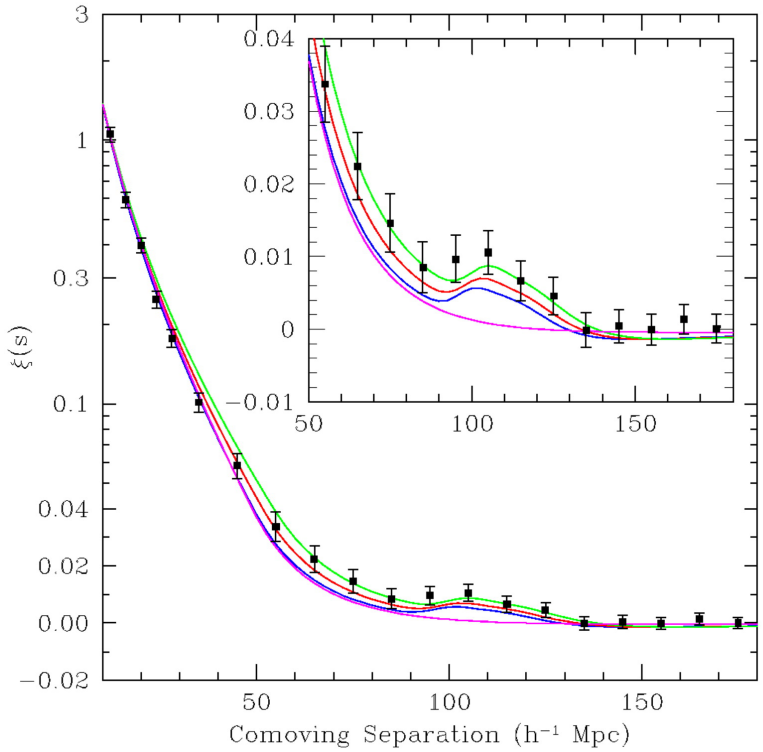

FIGURE 1.3: Two-point correlation function of the SDSS luminous red galaxies sample, represented by the black points. Coloured lines show ΛCDM model predictions with different values of the Ω_m parameter. The observed trend clearly shows a peak at $\sim 105\ h^{-1}$, corresponding to ~ 150 Mpc for $h = H_0/100\ \mathrm{km\,s^{-1}\,Mpc^{-1}} = 0.7$. Figure reproduced from Eisenstein et al. (2005).

of the Universe. For instance, the discrepancy between the amplitude of odd and even peaks depends on the ratio of baryon and photon density, Ω_b/Ω_γ, while the damping of higher-order peaks traces diffusion effects, further constraining Ω_b and Ω_m.

Among the constraints obtainable from the CMB alone, the most striking is that on Ω_k being very close to unity, a strong indication of the spatial flatness of the Universe.

Baryon acoustic oscillations

After the discovery and interpretation of the CMB, a prediction was made that an analogous peak in the power spectrum of temperature oscillations should be observed in the large-scale clustering of galaxies, being them the evolutionary result of those primordial overdensities. The CMB is indeed the result of the baryon-radiation decoupling, meaning that if a map of anisotropies is observed for the photons, the same map of overdensities should be seen in the baryons. After decoupling, the baryon waves stall, and the radius reached by the sound waves becomes imprinted as a preferred scale in the matter distribution. Since baryons and dark matter interact gravitationally, overdensities appear in both components, enhancing the probability that galaxies form separated by this characteristic scale.

In 2005, thanks to the high-volume of surveys like SDSS (Eisenstein et al., 2005) and the 2dF redshift (Cole et al., 2005; Percival et al., 2007), the imprint of these baryon acoustic oscillations was finally observed, detected as a bump in the galaxy two-point correlation function $\xi(r)$ at $r \sim 150$ Mpc, shown in Figure 1.3. It corresponds approximately to the sound horizon at the baryon drag epoch, $z_{\mathrm{drag}} \simeq 1060$,

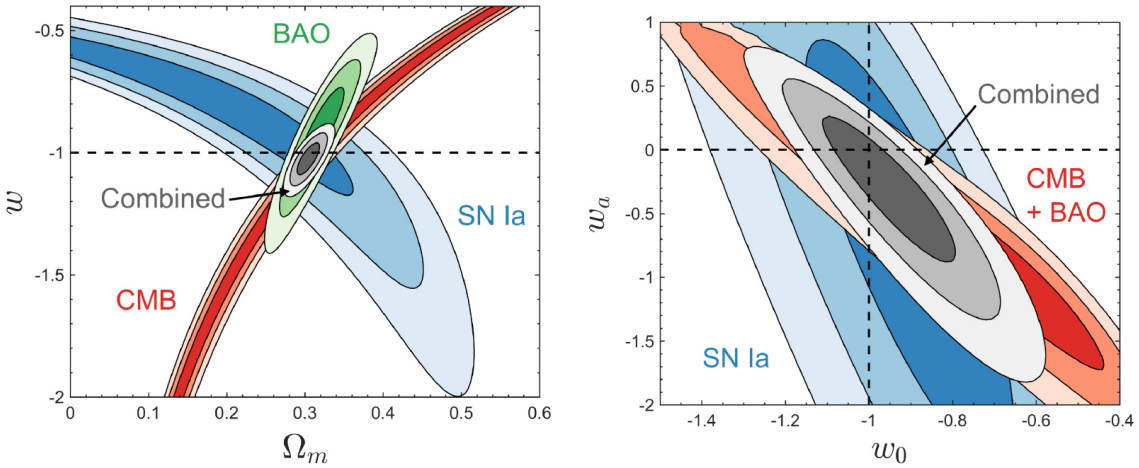

FIGURE 1.4: Constraints resulting from the combination of SNIa, BAO, and CMB, both for $w-\Omega_m$ with constant w, and on w_0-w_a assuming the CPL parametrization (Eq. 1.28). Figure reproduced from Huterer & Shafer (2018).

when baryons stopped being effectively coupled to photons, providing a spectacular confirmation of the standard cosmological model. Tracking the BAO scale across cosmic time has since become a key motivation for large galaxy surveys, offering a standard ruler to probe the expansion history of the Universe.

Each of the cosmological probes discussed so far provides valuable, yet only partial, information on the underlying cosmological parameters. This is because they are differently sensitive to the various quantities and affected by distinct sources of systematics and degeneracies. Moreover, they often trace the Universe across complementary redshift ranges, from the very early epochs probed by the CMB to the late-time acceleration mapped by SNIa and BAO. For this reason, it is only through their combination that their full constraining power can be expressed. This complementarity is clearly illustrated in Figure 1.4, where the joint analysis of these three primary probes, as reported in Huterer & Shafer (2018), shows how their overlap breaks degeneracies and significantly tightens the constraints on the cosmological parameters.

However, this perfect picture of mutual confirmation and remarkable agreement between probes was not destined to last. As increasingly precise data from dedicated surveys became available for each method, small discrepancies began to emerge in the inferred parameters and steadily grew in significance. The concordance picture gradually turned into a puzzle, suggesting the possibility of unrecognised systematic errors or the need for new physics beyond ΛCDM.

The H_0 and S_8 tensions

The value of the Hubble constant was one of the first parameters on which such discrepancies appeared. When derived from early-Universe observations like the CMB, it turned out to be smaller than that obtained from late-Universe techniques based on Cepheids and SNIa. The latest measurements, in particular, show a $4-5\sigma$ tension. Two reference cases, currently leading the Hubble tension, are the one inferred from Planck Collaboration et al. (2020) results assuming a ΛCDM model and the latest

constraint from the SH0ES collaboration (Riess et al., 2022):

$$H_0 = 67.27 \pm 0.60 \quad \mathrm{km\,s^{-1}\,Mpc^{-1}} \quad \text{(Planck)} \tag{1.34}$$

$$H_0 = 73.04 \pm 1.04 \quad \mathrm{km\,s^{-1}\,Mpc^{-1}} \quad \text{(SH0ES)} \tag{1.35}$$

This discrepancy has been extensively analysed in recent years (see, e.g., Di Valentino et al., 2021a; Abdalla et al., 2022; Di Valentino et al., 2025) and many different solutions have been proposed, from early dark energy models, to modified gravity, or yet unaccounted systematic effects. However, no single solution has proved to be fully convincing, and there is still no consensus inside the community on which direction offers the most promising route. In Figure 1.6, a collection of the latest H_0 measurements obtained with the most precise methods available to date is presented, including the two leading measurements mentioned above.

Another quantity showing some level of discrepancy, although with lower significance, is the S_8 parameter. It is usually defined as a combination of Ω_m and the σ_8 parameter, which is the matter power spectrum normalization at $8h^{-1}$ Mpc: $S_8 = \sigma_8 \sqrt{\Omega_m/0.3}$. It quantifies the matter clustering strength, that can be derived both from the primary anisotropies of the CMB and from low redshift gravitational lensing and galaxy clustering. Current measurements show a tension of $2-3\sigma$ between early- and late-Universe constraints (Di Valentino et al., 2021b; Abdalla et al., 2022).

More recently, the first results coming from the Dark Energy Spectroscopic Instrument (DESI, DESI Collaboration et al., 2016), have revealed hints that DE may not behave as a simple cosmological constant, but could instead evolve with time. The first two data releases of DESI, providing BAO constraints based on tens of millions of galaxies, QSOs, and Lyman-α forest tracers, indicate a departure from $w_0 = -1, w_a = 0$ with a significance of 2.5–3.9 σ, depending on the type of probe combination (see, e.g., Lodha et al., 2025a,b). The BAO signal detected with different tracers by the latest DESI results is shown in Figure 1.5, where a dashed line represents the evolving DE solution. While this evidence is not yet conclusive, and may still be subject to revisions, it surely adds another layer of complexity to the current picture.

Within this framework, the best option we have is to diversify our observational approach. In particular, we can investigate the expansion history of the Universe through multiple, independent observational probes, each providing a different and complementary perspective on the underlying cosmological model (for a review, see Moresco et al., 2022).

Among the alternative probes that have emerged and gained increasing relevance in recent years are:

- **Tip of the red giant branch (TRGB).** Old RGB stars with masses below $\sim 1.6\,M_\odot$ develop degenerate helium cores of very similar masses, around $0.5\,M_\odot$. At that point, nuclear burning ignites in this electron degenerate core, producing the so-called *helium flash*. Thanks to the similarity in the core mass, the luminosity of the helium flash is nearly equal, allowing this feature to be exploited as a standard candle. In the local Universe, the TRGB method provides the best alternative to classical Cepheids in constraining the distance ladder.

- **Time delay cosmography (TDC).** When a gravitational lens, like a galaxy cluster, produces multiple images of a background source, which is variable in time (like a quasar or a supernova), it is possible to measure the time delays between different images. This quantity is directly linked to the time-delay distance, a combination of angular diameter distances involving the position

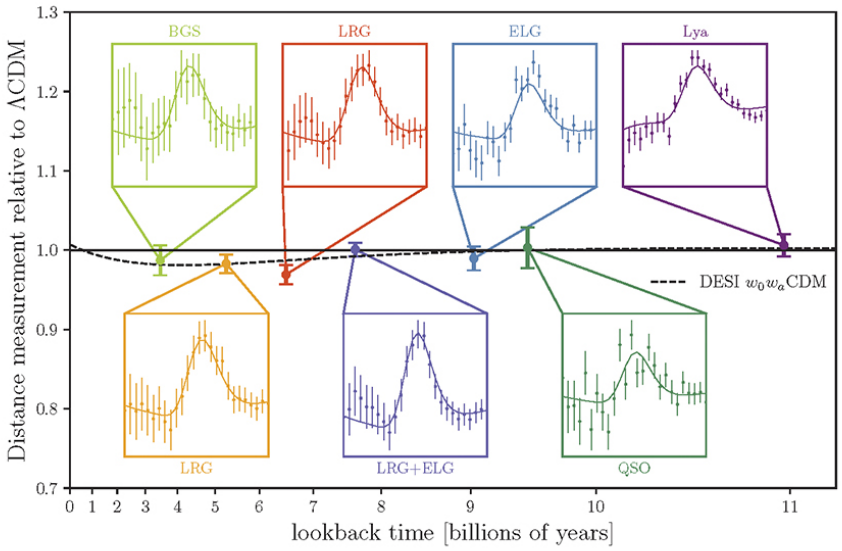

FIGURE 1.5: BAO signal detected from the latest DESI results in seven cosmic epochs (from 3 billion to 11 billion years ago). The solid horizontal line corresponds to the benchmark behaviour in a ΛCDM cosmology, while the dashed line allows for an evolving DE model (w_0w_aCDM). Figure reproduced from Dawson & Palanque-Delabrouille (2025).

of the lens, of the source, and of the observer. After a careful modelling of the lens mass distribution, TDC can provide powerful constraints on H_0.

- **Quasars (QSO).** Being the most luminous non-transient objects, they can be observed up to high redshift (current measurements reach $z \sim 7$). Thanks to the non-linear relation observed between their X-ray and UV luminosities, they allow for an indirect reconstruction of their luminosity distance (see, e.g., Risaliti & Lusso, 2015, 2019).

- **Gamma-ray bursts (GRB).** Very luminous transients observable in X/gamma rays, GRB are not, per se, standard candles, but show correlations between distance-dependent and rest-frame observable quantities, allowing them to be used as distance indicators. The most widely used correlation is the one from Amati et al. (2008), between the GRB peak energy, $E_{p,i}$, and its isotropic radiated energy, $E_{\rm iso}$.

- **Standard Sirens.** The merging of binary black holes and neutron stars produces ripples in the space-time metric (gravitational waves, GWs) which can now be "heard" through the large GW interferometers LIGO, Virgo, and Kagra. These events provide direct information onthe system's luminosity distance without any need for external calibration (like SNe). The redshift of the source, though, is strongly degenerate with binary masses and needs to be inferred from external information, like an electromagnetic counterpart or a galaxy catalog. In this case, these systems can be used as cosmological probes to constrain the expansion history of the Universe.

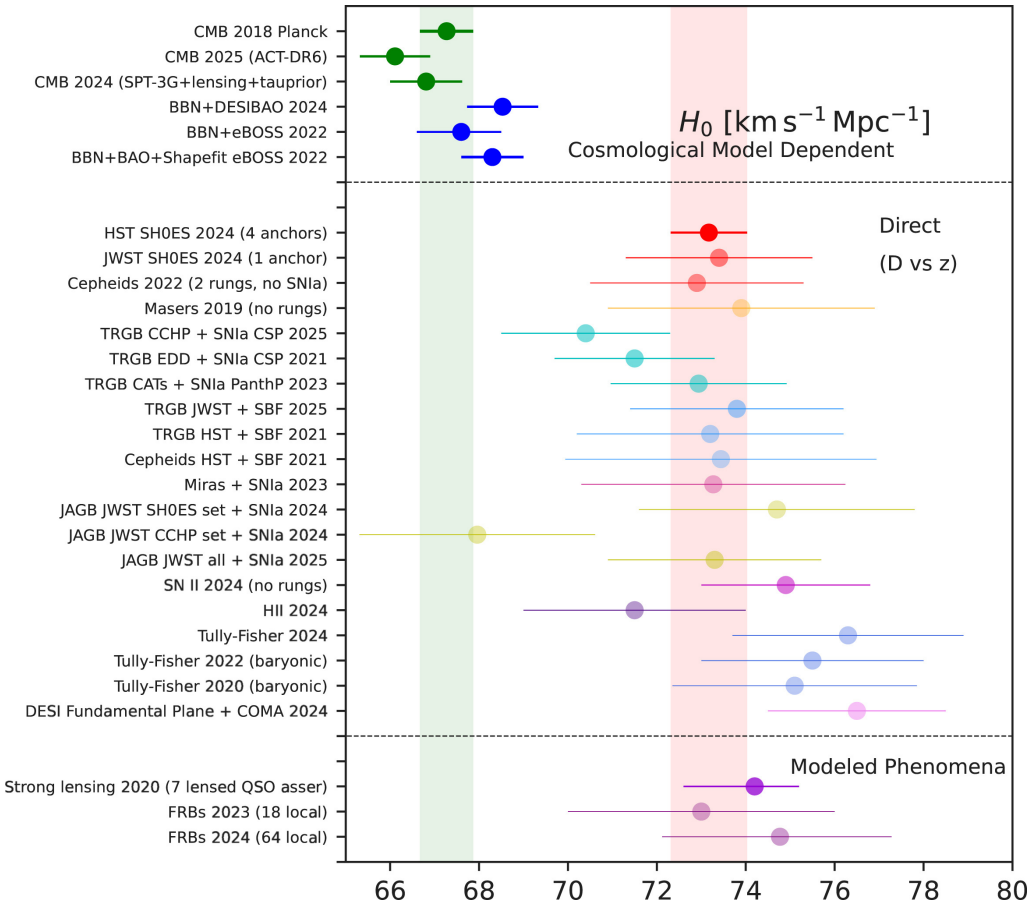

FIGURE 1.6: Summary of the most recent H_0 measurements from the currently most precise cosmological probes. Figure reproduced from Di Valentino et al. (2025).

It's about time! So far, we have discussed how observational cosmology can be pursued through a variety of approaches, all relying on two primary tracers: distances and luminosities. Standard candles, standard rulers, and, more recently, standard sirens, all constrain the expansion history of the Universe through geometric measurements, involving either the luminosity distance or the angular diameter distance. There exists, however, an alternative possible route, that does not rely on any distance measurement. Instead of constraining how far or how bright an astrophysical source appears, we can directly trace the temporal evolution of the Universe, making time itself the key observable. This can be achieved by probing the age of its most long-lived constituents, effectively behaving as *standard clocks* or *standard chronometers*. This alternative route will represent the main focus of this Thesis.

Before exploring the details of these alternative approaches, discussed in Section 1.2, a parenthesis is necessary to present the theory of structure formation, to understand which astrophysical objects can be used as standard clocks and chronometers, and why.

1.1.4 Structure formation in an expanding Universe

Many of the properties of the objects we observe in the present-day Universe have their roots in the earliest stages of cosmic history, well before the appearance of the first luminous sources, and even before the emission of the CMB. During the first few minutes after the Big Bang, in an epoch usually

called *Big Bang Nucleosynthesis* (BBN), the initial conditions in which cosmic structures would later evolve were established. Right after the Big Bang, as the primordial Universe began its expansion, the temperature dropped and the first nuclei could form: mainly hydrogen, *H*, helium, *He*, and a fraction of lithium, *Li*. Yet, the density was still too high to allow the production of heavier elements.

For a long time, approximatively 400'000 years, the Universe remained a hot, dense plasma in which the formation of neutral atoms was inhibited. As the expansion continued, however, the temperature eventually dropped enough for electrons and nuclei to combine. This transition, as already mentioned when discussing the CMB, was not instantaneous, but is commonly placed around $z = 1100$, when the temperature was about 3000 K, and most of the photons had underwent their *last scattering*.

From recombination onward, the Universe entered the so-called *Dark Ages*, a long and quiet epoch during which it was made only of neutral gas, and no luminous object existed yet. At that time, however, dark matter, decoupled from radiation long before recombination, had already started to collapse into gravitational wells. After recombination, the small inhomogeneities of the neutral gas, imprinted into the CMB, were no more sustained by radiation pressure, and could finally start to grow under the gravitational pull of DM.

Dark ages lasted roughly 100'000 Myr, after which the first generation of stars, known as *Population III* stars (PopIII), is thought to have formed within DM halos of $\sim 10^6 M_\odot$. Following the collapse of protostellar structures, the first thermonuclear reactions ignited in the cores of PopIII stars, irradiating their surroundings. This marked the beginning of the *Reionization era*, during which the very energetic ultraviolet radiation emitted by PopIII stars photoionised the neutral gas. The combination of a pristine chemical composition, high virial temperatures, and the absence of dust and magnetic fields, suggests that these first stars were extremely massive, likely reaching several hundred solar masses. For this reason, their evolution and following death occurred very rapidly, through violent supernova explosions. The energy release of such events prevented the DM haloes in which PopIII stars formed from retaining most of the expelled gas, delaying the formation of subsequent structures. Nevertheless, the existence and death of this pristine population filled the Universe with the very first metals, i.e., elements heavier than *He*. In particular, elements such oxygen (O), magnesium (Mg), calcium (Ca), or silicon (S), the so-called α-elements, and a small fraction of iron (Fe), began to enrich the surrounding gas clouds.

The formation of the first galaxies likely occurred after some hundreds millions years, in larger dark matter haloes of $\sim 10^8 M_\odot$. In a cold DM scenario, the growth of these halos follows a hierarchical assembly process, involving mergers with other halos and the accretion of diffuse dark matter. This characteristic threshold of $\sim 10^8 M_\odot$ is necessary to allow the collapse of enough mass to retain a significant part of the gas expelled during stellar evolution, thus prolonging the star formation and establishing the *baryon cycle*. In this framework, stars form in molecular clouds inside the galaxy, sharing the same initial chemical composition. They then evolve on timescales determined by their mass and ultimately die, returning metal-enriched material to the surrounding environment through supernova explosions or planetary nebulae.

The stellar populations following Pop III stars, that we can still observe in the present-day Universe, are classified as Population II (Pop II) and Population I (Pop I) stars. The first class formed from a gas that had been enriched in α-elements from the previous generation, but poorly in *Fe*. The second, on the other hand, formed from a gas that had already experienced multiple cycles of star formation, and thus contains a significant amount of iron and heavy elements originating from SNIa explosions. Differently from core-collapse ones, SNIa are indeed characterised by a complete disruption of the star, including the iron core, and is thus responsible for most of the pollution by iron-peak elements. For

this reason, metal-poor structures are generally considered the oldest objects in the Universe, whereas a metal-enriched environment is indicative of a younger star or stellar population. It is important to note, however, that in regions experiencing very intense and rapid star formation, the timescale for the first SNIa explosions can be as short as ∼40 Myr (see, e.g., Matteucci & Recchi, 2001). Consequently, the existence of very old but relatively metal-rich, α-element-poor systems is not prevented.

After these early phases, galaxy formation proceeded following different paths depending on many factors (i.e., interactions with other systems, merging, properties of the gas) leading to the wide range of galaxy types we observe today. The main class of galaxies of interest in this work is that of *early-type* galaxies (ETGs), mainly ellipticals and lenticulars, as opposed to *late-type* galaxies (LTGs), including spirals and irregulars. ETGs are typically very massive systems with little or no ongoing star formation, and are therefore often referred to as passive or quiescent. They are also characterised by red colours, which indicate the presence of very old and evolved stellar populations. LTGs, instead, display blue colours and high star formation rates, reflecting the dominance of a young and active stellar component.

The formation scenario of ETGs follows the *two-phase* model (Oser et al., 2010) in which a first rapid formation period happening *in-situ* is followed by a phase of external mass accretion via merging. In addition, numerous evidences suggest that the most massive systems are the ones to form first, in intense and short bursts of star formation, while less massive ones form later and take more time. This paradigm is known as *mass-downsizing* (Cowie et al., 1996; Cimatti et al., 2006; Thomas et al., 2010) and is now one of the pillars of galaxy formation models.

Besides theoretical modelling, galaxy formation and evolution can be investigated observationally through two complementary approaches. The *archaeological* approach focuses on present-day galaxies and aims to reconstruct their past histories from their current properties, effectively treating them as cosmic fossils. The *look-back* approach, on the other hand, relies on observations of galaxies at high redshift, providing a direct view of how their properties evolve over cosmic time.

1.2 Timing the Universe

In Section 1.1, we outlined the current cosmological framework, its main pillars, and the challenges it currently faces. We emphasised the need for alternative and independent methods to reconstruct the expansion history of the Universe and highlighted how using *time* as a direct tracer represents a promising avenue. In this section, we discuss the details of these approaches, which we will refer to from now on as *cosmic clocks* and *cosmic chronometers*.

1.2.1 Cosmic clocks

The cosmic clocks approach relies on a simple yet powerful, concept: the Universe must be older than any astrophysical objects it hosts. This means that if we are able to measure the age of the most long-lived structures in the Universe, like very old stars or globular clusters (GCs), these can provide a lower limit to the cosmic age itself.

From the cosmological perspective, we already discussed how, from the assumption of an FLRW metric, the cosmic time can be expressed as a function of redshift as in Eq. 1.12. The age of the Universe at the present time can be obtained from that equation simply by integrating the expression from $z = 0$ to $z = \infty$:

$$t_U = \frac{977.8}{H_0} \int_0^\infty \frac{\mathrm{d}z'}{E(z')(1+z')} [\mathrm{Gyr}], \tag{1.36}$$

where we recall that $E(z) \equiv H(z)/H_0$ and the multiplicative constant converts t_U to Gyr units. Inverting this relation immediately shows that constraining t_U provides a direct constraint on H_0: the larger the inferred cosmic age, the smaller the corresponding H_0.

To compute the integral in Eq. 1.36, however, a specific functional form must be assumed for $E(z)$, and therefore a cosmological model. For instance, in a flat ΛCDM cosmology, the previous equation can be expressed as:

$$t_U = \frac{977.8}{H_0} \int_0^\infty \frac{\mathrm{d}z}{(1+z)} [\Omega_m (1+z)^3 + (1-\Omega_m)]^{-1/2}, \tag{1.37}$$

Although the age of the Universe cannot be directly measured, we can still constrain it by targeting its oldest constituents. Suppose we measure the age, $t_\star$, of an old star at $z = 0$; then H_0 can be derived as:

$$H_0 = \frac{977.8}{t_\star} \int_0^{z_\mathrm{F}} \frac{\mathrm{d}z}{(1+z)} [\Omega_m (1+z)^3 + (1-\Omega_m)]^{-1/2}, \tag{1.38}$$

where z_F is the star's redshift of formation. This latter quantity cannot be constrained from observations, but for very old stars or GCs we can rely on theoretical models of stellar formation providing an upper limit for z_F (typically $z \sim 20-30$ for PopIII stars, see, e.g., Galli & Palla, 2013; Bromm & Yoshida, 2011), while spectroscopic confirmations of the most distant galaxies set an observational lower bound ($z \geq 11-14$, Curtis-Lake et al., 2023; Carniani et al., 2024).

One of the most recent studies applying the cosmic clocks approach to a collection of different objects can be found in Cimatti & Moresco (2023), whose results are reported in Figure 1.7. The constraints on H_0 were obtained applying Eq. 1.38 to a collection of the oldest objects in the Universe available in the literature, from the oldest metal-poor star to GC. In this case, z_F is assumed to vary uniformly in the range $11 < z_\mathrm{F} < 30$ and a Gaussian constraint on $\Omega_m = 0.3 \pm 0.02$ is applied, relying on late-Universe constraints (Jimenez et al., 2019).

To understand the relevance of this approach, for instance, in the context of the Hubble tension, we can apply Eq. 1.37 with the two measurements currently leading the tension: $H_0 = 67.4 \pm 0.5$ km/s/Mpc

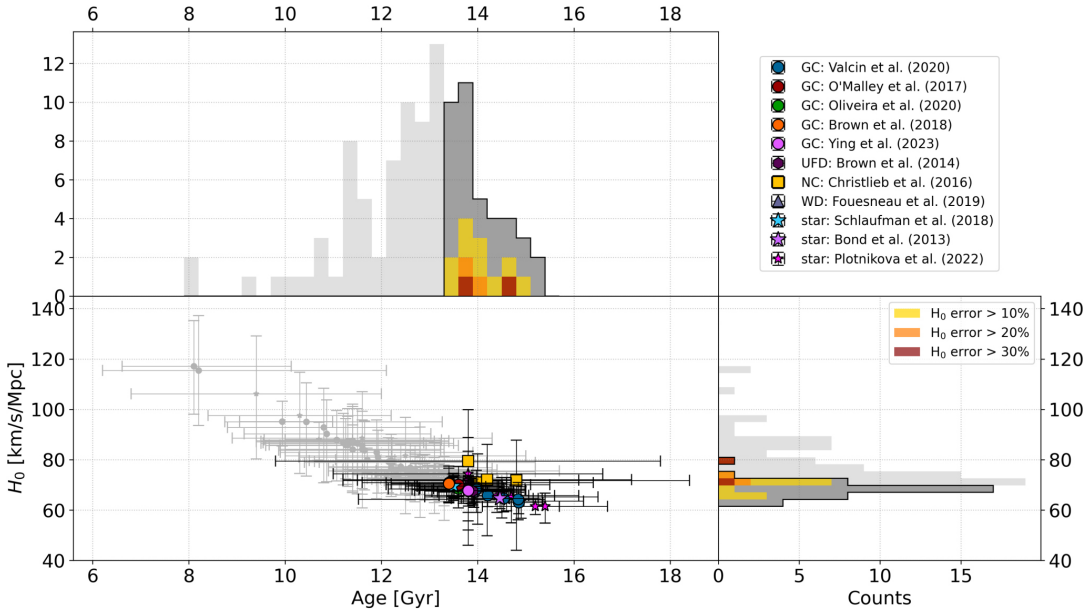

FIGURE 1.7: H_0-age measurements from Cimatti & Moresco (2023), derived from a sample of the oldest stars and GCs available in the literature. In grey, the whole age sample analysed is reported, while coloured points represent the tail of the oldest ones. The latter are also highlighted in the age and H_0 histograms.

(Planck Collaboration et al., 2020) and $H_0 = 73.04 \pm 1.04$ km/s/Mpc (Riess et al., 2022). In a flat ΛCDM model with $\Omega_m = 0.3$, they correspond to $t_U = 14.0 \pm 0.1$ Gyr and $t_U = 12.9 \pm 0.2$ Gyr, respectively. Therefore, measuring t_U with an accuracy of about 10% can provide independent and crucial insights into this subject.

Since this method relies on age measurements of intrinsically faint objects, it has so far been applied only locally, analysing stars and GCs in the Milky Way (e.g., O'Malley et al., 2017; Jimenez et al., 2019; Cimatti & Moresco, 2023; Valcin et al., 2025). However, with the advent of the *James Webb Space Telescope* (JWST), a plethora of potential local GC progenitors have been observed, thanks to JWST's unprecedented sensitivity combined with gravitational lensing. Indeed, in lensed fields, such stellar clumps could be detected up to very high redshift, like the *Firefly Sparkle* at $z \sim 8.3$ (Mowla et al., 2024), or the *Cosmic gems* at $z \sim 10.2$ (Adamo et al., 2024). Applying the cosmic clocks approach with these sources does not require any modification other than replacing the lower bound in 1.38 with the redshift at which they are observed.

1.2.2 Cosmic chronometers

The cosmic chronometers (CC) method is an emerging cosmological probe, providing a direct and independent way of measuring not only the local value of the expansion rate of the Universe (the Hubble constant, H_0), but more importantly, its evolution with redshift, traced by the Hubble parameter, $H(z)$ (for a review, see Moresco et al., 2022; Moresco, 2023). First proposed by Jimenez & Loeb (2002), it is based on the fundamental relation between cosmic time and redshift that we derived in Eq. 1.11:

$$H(z) = -\frac{1}{1+z}\frac{dz}{dt}, \tag{1.39}$$

directly resulting from the minimal assumption of an FLRW metric. This expression shows that it is possible to measure the value of $H(z)$ if we can probe the relation of cosmic time with redshift, specifically, its slope. As in the case of the clocks, cosmic time is not a direct observable, but its redshift evolution can be tracked by measuring the ageing of a population of objects mimicking the ageing of the Universe itself. On the one hand, if spectroscopic redshifts are available for the selected population, measuring z and its differential, $\mathrm{d}z$, is straightforward. On the other hand, particular care must be taken when measuring the time differential, $\mathrm{d}t$, involving the selection of a reliable CC sample and the robust and accurate measurement of their differential ageing.

The ideal astrophysical objects to be considered as CCs must be as coeval as possible, like chronometers that started ticking simultaneously, and observable across a wide range of cosmic epochs. Massive, passively evolving galaxies have proven to be the best CC candidates so far. As anticipated in Section 1.1.4, there is large consensus in literature on the fact that these galaxies have formed in the distant Universe[1] ($z > 2-3$, Citro et al., 2017; Carnall et al., 2018; Estrada-Carpenter et al., 2019), and in very short bursts ($\tau < 0.3$ Gyr Thomas et al., 2010; Carnall et al., 2018), after which they their evolution proceeded passively.

Selecting such homogeneous sample of passive galaxies is not trivial, and various works have shown how a single criterion is not enough for an accurate selection of purely passives, with no residual ongoing star formation (Moresco et al., 2013; Belli et al., 2017; Leja et al., 2019b). For this reason, a combination of different selection criteria is typically adopted, usually:

(i) a photometric criterion, removing from the sample most of the young UV-emitters. Colour-colour diagrams are usually adopted for this purpose, like the NUVrJ (Ilbert et al., 2013), the UVJ (Williams et al., 2009), or the NUVrK (Arnouts et al., 2013);

(ii) one, or more, spectroscopic cuts, targeting emission lines associated with potential ongoing star formation, as the [OII]λ3727, Hβ, [OIII]λ5007, or Hα. A selection based both on the equivalent width (EW) of the lines, and on their signal to noise (S/N) can be adopted for this purpose;

(iii) a cut in stellar mass, or equivalently, in velocity dispersion, to remove the less massive systems and ensure homogeneity of the CC sample, as expected in a mass-downsizing scenario. A cut around $\log(M/M_{\odot}) > 10.6-11$ is typically adopted.

We defer to the next section the discussion on how galaxy ages are estimated in practice. Here, instead, we focus on the main systematic effects that should be taken into account when applying the CC method (see Moresco et al., 2018, 2020, for a comprehensive discussion):

- Stellar population synthesis (SPS) models assumption. This is likely the main source of systematics in the CC method, although a comprehensive assessment of its impact is still required. For example, in Moresco et al. (2020), the aging of a selected CC sample was inferred using the D4000 spectral feature, a break at 4000 Å that correlates with the age of the stellar population. Using this approach, differences between SPS models contributed a 4.5% uncertainty to the final $H(z)$ measurement, while the choice of the initial mass function (IMF) had a smaller impact of 0.4%. While hese results are encouraging, the effect of SPS model variations must still be quantified when employing other age–dating techniques, such as full spectral fitting.

- Error in the star formation history (SFH). Massive passive galaxies are often modelled under the assumption that they formed in a single, instantaneous burst of star formation. However, even

[1] Thanks to JWST, massive and passive galaxies are now found even at $z > 4-5$ (Carnall et al., 2023, 2024).

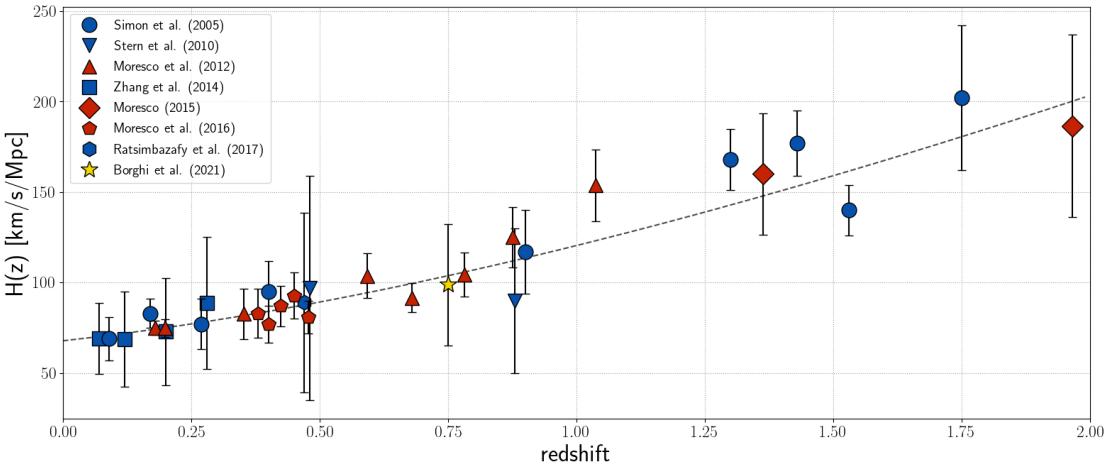

FIGURE 1.8: Collection of $H(z)$ measurements obtained with the cosmic chronometers method presented in Moresco et al. (2022). Different colours correspond to different methods used to constrain the ageing, specifically: full spectrum fitting (blue), D4000 feature (red), and Lick indices (yellow).

if their formation timescales were indeed short, this approximation is not fully realistic and may introduce biases in the final results. A careful evaluation of the star formation history (SFH) that best reproduces the observational data, as well as the impact of the adopted SFH model on the inferred ages and on $H(z)$ measurements, is therefore essential. We will investigate this aspect in more detail in Section 3.1.

- Rejuvenation effect. Although selected to be passive, some massive galaxies may experience minor episodes of residual star formation. Since they dominate the light in the blue part of the spectrum, even a very small fraction can bias the age estimate towards younger values, hence producing an overestimation of $H(z)$. To mitigate, and possibly erase this effect, the use of diagnostics like the H/K, defined as the relative strength of the Ca II H and Ca II K absorption lines, have been proposed to quantify the fraction of contamination from recently formed stars (see, e.g., Moresco et al., 2016; Borghi et al., 2022a).

- Progenitor bias. When selecting a passive population over a given redshift interval, one must consider that galaxies at the lower-z are naturally more evolved than those at higher redshift. As a consequence, a given selection criterion may preferentially remove a larger fraction of galaxies in the high-z part of the sample than in the low-z one, producing a bias in the reconstruction of the age-z trend. In the CC approach though, the redshift intervals considered are typically very narrow, which significantly reduces the impact of this effect. A quantitative assessment of this effect was done in Moresco et al. (2012) where a $\sim 1\%$ contribution was found on the estimated $H(z)$.

It is important to emphasize that the CC approach relies on the robustness of *differential* age measurements, meaning that all uncertainties that affect absolute age determinations largely cancel out when computing age differences between adjacent redshift bins. In Figure 1.8 a collection of all measurements obtained with the CC method to date is reported.

1.3 Measuring ages for astrophysical objects: stars, globular clusters and galaxies

Despite the wealth of information that can be extracted from stellar ages, measuring them represents one of the most persistent and delicate challenges in astrophysics. Unlike quantities such as mass, luminosity, or chemical composition, age is not something that can be accessed through a direct measurement. Instead, it needs to be reconstructed indirectly, by comparing theoretical models of stellar evolution with the limited observables available to us, be they surface temperatures and luminosities, oscillation modes, chemical abundances, or integrated spectra (see Soderblom, 2010, for a review). Each of the available methods introduces its own uncertainties and assumptions, which means that the age we assign to a star is always, to some degree, model-dependent. In fact, among all the stars we can study, the Sun remains the only one for which we possess a truly precise and accurate age estimate, measured through abundances and products of radioactive nuclides in meteoritic material. On the bright side, the age determination of the Sun provides a unique and invaluable benchmark, serving as a solid anchor for calibrating all stellar evolution models.

In this chapter, we provide an overview of the main approaches to stellar age dating, setting the stage for the methodologies that will be used throughout this Thesis. We begin with the fundamental building blocks: the determination of ages for individual stars and stellar clusters through isochrone fitting, a classical and widely adopted technique that lies at the basis of most stellar age determinations. We then broaden the perspective to methods based on integrated-light analyses, where the information contained in the spectra of entire clusters or galaxies is used to infer their ages. Among these, full spectrum fitting has emerged as a particularly powerful and flexible approach, capable of simultaneously constraining ages and other stellar population properties.

1.3.1 Deriving ages via isochrone fitting

Isochrone fitting builds upon the construction of theoretical stellar evolutionary tracks, which describe the path followed in the luminosity – effective temperature ($L - T_{\rm eff}$) plane by a star of given mass and chemical composition. These tracks populate what is classically known as the Hertzsprung-Russell diagram (HRD), a fundamental tool in stellar physics encapsulating the life cycle of stars in different evolutionary stages. In Figure 1.9a, the sketch of a stellar track highlights the different phases and durations of the evolution of a 5 $M_{\odot}$ star. In Figure 1.9b, stellar tracks for stars of different masses are shown. Once evolutionary tracks are defined, one can construct *isochrones*, theoretical curves obtained by interpolating the evolutionary tracks of stars that share the same age and initial chemical composition but differ in mass. Moving along an isochrone therefore corresponds to tracing how stars of different masses would appear at the same instant in time.

Stellar evolutionary grids, and then isochrones, are built on a set of input physics and parameters, like initial helium abundance, mixing-length parameter, or the treatment of convective overshooting. Over the past decades, several groups have developed and continuously refined stellar evolution models, each adopting slightly different prescriptions and input physics. Among the most widely used are the PAdova and TRieste Stellar Evolution Code (PARSEC, Bressan et al., 2012), the Bag of Stellar Tracks and Isochrones (BaSTI, Hidalgo et al., 2018), the Modules for Experiments in Stellar Astrophysics (MESA) Isochrones and Stellar Tracks (MIST, Choi et al., 2016), and the Dartmouth Stellar Evolution Program (DSEP, Dotter et al., 2008).

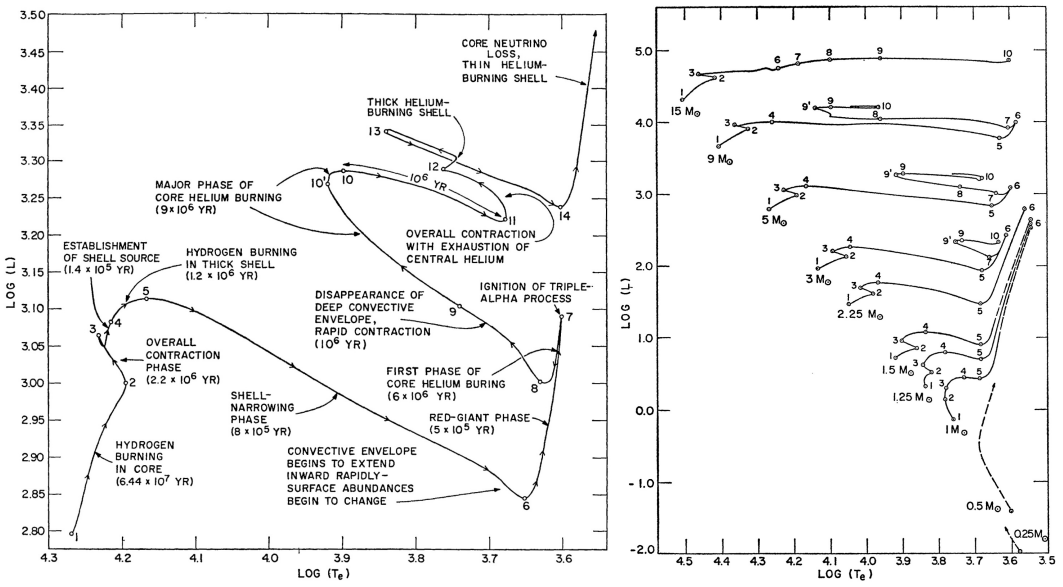

FIGURE 1.9: *Left*: The stellar track in the HRD diagram for a 5 $M_\odot$ star from the main sequence to the asymptotic giant branch. *Right*: Stellar tracks for metal-rich stars spanning masses from 0.25 $M_\odot$ to 15 $M_\odot$. (from Iben, 1967).

The isochrone fitting technique consists in matching the stars' observable properties to a set of isochrones, in order to infer key physical parameters such as metallicity, mass, and age. It can be applied both to ensembles of stars, such as open clusters (OCs) or globular clusters (GCs), or to individual stars, albeit with different observational requirements.

When analysing a stellar cluster, all its stars can be assumed to have formed from the same molecular cloud, thus sharing the same initial chemical composition and epoch of formation: the so-called simple stellar population (SSP). This inherent homogeneity allows the entire cluster to be fitted, in principle, with a single theoretical isochrone. This is highly advantageous for robust age dating, as several age-sensitive features of the isochrone – most notably the main sequence turn-off (MSTO) and the tip of the red giant branch (TRGB) – can be simultaneously used to anchor the model and accurately determine the population's age.
For star clusters, the theoretical HRD diagram is often observationally realised as the colour-magnitude diagram (CMD). This fundamental conversion is driven by two photometric substitutions: the star's intrinsic luminosity is traced by its apparent magnitude (m, e.g., m_V or m_I), while the colour index (e.g., $B-V$ or $V-I$) substitutes the effective surface temperature ($T_{\rm eff}$). The first is valid because all cluster members are assumed to be at the same distance, meaning that intrinsic and apparent magnitude are related by the constant distance modulus, combined with the appropriate bolometric corrections. Colour index, on the other hand, serves as a direct, robust temperature proxy that is calibrated through comprehensive model atmosphere calculations (Cassisi & Salaris, 2013). The key advantage of the CMD is that it is independent of the cluster's distance, making it the essential tool for evolutionary studies.

In contrast to the analysis of clusters, applying the isochrone fitting technique to a single star removes the crucial advantage of fitting a population that spans a wide mass range. Consequently, the

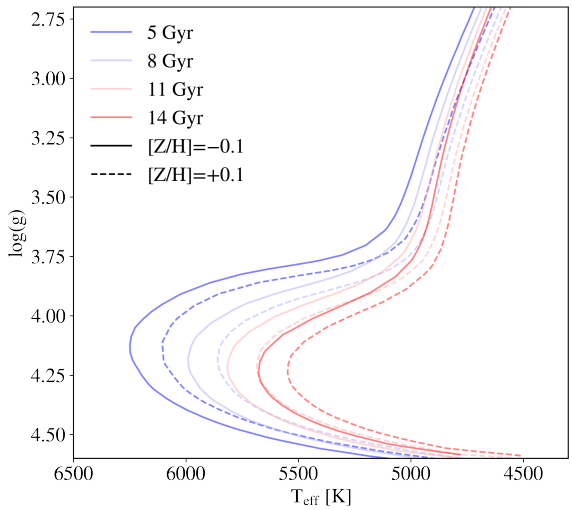

FIGURE 1.10: Examples of theoretical isochrones from the PARSEC (Bressan et al., 2012) models with different ages (5, 8, 11, or 14 Gyr) and metallicities ($[Z/H] = -0.1, +0.1$).

initial constraints required to assess the age of a star must be significantly more precise and numerous. Accurate information regarding the star's metallicity, in particular, becomes essential to break the inherent age-metallicity degeneracy, where the effects of age and chemical composition are difficult to disentangle. A similar degeneracy also exists with dust extinction, as reddening can mimic the photometric effects of an older or more metal-rich population, further complicating the interpretation of the observed colours.

For the analysis of single stars, a commonly employed alternative to the HRD diagram is the Kiel diagram, where the intrinsic luminosity is substituted by the logarithm of the surface gravity ($\log g$). This quantity is directly measurable from the spectroscopic analysis of stellar absorption lines and is thus independent of the star's distance. While $\log g$ and $T_{\rm eff}$ are known to be partially degenerate (Gray, 2008), as both parameters affect the broadening and shape of absorption lines, this degeneracy is most severe when relying on purely spectroscopic analyses over limited wavelength windows (e.g., see Kordopatis et al., 2011, 2013, in the context of the RAVE spectroscopic survey). Inclusion of asteroseismic surface gravity measurements into spectroscopic analysis offers a great solution to this degeneracy problem (Morel & Miglio, 2012; Worley et al., 2020), however they are available only for a small number of bright stars. Alternatively, combining astrometric, photometric and spectroscopic data significantly alleviates this issue, as the broad wavelength baseline and distance estimate provided by photometry and parallax offers strong leverage in separating stars at different evolutionary stages, effectively distinguishing between dwarfs and giants (i.e., high and low $\log g$ values, see Bensby et al., 2014; Guiglion et al., 2020, 2024).

A typical Kiel diagram, illustrating a set of theoretical isochrones, is presented in Figure 1.10. As evident from the figure, not all evolutionary phases are suitable for single-star age determination via this approach, as isochrones corresponding to different ages often lie too close to one another in certain diagram regions, preventing reliable separation. The areas of the MSTO and the sub giant branch (SGB), in particular, are the most suitable for precise age dating, given the broader separation of the isochrones.

As previously discussed, an isochrone represents the locus of stars on the HRD diagram that share a common age but cover a range of masses. Therefore, the critical missing component required to

accurately determine the age of a single star is its mass (M). Retrieving the mass is only possible if the star's distance is properly constrained, as can be understood from basic physical relations. Knowing the distance, indeed, allows the calculation of the intrinsic luminosity (L), which, combined with the effective temperature, yields the stellar radius (R) via the Stefan-Boltzmann law:

$$L = 4\pi R^2 \sigma T_{\rm eff}^4. \tag{1.40}$$

When both the radius and the surface gravity are constrained, the mass is in principle recoverable from:

$$\log(g) = \log\left(\frac{GM}{R^2}\right). \tag{1.41}$$

In practice, the inference process is considerably more complex, as all these quantities are derived simultaneously within a likelihood-based framework, where the distance acts as a crucial constraint that breaks degeneracies between parameters and anchors the star's position along the isochrone.

In this context, the *Gaia* space mission (Gaia Collaboration et al., 2016) has been truly revolutionary. Launched in 2014 and designed as a five-year astrometric mission by the European Space Agency (ESA), Gaia has measured the positions, parallaxes, and proper motions of more than a billion stars in the Milky Way with unprecedented precision, reaching parallax uncertainties on the order of just 1%. This breakthrough enabled highly accurate mass determinations for vast numbers of stars, thereby significantly improving the precision and reliability of single-star age estimates.

To leverage the high-quality, high-statistic data now available – including precise parallaxes, photometry, and spectroscopic measurements – it is necessary to rely on sophisticated computational codes that combine all these input data to retrieve the maximally probable constraints on stellar parameters. Prominent examples of such stellar parameter estimation codes include `StarHorse` (Queiroz et al., 2018, 2023), `PARAM` (da Silva et al., 2006), and `MINESweeper` (Cargile et al., 2020). In the following, we are going to employ the `StarHorse` code, and it is thus useful to provide a brief overview of its main characteristics.

The `StarHorse` code

`StarHorse` is a powerful Bayesian code designed to determine the fundamental stellar parameters of single stars by simultaneously fitting diverse observational data to theoretical stellar evolution models. In particular, it uses spectroscopically measured stellar parameters (typically $T_{\rm eff}$, $\log g$, and overall metallicity $[Z/H]$) combined with photometric magnitudes, m_λ, and parallaxes, π, to estimate the age, mass, distance, and V-band extinction for single stars.

The code operates within a Bayesian framework, meaning that, given a model $\mathcal{M}$ depending on a set of parameters $\boldsymbol{\theta}$, it computes the full posterior probability distribution (the probability of the model, given the data) for each stellar parameter through Bayes' theorem:

$$\mathcal{P}(\boldsymbol{\theta}|\mathbf{x}, \mathcal{M}) = \frac{\mathcal{L}(\mathbf{x}|\boldsymbol{\theta}, \mathcal{M})\, \mathcal{P}(\boldsymbol{\theta}|\mathcal{M})}{\mathcal{P}(\mathbf{x}, \mathcal{M})}, \tag{1.42}$$

where $\mathbf{x}$ is the set of observations and $\mathcal{L}(\mathbf{x}|\boldsymbol{\theta}, \mathcal{M})$ is the likelihood of obtaining these measurements given the model, and $\mathcal{P}(\boldsymbol{\theta}|\mathcal{M})$ is the assumed prior on the parameters $\boldsymbol{\theta}$. If the errors associated with the observed quantities, $\boldsymbol{\sigma_x}$, are Gaussian, the likelihood can be expressed as:

$$\mathcal{L}(\mathbf{x}|\boldsymbol{\theta}, \mathcal{M}) = \prod_i \frac{1}{\sqrt{2\pi}\sigma_{x_i}} \exp\left[-\frac{(x_i - \mathcal{M}(\boldsymbol{\theta})_i)}{2\sigma_{x_i}^2}\right]. \tag{1.43}$$

The model consists of a set of isochrones, drawn from the PARSEC (Bressan et al., 2012) library, computed for different ages, metallicities, and initial masses, and convolved with a grid of distances and extinctions. When parallax is included among the primary inputs, the range of distances is constrained to be consistent with that measurement within 3σ. At the same time, parallax measurements also provide constraints on extinctions, naturally emerging from the comparison of the dereddened distance modulus array, $(m-M)_0$, and the reddened one built from the apparent magnitudes, $(m_\lambda - M_\lambda)$. After the fit, `StarHorse` delivers the median of the marginalised posterior distribution, along with the 5^{th}, 16^{th}, 84^{th}, and 95^{th} percentiles, for all the model parameters.

1.3.2 Deriving ages via full spectrum fitting

Isochrone fitting has long been regarded as the standard and most straightforward technique for deriving the ages of stellar populations. However, this method requires individual stars to be spatially resolved within the stellar population, which limits its applicability to relatively nearby systems confined in the Local Group. Beyond this range, already at the distance of the Magellanic Clouds, this technique becomes increasingly challenging, as resolving individual stars demands extremely long exposure times or exceeds the capabilities of current instrumentation.

Nevertheless, the distant Universe holds a wealth of information encoded in the stellar ages of galaxies and unresolved stellar clumps. Accurately determining these ages is crucial for understanding galaxy formation and evolution, and even more to leverage stellar ages as cosmological probes. Developing methods that can reliably infer stellar ages without the need for resolved stellar populations has therefore become fundamental.

When the observed population cannot be resolved, all the information about its physical properties needs to be extracted from its integrated light, namely from the spectral energy distribution (SED) or, if available, from the spectrum. The modelling of the integrated emission from unresolved stellar populations is commonly referred to as stellar population synthesis (SPS, see Conroy, 2013, for a review). Over the past five decades, significant effort has been devoted by the astrophysical community to the development of increasingly sophisticated SPS models, aiming to reproduce the observed properties of galaxies across cosmic time (e.g., Bruzual & Charlot, 2003; Conroy et al., 2009; Vazdekis et al., 2010; Maraston & Strömbäck, 2011). These models are built on different prescriptions, but all share a common underlying framework.

The cornerstone of all SPS models is the simple stellar population, consisting of the SED of a single population of stars sharing the same age, metallicity, Helium content, and abundance pattern. Realising a synthetic SED, or spectrum, of a single SSP requires three main ingredients:

- stellar evolution models, already described in Section 1.3.1, implemented as isochrones. Given the age and the metallicity of the population, isochrones describe how stars of different masses populate the HRD (or Kiel) diagram at a fixed age.

- stellar spectral libraries, translating the stellar evolution outputs, $T_{\rm eff}$ and $\log g$, into stellar spectra. Stellar libraries can be theoretical or empirical, depending on whether the spectrum is generated synthetically from assumptions on atomic and molecular parameters, or if it comes directly from observations. Examples of the most widely used stellar libraries are MILES (Sánchez-Blázquez et al., 2006; Falcón-Barroso et al., 2011), STELIB (Le Borgne et al., 2003), both empirical libraries, BaSeL (Lejeune et al., 1997, 1998), PHOENIX (Husser et al., 2013), and Coelho (2014), which are instead theoretical.

- initial mass function (IMF), the distribution of stellar masses at the beginning of star formation (e.g.; see Bastian et al., 2010, for a review). It is typically described as a combination of power laws with different slopes across distinct mass ranges. Common examples include the Salpeter (1955), Kroupa & Boily (2002), and Chabrier (2003) IMFs. The first is often referred to as *bottom-heavy*, since low-mass stars dominate the total mass budget, whereas the latter two are considered *top-heavy*, with a relatively larger contribution from high-mass stars.

Then, these three components are combined to reproduce the integrated emission of an SSP as a function of time, t, and metallicity, Z:

$$f_{\lambda,\mathrm{SSP}}(t,Z) = \int_{m_{\mathrm{lo}}}^{m_{\mathrm{up}}(t)} f_{\lambda,\mathrm{star}}[T_{\mathrm{eff}}(M), \log g(M)|t,Z]\Phi(M)\mathrm{d}M, \tag{1.44}$$

where M represents the initial mass of the stars, namely the one they have on the zero-age main sequence (ZAMS), $\Phi(M)$ is the IMF, and $f_{\lambda,\mathrm{star}}$ is the stellar spectrum of a star as a function of wavelength, whose location in the Kiel diagram ($T_{\mathrm{eff}} - \log g$) is uniquely determined by its age, metallicity and mass. The integration limits represent the lower and upper limit of the mass range covered by the SSP, the first typically in the range 0.08–0.1 $M_\odot$ (the hydrogen burning limit), the second being the most massive star still alive in the SSP, thus dictated by the stellar evolution model.

In the real Universe, stellar clusters represent the closest observable counterparts to an ideal SSP, as demonstrated by the remarkable agreement between SSPs' theoretical isochrones and the observed CMDs of GCs and OCs. When moving from star clusters to galaxies, the picture becomes considerably more complex, as additional factors come into play. In particular, star formation may occur over an extended time interval, so the single-age assumption could be too simplistic, the metallicity may not be necessarily uniform throughout the whole period of star formation, and dust could significantly affect the observed emission. Incorporating these effects into the framework of SSPs gives rise to the so-called composite stellar populations (CSPs). The main additional ingredients introduced when moving from an SSP to a CSP are:

- star formation history (SFH), describing how the star formation rate (SFR) varies with time. The simplest prescription is a single burst SFH, equivalent to the SSP assumption, while more realistic and commonly adopted forms are the exponentially declining or the double-power-law SFHs. These are all parametric SFHs, meaning that they can be described by a functional form depending on a limited number of parameters. Another possibility is to adopt a non-parametric approach, where the SFH is reconstructed with multiple constant components. Further details on the various SFH types are provided in the next section.

- dust attenuation and emission. Interstellar dust is present in the majority of galaxies, especially in the star-forming ones, and acts both in obscuring light emitted in the ultraviolet (UV) and in emitting light in the infra-red (IR). In the CSP modelling, these two effects are often decoupled. The first can be implemented through attenuation curves, as the ones from Calzetti et al. (2000) or Charlot & Fall (2000). The second, the thermal emission from dust grains, is often described with a grey body model or with more sophisticated prescriptions accounting for grain size and optical properties (Draine, 2003).

In Figure 1.11, a visual overview of the SPS technique is shown. Combining all the ingredients outlined above is a non-trivial task, for which numerous codes have been developed since the early 2000s[2].

[2]Even if the first studies date back to the 1980s (e.g., Bruzual A., 1983).

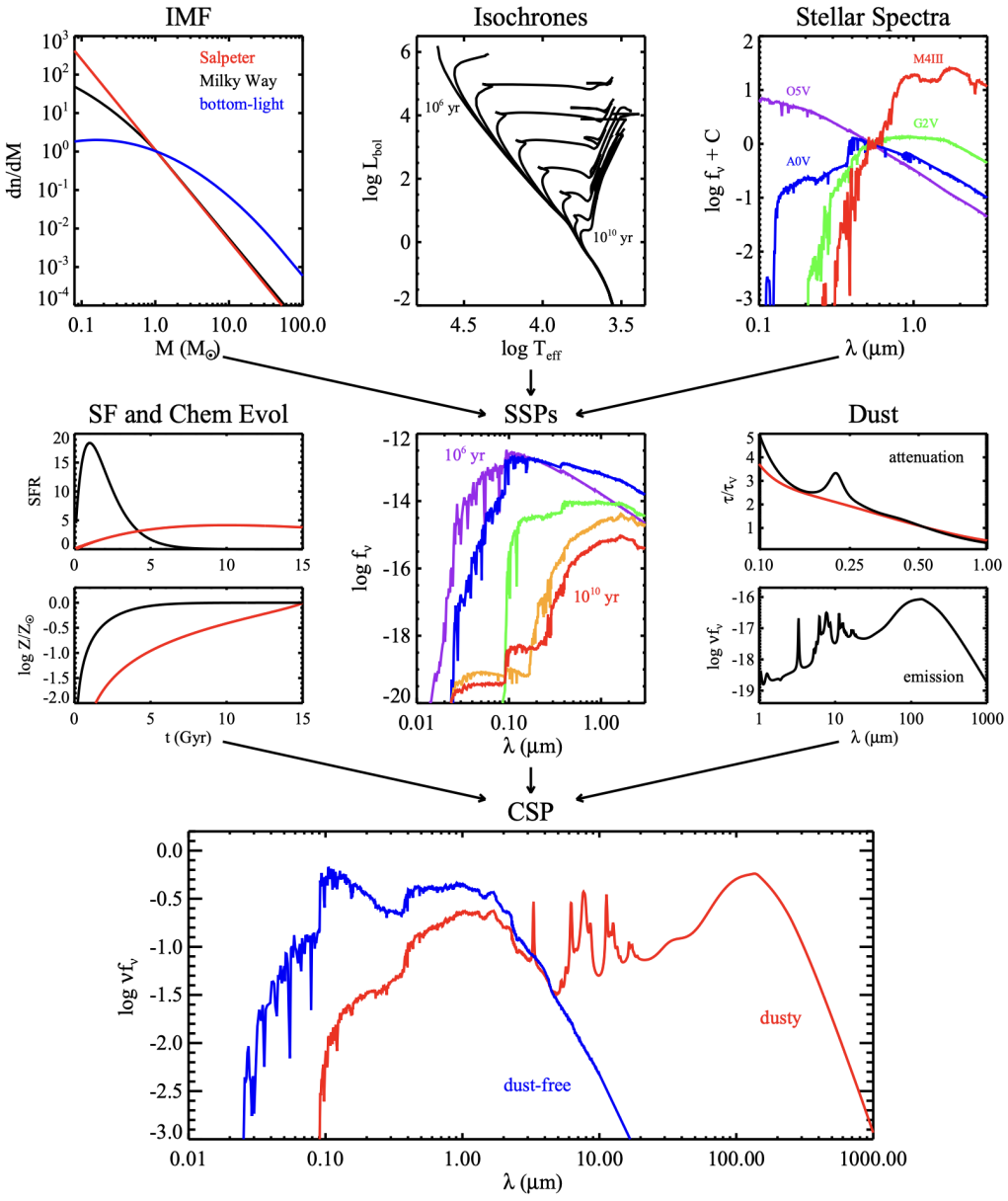

FIGURE 1.11: Visual diagram describing the SPS approach. From the top, examples of the main ingredients for an SSP are shown. In the central row, the resulting SSP spectra are then combined with prescriptions concerning the SFH, chemical evolution and dust attenuation and emission. The final product, in the lower panel, is the spectrum of a CSP (from Conroy, 2013).

These tools not only generate synthetic spectra of CSPs, but, more importantly, they can fit these models to observed SEDs or spectra in order to infer the physical parameters of the underlying stellar population, an approach commonly referred to as SED-fitting or full-spectrum fitting (FSF). Among the most widely adopted, we can mention `BAGPIPES` (Carnall et al., 2018), `Prospector` (Johnson et al., 2021), `pPXF` (Cappellari, 2017), `Beagle` (Chevallard & Charlot, 2016), and `STARLIGHT` (Cid Fernandes et al., 2005). In this Thesis, due to its versatility, we make extensive use of the `BAGPIPES` code, for which a brief overview is provided below.

The `Bagpipes` code

The Bayesian Analysis of Galaxies for Physical Inference and Parameter EStimation (BAGPIPES, Carnall et al., 2018) is a full-spectrum fitting code that enables the joint fitting of spectra and photometry within a Bayesian framework. This means, as discussed in Section 1.3.1, that once a model $\mathcal{M}$ depending on a set of parameters $\boldsymbol{\theta}$ is chosen, the synthetic spectrum is modelled to maximise the posterior probability on θ, $\mathcal{P}(\boldsymbol{\theta}|f_\lambda, \mathcal{M})$, as defined in Eq. 1.42, with the observed spectrum and/or photometry, f_λ taking the place of the set of observables, $\mathbf{x}$. In `BAGPIPES`, the posterior probability is sampled using a nested sampling algorithm described in Skilling (2006) and implemented via the `MultiNest` package (Buchner, 2016). In particular, as extensively described in Carnall et al. (2018) and Carnall et al. (2019), the model is built with four main components:

- SSP(λ, age, Z), generating the synthetic spectra of simple stellar populations given the wavelength range λ, the age of the stellar population, and its overall metallicity Z. The stellar population synthesis (SPS) models, implemented in the form of grids of SSPs, are the 2016 version of Bruzual & Charlot (2003) (BC16, see Chevallard & Charlot, 2016). They are constructed using a Kroupa & Boily (2002) IMF and rely on the MILES (Falcón-Barroso et al., 2011) library of empirical spectra.

- The SFH, SFR(t), resulting from the sum of one or more components. Each SFH component can be either described by a functional form (e.g., single burst, constant, exponentially declining, double power law), or be non-parametric. In the second case, the implementation follows the approach adopted in Leja et al. (2019a).

- T^{+}(age, λ), which is the transmission curve of the ionised interstellar medium (ISM) as described in Charlot & Longhetti (2001), including absorption and emission from warm dust in $\mathrm{H_{II}}$ regions. It is implemented through the 2017 version of the `CLOUDY` photoionization code (Ferland et al., 2017). This component is referred to as *nebular* and, unlike the ones above, is optional.

- T^{0}(age, λ) transmission curve of the neutral ISM, which is mainly due to dust absorption and emission. Different models are implemented in the code, including those of Calzetti et al. (2000), Cardelli et al. (1989), or Charlot & Fall (2000). This is also an optional component and is referred to as *dust*.

All the ingredients are then combined to provide the CSP luminosity as:

$$L_\lambda = \sum_{j=1}^{N_c} \sum_{i=1}^{N_a} \mathrm{SFR}_j(t_i)\mathrm{SSP}(\lambda, a_i, Z_j)T^{+}(a_i, \lambda)T^{0}(a_i, \lambda)\Delta a_i, \tag{1.45}$$

where N_c is the number of SFH components, N_a is the number of age bins, a_i, and Δa_i is their width. Time, t_i, and age are related through: $a_i + t_i = t(z_{\mathrm{obs}})$, where $t(z_{\mathrm{obs}})$ is the age of the Universe at the redshift of observation.

In addition to these, two optional and non-physical components can be included: *noise* and *calibration*. The first one acts on the error spectrum to correct possible underestimations and can be implemented as either white noise or correlated noise. Calibration, instead, perturbs the spectrum with a second-order Chebyshev polynomial to fix possible calibration issues. This component becomes particularly relevant when spectra and photometry are fitted simultaneously, as it allows the code to compensate for signal losses in the spectra and recover them by matching the photometry.

Concerning the SFH, we already mentioned that `BAGPIPES` is able to combine multiple SFHs, one for each stellar population, with different functional forms. Here, we outline three of the most extensively used, on which we focus our analysis.

– The single burst is the simplest SFH, described by a Dirac function, implying that the formation of the whole stellar population is instantaneous. While clearly the least realistic, this model is still effective in characterizing the emission of a population formed in a very short and intense episode of star formation.

– The delayed exponentially declining (DED) SFH, is given by the equation

$$\mathrm{SFR}(t) \propto \begin{cases} (t - T_0)\, \mathrm{e}^{-\frac{t-T_0}{\tau}}, & t > T_0 \\ 0, & t < T_0 \end{cases}, \tag{1.46}$$

where τ sets the width of the SFH while T_0 is the age of the Universe when the star formation begins.
This SFH is frequently used (Citro et al., 2017; Carnall et al., 2018) for passively evolving galaxies, characterised by a single and strong episode of star formation followed by passive evolution, because it is able to reproduce a realistic star formation process using only two parameters.

– The double-power-law (DPL) SFH, given by

$$\mathrm{SFR}(t) \propto \left[\left(\frac{t}{\tau}\right)^{\alpha} + \left(\frac{t}{\tau}\right)^{-\beta} \right]^{-1}, \tag{1.47}$$

where α and β describe, respectively, the falling and rising slope of the curve, while the τ parameter is related to the SFH peak. This type of functional form allows the SFH more freedom in shape by decoupling the rising and falling phases of the star formation, but the increased number of free parameters should be carefully studied since it might induce a non-physical correlation between the two.

When the SFH encodes a parameter identifying the beginning of the star formation, T_0, the age of the galaxy can be directly retrieved as:

$$\mathrm{age} = t(z_{\mathrm{obs}}) - T_0, \tag{1.48}$$

where $\mathrm{t}(\mathrm{z}_{\mathrm{obs}})$ is the age of the Universe at the redshift of observation. If this parameter is not available, as in the case of a DPL, age can be estimated as:

$$\mathrm{age}_{\mathrm{mw}} = t(z_{\mathrm{obs}}) - \frac{\int_0^{t_{\mathrm{obs}}} t\mathrm{SFR}(t)\mathrm{d}t}{\int_0^{t_{\mathrm{obs}}} \mathrm{SFR}(t)\mathrm{d}t}, \tag{1.49}$$

which defines the mass-weighted age. It is similar to Eq. 1.48, but the onset of star formation is weighted by the star formation rate, thus providing a measure that accounts for the assembly history of the CSP.

Another distinction worth clarifying here is that between the mass formed (M_{formed}) and the stellar mass ($M_\star$). The two differ in that the former includes all the mass converted into stars from $t = 0$ up to the observation time t:

$$M_{\mathrm{formed}} = \int_0^t \mathrm{SFR}(t')\mathrm{d}t'. \tag{1.50}$$

The latter instead represents only the mass locked into living stars at time t, and can be expressed as:

$$M_\star = (1 - R) \int_0^t \mathrm{SFR}(t')\mathrm{d}t', \tag{1.51}$$

where R is the return fraction, defined by the SSP models, representing the percentage of mass in stellar remnants or returned to the inter stellar medium by evolved stars. In the following, we refer to M_{formed} when discussing the total stellar mass formed, and to $M_\star$ when referring specifically to the mass contained in living stars.

After the fit, the code provides, for each galaxy, a best-fit spectrum and an estimate to the 16^{th}, 50^{th}, and 84^{th} percentiles of all the parameters involved in the fit. At the same time, it can provide estimates of derived quantities, like the SFR or the mass-weighted age mentioned above, parameters that are not directly involved in the fit.

Removing cosmological priors on the stellar ages For the purpose of this work, it is important to emphasize that stellar ages must not be derived using a cosmological prior. In particular, for the oldest stellar populations (which are a focus of this Thesis), adopting such a prior would artificially restrict the maximum allowed age to the age of the Universe at a given redshift. If these ages were then used to constrain cosmology, one would fall into a circular argument, inevitably recovering the same cosmology assumed as input.

For this reason, the version of `BAGPIPES` employed in this work differs from the original one in its treatment of the prior on stellar population ages.
In the original implementation, the code assumes a cosmological prior on ages, requiring that the maximum fitted age does not exceed the age of the Universe at the corresponding redshift, given a flat ΛCDM model with parameters $\Omega_m = 0.3$, $\Omega_\Lambda = 0.7$ and $H_0 = 70$ km s^{-1}Mpc^{-1}. Although this effect is of relative interest in stellar population studies and is typically neglected, it cannot be ignored in cosmological analyses, where derived ages would be artificially constrained by the adopted cosmological model, effectively recovering the prior itself rather than the true age distribution.

This is why we employ a version of `BAGPIPES`, described in Jiao et al. (2023), that deviates from the original in handling the priors on the stellar population age, allowing them to vary up to a cosmology-independent value (e.g., 15 Gyr, 20 Gyr) at any redshift. This modification has already been tested and validated in the LEGA-C survey (Jiao et al., 2023).

Analogously, in deriving stellar ages with `StarHorse`, the full range of isochrone models was allowed, spanning up to 20 Gyr.

All of the results presented in this Thesis, then, are entirely cosmology-independent. This represents a significant and novel aspect of this work with respect to the literature: studies focused on galaxy or stellar evolution almost always impose a cosmological prior on the inferred ages. The methodology adopted here ensures that the age estimates rely solely on the observational data and stellar population modelling.

1.4 Aim of the Thesis

In Section 1.1, we introduced the cosmological framework and discussed the major open questions in modern cosmology. Despite the remarkable progress achieved in the past decades, several aspects of the Universe's evolution remain uncertain, including the nature of dark energy and dark matter, and the origin of the observed tensions in the standard ΛCDM model. In this context, we also discussed how the ages of the oldest astrophysical objects provide a powerful, independent means of constraining the cosmic expansion history and testing cosmological models.
The *cosmic clocks* approach relies on the simple yet fundamental idea that the age of the Universe must be greater than the age of its oldest inhabitants, thus providing, at any redshift, a direct lower limit on the cosmic age. This can then be translated into an upper limit to the value of the Hubble constant, H_0. The *cosmic chronometers*, on the other hand, reconstructing the evolution of the Universe through the ageing of passively evolving galaxies, represent one of the few direct probes of the Hubble parameter at high redshift. In different ways, they both complement other cosmological observables such as supernovae Type Ia, baryon acoustic oscillations, and the cosmic microwave background.

In Section 1.3, we then described how stellar ages can be determined across different astrophysical regimes. From individual stars and local stellar clusters, where isochrone fitting remains the most direct and robust approach, to unresolved systems such as lensed clusters and galaxies, where full-spectrum fitting and spectral energy distribution analysis are required to recover their time of formation.

In this Thesis, we aim to explore these alternative and promising cosmological probes through the different age-dating methods available, employing different classes of astrophysical objects as tracers of cosmic time. By combining these approaches, we seek to investigate how the most ancient stellar populations can serve as reliable tools to constrain the expansion history of the Universe and shed light on its evolution.
Figure 1.12 provides a visual summary of the constraints attainable with each approach and the range of applicability for different tracers. In particular, we focus on four main classes: Milky Way stars, local GCs, lensed GCs, and cosmic chronometers (i.e. specifically selected passively evolving galaxies). These are indeed the four types of objects analysed throughout this Thesis. The application of the cosmic clock approach is presented in Section 2.1 for Milky Way stars, in Section 2.2 for local GCs, and in Section 2.3 for lensed GCs. Two different applications of the cosmic chronometers approach are instead discussed in Sections 3.1 and 3.2.

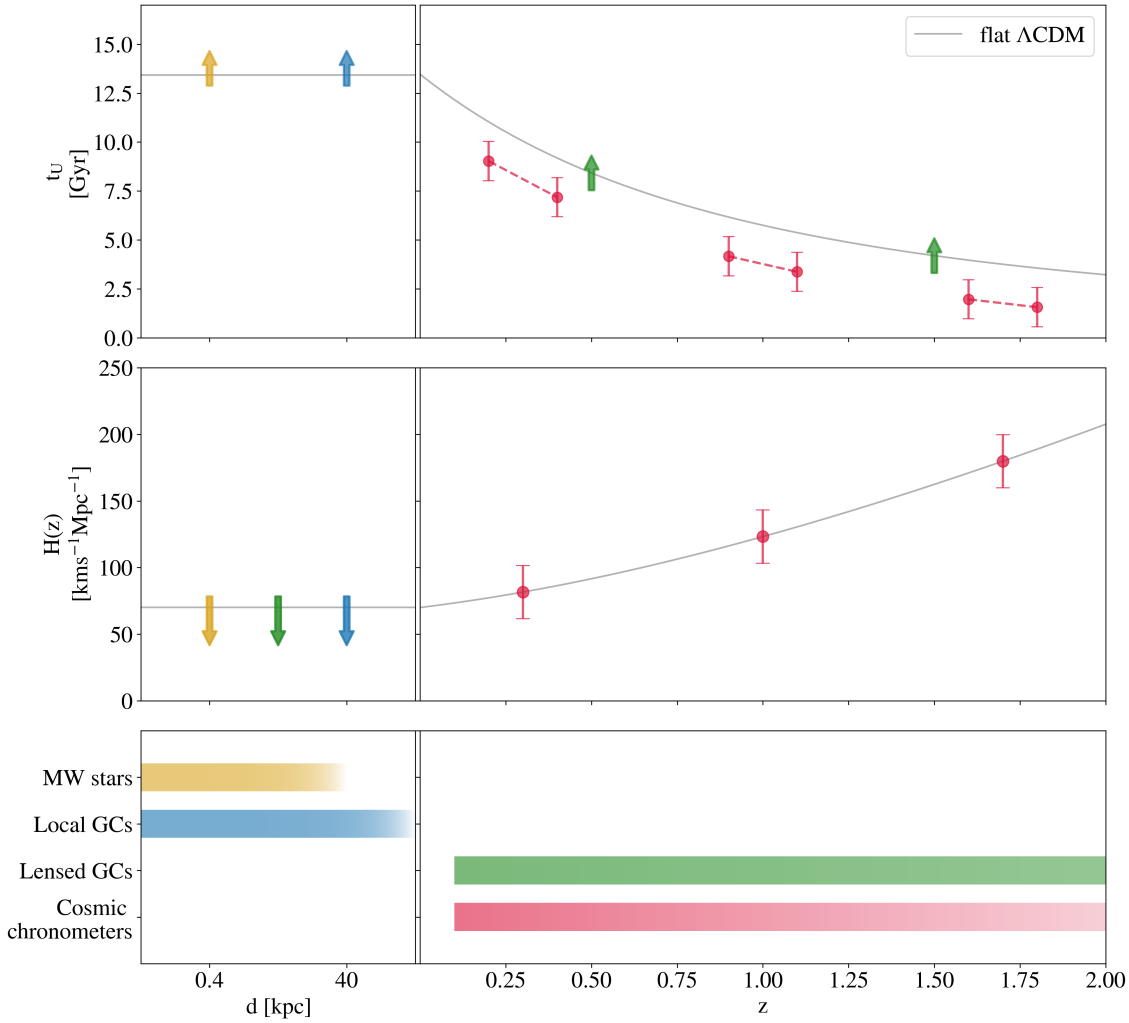

FIGURE 1.12: Visual summary of the constraints attainable with the cosmic clocks and the cosmic chronometers approaches. The solid line shows the age of the Universe (top) and Hubble parameter (centre) trends with redshift in a flat ΛCDM with $\Omega_m = 0.3$. The lower panel shows the typical ranges of applicability of the methods depending on the astrophysical object. With corresponding colours, the typical constraints obtainable with each tracer are shown, both in cosmic time and $H(z)$. Arrows refer to the cosmic clocks approach, representing lower bounds for t_U and upper limits for H_0. We underline that while individual clocks constrain the age of the Universe at their redshift, when propagated through a chosen cosmological model, this information constrains the present-day expansion rate H_0, independently of the source's redshift. Pairs of points connected by a dashed line illustrate the ageing of a cosmic chronometers population; each pair produces an $H(z)$ constraint shown in the central panel. Together, these two complementary approaches enable a time-based reconstruction of the expansion history of the Universe, offering a direct and independent way to constrain the Hubble parameter across different cosmic epochs.

Cosmology with Cosmic Clocks

In Section 1.1 we discussed how the age of the Universe (t_U) can play a crucial role in cosmology, given its sensitivity to the Hubble constant, H_0. In a flat ΛCDM cosmology, for instance, assuming Ω_m=0.3 and Ω_Λ=0.7, t_U can span a range from ∼14.1 Gyr if $H_0 = 67$ km s^{-1} Mpc^{-1} to ∼12.9 Gyr if $H_0 = 73$ km s^{-1} Mpc^{-1}. This means that measuring the absolute ages of *cosmic clocks*, the most long-lived objects at $z = 0$, can be critical, since they naturally place a lower limit on the current age of the Universe and, in turn, an upper limit on H_0. Not only does this yield independent constraints on the Hubble constant, but it also provides valuable information for investigating the origin of the observed Hubble tension.

In this chapter, we aim to employ the cosmic clocks approach with various kinds of astrophysical objects, for which age is measured with different methods and is thus prone to different systematic effects. Section 1.1 presents a brief overview of the cosmic clocks method, while the subsequent sections detail the original contributions of this Thesis. In particular, in Section 2.1 the oldest stars in the Milky Way are considered, in Section 2.2 the age of the oldest globular clusters is used, and in Section 2.3 this approach is extended to the distant Universe by deriving the ages of lensed globular cluster candidates.

The main reference articles for the analyses presented in this chapter are:

- **Elena Tomasetti**, Cristina Chiappini, Samir Nepal, Michele Moresco, Carmela Lardo, Andrea Cimatti, Friedrich Anders, Anna B. A. Queiroz, and Guilherme Limberg. *The oldest Milky Way stars: New constraints on the age of the Universe and the Hubble constant*, in press for Astronomy and Astrophysics. [arXiv:2509.02692]
- **Elena Tomasetti**, Michele Moresco, Carmela Lardo, Andrea Cimatti, and Raul Jimenez. *Globular clusters as cosmic clocks: New cosmological hints from their integrated light*, Astronomy & Astrophysics (2025) [arXiv.2410.22466]
- **Elena Tomasetti**, Michele Moresco, Carmela Lardo, Frédéric Courbin, Raul Jimenez, Licia Verde, Martin Millon, and Andrea Cimatti. *Time to Sparkler: Accurate ages of lensed globular clusters at $z = 1.4$ with JWST photometry*, Astronomy & Astrophysics (2025) [arXiv.2412.06903]

2.1 The oldest Milky Way stars as cosmic clocks

In recent years, interest has been growing in the use of stellar ages as promising cosmological probes (O'Malley et al., 2017; Jimenez et al., 2019; Valcin et al., 2020; Valcin et al., 2021; Di Valentino et al., 2021c; Boylan-Kolchin & Weisz, 2021; Moresco et al., 2022; Vagnozzi et al., 2022; Valcin et al., 2025), independent of the standard ones and of any cosmological model. Various methods and types of objects

have been employed for this purpose, most notably isochrone fitting, applied to globular clusters (GCs) and individual stars (e.g. Valcin et al., 2025), or techniques based on white dwarf cooling sequences and nucleochronometry (see Cimatti & Moresco, 2023, for a collection of different approaches).

Thanks to the tremendous increase in the quality and statistics of the data for field stars in the Gaia era, very high precision is currently achievable in measuring ages. Accuracy, on the other hand, represents a persistent challenge due to the presence of systematic uncertainties (Soderblom, 2010; Valcin et al., 2021; Joyce et al., 2023), mainly arising from stellar models' dependencies, typically dominating over the internal precision of each method. Moreover, the previously mentioned studies generally relied on small samples (a few tens of old GCs or a handful of single stars) as precise age estimates were available for a few objects, limiting the statistical robustness of the resulting cosmological inferences.

Nowadays, precise age determinations can be obtained for main-sequence turnoff (MSTO) and subgiant branch (SGB) stars, via isochrone fitting, thanks to the very high-quality data and stellar parameters obtained with cutting-edge facilities like the ESA Gaia (Gaia Collaboration et al., 2016). In this work, we take advantage of the high-quality age measurements obtained in Nepal et al. (2024, N24 hereafter) for a sample of about 200'000 MSTO and SGB stars, with extremely precise parallaxes (<1%) and extinction uncertainties (<0.2 mag). Extending the methodology adopted in N24, where stellar ages were constrained by a cosmological prior of 13.73 Gyr, the ages adopted here were derived without any such upper bound, spanning the full range of the isochrone models (0.025–20 Gyr). This unprecedented dataset allowed us to use stellar age dating as a cosmological probe, for the first time, with both high statistical power and internal homogeneity, while also enabling a detailed assessment of the systematic uncertainties affecting age measurements.

2.1.1 Data

This study is based on a sample of 202,384 stars presented in N24, soon to become publicly available (Nepal et al., *in prep.*), identified as the "age sample", where ages are derived using the Bayesian isochrone fitting code `StarHorse` (Santiago et al., 2016; Queiroz et al., 2018, 2023, see Section 1.3.1 for a brief overview). The `StarHorse` code estimates stellar ages, extinctions, and distances by comparing observed data to the PARSEC stellar evolutionary models (Bressan et al., 2012). In particular, the main observables used as input are the stars' atmospheric parameters, photometric magnitudes, and parallaxes. Specifically, atmospheric parameters such as effective temperature ($T_{\rm eff}$), surface gravity ($\log g$), and overall metallicity ($[Z/H]$) are derived in Guiglion et al. (2024) analysing spectra from the Radial Velocity Spectrometer (RVS) onboard Gaia using a hybrid convolution neural network (`hybrid-CNN`). The photometric magnitudes G, B_p, and R_p are from the third data release of Gaia, *Gaia*-DR3 (Gaia Collaboration et al., 2023), while infrared photometry (*JHKs*) is taken from the Two Micron All Sky Survey (2MASS, Skrutskie et al., 2006). `StarHorse` then provides a posterior probability distribution for each of the output quantities. We consider the 50^{th} percentile of this distribution as the parameters' best-fit value, with an associated Gaussian error equal to half of the $84^{th} - 16^{th}$ percentiles interval.

The age sample is composed of only MSTO and SGB stars, based on their position in the Kiel diagram, following the selection presented in Queiroz et al. (2023). As anticipated in Section 1.3.1, these evolutionary stages represent the optimal "sweet spot" for age determination through isochrone fitting, as the shape of the curves varies significantly with age. Leveraging this variability, along with the high-quality stellar parameters from Guiglion et al. (2024), and Gaia's very precise parallaxes, the sample achieves a mean statistical uncertainty of just 12% in age and 1% in distance.

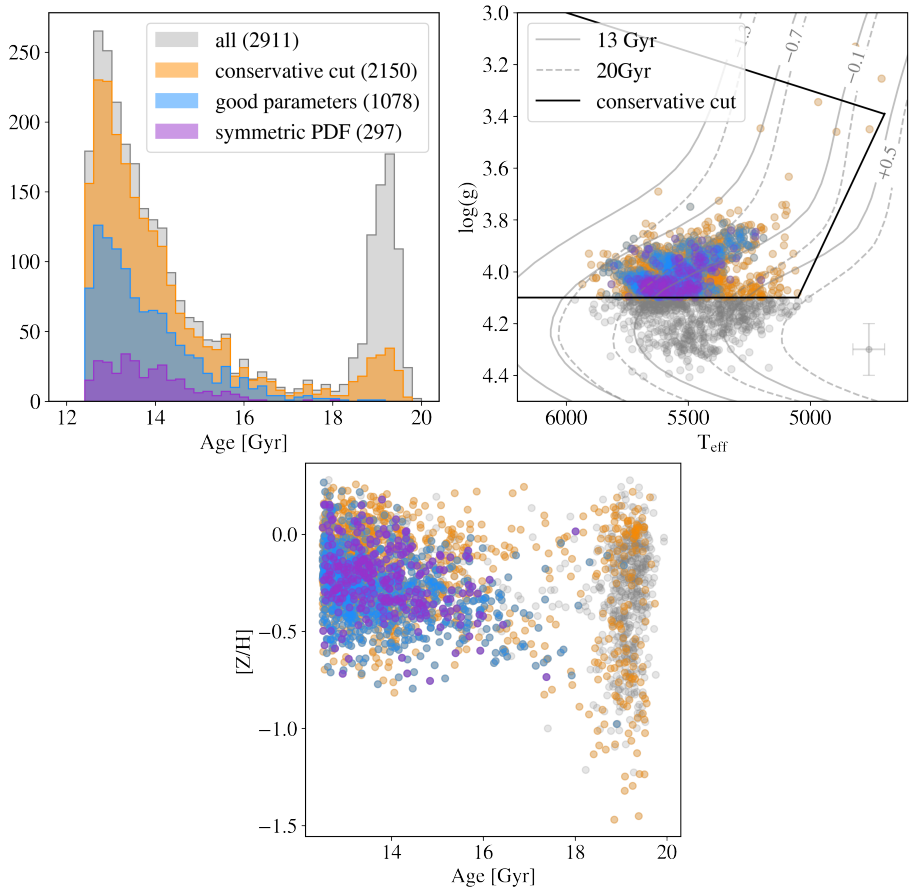

FIGURE 2.1: Age distribution (left), Kiel diagram (right), and age-metallicity coverage (bottom) for each step of the selection process, before visual inspection. In the right panel, PARSEC isochrones at different ages and metallicities are shown in grey, and at the bottom right, the average error in $\log g$ and $T_{\rm eff}$ for the full sample is shown. The peak at 19 Gyr visible in the histogram is due to contaminants, as explained in Section 2.1.2.

In N24, the set of isochrones used spans metallicities from $[Fe/H] = -2.2$ to $+0.6$ and ages from 0.025 to 13.73 Gyr, with the upper age limit set by the value of t_U in a flat ΛCDM cosmology. This work is based on the same dataset and uses parameters derived with the same methodology. However, aiming to obtain estimates suitable for use in a cosmological context, independent of any prior assumptions, we recomputed the ages with `StarHorse`, extending the explored range from 0.025 to 20 Gyr.

2.1.2 Analysis

This section describes the selection process of an optimal age sample, the analysis of the systematic effects involved, and details the approach taken to identify the oldest stars in the dataset.

The selection process

The primary goal of this analysis is to obtain reliable, cosmology-independent age estimates. To achieve this, we implemented a rigorous selection process, as described below.

(1) Parent sample. From the full age sample of N24, we selected stars older than 12.5 Gyr with age uncertainties below 1 Gyr (hereafter the parent sample), yielding 2,911 objects, about 10% of the original sample. The 1 Gyr uncertainty threshold ensured high-quality measurements while still retaining a statistically robust dataset[1]. We underscore that this choice did not introduce any bias towards younger ages: even though a positive correlation between age and age error does exist, this holds only up to approximately 10 Gyr, after which errors remain comparable in the range 10 – 15 Gyr. Conversely, in adopting this cut in precision, we found an overdensity at very old ages, due to solutions converging towards the edge of the prior, thus exhibiting artificially small errors (see discussion in N24). This can be observed in the left panel of Figure 2.1, where the age distribution for the parent sample is shown in grey, revealing a clear double-peak in age: one around 13 Gyr and the other near 19 Gyr.

(2) Conservative MSTO-SGB stars cut. As anticipated in Section 2.1.1, a cut in the Kiel diagram was already applied to the age sample to select only MSTO and SGB stars. Following what was already presented in N24, we adopted a more restrictive cut in $\log g - T_{\rm eff}$ plane:

$$\begin{cases} \log g < 4.1 \\ \log g > -0.0003 \times T_{\rm eff} + 4.8 \\ T_{\rm eff} > 500 \times \log g + 3000 \end{cases}, \tag{2.1}$$

This is shown with a solid line in the right panel in Figure 2.1, while the resulting sample, of 2150 objects, is shown in orange. The cut in $\log g < 4.1$, in particular, is what impacted most on the parent sample and removed most of the stars older than 18 Gyr. Above this threshold, as is clear from the right panel in Figure 2.1, we would select stars that overlap with the turn-off, but potentially still in MS. The simple scatter of MS stars, but also the presence of unresolved binary systems[2], could imply a lower surface gravity (see, e.g., Price-Whelan et al., 2020; Anders et al., 2022, for a discussion on binarity). This has a different effect on the resulting age depending on the position in the diagram: above $\log g \sim 4.1$, around the turn-off, this can drag the age to much older values because isochrones of different age around the MS are very close by; below $\log g \sim 4.1$, above the turn-off, instead, such upwards shift would typically result in a younger age, but with a much less dramatic effect because the isochrones of different age are distinct parallel lines after the turn-off. We underline that by selecting this region of the Kiel diagram, we are not removing by definition the oldest solutions: isochrones of ages up to 20 Gyr are still included in the selected area, as visible in the right panel of Figure 2.1. This cut was highly effective in suppressing the 19 Gyr peak, suggesting that this overdensity was primarily due to contamination.

(3) Consistency of input–output parameters. Age estimates can also be affected by parameter degeneracies, which may introduce systematic biases. In particular, the age–metallicity degeneracy displayed a clear trend: more metal-poor stars ($[Z/H] < -0.5$) were systematically shifted toward higher metallicities by 0.1–0.2 dex, while yielding old ages exceeding 18 Gyr. In Figure 2.2, the difference is shown between the `StarHorse` overall metallicities and the values from Guiglion et al. (2024), used as priors, for the sample selected after the conservative cut (2148 stars). It clearly highlights how the oldest ages, above 18 Gyr, are all related to an overestimation of the input metallicity by up to 0.2 dex. From the histogram on the right, it is also clear that these stars are just a very small fraction, less than

[1] We note that adopting a more stringent uncertainty cut of 0.75 Gyr would have reduced the parent sample to roughly one third of its current size, while decreasing the final age estimate by only 0.1 Gyr.

[2] Wide binaries are already excluded in the original selection from N24.

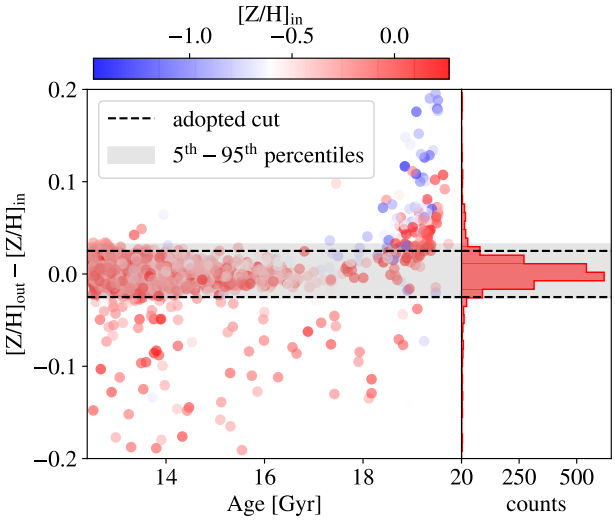

FIGURE 2.2: Discrepancy in $[Z/H]$ between StarHorse's output and the measurements from Guiglion et al. (2024), used as a prior.

5% of the entire population. To mitigate this effect, we imposed a constraint on the maximum allowed discrepancy between the input and output values of $[Z/H]$. We chose a symmetric cut, discarding the 5% tails of the $\Delta[Z/H]$ distribution, namely $|\Delta[Z/H]|$ <0.025. Following the same logic, we imposed similar cuts on $T_{\rm eff}$, $|\Delta T_{\rm eff}|$ <30 K, $\log g$, $|\Delta \log g|$ <0.05, and dust extinction, $|\Delta A_{\rm V}|$ <0.1 mag. This further reduced the sample to 1078 stars.

(4) Removing strongly degenerate solutions. Next, we considered the symmetry of the posterior distributions in age and mass as quality indicators, as these two parameters are not constrained by Gaussian priors and are therefore more prone to asymmetries or anomalies in their posterior shapes. First, we discarded age measurements for which the asymmetry (difference between the upper and lower uncertainties) exceeded 0.1 Gyr. We then applied a Kolmogorov-Smirnov test to assess how well each posterior probability distribution function (PDF) conformed to a Gaussian, excluding all cases where the probability of deviation from Gaussianity exceeded 99.5%. This reduced the sample to 297 stars.

(5) Visual inspection. As a final step, we visually inspected the corner plots to exclude anomalous cases missed by previous cuts. This "blind" inspection, performed without viewing parameter values, focused on identifying asymmetries or double peaks in the posterior distributions. Based on PDF shape, stars were classified into three quality tiers: *great* (78 stars, symmetric and clean), *good* (107 stars, minor tail features), and *bad* (112 stars, significant asymmetries or almost double peaks), with the latter excluded from the final sample. In Figure 2.3, three corner plots are shown for stars representing different levels of quality in their posterior probability distribution functions (PDFs) for mass and age. The top left panel illustrates one of the best cases, characterized by a Gaussian and symmetric distribution in both parameters. The top right panel presents a good-quality PDF, with a single peak and an overall Gaussian-like shape, but slight asymmetries appear in the tails beyond the 1σ range. The bottom panel shows a poor-quality fit that was excluded from the final sample. Although the main peak is visible, a secondary peak appears at higher masses and lower ages, close enough to

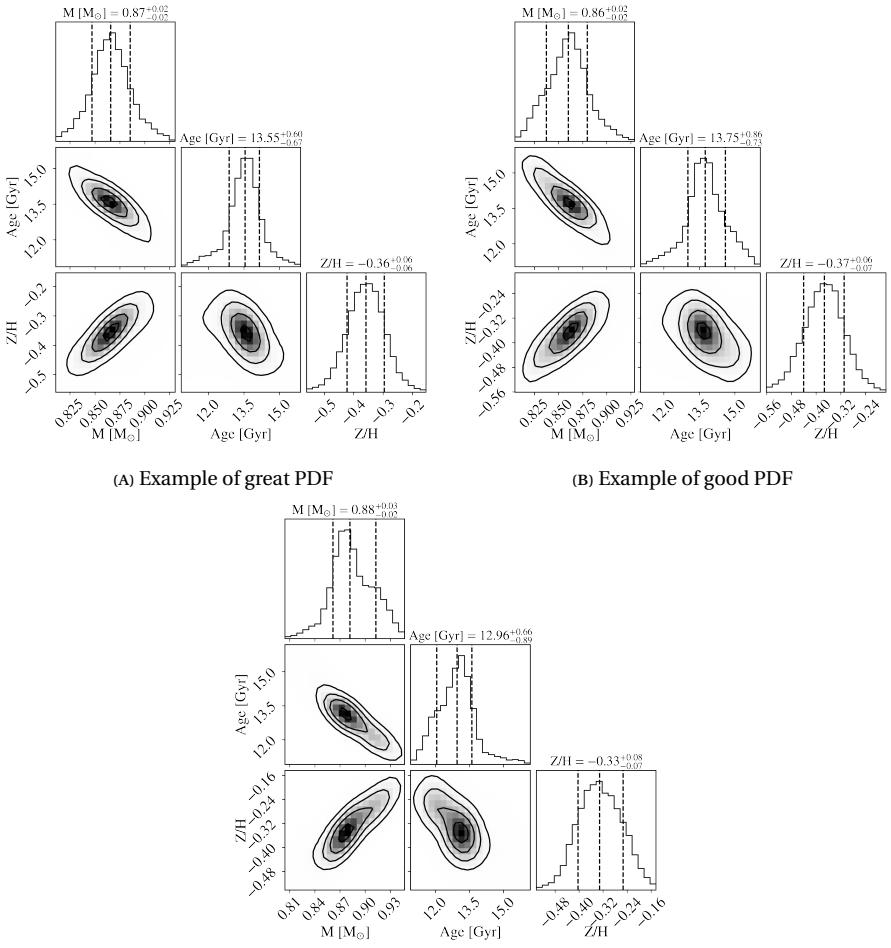

(A) Example of great PDF

(B) Example of good PDF

(C) Example of bad PDF

FIGURE 2.3: Examples of corner plots of different quality, classified in the visual inspection phase into best, good, and bad PDFs.

the main one that it was not flagged in earlier selection steps. The skewness of this distribution suggests a non-negligible probability assigned to a different solution, reducing the robustness of the fit for the purposes of this study.

Finally, we arrived at a refined final sample of 185 stars with precise age determinations, robust stellar parameters, and well-behaved posterior distributions. Within this set, we also defined a «golden sample» consisting of the 78 stars that exhibit the highest-quality PDFs. Both samples show a 5% (stat) precision in age and 2% (stat) precision in mass, on average.
The selection favours the more metal-rich part of the parent sample ($[Z/H] > -0.5$, see bottom panel in Figure 2.1) with low α-enhancement ($[\alpha/Fe] < 0.15$), mainly because it is where the `hybrid-CNN` delivers its most precise metallicity estimates – key for reliable ages. Even though one would expect the oldest stars to be more metal-poor ($[Z/H] < -1$), recent studies (e.g. Trevisan et al., 2011; Anders et al., 2018; Miglio et al., 2021b; Nepal et al., 2024; Borbolato et al., 2025, and references therein) have already shown the existence of old, more metal-rich, low-alpha stars, compatible with a high-star formation rate and rapid metal enrichment in the early Milky Way. At high-redshift, while direct stellar observations are currently not possible, recent studies of gas phase metallicities have revealed a large dispersion, including super-solar estimates (e.g. Huyan et al., 2025; Deepak et al., 2025). Most stars

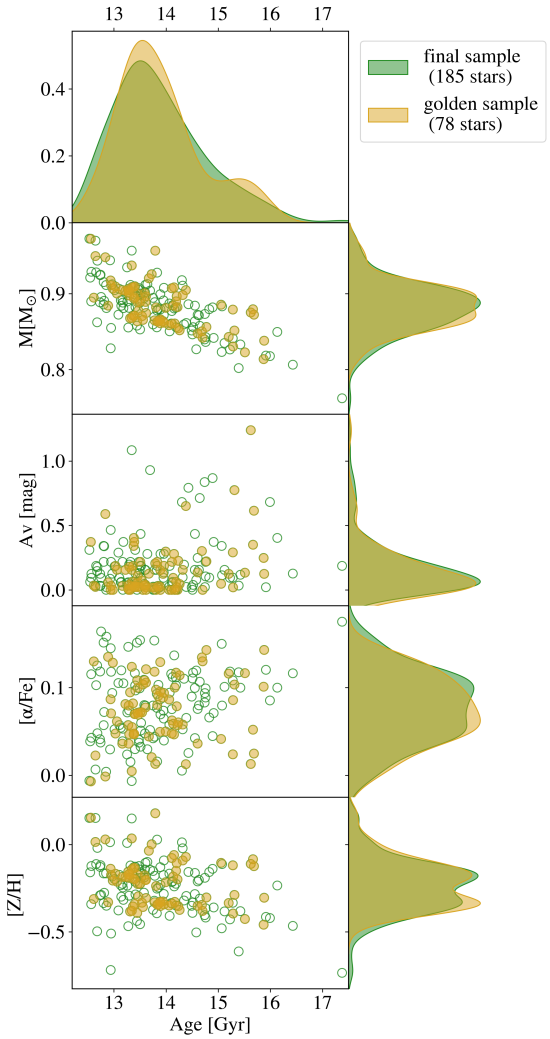

FIGURE 2.4: Trends with age of the main parameters, from the bottom: mass, dust reddening, overall metallicity and α-enhancement. On the right, the corresponding normalised distributions are shown for each parameter, and at the top is the distribution in age.

also show low extinction ($A_V < 0.5$ mag) as the whole final sample is confined within ~700 pc from the Sun.

In Figure 2.4, we show the distribution of the main physical parameters (α-enhancement, metallicity, dust reddening, and mass) versus age for the final and golden sample. The histograms show that our sample does not deviate much from solar values. Considering the final sample, the mean and standard deviation for each quantity are:

$$\langle M/M_\odot \rangle = 0.88 \pm 0.03$$
$$\langle [\alpha/Fe] \rangle = 0.17 \pm 0.21$$
$$\langle A_V \rangle = 0.08 \pm 0.04 \text{ mag}$$
$$\langle [Z/H] \rangle = -0.24 \pm 0.15$$

We also observe an inverse correlation between age and mass, with the least massive stars exhibiting the oldest ages. While this trend is expected, it may also hint at potential contamination, particularly in the low-mass tail, where a noticeable peak appears in the age distribution of the golden sample. These stars, with masses as low as 0.8 $M_{\odot}$, could represent remnants of originally more massive stars, evolved in binary systems that stripped away part of their gas. Recent evidence suggests that the fraction of mass transfer, degenerates, and mergers could represent about ~20% of Population II stars (Fuhrmann & Chini, 2021), so we will need to account for this component in the following.

Systematic effects

An important aspect to account for when relying on absolute age determination are the systematic effects at play. When performing isochrone fitting, two main sources of systematic uncertainties are involved: the first arising from the choice of the stellar models (see, e.g., Lebreton et al., 2014; Nsamba et al., 2021, and references therein), the second depending on potential biases affecting parameters like metallicity or α-enhancement assumed in the fitting process.

In N24, it is observed how the α-elements abundance could be under-predicted for some MSTO stars by up to 0.08 dex, owing to a comparison with common GALAH DR3 (Buder et al., 2021) stars. This little shift, if present, would cause an underestimation of the overall metallicity on which a Gaussian prior is assumed, thus overestimating the derived age. To account for this possible bias, following the approach adopted in N24, we perturbed the assumed [α/Fe] by ±0.1, finding, on average, a shift of ±0.28 Gyr. However, as we discussed before, most of our selected stars have rather low α-enhancements (see Figure 2.4).

In terms of stellar models, a positive note is that their difference is minimal for solar-like objects, as all models are calibrated to reproduce observations of the Sun, and our final sample shows properties that deviate very little from solar-like values. Nevertheless, different assumptions (e.g., on the initial helium fraction, mixing length, or treatment of diffusion) can lead to different results. Joyce et al. (2023), in particular, identifies variations in the convective mixing length parameter ($\alpha_{\rm ML}$) as one of the dominant sources of systematic uncertainty in stellar age estimates. They consider a wide range of fluctuations for this parameter – 1.4 to 2.3 for MSTO and SGB (see Figure 11 in Joyce et al., 2023). In order to reflect this variation into the age measurements, they perform a Monte Carlo simulation perturbing the set of isochrones by 200 K in $T_{\rm eff}$ and 0.17 dex in $\log g$, finding an average shift in ages of 1-2 Gyr, where a higher $\alpha_{\rm ML}$ produces older ages. In order to adapt this analysis to our case, we need to make three considerations.

First, the range adopted for $\alpha_{\rm ML}$ is very wide if compared to the typically used values in most stellar models, ranging mostly from 1.6 to 1.9 (see, e.g., Table 4 in Amard et al., 2019, for a summary). The models used in this work, PARSEC, set $\alpha_{\rm ML} = 1.74 - 1.77$, which is in the middle of this interval.

Second, the Kiel diagram area covered by the final sample in this work is confined between 5400-5700 K in $T_{\rm eff}$ and 3.8-4.1 in $\log g$, where the effect of $\alpha_{\rm ML}$ is minimal and fully horizontal (i.e., it produces only a shift in $T_{\rm eff}$). Considering the full range 1.4-2.3, this produces shifts of ±100-150 K from the mean value, while considering the most used range 1.6-1.9, this implies fluctuations of ±30-50 K.

Third, the uncertainties in $T_{\rm eff}$, $\log g$, and metallicity in this work are up to 4-5 times smaller than the ones considered in Joyce et al. (2023).

Owing to these considerations, we conclude that the lower bound of the interval identified in Joyce et al. (2023) – 1 Gyr – is an overly conservative choice to account for the systematic component of the error related to the stellar models in this work.

Systematic uncertainties may also arise from discrepancies between the actual stellar helium content and the values assumed in model grids (see Lebreton et al., 2014; Nsamba et al., 2021, for a detailed discussion). These studies show that adopting different assumptions for the initial helium content – either reading it as a free parameter or rising it via a $\Delta Y/\Delta Z$ relation – can introduce systematic effects of the order of a few percent in mass and, therefore, in age. However, for our sample, most stars have metallicities close to solar, so their helium abundances are expected to be similar to those assumed in standard stellar models (solar mixture).

Another potential systematic effect linked to the stellar models is the one of atomic diffusion, causing the exterior of the star to appear more metal-poor with respect the internal, initial value of metallicity (see, e.g., Korn et al., 2007). The effect of diffusion is, anyway, already included in the PARSEC models and, even if the current knowledge of this process is still incomplete, it should be less and less relevant moving towards older ages and to metallicities around solar (see Figure 3 in Dotter et al., 2017). For this reason, we decided not to add another source of systematic error owing to this effect.

Identifying the tail of spurious ages

As noted in Section 2.1.2, the tail towards oldest ages could be contaminated by stars that lost some mass, causing them to appear artificially older, but also by undetected binaries with unequal mass, as shown in Woody et al. (2025). Being close to the physical limit imposed by t_U, these spurious solutions should pop out as a secondary distribution at older ages. To test this, we fit a Gaussian Mixture Model to both the good and golden samples, allowing the data to determine the optimal number of components. Based on both the Bayesian and Akaike Information Criteria, the fit favoured two populations: a narrow peak at 13.4±0.8 Gyr and a broader one at 14.8±1.5 Gyr.

Given the presence of this secondary component, we opted for a more careful estimation of the contamination fraction with a hierarchical Bayesian model implemented through `PyMC`. In particular, we fit our distribution as the combination of a true and a contaminant population, following the approach described in detail in Miglio et al. (2021b).
Assuming a combination of two normally distributed samples, the first with mean μ and intrinsic dispersion σ, the second represented by a fraction, f_c, with mean μ_c and dispersion σ_c, the model can be summarised by the following likelihood function:

$$\begin{aligned}\mathcal{L}(\theta \mid \mathbf{x}, \sigma_{\mathbf{x}}) = \prod_{i=1}^{N} \Big[& (1 - f_c)\, \mathcal{TN}(\mu,\ \sigma^2 + \sigma_{x,i}^2,\ 12,\ 20) \\ & + f_c\, \mathcal{TN}(\mu_c,\ \sigma_c^2 + \sigma_{x,i}^2,\ 12,\ 20)\Big],\end{aligned} \tag{2.2}$$

where $\mathcal{TN}(\mu, \sigma^2, a, b)$ is a normal distribution truncated in the range $[a, b]$ and $(\mathbf{x}, \sigma_{\mathbf{x}})$ is the set of age measurements and associated errors.
We adopt uniform, wide, priors on μ and μ_c, respectively in the range 0–20 Gyr and 13–20 Gyr. On σ and σ_c, we adopt lognormal priors, centred at 1 Gyr with standard deviation 0.5 Gyr. For the contamination fraction, f_c, we use a β-function with parameters $a = 2$ and $b = 8$.
For the sampling of the posterior probability distribution, performed in `PyMC` with the No-U-Turn Samples (NUTS), we use four chains of 2000 steps, after performing 1000 burn-in steps, totalling 8000 samples.

The joint posterior distribution for the five parameters is shown in Figure 2.5, where the inset shows the decomposition in the final sample distribution. The median values and 68% contours for each

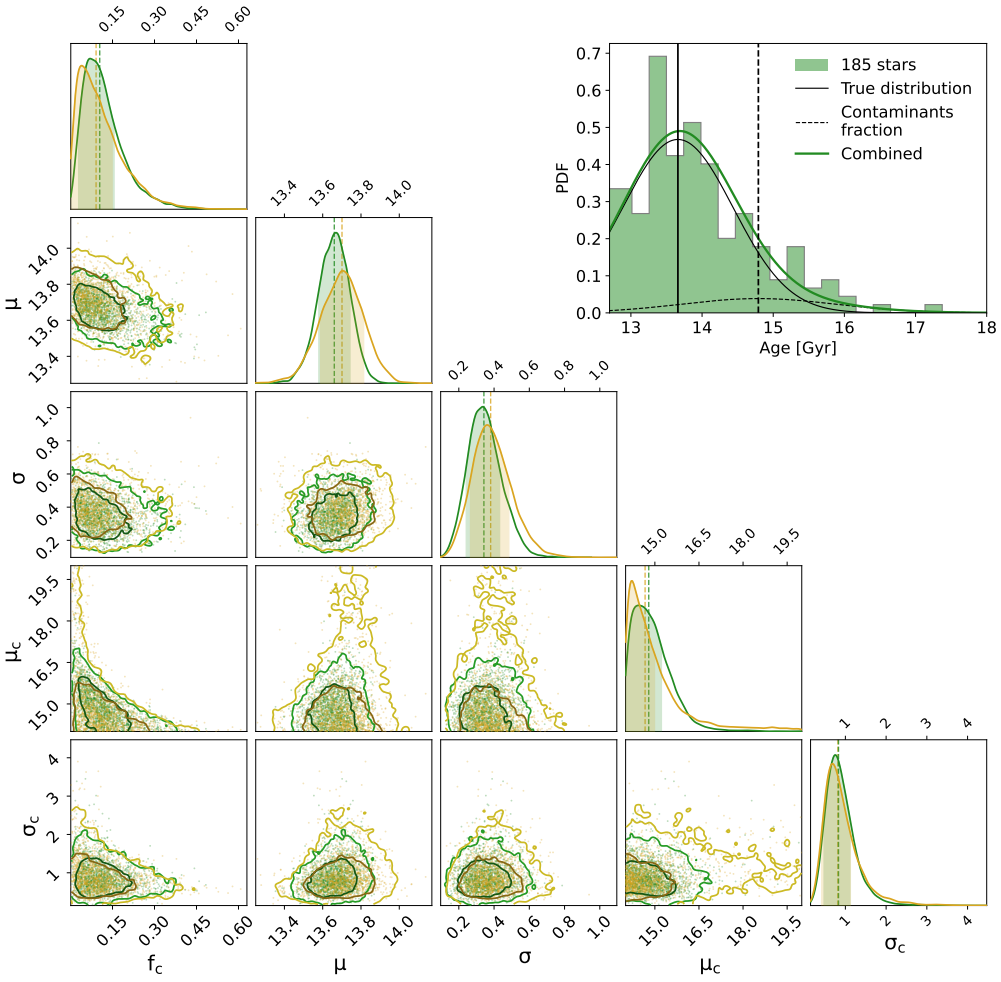

FIGURE 2.5: Joint posterior distribution of the five parameters included in the model reproducing the age distribution. Contours obtained with the final sample are shown in green, and in yellow for the golden sample. The inset shows the age distribution of the final sample and the two components resulting from the fit.

parameter are the following:

$$\text{Final sample} \quad \begin{cases} f_c = 0.10^{+0.08}_{-0.05} \\ \mu = 13.66^{+0.08}_{-0.08}, \quad \sigma = 0.34^{+0.10}_{-0.09} \\ \mu_c = 14.79^{+0.72}_{-0.52}, \quad \sigma_c = 0.83^{+0.37}_{-0.28} \end{cases}$$

$$\text{Golden sample} \quad \begin{cases} f_c = 0.09^{+0.10}_{-0.06} \\ \mu = 13.70^{+0.11}_{-0.11}, \quad \sigma = 0.38^{+0.12}_{-0.10} \\ \mu_c = 14.67^{+1.03}_{-0.49}, \quad \sigma_c = 0.82^{+0.47}_{-0.28} \end{cases}$$

We then removed from the sample all stars with a probability of being contaminants higher than 20%, computed as follows:

$$P(i = \text{contam}|x_i) = \frac{f_c\, \mathcal{N}(x_i; \mu_c, \sigma_c)}{f_c\, \mathcal{N}(x_i; \mu_c, \sigma_c) + (1 - f_c)\mathcal{N}(x_i; \mu_t, \sigma_t)}, \tag{2.3}$$

where x_i is a single age measurement, and $\mathcal{N}(a; b, c)$ is the value of a normal distribution with mean b and sigma c evaluated at a. For each star, when possible, we computed this probability using the best-fit values obtained from fitting both the final sample and the golden sample, as listed in Figure 2.5. This process led us to discard 11 stars from the golden sample and 25 stars from the final sample, with all contaminants present in the first also identified in the second. The cumulative PDFs of the clean final and golden sample peak at 13.6±1.0 Gyr and 13.6±0.9 Gyr, respectively, confirming no significant difference between the two samples. Hence, we adopted the clean final sample (160 stars) as our reference.

2.1.3 Implications for cosmology

From the stellar ages to the age of the Universe

To convert the stellar ages into constraints on t_U we need to take into account the delay, δt, between the Big Bang and the moment these objects formed. As the ages of the oldest objects represent a lower limit to t_U, a conservative choice would imply accounting for the smallest possible value for δt. Theoretical models of stellar formation (Galli & Palla, 2013; Bromm & Yoshida, 2011) and spectroscopically confirmed observations of the most distant galaxies (Curtis-Lake et al., 2023; Carniani et al., 2024) show that the very first stars have formed at $z \gtrsim$11–14, and not earlier than $z \sim$20–30, the expected redshift of formation for Pop III stars. This corresponds to an interval δt of about 0.2–0.4 Gyr.

In Figure 2.6, we show the cumulative PDF of our final and golden sample. With lines in the same colours, we report the cumulative distribution obtained by adding the systematic errors in quadrature to each star, as discussed in Section 2.1.2. The final cumulative PDF, shows a mean and standard deviation of:

$$\text{age} = 13.6 \pm 1.0\,(\text{stat}) \pm 1.3\,(\text{syst})\ \text{Gyr}.$$

Accounting also for the minimum formation time for these stars, this produces a lower limit to the age of the Universe:

$$t_U \geq (13.8 - 14.0) \pm 1.0\,(\text{stat}) \pm 1.3\,(\text{syst})\ \text{Gyr},$$

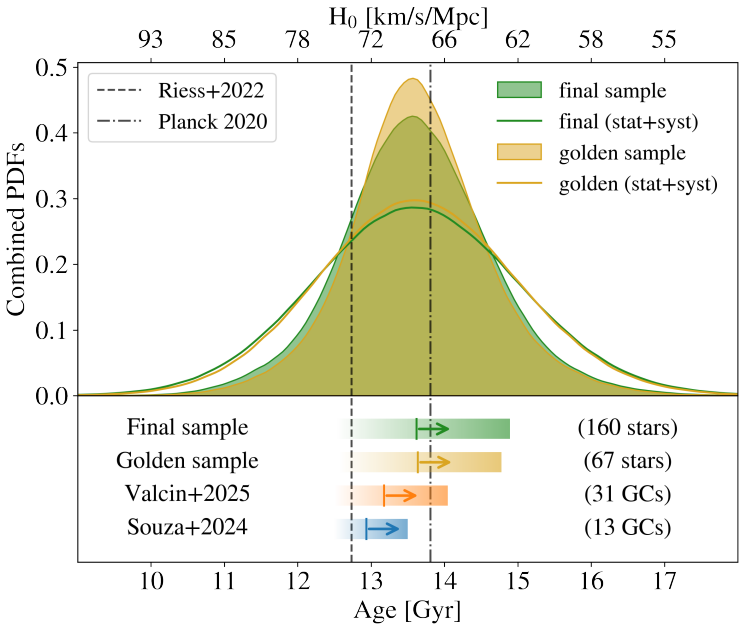

FIGURE 2.6: Cumulative posterior distribution in age for final and golden sample. The distributions including the systematic component of the error are shown with solid lines in the same colours. The upper axis shows the corresponding H_0 value, assuming z_F=20. In the lower panel, the age ranges covered by the stars in the final and golden samples and their means are shown in comparison with the oldest (> 12.5 Gyr) GCs in Valcin et al. (2025) and the oldest bulge GCs in Souza et al. (2024).

which would increase, should these stars have formed at z<11.

In the upper axis of Figure 2.6, the values of the Hubble constant H_0 are also reported assuming a redshift of formation for the sample $z_F = 20$. Under these assumptions, the lower limit on the age of the Universe translates, in terms of H_0, into:

$$H_0 \leq 68.3^{+5.4}_{-4.7}\,(\text{stat})\,^{+7.2}_{-5.9}\,(\text{syst})\,\text{km/s/Mpc},$$

and would further decrease by 1.2 km/s/Mpc assuming $z_F = 11$. For comparison, the two values currently leading the Hubble tension, Planck Collaboration et al. (2020) and Riess et al. (2022), are also shown with dashed lines. We underline that the assumptions made here to connect H_0 and t_U are commonly adopted, but represent a particular case. The relation between H_0 and t_U can be influenced by different factors, especially the value assumed for Ω_m, but also by the cosmological model in general. In Section 2.1.3, we discuss this aspect in more detail. Regardless of the implications on the value of H_0, the sample identified in this work provides important and direct constraints on the age of the Universe itself, representing an observational anchor point to any cosmological model.

Considering the single PDFs of the 160 stars in the final sample (excluding, for now, systematic uncertainties) and shifting them by the minimum possible delay (0.2 Gyr), we find that at the 90% confidence level (CL), 70 stars indicate an age of the Universe older than 13 Gyr, and 29 stars suggest an age older than 13.5 Gyr, while no star exceeds 14.1 Gyr at 90% CL. Notably, in order for the data to indicate a significant drop in ages at 13 Gyr or younger, the full systematic error budget would be needed, consistently shifting the results towards younger ages. While this may be plausible for the [α/Fe] estimation

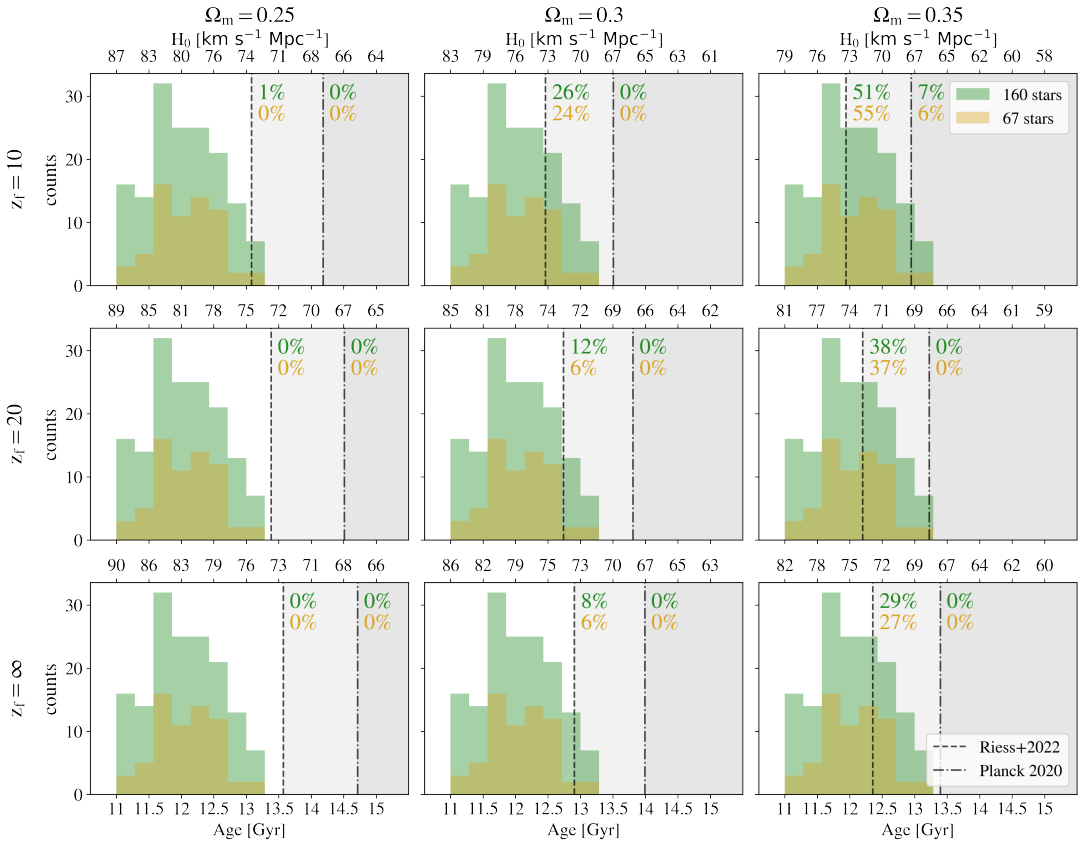

FIGURE 2.7: Distribution of the 10^{th} percentile in age for the clean final (green) and golden (gold) samples. In each panel, the top axis shows the corresponding H_0 values assuming a flat ΛCDM and a different value of Ω_m and z_F: rows from top to bottom set $z_F = 10, 20, \infty$, columns from left to right fix $\Omega_m = 0.25, 0.3, 0.35$. The dashed and dashed-dotted lines report the H_0 measurements from Riess et al. (2022) and Planck Collaboration et al. (2020), respectively. Next to each one of them, the percentage of stars in the final (green) and golden (gold) samples pointing to a lower H_0 at 90% CL (stat+syst) is reported.

component (0.3 Gyr in the error budget), there is no evidence favouring stellar models that predict systematically younger ages. On the contrary, considering models with higher $\alpha_{\rm ML}$, age estimates could increase by up to 1 Gyr.

The results of this work are also complemented and supported by independent age estimations obtained for very old GCs, as the ones in Valcin et al. (2025) and the bulge GCs in Souza et al. (2024). In the lower panel of Figure 2.6, we show the age ranges and mean values from both studies restricted to clusters older than 12.5 Gyr, consistent with our selection. The figure highlights how the tail of the oldest GCs overlaps with the age distribution of our sample. Although the stellar models adopted in those studies differ from those used here, the age ranges of the oldest GCs vary by less than 1 Gyr, with average ages differing by only ~0.5[3] Gyr (Valcin et al., 2025) and ~0.7 Gyr (Souza et al., 2024). Remarkably, both samples show metallicities comparable to those in our sample, reinforcing the conclusion that such old ages are achievable even at these metallicities, supporting a scenario of rapid early formation.

[3]Peculiar GCs showing a spread in metallicity (namely NGC5286, NGC5139, and NGC7089) were removed from the sample.

Alternative cosmological assumptions

In Figure 2.7 we show how the upper axis of Figure 2.6 changes when changing the values of the matter density parameter Ω_M and of the assumed redshift of formation for these stars, z_F.
To construct the histograms, we first broadened the age PDF of each star by summing the statistical and systematic uncertainties in quadrature. We then computed the 10^{th} percentile of each PDF. These values, representing the ages above which the stars lie with a 90% CL, were used to populate the histograms. This approach serves a dual purpose: using the entire sample mitigates the impact of statistical fluctuations, while selecting the 10^{th} percentile ensures a conservative estimate for the lower limit of $t_{\rm U}$ and translates into a broader upper bound on H_0.
All panels share the same lower horizontal age axis, while the upper one, in H_0, varies depending on the assumed value of Ω_m and z_F. This allows us to show how the distribution found in this work compares with the measurements from Planck Collaboration et al. (2020) and Riess et al. (2022), represented by a dashed and a dashed-dotted line, respectively, at varying cosmological assumptions. The percentages reported in each panel, next to these lines, show the fraction of stars older than the respective ages of the Universe at 90% CL (stat+syst), thus pointing to a lower H_0 value at 90% CL.

The setting adopted in Figure 2.6 corresponds to the one in the central panel in Figure 2.7. Overall, this shows how z_F and Ω_m act when translating the age of the oldest objects into H_0: the higher z_F is assumed, the higher H_0 is retrieved, while the opposite is true for Ω_m. In the context of the Hubble tension, this shows that the sample in this work points to H_0 lower than the CMB value only when $\Omega_m = 0.35$ and $z_F = 10$. Compared to Riess et al. (2022), instead, all configurations with $\Omega_m \geq 0.3$ show at least 6% of stars, up to 51%, pointing to a lower value of H_0 at 90% CL. The only configurations showing no tensions with any of the two measurements are the ones with $\Omega_m = 0.25$.

2.1.4 Conclusions

In this work, the ages of the oldest stars from Gaia DR3 are used to constrain the age of the Universe, t_U, representing the first attempt to use the ages of single stars as cosmic clocks with a statistically significant sample.

We considered the ~200,000 stars from N24, with ages and masses estimated via the Bayesian code `StarHorse`, but allowing ages to vary up to 20 Gyr without a cosmological prior. We selected the ~3,000 stars older than 12.5 Gyr with age uncertainties below 1 Gyr. Through a careful selection process including cuts in the Kiel diagram, stellar parameter quality, symmetry of posterior distributions, and a final visual inspection, we removed stars with potentially biased age estimates, especially those skewed to older values, to obtain a conservative and robust lower limit on stellar ages and thus on t_U.

We identified two sub-populations in age, one at ~13.7 with very little dispersion (~0.3 Gyr) and an older one, at ~14.8 Gyr, with a dispersion of ~0.8 Gyr. Assuming a fraction of stars could be composed of older contaminants (e.g., mass-stripped stars, binaries), appearing older than they are, we conservatively excluded all stars belonging to the second peak (~ 11%).

The final sample counts 160 stars, with a cumulative posterior distribution peaking at 13.6 ±1.0 (stat) ±1.3 (syst) Gyr. The main source of systematic error comes from stellar models. Accounting for the minimum possible delay between the Big Bang and the formation of these stars, 0.2 Gyr at $z_F = 20$,

we derive a conservative lower limit on t_U, and an upper limit on H_0:

$$\begin{aligned} \text{age} &\geq 13.8 \pm 1.0\,(\text{stat}) \pm 1.3\,(\text{syst})\ \text{Gyr}, \\ H_0 &\leq 68.3^{+5.4}_{-4.7}\,(\text{stat})\,^{+7.2}_{-5.9}\,(\text{syst})\ \text{km s}^{-1}\ \text{Mpc}^{-1}. \end{aligned}$$

Considering them one by one, 70 stars indicate an age of the Universe older than 13 Gyr, while no star exceeds 14.1 Gyr at 90% CL (stat). Notably, the full systematic error budget would be needed, consistently pointing towards younger ages, to move this drop to 13 Gyr or less.

In conclusion, this work shows how the ages of single stars derived from isochrone fitting can provide stringent constraints on t_U, and a robust anchor point to any cosmological model. While this represents a significant first step, future data releases from *Gaia* will enable similar analyses on larger stellar samples with improved precision. Furthermore, the accuracy and reliability of age determinations can be improved by obtaining metallicities from high-resolution spectroscopy, minimising, at the same time, the systematic error due to the α-enrichment. However, only with missions such as Haydn (Miglio et al., 2021a) will it be possible to achieve accurate ages for field stars in the MW.

2.2 The oldest globular clusters as cosmic clocks

Globular clusters are among the oldest objects in the Universe for which we can accurately determine the age (VandenBerg et al., 1996; Soderblom, 2010; Brown et al., 2018; Oliveira et al., 2020; Massari et al., 2023). Composed of roughly one million stars that formed simultaneously with similar composition (though see reviews by Bastian & Lardo, 2018; Gratton et al., 2019; Milone & Marino, 2022, for discussions on the multiple population phenomenon in massive clusters), these clusters have remained gravitationally bound for up to a Hubble time. Each GC thus serves as an observable record of the age, metallicity, and kinematics from the time of its formation.

The most straightforward method to determine the age of a GC, as detailed in Section 1.3.1, is to exploit the fact that the position of the MSTO in the $T_{\rm eff} - L$ plane changes with age (or mass). Isochrones, or theoretical tracks of stars with the same chemical composition, are fitted to the MSTO region CMDs to estimate the age. Even if this is a well-established and robust method, it is important to explore new and complementary approaches that can address the case when the CMD is not available. In need of a spatially resolved stellar population, indeed, isochrone fitting can be applied only to nearby systems, while moving further than the Magellanic Clouds (e.g. Niederhofer et al., 2025) becomes either very expensive in terms of exposure time or even impossible[4]. Moreover, recent JWST observations of lensed fields highlighted the presence of GC candidates around lensed galaxies, like the Sparkler (Mowla et al., 2022) at z=1.38, which, if confirmed with spectroscopy, would extend the study of GCs at high redshift. To do so, we need to explore methods relying on GCs' integrated light and validate them against the traditional methods. In this scenario, one of the best ways to leverage all the integrated light information is to perform FSF, a technique that enables one to measure, alongside the age, all the physical properties of the GC, such as metallicity, mass, and dust reddening.

Previous works have derived physical parameters of GCs like age and metallicity using the integrated light provided by Schiavon et al. (2005) for 41 MW GCs (e.g. Koleva et al., 2008; Cezario et al., 2013; Cabrera-Ziri & Conroy, 2022), testing different algorithms, like `STECKMAP` (Ocvirk et al., 2006), `NBURSTS` (Chilingarian et al., 2007), `ULySS` (Koleva et al., 2009), or `ALF` (Conroy & van Dokkum, 2012), and different SSP models (Bruzual & Charlot, 2003; Prugniel & Soubiran, 2004; Vazdekis et al., 2010, 2015). Others have benefited from the larger spectral coverage and higher resolution of the WiFeS Atlas of Galactic Globular cluster Spectra project (WAGGS, Usher et al., 2017, 2019a), providing integrated spectra for 113 GCs in the MW and its satellite galaxies (Usher et al., 2019b; Gonçalves et al., 2020; Cabrera-Ziri & Conroy, 2022). While there is broad agreement that the ages of younger GCs can be reliably determined through FSF, these studies highlighted the challenges in dating the oldest GCs from their integrated spectra, often yielding results significantly younger than those from isochrone-fitting methods.

Here, we focus on the oldest tail of the WAGGS GCs, analysing 82 GCs in the MW. We take advantage of the high-quality integrated spectra provided by WAGGS, along with the wealth of data available for these objects, the independent age estimates derived with different techniques, and the fact that GCs are among the simplest stellar systems in the Universe, the closest templates to an SSP we have. We adopt a parametric FSF method, enabling the reconstruction of GCs' integrated emission within a high-dimensional parameter space. For this purpose, we use the FSF code `BAGPIPES` (Carnall et al., 2018), for which an outline is provided in Section 1.3.2. Previous studies in the literature have typically derived parameters such as age, metallicity, mass, and dust reddening while assuming a cosmological

[4] For example, we note that, in the case of Local Group galaxies, high-quality integrated spectra often yield results that surpass those obtained from shallow CMD studies (e.g. Ruiz-Lara et al., 2018).

prior on the age. In contrast, the novelty of this study lies in removing this prior to explore how the derived ages are affected, as was done by Tomasetti et al. (2023) and Jiao et al. (2023), in order to test the potential of the results in a cosmological framework. By testing this approach, we aim to assess its potential in a cosmological context, by using these cosmology-independent results to place new constraints on H_0, setting the stage for future applications in studying the distant Universe.

2.2.1 Data

The WAGGS project (Usher et al., 2017) is a library of integrated spectra of GCs in the MW and the Local Group, obtained with the WiFeS integral field spectrograph on the Australian National University 2.3 m telescope. With 112 spectra of GCs in the Local Group, it is one of the largest GC spectral libraries currently available, with a wide wavelength coverage (3270-9050 Å) and high spectral resolution (R $\sim$ 6800). The spectra we work with are normalised and consist of four different gratings, each with its own sampling: 3270-4350 Å (0.27 Å per pixel), 4170-5540 Å (0.37 Å per pixel), 5280-7020 Å (0.44 Å per pixel), and 6800-9050 Å (0.57 Å per pixel). To perform FSF across the entire spectrum, certain adjustments were required.

First, we had to re-scale each spectrum to match its literature photometry, to retrieve the fluxes in physical units. We used the UBVRI integrated photometry from the 2010 edition of the Harris catalogue (Harris, 1996, 2010). The correction factor, C, derived via χ^2 minimisation, can be written as:

$$\mathrm{C} = \frac{\sum(\mathrm{p_J}/\mathrm{e_J})^2}{\sum \mathrm{f_J p_J}/\mathrm{e_J^2}}, \tag{2.4}$$

where p is the photometry in the J-th filter, and f and e are, respectively, the average flux and corresponding error estimated on the spectrum on a window of 10 Å. We then multiplied the spectrum in each grating by the corresponding factor, C.

Here, we must underline that UBVRI photometry is not available for all the objects in WAGGS, but only for the 82 GCs belonging to the MW. For the younger GCs in the LMC and SMC and in the Fornax dwarf spheroidal, only BV photometry is available, respectively, from van den Bergh (1981) and van den Bergh (1969). Anyway, in this work, we want to focus on the oldest tail of the local GCs, so we limit our sample to the MW GCs. Before proceeding with the analysis we performed a visual inspection of the spectra, removing five GCs showing either visibly corrupted or very noisy regions (S/N<10 in more than 40% of the spectrum), namely NGC6144, NGC6401, NGC6517, NGC6712, and NGC7492. The sample we analyse here is then constituted of 77 GCs.

To combine the four gratings into a single spectrum, we interpolated all of them onto a common wavelength grid, matching the largest spectral sampling value (0.57 Å per pixel). In the overlap regions, the flux and associated error were estimated by averaging the spectra from the consecutive gratings.

Throughout this section, we compare our results to literature values of age, mass, and metallicity, and we also consider additional quantities to complement and expand our analysis, like dust reddening, radial velocities, and the distances of the GCs. We use as a reference the values listed in Usher et al. (2017) for ages and masses, in Harris (2010) for metallicities ($[Fe/H]$) and dust reddening ($E_{\mathrm{B-V}}$) and in Baumgardt et al. (2023) for radial velocities, distance from the Sun, and associated errors.

As for the uncertainties on metallicities, we considered the errors found in other spectroscopic investigations based on integrated spectra of Galactic GCs. These are approximately ±0.15 dex (see Roediger et al., 2014; Colucci et al., 2017).

On ages, the error budget based on MSTO fitting involves several key contributors. The most significant is distance uncertainty; an error of approximately 0.1-0.15 mag can result in an uncertainty in age of about 10%. The error in the initial helium content, known within ~2%, translates to an uncertainty in age of about 2%. An error in the global metallicity of ~9-10% and of ~0.15 dex in iron content leads to an error in age of approximately 4-5%. An uncertainty of ~0.15-0.2 dex in alpha elements translates to an error in age of about 4% (see a discussion in Cassisi & Salaris, 2013). Combining these factors, the overall uncertainty in age can be around 10-20% (e.g. O'Malley et al., 2017). For the sake of comparison, we consider a fixed error of ±1.5 Gyr.

On mass, a typical uncertainty of ~10% is generally found on single measurements, corresponding to 0.05 dex in $\log(M_\star/M_\odot)$ (Hénault-Brunet et al., 2019). Nevertheless, a difference of ~0.2 dex on average can be observed among different catalogues (e.g. Usher et al. (2017) with respect to Baumgardt et al. (2023)). For this reason, we adopt a typical error on the mass of 0.2 dex.

2.2.2 Spectroscopic analysis

Before estimating the physical parameters of our GC sample with FSF, we want to derive measurements of the spectroscopic features in our sample and use those to have a preliminary assessment of the age and metal content of our GCs. At high redshift, the study of Lick indices (Burstein et al., 1984; Faber et al., 1985) or spectral breaks is often used to constrain stellar population properties. Here we want to see how GCs, the astrophysical objects that most resemble SSPs, fit inside this framework.

To do so, we first measured all the absorption features detectable in the spectra using the public code `PyLick` (Borghi et al., 2022a). We want to compare these data with theoretical models estimated by Thomas et al. (2011) at different ages, metallicities and alpha-enhancements ([α/Fe]). Since these models are built with MILES resolution (~2.7 Å FWHM), we downgraded the spectral resolution of our sample to match the models. Moreover, if an index lies in the overlap region of two spectral gratings, we ran `PyLick` on both spectra and then averaged the two values weighting them with their associated errors.

In particular, we measured indices of the Balmer series, like Hβ and Hγ, indices of the iron group like Fe5270 and Fe5335 or Mgb and broader features like the D4000, a spectral break at 4000 Å. These features are particularly relevant in the study of stellar populations in that they are known to independently correlate with age (like D4000 and Hβ) and metallicity (like the iron group), so their analysis can give important insights into the physical properties of the GCs, as we discuss in the following sections.

Index-age analysis

After measuring the spectral features, we can compare their trend with age to the theoretical ones. A variety of stellar libraries are available in the literature, like Bruzual & Charlot (2003), Maraston & Strömbäck (2011), and Conroy & van Dokkum (2012), adopting different stellar evolutionary models, libraries of stellar spectra, and procedures to compute the integrated spectra. In Moresco et al. (2012), however, it is shown how the assumption of different SPS models has a negligible impact on the slope of the index-age trend, in particular in the case of the D4000. To compare our measurements with theoretical trends, here we are considering the 2016 version of Bruzual & Charlot (2003) models (hereafter BC16), since these are the same SPS models implemented in `BAGPIPES`.

In Figure 2.8a, the measured D_n4000 is shown as a function of the GC literature age for the 75 GCs for which an age estimate is provided in the literature, divided into six metallicity bins. For a qualitative comparison, we report the theoretical trends from BC16 with $[Fe/H]$ varying from −0.33 to −2.25 and

alpha-enhancement ([α/Fe]) fixed to solar value. The trends are almost flat in this age interval, as is expected in these ranges of ages and metallicities (see, e.g., Moresco et al., 2022), but show an evident gradient with metallicity, that is in good agreement with the theoretical distribution, with the D_n4000 increasing as metallicity raises.

Analogous to the D_n4000, in Figure 2.8b the trends in age are shown for the Balmer index, Hβ, in comparison with the theoretical trends in the same metallicity bins. The distribution of this feature shows a good agreement with the models as well, this time decreasing with increasing metallicity.

Testing these observables against the stellar models in the case of GCs, objects for which independent and robust measurements of age and metallicities are available, is of great importance in order to validate the models and their use in cosmological analyses. In the application of cosmic chronometers (Jimenez & Loeb, 2002), for instance, especially when the D4000 is directly used to trace the age evolution in redshift (Moresco et al., 2012; Moresco, 2015; Moresco et al., 2016) it is fundamental that the D4000 traces correctly the stellar population evolution in time (i.e. the D4000-age slope).

Index-index diagrams

While in the previous section we studied the sensitivity of single features to the age and metallicity of the population, it is also possible to combine them in the analysis, taking advantage of their different sensitivity to parameters like age, metallicity, and alpha-enhancement. In this case, we are considering a different set of theoretical models to compare them with, specifically developed to take into account also a variation in the chemical composition (Thomas et al., 2011, TMJ11). Historically, this method has been applied in galaxies (e.g. Onodera et al., 2015; Scott et al., 2017; Lonoce et al., 2020; Borghi et al., 2022a) but also in GCs (e.g. Strader & Brodie, 2004; Proctor et al., 2004; Mendel et al., 2007; Annibali et al., 2018) to derive constraints on the physical properties of these objects. Applying this method, we selected and compared indices that are mostly sensible to age, metallicity, or α-enhancement variations so that we could disentangle their contributions to the feature's equivalent width. The most widely used are indices of the Balmer series, the iron-group ones, like Fe5270 and Fe5335, and Mgb. As for BC16, the models in TMJ11 have MILES resolution, but differently from BC16, they produce a forecast only for the set of Lick indices and not the entire spectrum. In particular, they model the indices values on a grid of ages, metallicities, and alpha-enhancements. Generally, an age-sensitive and a metallicity-sensitive index are plotted one against the other, and compared to a model grid with varying age and $[Fe/H]$ but fixed [α/Fe]. In Figure 2.9 we present two examples of these diagrams, Hβ-Mg_b and Hγ_F-[Mg/Fe]', where the latter is defined as:

$$[\mathrm{Mg/Fe}]' = \sqrt{\mathrm{Mg_b}(0.72 \times \mathrm{Fe5270} + 0.28 \times \mathrm{Fe5335})}. \tag{2.5}$$

Here, the [α/Fe] is fixed at 0.3, which is the closest to the typical value found in the literature for our sample of GCs, around 0.35 (e.g. Pritzl et al., 2005; Mendel et al., 2007).

This method allows us to obtain a first estimate of the population's age and metallicity, which aligns well with the literature values, obtained with the independent traditional methods. In terms of age, the sample of GCs populates the area of the oldest objects in the diagrams, with a percentage of data points compatible with an age older than 12 Gyr of 66% and 88%, respectively, in the Hβ-Mg_b and Hγ_F-[MgFe]'.

From inspecting Figure 2.9, we note that metal-rich GCs consistently fall below the oldest ages predicted by the models. To some extent, this may be caused by the lower α-enhancement characterising metal-rich GCs; the effect is indeed mitigated if we consider the dashed grey grid lines corresponding to models with [α/Fe]=0. The observation that other metal-rich GCs exhibit similarly low Balmer line

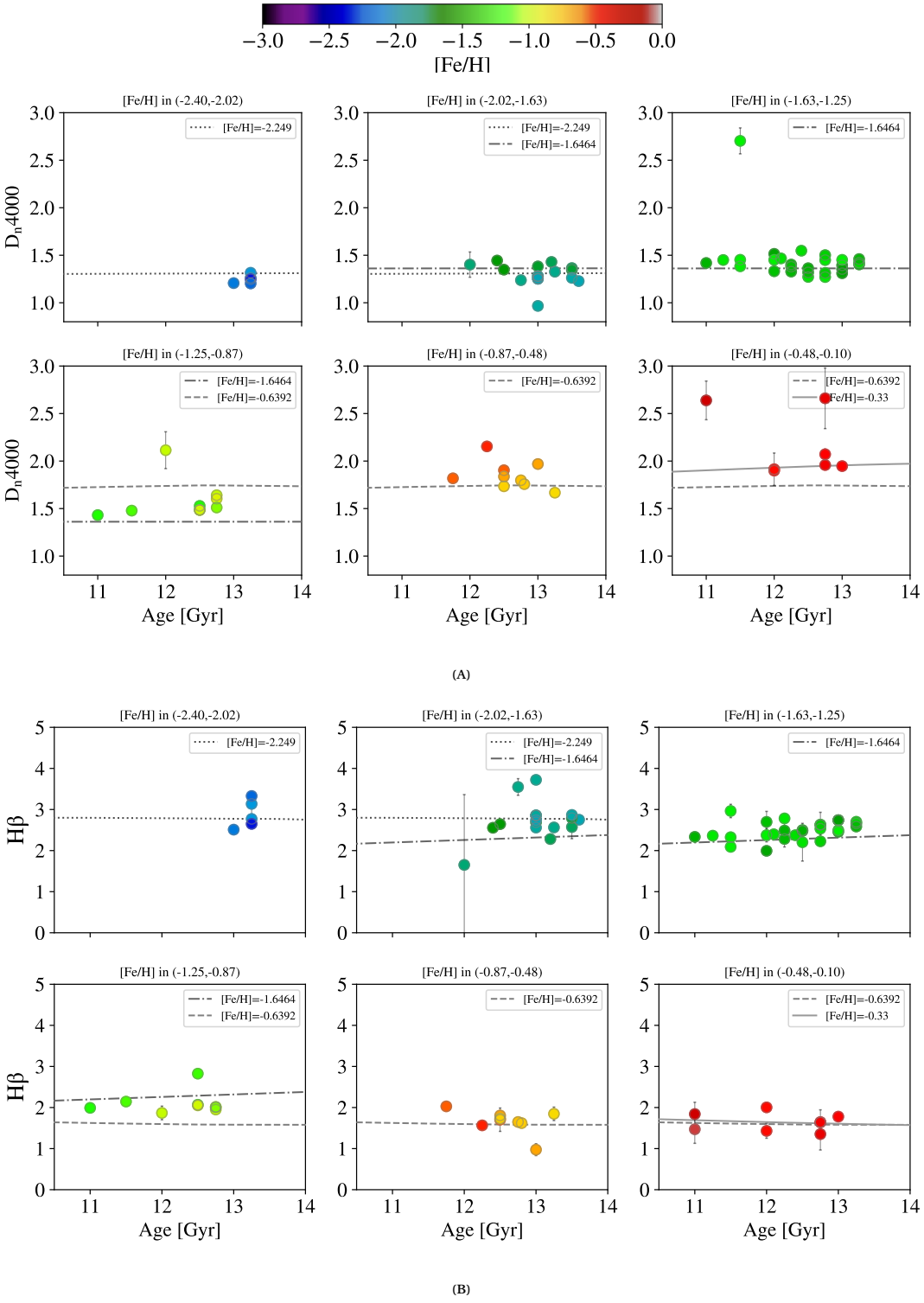

FIGURE 2.8: D_n4000 (top) and Hβ (bottom) trends with age and metallicity. The indices are shown for a sample of 75 GCs for which a literature value of age is available, divided into six $[Fe/H]$ bins and colour-coded according to it. In the background, the stellar models from BC16 relative to each $[Fe/H]$ bin are shown with different line styles.

strengths compared to model predictions suggests a systematic problem with the zero-point calibration of current stellar population models [5] (see Gibson et al., 1999; Vazdekis et al., 2015). Previous

[5] Interestingly, this zero-point issue in the models relative to metal-rich GCs is also observed in studies of old elliptical galaxies.

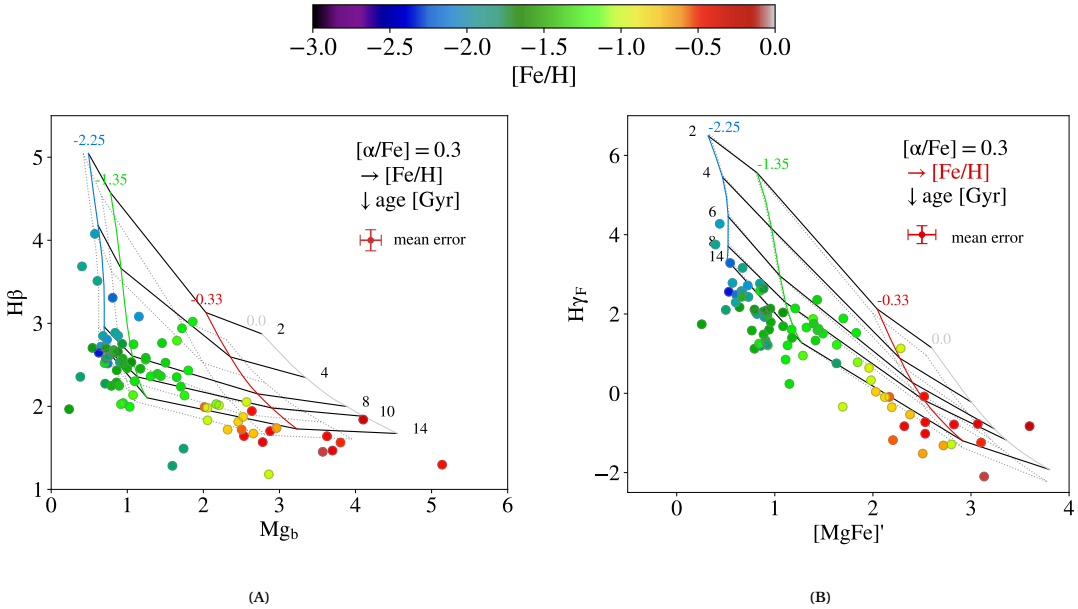

FIGURE 2.9: Index-index diagnostic diagrams, on the left Hβ-Mg$_b$ and on the right Hγ_F-[MgFe]'. The points are colour-coded by their literature value of $[Fe/H]$. We report TMJ11 models as a grid with varying metallicity (vertical lines) and varying age (horizontal lines), the first with the same colour code as the data points. Solid lines refer to models with $[\alpha/Fe]$=0.3, while the dashed lines in the background represent the solar-scaled grid.

studies have shown that factors such as α-element enhancement and atomic diffusion (Cassisi et al., 1998; Salaris et al., 2000) in evolutionary models may provide a plausible explanation for the observed weakening of Balmer lines. These effects influence the temperatures of turnoff stars, which are the primary contributors to the Balmer lines in old, metal-rich stellar populations.

From the diagrams in Figure 2.9 we can also see a small percentage of GCs in the area of typically younger objects, above the 8 Gyr grid-line. In particular, in the Hβ-Mg$_b$ this happens for 17 GCs, while in the Hγ_F-[MgFe]' for 11 GCs.

This behaviour can be attributed to the possible presence of an extended horizontal branch (HB), which can make the spectrum appear much bluer than expected for an old population and exhibit prominent Balmer lines, resembling a younger object. This is a very well-known effect, that has always made the study of GCs from integrated light challenging, mostly because the parameters determining the presence and the extent of the HB are not fully predictable with the current stellar evolution models. Various works have made progress in developing diagnostics to identify elongated HBs from integrated light, based on the Balmer lines (Lee et al., 2000; Schiavon et al., 2004) or on CaII and Mgb (Percival & Salaris, 2011). Others have managed to include the HB contribution on top of the SSP models (Jimenez et al., 2004; Koleva et al., 2008; Cabrera-Ziri & Conroy, 2022), modelling the emission from the HB hot stars as identified in the GCs' CMD. However, we still lack of a complete modelisation of the HB component, due to the many uncertainties around its origin. Modelling the HB component is beyond the scope of this study, instead, our primary goal is to assess how this un-modelled component may impact studies of integrated populations, using methods commonly employed in galaxy evolution analyses.

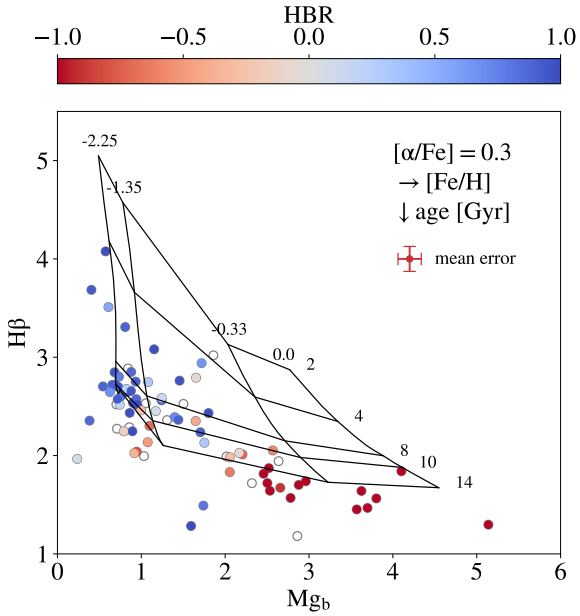

FIGURE 2.10: Hβ-Mg$_b$ diagram, colour-coded by the value of HBR index. Blank points are GCs for which the HBR estimate is not available in Harris (1996) (2010 version). TMJ11 models are represented as a grid with varying metallicity (vertical lines) and varying age (horizontal lines).

The most common parameter used to quantify the HB extent is the morphology index HBR (Lee, 1989; Lee et al., 1994), defined as:

$$\mathrm{HBR} = \frac{\mathrm{B} - \mathrm{R}}{\mathrm{B} + \mathrm{R} + \mathrm{V}}, \tag{2.6}$$

where B and R are the number of stars bluer and redder than the RR Lyrae instability strip, and V is the number of RR Lyrae stars. Although this parameter does not fully capture the distribution of stars along the HB, it still provides valuable information about the HB morphology, indicating whether it is predominantly red (HBR~ -1) or blue (HBR$\sim$1). In Figure 2.10 we report the same Hβ-Mg$_b$ diagram as in Figure 2.9a, but this time colour-coded by the HBR value listed in Harris (1996) (2010 edition), which is known for 69/82 objects (coloured points). According to this index, among the 14 GCs populating the area above the 8 Gyr grid line and for which the HBR is known, 13 show a blue HB, and for 11 of those the HBR is even higher than 0.5, a clue of a very elongated blue HB. The fraction of objects with HBR above zero decreases as we move to the areas belonging to older ages: 72% (18/25) between 8 Gyr and 12 Gyr and 33% (10/30) over 12 Gyr. The same trend can be observed moving from lower to higher $[Fe/H]$, with a percentage of GCs showing blue HBs decreasing from 68% (23/34) at $[Fe/H] < -1.35$ to 49% (13/29) in the range -1.35 $\leq [Fe/H] \leq$ -0.33 and dropping to zero at $[Fe/H] > -0.33$.

As was anticipated, stellar evolution models do not currently account for the presence of an extended blue HB, so this must be considered in the FSF analysis, where objects with extended HB morphology might be mistakenly identified as young stellar populations (Schiavon et al., 2004; Jimenez et al., 2004; Koleva et al., 2008; Cabrera-Ziri & Conroy, 2022). From our initial qualitative analysis using indices, we expect this issue to be more prevalent in metal-poor objects with prominent Hβ, which tend to show the highest HBR.

2.2.3 Method and analysis

In this section, we present the method adopted to estimate the ages and physical properties of the GCs sample, the code used, its settings, and the results obtained.

Full spectrum fitting with BAGPIPES

We performed FSF using the public code BAGPIPES (Carnall et al., 2018), which allows us to fit spectra and/or photometry adopting a parametric Bayesian approach. A detailed description of all the code's features is presented in Carnall et al. (2019) and Carnall et al. (2022), while a brief overview is presented in Section 1.3.2. Here, we recap the main features of the code, highlighting the aspects that are relevant to this work.

BAGPIPES is able to model synthetic spectra and photometry, based on a set of instructions, and then fit the so-modelled spectro-photometry to the observed one via a Bayesian approach.

The code allows one to combine different SFHs, but dealing with GCs we implement a single SFH, assuming a unique star formation episode. In particular, we adopt the DED SFH, which is described by Eq. 1.46. Using a single DED is recommended when dealing with a stellar population whose timescale of formation is much shorter than its age, as we expect for GCs.

Dust absorption and emission is particularly important to model the redder part of the spectrum, which can be largely depressed due to the presence of dust in the system. In the context of MW GCs, this component is necessary to account for the MW dust on the line of sight, for which WAGGS spectra are not corrected. The model implemented here is the Salim et al. (2018), represented by a power-law, as in Calzetti et al. (2000), with an additional parameter, δ, representing a slope deviation.

We also include the non-physical noise component, which can be added to the error spectrum to account for any potential underestimation, introduced as white noise.

After running the code, we obtain a best-fit spectrum and the posterior distributions for all the parameters involved, like age, mass formed, overall metallicity, and dust extinction. In terms of mass, the code distinguishes between mass formed M and stellar mass $M_\star$, differing in that the first comprises also the mass of stellar remnants (see Section 1.3.2 for further details). In this section, we refer to $M_\star$ as the mass of the objects.

We recall that, since we aim to use the resulting ages in a cosmological framework, we employ a version of BAGPIPES, described in Jiao et al. (2023), that deviates from the original in handling the priors on the stellar population age, allowing them to vary up to a cosmology-independent value (e.g. 15 Gyr, 20 Gyr) at any redshift. Below, we are going to test the effect of different assumptions of age prior on the sample of GCs.

Full spectrum fitting in WAGGS

Before inputting the cluster spectra into BAGPIPES, some adjustments were necessary. First, we downgraded the spectral resolution to approximately 2.7 Å FWHM, consistent with the BC16 models used in the code. Next, we aligned the spectra to the correct frame using distances from Baumgardt et al. (2023) and corrected for radial velocity variations, which could cause minor blueshifts or redshifts in the spectra. To prevent underweighting the blue features in the fit – due to the non-uniform error spectrum, with S/N ranging from a few tens to a thousand – we set an upper limit for the S/N at 100 and adjusted the error spectrum accordingly. We tested various S/N thresholds (e.g. 20, 50), finding that they had minimal impact on the results, except when the S/N ratio between the blue and red ends

of the spectrum differed by more than a factor of ten, which resulted in very low weight for the blue features in the fit.

After these adjustments, we performed multiple tests to optimally use BAGPIPES on GCs spectra and find the best-fit configuration to reproduce their spectral features accurately. In particular, this process involved: adopting different SFHs (e.g. single burst, delayed exponentially declined) with different priors on the parameters; fitting different wavelength ranges, either moving the lower limit to longer wavelengths to reduce the contamination by HB stars or pushing the upper limit to redder features to better constrain dust reddening; testing different priors on the GC's $[Z/H]$ and mass (e.g. uniform, Gaussian, logarithmic) to assess their impact on the estimation of these parameters, as well as the influence on ages, given the degeneracies at play. It is worth mentioning here that the mass and metallicity estimates proved to be very stable against all the different changes in the fit setup, while ages were mainly affected by the choice of prior, as we discuss in the following.
In the end, we converged to a fit configuration in which: *(i)* as often done in literature (Koleva et al., 2008; Gonçalves et al., 2020) we fit the range 3700-6000 Å to avoid the redder telluric lines and we mask the interval 5870 – 5910 Å, where the spectra show a very deep sodium doublet absorption line, since it could be potentially contaminated by interstellar absorption; *(ii)* we consider a single DED SFH, a dust component and a noise component; *(iii)* on all the parameters we set uniform, uninformative priors.

To assess the impact of the cosmological prior on the results, we tested two different upper limits for the age parameter: 13.47 Gyr, age of the Universe in a flat ΛCDM model with $\Omega_{m,0} = 0.3$, $\Omega_{\Lambda,0} = 0.7$, H_0 = 70 km/s/Mpc; 15 Gyr, a loose limit independent of any cosmology. We refer to the first configuration as *Config. 13.5* and to the latter as *Config. 15*. A summary of the main parameters and relative priors for the two configurations can be found in Tab. 2.1. We highlight that we assume uniform priors on all the parameters, along with wide ranges so that the results are not constrained by any previous knowledge of the GC's mass, metallicity, dust extinction or age.

As was anticipated, BAGPIPES adopts the overall metallicity $[Z/H]$ as the metallicity parameter. To compare our results with $[Fe/H]$ values from the literature, we need to perform a conversion. We used the conversion formula from Salaris & Cassisi (2005):

$$\begin{aligned}[Z/H] = \log\left(\frac{Z}{Z_\odot}\right) = \\ = [Fe/H] + \log_{10}\left(10^{[\alpha/Fe]}0.694 + 0.306\right).\end{aligned} \tag{2.7}$$

For objects with $[Fe/H] \leq -1$, we applied this formula with an alpha-enhancement of $[\alpha/Fe]$=0.35, which is typical of the metal-poor MW GCs (e.g. Pritzl et al., 2005; Mendel et al., 2007), while for GCs with $[Fe/H] > -1$ we use $[\alpha/Fe]$=0.15, average alpha-enhancement at these metallicities (see, e.g., Pagel & Tautvaisiene, 1995; Pancino et al., 2017). From now on, we refer to the quantity $[Z/H]$ as the metallicity of the GCs.

It should be noted that in this work, due to their integration within the BAGPIPES framework, we adopted the BC16 models, which rely on solar-scaled evolutionary tracks. We recognise that this approach can lead to slightly older age estimates compared to α-enhanced isochrones of similar metallicity (Salasnich et al., 2000; Thomas & Maraston, 2003). Alternative SSP models that include non-solar compositions and adequate metallicity coverage (Thomas et al., 2003, 2004; Lee & Worthey, 2005) typically have a maximum age of 12–15 Gyr (see, e.g., Proctor et al., 2004; Mendel et al., 2007, for discussion). Consequently, they do not enable the removal of the age prior as effectively as required for this

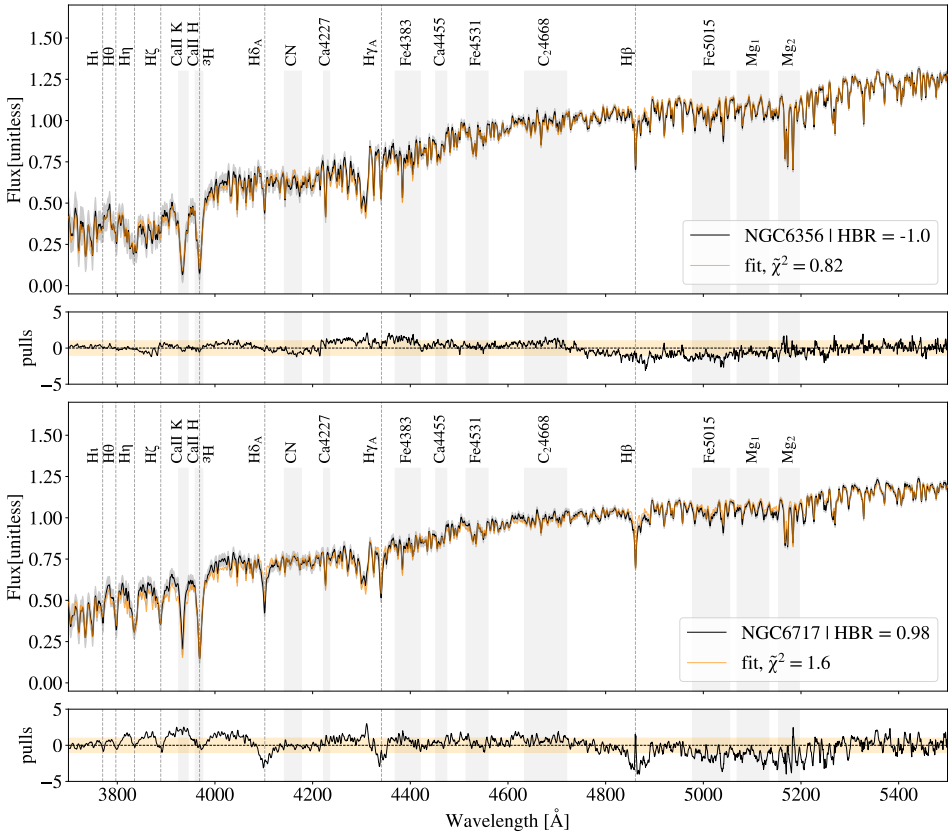

FIGURE 2.11: Examples of good fits. In the top panels, the observed spectra are shown in black and the posterior ones in orange. Dashed lines identify the Balmer absorption series, while other main absorption features are highlighted with shaded grey boxes. In the bottom panels, the pulls of each fit ((observed - fit)/error) are shown, with the orange horizontal area representing a 1-σ fluctuation.

analysis. We emphasise the need for models with non-solar compositions to refine age estimates in future studies (e.g., Park et al., 2024).

2.2.4 Results

We performed a visual inspection to evaluate the quality and convergence of the fits. Specifically, we identified fits that either failed to recover the spectral lines or continuum or exhibited double- or multiple-peaked posterior distributions. As a result, we discarded a significant number of poor fits, totalling 11 objects in both *Config. 13.5* and *Config. 15*, which represent about 14% of the sample. Among these, eight GCs had an HBR>0, and we found that, in these cases, the posterior spectrum underestimated the emission in the wavelength range bluewards of 4000 – 4500 Å. This issue is likely due to the blue HB emission, which the models cannot fully reproduce. Consequently, the fits converge to younger ages, as is observed in these cases in which all eight poor fits have ages younger than 10 Gyr. As is discussed in Section 2.2.2, various studies have successfully included a contribution of the HB

TABLE 2.1: Parameters and priors for different configurations.

	λ range [Å]	Age [Gyr]	SFH	τ [Gyr]	$\log(\frac{M_\star}{M_\odot})$	$[Z/H]$	A_V [mag]	σ [km/s]
Conf. 13.5	3700 - 6000	U(0,13.8)	DED	U(0,0.15)	U(1,6.3)	U(-2.3,0)	U(0,4)	U(0,15)
Conf. 15	3700 - 6000	U(0,15)	DED	U(0,0.15)	U(1,6.3)	U(-2.3,0)	U(0,4)	U(0,15)
1	3700 - 6000	U(0,15)	DED	U(0,1)	U(1,6.3)	U(-2.3,0)	U(0,4)	U(0,15)
2	3700 - 6000	U(0,15)	burst	-	U(1,6.3)	U(-2.3,0)	U(0,4)	U(0,15)
3	3350 - 9000	U(0,20)	DED	U(0,0.15)	U(1,6.3)	U(-2.3,0)	U(0,4)	U(0,15)
4	3700 - 6000	U(0,15)	DED	U(0,0.15)	U(1,6.3)	G(val, 0.01)	U(0,4)	U(0,15)
5	3700 - 9000	U(0,15)	DED	U(0,0.15)	U(1,6.3)	U(-2.3,0)	U(0,4)	U(0,15)
6	3700 - 6800	U(0,15)	DED	U(0,0.15)	U(1,6.3)	U(-2.3,0)	U(0,4)	U(0,15)
7	4828 - 5634	U(0,15)	DED	U(0,0.15)	U(1,6.3)	U(-2.3,0)	U(0,4)	U(0,15)
8	3700 - 6000	U(0,15)	DED	U(0,0.15)	-	U(-2.3,0)	U(0,4)	U(0,15)

on top of the SSP models (e.g. Jimenez et al., 2004; Koleva et al., 2008; Cabrera-Ziri & Conroy, 2022). However, incorporating this component into `BAGPIPES` is outside the scope of this work. Removing bad fits, the clean sample counts 66 GCs in both configurations.

In Figure 2.11 two examples of good fits are reported, both converging to ages older than 13 Gyr, one presenting a red HB (NGC6356, HBR=-1) while the other shows a blue HB (NGC6717, HBR=0.98). The pulls highlight how in the case of NGC6356 the stellar models, plus the dust components, are able to accurately reproduce the GC's spectrum, with residuals compatible with 1-σ fluctuations at all wavelengths. In the case of NGC6717, the quality of the fit is still good, but the pulls clearly show a residual at bluer wavelengths, especially concerning the Balmer absorption lines, pointing out the unmodelled hot stars component. This suggests that for GCs characterised by blue HBs may still produce a reliable age estimation, as long as the blue HB stars do not outshine the blue end of the spectrum.

The quality of both considered setups is highlighted by the median reduced chi-squares, $\tilde{\chi}^2 = 1.21$ in *Config. 13.5* and $\tilde{\chi}^2 = 1.26$ in *Config. 15*. This is quite noticeable since in this case we adopted the formal spectrum error provided by the analysis, with the correction described in Section 2.2.3. These values are further (as was expected) reduced if we take into account the noise parameter, which acts in correcting the error spectrum for potential underestimations, leading to $\tilde{\chi}^2 = 0.99$ in *Config. 13.5* and $\tilde{\chi}^2 = 0.98$ in *Config. 15*. To analyse the derived physical properties, we consider, for each parameter, the median and the 16^{th} and 84^{th} percentiles of the posterior distribution, respectively, as the best-fit value, lower and upper error.

Configuration 13.5 In *Config. 13.5* we observe that metallicities and GC masses are in good agreement with literature values, with mean deviations of $\langle \Delta[Z/H] \rangle = 0.09 \pm 0.21$ dex and $\langle \Delta \log(M_\star/M_\odot) \rangle = -0.09 \pm 0.24$ dex, respectively, consistent with the typical errors associated with these quantities (see Section 2.2.1). In terms of stellar age, instead, a clear bimodality is present. While 17% of the sample (11 GCs) turns out to have ages older than 10 Gyr and only ~0.16 Gyr younger than literature values on average, most of it (55 GCs) shows ages significantly younger than 10 Gyr, ~8.9 Gyr lower on average. We investigate this difference in the following.

In Figure 2.12a and 2.12b, we show the differences in stellar mass and metallicity as a function of this age gap, colour-coded by HBR index. This highlights two important aspects.

The first is, again, the trend with HBR, showing that when this index is positive (blue HB), the code misinterprets the blue shape of the spectrum and the deep Balmer lines for a young population 87% of

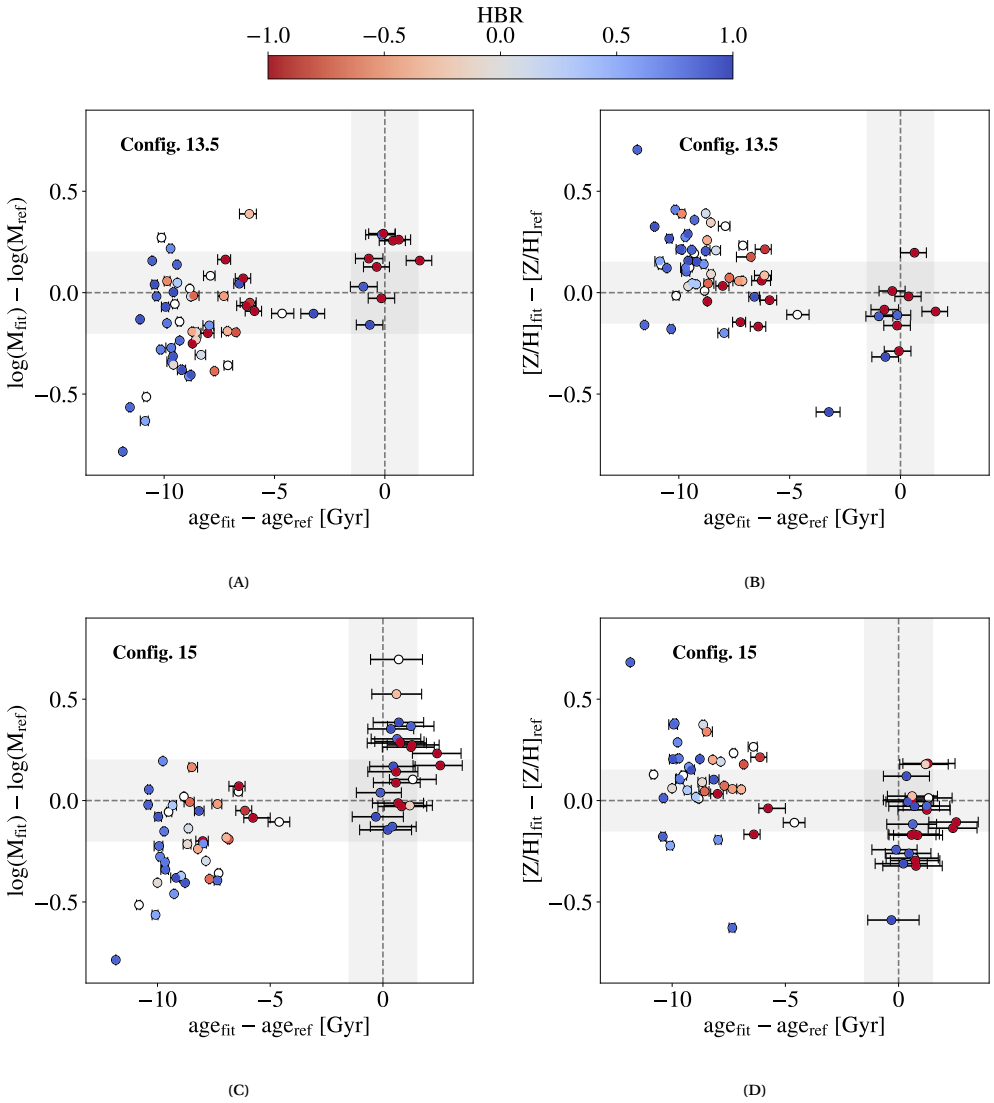

FIGURE 2.12: Differences in stellar mass ($\Delta \log(M_\star/M_\odot)$) and metallicity ($\Delta$[Z/H]) as a function of the difference in age as estimated in this work with respect to literature values. The dashed lines correspond to a null difference, and the shaded grey areas represent an average representative error on literature values, namely 0.2 dex in mass, 0.15 dex in metallicity, and 1.5 Gyr in age. The top two panels refer to *Config. 13.5* while the bottom ones to *Config. 15*. All the points are colour-coded by their HBR index.

the time (27/31), resulting in ages on average 8.4 Gyr younger than expected from the literature. This exact behaviour is also observed for most of the red HB population, but in a smaller fraction (73% of the cases, 19/26 GCs) and with a less significant age discrepancy of 5.1 Gyr on average. A similar result was already found both in Koleva et al. (2008) and Cabrera-Ziri & Conroy (2022), where the issue was mitigated by adding a fraction of hot stars on top of the SPS models, but, as was anticipated, including the HB component goes beyond the purpose of this work. In Section 2.2.4, though, a detailed comparison with the results in Cabrera-Ziri & Conroy (2022) can be found.

The second is the existence of a degeneracy among the parameters involved. A lower cluster mass or a higher metallicity can easily mislead the fit to ages much younger than the literature one. This is clear if we compute the median differences in metallicity and mass separately for the GCs resulting older and younger than 10 Gyr: for the former, we find average deviations of $\langle \Delta[Z/H] \rangle = -0.14 \pm 0.19$

dex and $\langle \Delta \log(M_\star/M_\odot) \rangle = 0.16 \pm 0.15$ dex, for the latter instead $\langle \Delta[Z/H] \rangle = 0.13 \pm 0.18$ dex and $\langle \Delta \log(M_\star/M_\odot) \rangle = -0.13 \pm 0.24$ dex.

Configuration 15 In *Config. 15* the good agreement of metallicity and GC mass estimates with literature values holds, with average differences of $\langle \Delta[Z/H] \rangle = -0.02 \pm 0.23$ and $\langle \Delta \log(M_\star/M_\odot) \rangle = 0.04 \pm 0.28$. Concerning the stellar ages, even though the only difference with respect to *Config. 13.5* is the removal of the cosmological prior, the results improve significantly. Here 36% (24 GCs) of the sample shows ages older than 10 Gyr, more than twice the old population of *Config. 13.5*. Among these 24 GCs, the ages result compatible with literature values 92% of the times (22 GCs), on average 0.67 Gyr older, and we find average discrepancies in $[Z/H]$ and mass of $\Delta[Z/H] = -0.11 \pm 0.18$ and $\Delta \log(M_\star/M_\odot) = 0.20 \pm 0.20$.

In Figure 2.12c and Figure 2.12d we show the analogous of 2.12a and Figure 2.12b for *Config. 15*. We can see that both the trend in HBR and the age-metallicity and age-mass degeneracies are present but with important differences. This time, removing the upper limit on the age parameter has reduced the fraction of blue HB GCs mistaken for young populations to 71% (22/31) and the one of the red HB GCs to 54% (14/26). This means that 13 GCs previously resulting younger than 10 Gyr are now recognised as old populations, representing a 20% increment. The degeneracies cited above play an important role in this because all of these 13 GCs are here characterised by a lower metallicity ($\Delta[Z/H] \sim -0.18$ dex) and a higher mass ($\Delta \log(M_\star/M_\odot) \sim 0.19$ dex) than the one found in *Config. 13.5*, yet mostly in agreement with literature values within errors. This suggests that for a fraction of GCs an old, more realistic solution does exist beyond the cosmological limit usually set when performing FSF and that it may also be preferred to the younger one if this area of the parameter space is made accessible. For this reason and in light of the subsequent cosmological analysis, we consider *Config. 15* our benchmark.

Systematic effects

As was anticipated in Section 2.2.3, we performed multiple tests with different settings to find the optimal fit configuration. These analyses have been used to assess the systematic error induced in the age determination with our approach. Specifically, we examined eight configurations, each differing from our benchmark in one or two key aspects, including variations in SFH type (burst or DED), age prior (15 Gyr or 20 Gyr) metallicity prior (uniform or Gaussian), wavelength range of the fit, and in fitting spectra in physical units or normalised in the window 4500-5000 Å. The latter was applied in just one configuration, the only case in which the mass parameter could not be determined due to the normalisation. All the characteristics of the different configurations are outlined in Tab. 2.1, numbered from one to eight.

In this analysis, we discarded all the spurious young solutions with a best-fit age below 10 Gyr for the same reasons discussed in Section 2.2.4, and all the bad fits in *Config. 15* and in each of the eight test configurations. In this way, we end up with a sample of 18 GCs having a good fit in at least five out of the nine runs. For each object, we computed the standard deviation of the age distribution in the nine runs. Finally, we estimated a global systematic contribution to the age uncertainty as the average of these standard deviations, weighted on the number of good fits for each GC, resulting in 0.71 Gyr[6].

In addition, we considered the possibility of a systematic effect induced by mass segregation. The large apparent sizes of Galactic GCs on the sky, combined with the relatively small field of view of the WiFeS spectrograph (38×25 arcsec, comparable to the median core radius of an MW GC, Harris, 2010), pose significant challenges for integrated light observations of Galactic GCs. Usher et al. (2017) used a

[6]We note here that taking the median provides a similar, yet a bit more optimistic result, estimating a 0.64 Gyr systematic contribution to the error budget.

single, central pointing for each GC in their study. However, the MW GCs in their sample span a wide range of heliocentric distances – from 2.2 kpc for NGC 6121 to 41.2 kpc for NGC 7006 – causing the fraction of GC light sampled to vary considerably. When the WiFeS field of view covers only a small portion of a GC's area, stochastic effects may prevent proper sampling of all stages of stellar evolution, particularly in lower-mass clusters. Additionally, mass segregation – whereby more massive stars migrate towards the cluster centre due to dynamical evolution – further complicates observations. This effect alters the slope of the mass function with radius (e.g. Beccari et al., 2015), potentially mimicking weak radial variations in the IMF. To assess these biases, we examined potential correlations between the age differences estimated in this work and those reported in the literature, as well as with cluster mass and the ratio of the core radius or half-light radius to the equivalent radius of the WiFeS field of view (17.4 arcsec). We found no evidence of statistically significant correlations among these quantities.

The role of metallicity

In Section 2.2.2 we observed that not only the presence of an extended blue HB, but also a low metallicity could produce some spectral features that can drag the fit to younger ages due to their degeneracy. Here we want to verify if this trend is present in our results. In Figure 2.13a, we plot the metallicity obtained from our fit against the values found in the literature, colour-coded by the difference between the age estimated from the fit and the literature one.
First, we can observe that GCs where the resulting age is in good agreement with literature values (green points) are present across almost the full metallicity range, down to $[Z/H]_{\rm lit} = -1.5$. While most of these also show a remarkable agreement in terms of metallicity, lying close to the one-to-one relation, a few green points fall below the −0.2 dex line, with a fitted metallicity lower than the literature value. This behaviour may stem from the conversion from literature $[Fe/H]$ to $[Z/H]$ through Eq. 2.7, in which we adopted a fixed value for the α-enhancement depending on the metallicity range. The discrepancy would decrease if the $[\alpha/Fe]$ for these GCs were lower, as a reduction of 0.15 dex would be sufficient to make this difference irrelevant in all cases. Alternatively, this may be the effect of degeneracies like the age-metallicity one, possibly converging to lower metallicities in favour of slightly older ages.
The part of the GC sample where fitted ages result much younger than literature values (red points), instead, are preferentially located at lower metallicities. To perform a quantitative comparison, we divided our sample into metallicity sub-samples, considering three intervals equally spaced in $[Z/H]_{\rm lit}$: a metal-rich $[-0.7, 0.0]$, a metal-intermediate $[-1.4, -0.7]$ and a metal-poor $[-2.1, -1.4]$.

The metal-poor sample counts 15 GCs, among which only the 20% (3/15) is recognised as older than 10 Gyr. This can be better understood by examining the top panel of Figure 2.14, where the median stacked spectrum of the metal-poor sample is compared to two synthetic spectra, one 13 Gyr old and the other 4 Gyr old, while all the other parameters (e.g. $[Z/H]$, mass, dust) are fixed to the median literature values characterising this sub-sample. The spectral shape does indeed resemble the one of a young population, with a stronger emission bluer than ∼ 4400Å with respect to the spectrum of an old population, and stronger Balmer lines. However, in Figure 2.13b, where discrepancies in the reproduction of CaII K and Hβ are shown as a function of literature metallicity, we can see that for most of the metal-poor GCs, the Hβ line is actually overestimated. This means that the young solution, even if preferred by the fit, does not precisely follow the observed features. In terms of metallicity and mass, the agreement with literature values is very good, with average deviations of $\langle \Delta[Z/H] \rangle = -0.02 \pm 0.35$ dex and $\langle \Delta \log(M_\star/M_\odot) \rangle = -0.2 \pm 0.2$ dex, respectively.

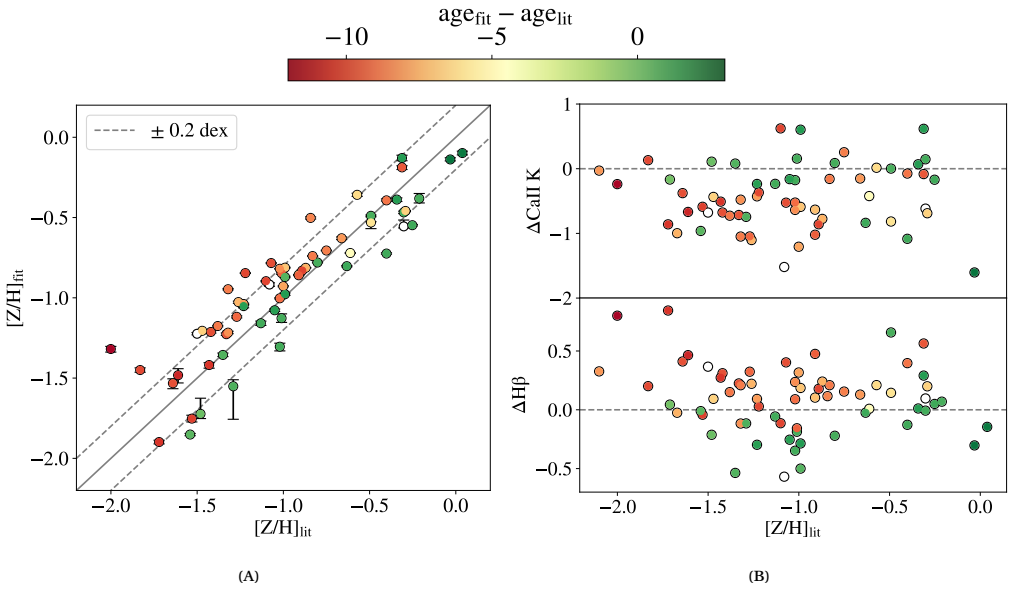

FIGURE 2.13: Metallicity and differences in CaII K and Hβ measurements as a function of literature metallicity. *Left*: $[Z/H]$ obtained in this work against literature $[Z/H]$, colour-coded by the corresponding difference in age. The continuous line represents the one-to-one relation, and the dashed lines the 0.2 dex scatter. *Right*: Differences in CaII K and Hβ as measured on the posterior spectra with respect to the observed ones, colour-coded by the difference in age.

The metal-intermediate is the largest sub-group, with 33 GCs, and shows a higher percentage of GCs older than 10 Gyr compared to the metal-poor sample, equal to 33% (11/33). Its median stacked spectrum has a better agreement with an old population in terms of the continuum but still fails to reproduce some observed lines of the Balmer series, as we can see in the central panel of Figure 2.14. This is mostly evident for the Hβ line, falling in the region 4500 − 5000Å where the spectra have been normalised, which is clearly better reproduced by a young population, as in the metal-poor case. This suggests that there is still non-negligible contamination by hot stars, deepening the Balmer series. We can observe this in more detail in Figure 2.13b where to obtain old solutions, the fit has to underestimate the Hβ feature. In contrast, for the young ones, it is either compatible with observations or overestimated. In this metal-intermediate group, we can also observe the importance of reproducing the CaII K line in recovering ages. In fact, while the old solutions all scatter around ΔCaIIK ~ 0, the young ones systematically underestimate this feature. Regarding the metallicity, this sub-group shows a good agreement with literature values, with a $\langle\Delta[Z/H]\rangle = 0.10 \pm 0.15$ dex, and a discrepancy in mass smaller than before $\langle\Delta \log(M_\star/M_\odot)\rangle = -0.04 \pm 0.30$ dex.

In the metal-rich sample instead, we are able to obtain ages older than 10 Gyr for 56% (10/18) of the sample. This fraction increases as we move to solar values, reaching 70% for $[Z/H]_{lit} \geq -0.4$. In the bottom panel of Figure 2.14 we can see that, among the three samples, the metal-rich is the most distant from a young population with a much redder continuum. In addition, the metal-rich is the only stacked spectrum in which the Hβ region is better reproduced by the old synthetic spectrum instead of the young one, even if a residual, going in the opposite direction, is still visible [7]. Looking at Figure

[7]We note that the stacked spectra for all three populations show clear residuals, albeit to varying degrees, particularly in metallic features such as the Mg triplet around 5171 Å. Besides the fact that they are not fit to observations, this likely reflects the limitation of BC16 models, which do not account for variations in abundance ratios in the stars used to construct the SSPs, and supports the evidence that current stellar population synthesis models used to interpret the integrated light of stellar systems may suffer from significant zero-point issues (see Section 2.2.2).

2.13b, the metal-rich sample is the only one for which both Hβ and CaII K are well reproduced. In terms of metallicity and mass here we find $\langle\Delta[Z/H]\rangle = -0.08 \pm 0.15$ dex and $\langle\Delta \log(M_\star/M_\odot)\rangle = 0.09 \pm 0.16$ dex with respect to literature values.

The fact that we can recover ages well in this metallicity range is a remarkable result also in the context of galaxy evolution studies, for which GCs have always been an important test bench, since it shows the reliability of the FSF method in recovering the main physical parameters of the stellar population in a metallicity interval that is typical of high redshift galaxies (see, e.g., Kriek et al., 2019; Lonoce et al., 2020; Carnall et al., 2022; Borghi et al., 2022a). Moreover, we show that spectral features like Hβ and CaII K prove to be very sensible to possible spurious age determinations and thus can be used as diagnostics to determine the quality of the age estimates.

Comparison with previous works

As anticipated at the beginning of this section, different works have already been published investigating the potential of analysing GCs' integrated spectra, either relying on different datasets or adopting different fitting codes. Here we focus on the work from Cabrera-Ziri & Conroy (2022) (CC22, hereafter), where they use the observations from Schiavon et al. (2005) for a common sub-sample of GCs, and then on the results from Gonçalves et al. (2020) (G20, hereafter), where they analyse the same data but adopt a non-parametric approach.

Comparison with Cabrera-Ziri & Conroy (2022) CC22 used a similar, but non-parametric, FSF approach with the code ALF (Conroy & van Dokkum, 2012) to estimate the ages and metallicities of 32 Galactic GCs from Schiavon et al. (2005), fitting normalised spectra in the range $\sim 3300 - 6500$Å. As in *Config. 13.5*, CC22 initially performed the analysis with a standard setting, using a cosmological prior of 14 Gyr. They obtained ages compatible with literature values within 1.5 Gyr for seven GCs, which constitutes 22% of their sample. To compare the results, we consider the 31 GCs included both in their sample and our good fits. For those, in *Config. 13.5* we obtain ages within 1.5 Gyr from literature values for 13% of the sample (4/31) while this fraction is more than doubled when we remove the cosmological prior, reaching 32% (10/31).

Compared to CC22, the performance in recovering old ages with *Config. 13.5* is comparable but slightly worse. This is likely due to the additional degrees of freedom in our setting, such as the inclusion of dust and mass parameters, along with the lower age prior. If adopting a multi-component model can help in reproducing all the spectral features in more detail, this approach is also more prone to possible degeneracies, as we underlined in different steps of our analysis. Nevertheless, this same choice allows us to obtain better results when removing the cosmological prior, with an increase in the fraction of old objects of 20% with respect to our *Config. 13.5* and 10% with respect to the standard setting in CC22.

In CC22, an additional fit was performed that included a component to account for the hotter fraction of HB stars. This approach allowed them to recover ages older than 10 Gyr for 27 out of 31 GCs, with 24 of these being compatible with literature values within 1.5 Gyr. As already discussed, modelling the HB component is outside the purpose of this work, but represents a promising possibility to be explored in future analyses.

Comparison with Goncalves et al. (2020) In G20 the authors focus on the impact that the wavelength range choice has on the results, adopting the FSF code `STARLIGHT` (Cid Fernandes et al., 2005).

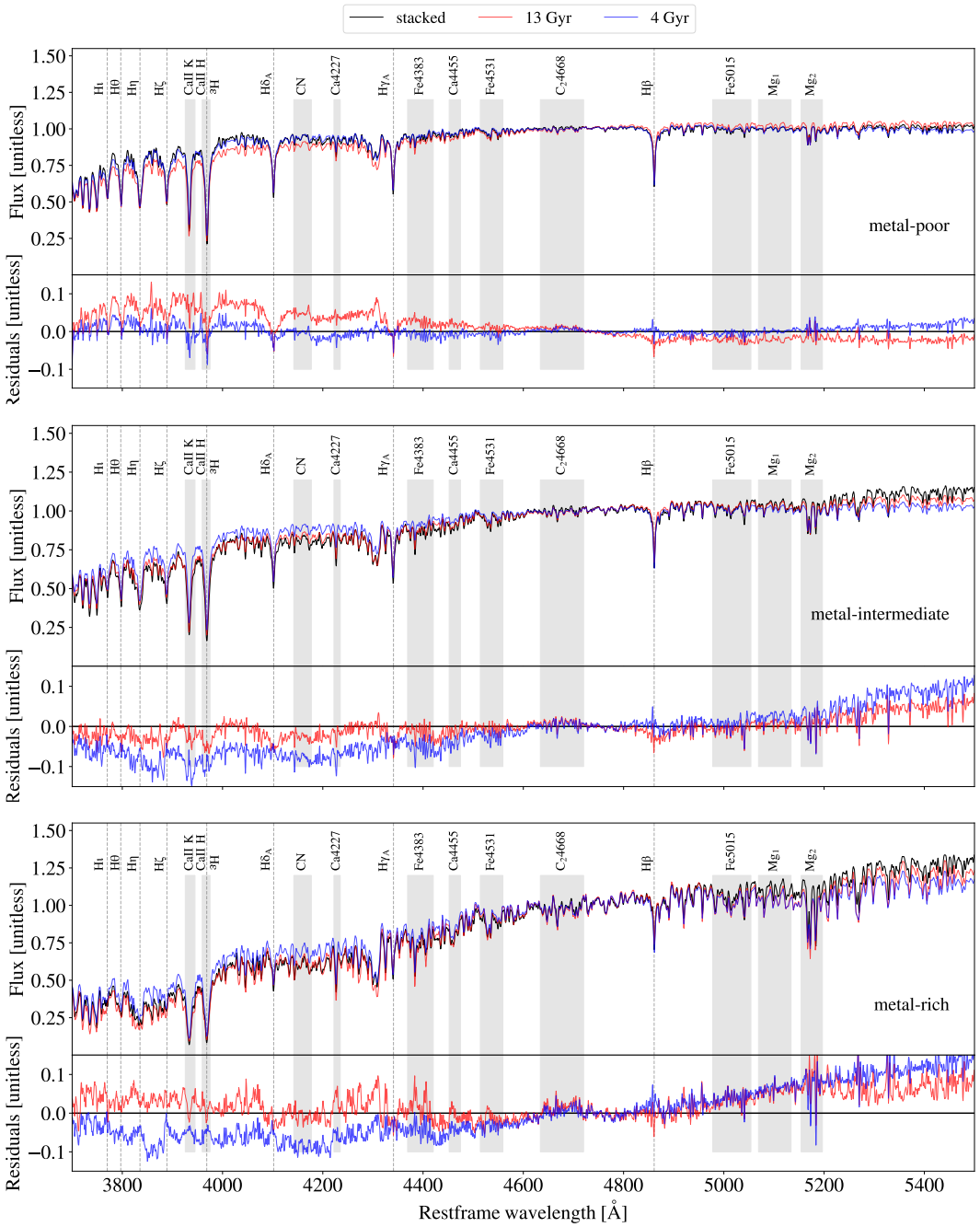

FIGURE 2.14: Stacked spectra of the metal-poor (top panel, $[-2.2, -1.4]$), metal-intermediate (central panel, $[-1.4, -0.6]$) and metal-rich (bottom panel, $[-0.6, 0.2]$) subsamples, in comparison with a 4 Gyr (in blue) and 13 Gyr old (in red) synthetic spectra. The values of mass, dust absorption and velocity dispersion of the synthetic spectra are set to the median literature values of each subgroup. All the spectra are normalised in the window 4500-5000 Å. At the bottom of each panel the residuals of the stacked spectra with respect to the synthetic ones are shown with corresponding colours. The Balmer series is indicated with dashed lines, other relevant spectral features are highlighted with grey boxes. It can be noticed how the different sub-groups show different continuum and spectral features properties, and how the models are able to reproduce more accurately the high-metallicity ones.

They fit normalised spectra using MILES SSP models (Vazdekis et al., 2015) with ages up to 14 Gyr, $[Fe/H]$ in the range from -2.27 to 0.26 and alpha enhancement either absent or equal to 0.4. Dust reddening is implemented in the code, modelled as in Cardelli et al. (1989). We compare our results to the ones published in Goncalves et al. (2023), obtained by fitting the interval 4828 - 5634 Å, a narrow range where the main features detectable are Hβ, Mgb triplet, Fe5015, Fe5270, and Fe5335.

We consider the 58 MW GCs for which we obtain a good fit among the 64 MW GCs published in G20; in this sample, they obtained ages compatible with literature values within 1.5 Gyr for nine GCs, representing 15% of the total. In this same sub-group, we have seven GCs compatible with literature ages in *Config. 13.5*, and 15 in *Config. 15*, corresponding to 12% and 26% of the sample, respectively. As in the comparison with CC22, also in the case of G20 our results when the cosmological prior is applied are comparable but slightly worse, and as commented above the reason probably resides in the higher number of parameters involved and the lower age prior. Again, when we remove the cosmological prior, we obtain a major improvement in the fraction of ages compatible with literature, both with respect to our *Config. 13.5* (+14%) and to G20 (+11%).

It is worth mentioning here that we also tested the impact on the results of fitting the wavelength range adopted in G20, first suggested in Walcher et al. (2009), and we considered it when computing the systematic uncertainty on ages in Section 2.2.4. Avoiding all the features bluer than 4828 Å, polluted by the hot HB component, this configuration performs much better for the blue HB, low-metallicity GCs in our sample. In particular, it allows us to recover ages older than 10 Gyr for 63% of metal-poor GCs and 73% of metal-intermediate ones. For the metal-rich sample, instead, it yields worse results compared to *Config. 15*, with 47% of GCs resulting older than 10 Gyr. Nevertheless, the latter sub-group is the one in which the stellar models should be most effective, thanks to the absence of an extended HB component and low alpha-enhancement in the systems, so *Config. 15* was still preferable in terms of the robustness of the results.

2.2.5 Application to cosmology

In this section, we analyse what impact our results for GCs' ages, interpreted as lower limits on the age of the Universe, t_U, can have in the determination of the Hubble constant H_0 (Jimenez et al., 2019; Valcin et al., 2020; Valcin et al., 2021; Vagnozzi et al., 2022; Cimatti & Moresco, 2023).

Method

As anticipated in Section 1.2, and widely described in Cimatti & Moresco (2023), H_0 is very sensitive to the value of t_U, and the two are linked by Eq. 1.36. The analytical expression of $E(z)$ depends on the cosmological model assumed, in particular, in a flat ΛCDM model it can be expressed as a function of redshift and matter density parameter Ω_m, as in Eq. 1.38, that we report here for convenience:

$$H_0 \propto \frac{1}{t} \int_0^{z_F} \frac{1}{1+z} [\Omega_m (1+z)^3 + (1-\Omega_m)]^{-1/2} dz. \tag{2.8}$$

When applying the method to the oldest objects, H_0 can be estimated via a Bayesian approach, in which the likelihood is built on the difference between the measured age and the one predicted by the cosmological model ($\mathrm{age_m}$), accounting for the age error (σ_{age}):

$$\mathcal{L}(\mathrm{age}|\mathbf{p}) = -0.5 \sum_i \frac{[\mathrm{age}_i - \mathrm{age}_m(\mathbf{p})]^2}{\sigma_{\mathrm{age},i}}, \tag{2.9}$$

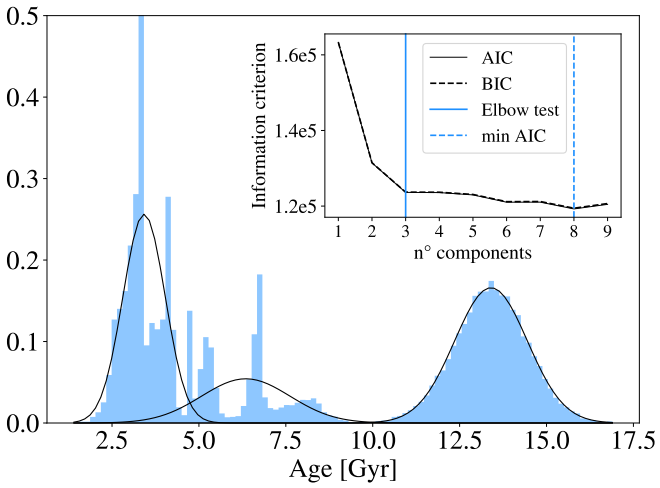

FIGURE 2.15: Combined distribution of all the 66 GCs ages. For each GC, a normal distribution peaked on the best-fit value and with σ equal to the associated error is drawn. In black, the three Gaussian components identified with a GMM are shown. In the inner panel, AIC and BIC curves are reported, highlighting the minimum AIC and the elbow test value.

where $\mathbf{p} = (H_0, z_F, \Omega_m)$ in a flat ΛCDM cosmology. The posterior distribution then, can be sampled with a Monte Carlo Markov Chain approach like the one implemented in the affine-invariant ensemble sampler `emcee` (Foreman-Mackey et al., 2013). In the choice of priors, a flat, uninformative one can be adopted on H_0 and z_F, while a Gaussian prior is preferable for Ω_m in order to break its intrinsic degeneracy with H_0.

As a final note on the method, it is interesting to highlight that nowadays, with facilities like JWST, this approach is no longer limited to the study of local objects but can be extended to higher redshifts thanks to the first detections of GCs around lensed galaxies. A great case-study is that of the Sparkler, a galaxy discovered in Webb's First Deep Field (Mowla et al., 2022), showing a population of compact objects associated with it, to which the whole Section 2.3 is dedicated. In the context of our cosmological analysis, extending the method at higher redshift would just require replacing the lower limit of the integral in Eq. 2.8 with the redshift of the lensed GC. In the case of the Sparkler at redshift 1.38, for example, the age of the Universe ranges from 4.3 Gyr to 4.7 Gyr adopting the reference values for H_0 given above, 73 km s^{-1} Mpc^{-1} and 67 km s^{-1} Mpc^{-1}, respectively.

Results

As was anticipated in Section 2.2.4, we adopted as benchmark *Config. 15*, where the cosmological prior is removed. To identify the tail of the oldest objects, we adopt a Gaussian Mixture Model (GMM) on the whole sample, combining normal distributions peaked on the best-fit ages, with 1-σ equal to relative uncertainties. We then let the fit decide the optimal number of subsamples in which to split our data. Both considering the Bayesian Information Criterion (BIC) or the Akaike Information Criterion (AIC), we find that the optimal number of components is three: a first peak identifying the youngest, blue-HB, spurious solutions; a second one for the intermediate ages; a third one comprising all the 24 oldest GCs, peaking at 13.4 ± 1.1 Gyr. The latter represents the oldest tail of the GCs' age distribution. The

cumulative distribution in age and the three components identified with the GMM are reported in Figure 2.15, where the inset also shows the AIC and BIC trends.

We applied the method described in Section 2.2.5 for each of these GCs separately, and then on their average, adopting the following priors: uniform on $H_0 \in [0, 150]$ km s^{-1} Mpc^{-1} and on $z_F \in [11,30]$, Gaussian on $\Omega_m = 0.30 \pm 0.02$. The lower limit on z_F is based on the highest redshift at which galaxies have spectroscopic confirmations (Curtis-Lake et al., 2023), the higher limit instead relies on the values found in theoretical models for the redshift of formation of the very first stars (Galli & Palla, 2013). As regards Ω_m, the value chosen here comes from the combination of different low-redshift results (Jimenez et al., 2019), thus independent of the CMB.

Our 24 old GCs span the age range 13.2-13.6 Gyr, with errors around 1 Gyr, thus the resulting H_0 range we find covers the interval 69.5-71.7 km s^{-1} Mpc^{-1}, with typical uncertainties of ~5 km s^{-1} Mpc^{-1}. To provide a single H_0 measurement, we also ran the MCMC using mean and standard deviation of the old peak found in the GMM fit: 13.4 ± 1.1 Gyr. This results in a final value for $H_0 = 70.4^{+6.7}_{-5.7}$ km s^{-1} Mpc^{-1} (stat).
To account for the systematic contribution to the error budget computed in Section 2.2.4 we summed it in quadrature to the standard deviation of the distribution and ran again the MCMC. The final result, comprising both statistics and systematic effects is:

$$H_0 = 70.5^{+7.7}_{-6.3} \text{ km s}^{-1} \text{ Mpc}^{-1} \quad \text{(stat + syst)}.$$

In Figure 2.16 the 24 GCs' ages and the corresponding H_0 estimates found after the MCMC run are represented as Gaussian distributions, in the respective domains and combined as ellipses in the H_0-age plane. The corresponding Gaussian curves and ellipses relative to the combined age and H_0 are shown as solid black lines. For comparison, the values from Riess et al. (2022) and Planck Collaboration et al. (2020) are represented, respectively, with dashed and dotted lines.

Of course, the results that we obtain here are not able to address the tension. Still, they represent a pilot exploration of the use of GCs' ages for cosmological purposes, especially in view of future missions that could potentially discover such objects at higher redshifts.

2.2.6 Conclusions

In this work, we analysed the integrated spectra of a sample of 77 MW GCs from the WAGGS project (Usher et al., 2017) and measured their physical properties via FSF with the code `BAGPIPES` (Carnall et al., 2018). In doing this, we aimed to study how well FSF can recover the GCs' ages and physical parameters, and assess, in particular, how the age estimates are affected by the presence or absence of a cosmological prior. This required a modification on the code, already tested and validated in Jiao et al. (2023) and Tomasetti et al. (2023), thanks to which a flat non-cosmological prior can be set at 15 Gyr. At the same time, this allowed us to obtain a cosmology-independent lower limit on the age of the Universe, that we used to derive a new constraint on H_0, performing a pilot study for future potential applications at higher redshift.

Our results are summarised as follows:

1. Measuring age-related spectral features detectable in the spectra, like D_n4000 and Hβ, allowed us to build index-age diagrams for these features in different metallicity bins, showing a distribution that well aligns with the trends from theoretical spectral models.

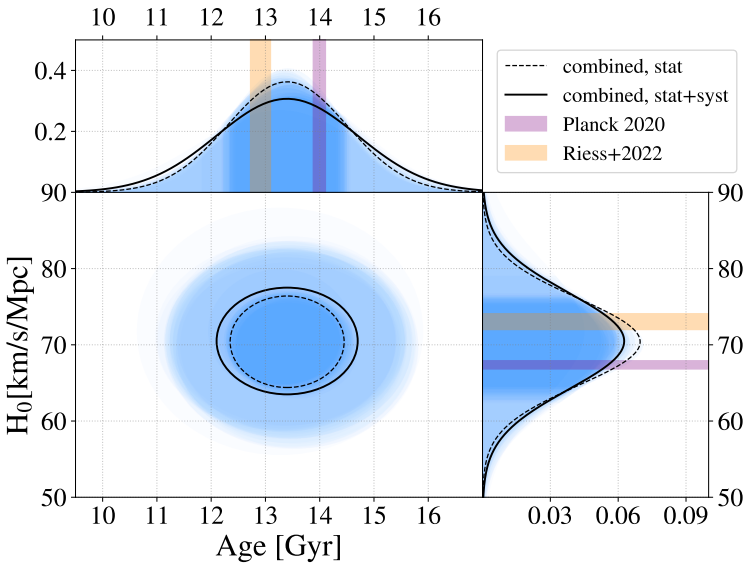

FIGURE 2.16: H_0 versus age for the sample of 24 old GCs. The ages and corresponding H_0 estimates are shown as Gaussians peaked on the best-fit values and 1-σ equal to the relative uncertainties. The 1-σ limits are also highlighted in a darker blue. The solid black curves correspond to the average GC's age and relative H_0 estimate. For comparison, the values from Riess et al. (2022) and Planck Collaboration et al. (2020) are represented, respectively, with dashed and dotted lines in the H_0 domain, and in the age-domain we report the corresponding ages of the Universe as computed in a flat ΛCDM with $\Omega_m = 0.3$ and $\Omega_\Lambda = 0.7$.

2. Combining age-related and metallicity-related spectral features we built two different types of index-index diagrams, Hβ-Mg$_b$ and Hγ_F-[MgFe]', able to disentangle age and metallicity contributions to the spectral features. Based on how the GCs populated these diagrams, we could have a first estimate of their properties, showing an overall good agreement with the corresponding literature values. Ages, however, appeared underestimated for a fraction of the sample characterised by low metallicity ([Fe/H]<-0.33) and blue HB (HBR>0), that, showing a more prominent Hβ, populated the area of ages younger than 8 Gyr. This anticipates how the presence of an unmodelled HB component in the spectra can bias the results towards younger solutions.

3. Performing FSF with `BAGPIPES` we could measure simultaneously the age, metallicity, and mass of the GCs. We tested multiple fit configurations, with different choices of priors, model components, SFHs, and wavelength ranges. Metallicity and mass proved to be very stable against the changes in fit configurations, while age was mostly sensible to the prior limit. In particular, we tested two configurations, one with a cosmological prior set at 13.5 Gyr and another at 15 Gyr (*Config. 15*), thus independent of cosmology. The percentage of GCs for which ages result compatible with the literature values within ±1.5 Gyr increases by 20% removing the cosmological prior, demonstrating the relevance of this limit in stellar population studies. In *Config. 15* the agreement with literature values is maximum for the sub-group of GCs with [Z/H]>-0.4, the least affected by the presence of blue HBs, reaching 70%. Metallicity and mass always result well compatible with reference values independently of HBR, [Z/H] or fit setting, with average discrepancies on the whole sample of $\langle\Delta[Z/H]\rangle = -0.02 \pm 0.24$ dex and $\langle\Delta \log(M_\star/M_\odot)\rangle = 0.04 \pm 0.28$, compatible with the typical uncertainties associated with these quantities.

4. Performing a GMM fit on the whole age distribution as derived in *Config.15*, we identified a tail of 24 old GCs with $\langle \text{age} \rangle = 13.4 \pm 1.1$ Gyr. In a cosmological framework, this value can be used as a lower limit on the age of the Universe to constrain the Hubble constant. In particular, by fitting the $H_0 - t_U$ relation in a flat ΛCDM cosmology and assuming $\Omega_m = 0.30 \pm 0.02$, from low-z measurements, we obtained $H_0 = 70.4^{+6.7}_{-5.7}$ km s^{-1} Mpc^{-1} (stat). Taking into account a systematic contribution to the age error of 0.71 Gyr, based on the age fluctuations in eight different fit configurations, we obtained:

$$H_0 = 70.5^{+7.7}_{-6.3} \text{ km s}^{-1} \text{ Mpc}^{-1} \quad \text{(stat + syst)}.$$

While we acknowledge that the method adopted in this work is not intended to compete with other age estimation techniques (e.g. isochrone fitting) for local and resolved objects, it does offer a viable alternative. In addition, high-quality spectra comparable to WAGGS are unlikely to be obtained in the near future for cosmologically relevant GCs, particularly in terms of signal-to-noise ratio, resolution, and wavelength coverage. Therefore, it is crucial to extend these types of studies to spectra that are realistically obtainable in the near or intermediate term. In the next section, for instance, we expand on the analysis presented here by applying it to the multiwavelength photometry of GCs observed in the Sparkler galaxy (Mowla et al., 2022), aiming to explore the potential for deriving reliable, cosmology-independent ages using photometric data alone.

Finally, it is worth noting that detailed modelling of HB populations – or other stellar populations such as blue stragglers – may not significantly affect studies of GCs at higher redshifts. A well-populated HB typically emerges only in clusters older than 6–8 Gyr. For the Sparkler GCs, with predicted ages of less than 4 Gyr at z=1.38 (Mowla et al., 2022; Claeyssens et al., 2023; Adamo et al., 2023), the influence of an extended HB is expected to be minimal.

This study serves as an initial pilot investigation into the feasibility of using only spectroscopic information to determine GC ages, an approach that may be particularly useful for investigating the properties of lensed GCs at higher redshifts, where isochrone fitting is not feasible. Future developments will include expanding the tests to incorporate models with an extended HB. Nonetheless, even without these enhancements, this work provides valuable diagnostics for identifying the most robust and reliable fits.

2.2.7 Multiple stellar populations: a future challenge

In this section, we have analysed a sample of local GCs with a FSF technique, modelling their integrated emission treating these sources as simple stellar populations. In the last decades, though, the conventional view of GCs as SSPs with stars of uniform age and chemistry has evolved dramatically. GCs are currently known to host multiple populations of stars exhibiting variations in helium and light elements such as C, N, O, Na, Mg, and Al, with a minority also showing iron spreads (see, e.g., Bastian & Lardo, 2018; Gratton et al., 2019; Milone & Marino, 2022). The prevailing view is that MPs arise from at least two distinct generations of stars. A first generation (P1), with primordial composition, forms during the initial collapse of the proto-cluster cloud. Subsequently, a second generation (P2) forms from gas that has been enriched by the products of massive P1 stars. The nature of the P1 polluters responsible for this enrichment remains debated, with proposed candidates including fast-rotating massive stars, asymptotic giant branch stars (AGBs), interacting binaries, and super-massive stars (Bekki et al.,

2017; Renzini et al., 2022). Current models face significant challenges in reproducing the full complexity of the observed chemical patterns and their correlations with cluster mass, and no consensus has been reached on the dominant formation mechanism (Kruijssen, 2015; Bastian & Lardo, 2015).

Despite the lack of a coherent picture, the age spread associated with MPs should be limited. Depending on the advocated polluter, it is expected to span from a few Myr in scenarios involving massive or super-massive stars (Denissenkov & Hartwick, 2014; Gieles et al., 2018) to a maximum of ~100–200 Myr in AGB-driven models (D'Ercole et al., 2008; Conroy & Spergel, 2011). In either case, from the perspective of integrated-light spectroscopy, such spreads remain well below the resolution of composite stellar population models and smaller than the typical age uncertainties derived from spectral fitting. Similarly, metallicity variations within genuine GCs are generally modest and do not significantly affect integrated properties, provided the element mixture is approximately solar-scaled.

Concerning this, the aspect that could affect the results most significantly is not MPs per se, but rather the chemical abundance variations they introduce. Beyond α-element spreads, MPs produce variations in CNO abundances, which are among the primary sources of opacity in stellar atmospheres, as well as in helium content, which directly affects stellar structure and evolution (see, e.g., Cabrera-Ziri et al., 2019). Current models cannot account for such variations, as they rely on solar-scaled chemical mixtures. Assessing the impact of this limitation on integrated-light analyses is not trivial, since the magnitude of the bias may depend on the wavelength coverage of the observations, as well as on the relative weight of iron-peak lines versus α- and light-element features in the fitting process. Recent studies (Park et al., 2025) suggest that fitting α-enhanced populations with solar-scaled models tends to produce systematically older ages, as the fitting algorithm compensates for the stronger α-element absorption features by shifting toward older, cooler templates with deeper spectral lines, rather than correctly attributing them to an enhanced chemical mixture. As much as this remains an open issue that warrants further investigation, the results presented in this work already suggest that the systematic bias potentially introduced by the use of solar-scaled SSP models has a limited impact on the inferred ages, as our estimates are on average only ~0.6 Gyr older than literature values (see discussion around Configuration 15 in Section 2.2.4). Nevertheless, quantifying this effect in a systematic way, incorporating α-enhanced model libraries in FSF, is a future line of research that we plan to pursue as soon as these templates become more widely available.

2.3 Lensed globular clusters as cosmic clocks

In the previous section, we have shown that reliable ages can be derived from GCs' integrated light, while demonstrating the feasibility of using these systems as cosmic clocks. This naturally motivates extending the approach to the distant Universe, applying the method to extragalactic GCs at higher redshift.

GCs are intrinsically faint, with absolute V-band magnitudes of $M_V = -7.5$ (Baumgardt et al., 2020). They are hardly visible at any redshift $z > 0.1$. At $z = 1$ they have apparent magnitudes fainter than $V = 32$, clearly beyond the reach of any currently planned telescope. Fortunately, one can exploit gravitational lensing as a natural telescope that magnifies the apparent brightness of high-redshift GCs. As is the case for high redshift galaxies (Frontier Fields lensing clusters; Lotz et al., 2017), strong gravitational lensing magnifies the light of GCs, bringing them above the detection limits of current telescopes, particularly JWST.

Unlike high-redshift galaxies, GCs have extremely small angular sizes – a typical GC with $R_{\rm eff} \sim 50$ pc subtends only a few milliarcsec at $z = 1$–1.5 – and exhibit very uniform stellar populations across their profiles. This allows for large lensing magnifications without introducing chromatic distortions in their SEDs, enabling clean age measurements.

Observing evolved GCs at $z \gg 0.1$ has the added benefit that younger stellar populations provide stronger age sensitivity (see Figure 6 in Valcin et al., 2020). Thus, JWST observations of lensed GCs at $z \sim 1.5$ – about one third of the present cosmic age in ΛCDM – offer a promising new avenue.

In this work, we exploit this opportunity by using, for the first time, highly magnified GCs in a galaxy at $z > 1$ as cosmic clocks. Our target is the Sparkler galaxy, lensed by the $z = 0.39$ cluster SMACS J0723.3-7327 (Pontoppidan et al., 2022). With a magnification of 10–100, the source is a low-mass system at $z = 1.38$ (Caminha et al., 2022; Mahler et al., 2023), with an intrinsic stellar mass of $(0.5–1) \times 10^9$, $M_\odot$ (Mowla et al., 2022; Claeyssens et al., 2023; Adamo et al., 2023). The galaxy is surrounded by compact sources, most of which remain unresolved even with JWST. Five of these 'sparkles' are strong GC candidates (Mowla et al., 2022), identified through the lack of [OIII] λ5007 emission – seen in the host's star-forming regions but absent at their positions – and their urJ colours, consistent with quiescent stellar populations. In the following, we treat these objects as bona fide GCs.

Accurate and precise photometry of these objects is crucial to derive reliable ages from SED fitting. However, obtaining reliable photometry of faint point sources superposed on a complex light distribution that changes morphology between bands and in presence of a very complex point-spread function (PSF) is a challenging task. After the previous analyses of the 'sparkles' were published (Mowla et al., 2022; Claeyssens et al., 2023; Adamo et al., 2023), STARRED (Millon et al., 2024; Michalewicz et al., 2023), a sophisticated photometry pipeline, specially developed to handle this challenge, became available. Here, we apply this new methodology to the Sparkler and illustrate how these objects can be used as cosmic clocks.

2.3.1 Data and Methodology

The data used in this work are the reduced JWST NIRCam images of SMACS J0723.3-7327 in the F090W, F150W, F200W, F277W, F356W and F444W bands provided by Mowla et al. (2022) (M22 hereafter). These images have been reduced with a combination of a modified *JWST* pipeline and the `Grizly` software (Brammer & Matharu, 2021) and have a pixel scale of 0.04" per pixel. All the details about image processing are provided in Noirot et al. (2023).

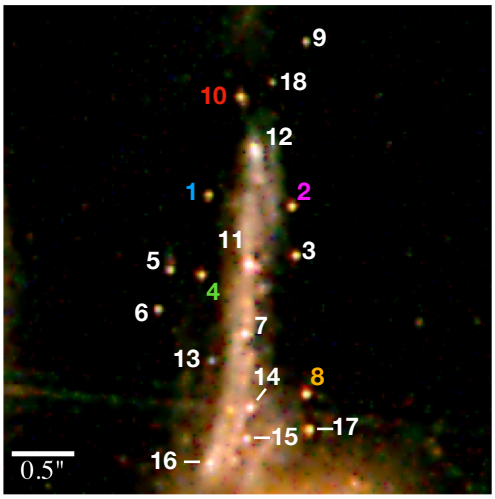

FIGURE 2.17: Colour composite region of 4″ on-a-side around the Sparkler. The figure is adapted from Millon et al. (2024) and indicates the labeling of the different objects. The colour code corresponds to the one in Figure 2.19. The PSF in this STARRED-deconvolved image is a circular Gaussian with a FWHM of 0.04″.

Previous studies on the Sparkler system have relied on different photometric methods to derive the properties of its compact sources. M22 used fixed-aperture photometry, while Claeyssens et al. (2023) employed PSF-fitting techniques following the approach of Messa et al. (2019, 2022)). Adamo et al. (2023) further reanalysed both photometric datasets using a different SED-fitting code. In this work, we present a completely new photometric analysis of the Sparkler, based on a deconvolution pipeline specifically developed to disentangle point-like sources from the surrounding extended emission.

STARRED photometry

STARRED (Millon et al., 2024; Michalewicz et al., 2023) performs deconvolution photometry, making it uniquely well suited to isolate the emission from the sparkles from the lensed arc of the host galaxy. In particular, the STARRED algorithm avoids producing Gibbs oscillations around point sources (Magain et al., 1998) and allows the shape of the PSF in the deconvolved image, a.k.a. the target PSF, to be chosen.

Because Gaussians do not contain high spatial frequencies, the target PSF is chosen to be a (circular) Gaussian, as opposed to a Dirac function as done in all other algorithms. The deconvolved images are also decomposed into two channels, one containing all analytical Gaussian point sources, and one containing a pixelated image of anything extended. Wavelet regularisation is applied to the latter to enforce the sparsity of the final deconvolved data.

The output is a list of positions and intensities of all point sources along with error bars, and an image of the extended light in the data, with no need to introduce any analytical representation. The same method can be used to obtain very accurate PSFs, even as complex as the JWST ones, including all Airy rings, spikes, and diffraction artifacts. A recent example of an application of this algorithm is light curves of very blended lensed quasars images (see Figure 2 of Dux et al., 2025).

The photometry and the PSF used in the present work are the same as in (Millon et al., 2024), which uses the Sparkler as a test case for the method. STARRED was applied to the JWST data for all six bands available for the Sparkler (see Figure 2.17). Note that the spatial resolution achieved on the Sparkler with STARRED is 0.04″ (Figure 2.17). This is at least 10 times larger than the physical size of GCs at

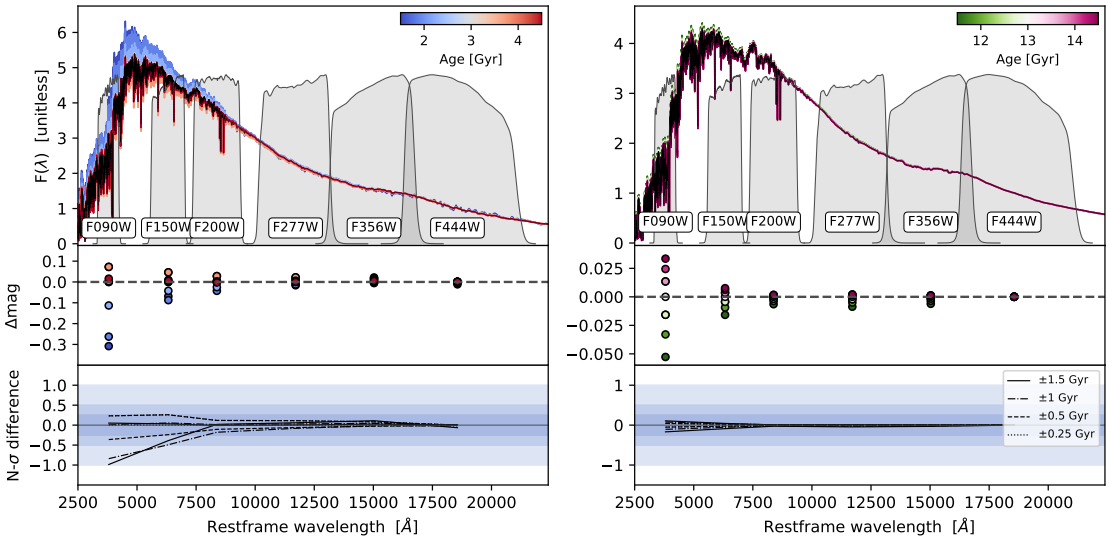

FIGURE 2.18: Sensitivity of GC's SED to absolute age, estimated for the six photometric bands considered in this study. The SEDs are shown in the top panels, for a delayed SFH with τ = 0.1 Gyr and Kroupa IMF (Kroupa, 2001) (see Section 2.3.1 for more details), along with the filter transmission functions used for studying the Sparkler. The left panels show the typical SED of a young population (age ~1.5-4.5 Gyr), while the right panels present an older population (age ~11.5-14.5 Gyr). All SEDs are normalised to the flux in the redder photometric band (the one with the smaller error). The middle panels show the difference in magnitude with respect to a reference age, considering 3 Gyr and 13 Gyr, respectively for the left and right panels. The bottom panels report the significance of the estimated differences normalised by the typical errors in the various bands for the Sparkler's photometry, where the shaded regions show the 0.25, 0.5, and 1−σ regions.

z = 1.38, leaving them undistinguishable from point sources. Indeed, the extended channel of the deconvolved images does not show any trace of residual extended light in any band.

As STARRED also offers the possibility to compute non-analytical and sub-sampled PSFs as well as a wavelet-regularised treatment of the extended arc, we consider only the STARRED photometry in the following (as listed in Table 3 of Millon et al., 2024). In particular, we analyse all 18 compact objects detected by Millon et al. (2024), including newly identified point sources (IDs 13–18) that are not present in the M22 catalogue (see Figure 2.17). The candidate GCs, already identified in M22 owing to the absence of [OIII] λ5007 emission and their urJ colours, are here outlined with Source IDs 1, 2, 4, 8, and 10. Notably, Source IDs 5, 6, 7, 11, and 12 appear extended, with flux residuals observed in the extended channel near these point sources (see Millon et al., 2024, for further discussion). While it is not clear whether these spatial extensions are physically associated with the objects or if they are unrelated, STARRED decontaminates by construction the flux of the point-like objects from the flux of anything present in the extended channel of the deconvolved image.

Finally, let us note that the magnification by the lensing galaxy cluster is about μ = 12 (Claeyssens et al., 2023, C23 hereafter) all over the field of view of Figure 2.17, illustrating that the lensing caustic is shallow and that chromatic effects due to lensing are negligible, even if intrinsic colour gradients would be present in the lensed sources.

Determining ages and metallicities

We measure the age, metallicity, and dust reddening of all the sources detected by Millon et al. (2024) using the code `BAGPIPES` (Carnall et al., 2018), already introduced in the previous sections.

To date, SED fitting on the sparkles has been performed either via a non-parametric approach – as in M22 with `DenseBasis` (Iyer & Gawiser, 2017) – or adopting a SFH with fixed duration – as in C23 (instantaneous, 10 Myr or 100 Myr long) using SSP models (Yggdrasil, Zackrisson et al., 2011) or in Adamo et al. (2023) (single burst) using `MCMAME` (Usher et al., 2019b). In all cases, ages could range up to 4.5–5 Gyr at maximum, as this is approximately the expected age of the Universe at $z = 1.38$. Here we opt for a parametric approach, thus choosing a functional form for the SFH, but allowing the fit to decide on the optimal SFH length, together with all other physical parameters of the population. The other key difference of this study compared to others in the literature is the removal of the cosmological prior on the age of the stellar population, which allows us to discuss our results within a cosmological context.

In this work, we assumed a SFH following a delayed exponentially declining law, $\propto (t-T_0)\exp^{-(t-T_0)/\tau}$. In this model, T_0 represents the age of the Universe at the onset of star formation, while τ sets the width of the SFH. We adopt a uniform prior for τ, ranging from 0 to 1 Gyr. As done for the local GCs in Section 2.2, a key modification to `BAGPIPES` is applied to allow T_0, and consequently the age of the stellar population, to span the full range of 0-15 Gyr independently of redshift, thus removing the effects of cosmological assumptions in the age priors.
The third component is dust absorption, modelled with a Calzetti et al. (2000) law to account for the potential presence of dust in the system. A uniform prior is adopted on the parameter A_V in the range 0 – 4 mag.

In total, we vary six parameters: 1) the age of the oldest stellar population, 2) the SFH width (τ), 3) overall metallicity ([Z/H]), 4) dust attenuation (A_V), 5) velocity dispersion (σ_v) and 6) stellar mass. Stellar mass and velocity dispersion are effectively nuisance parameters that have no effect on the other parameters and therefore are not reported. Stellar mass, in particular, acts as a normalisation factor for the SED, while it does not impact the SED shape, mostly affected by age, metallicity, and dust attenuation. Before fitting, we correct the flux in each filter to account for the Milky Way's foreground extinction, listed in Table 1 of C23.

It is worth observing here that in the age range typical of objects at z~1.4, population synthesis models can effectively distinguish between younger and intermediate-age populations, which feature intermediate-mass stars with unique photospheric properties. Notably, it is not just the main-sequence turn-off but also the entire sub-giant branch that is sensitive to age. On the other hand, age determination becomes increasingly challenging for older populations reaching 12 Gyr or more. This is illustrated in Figure 2.18 where the sensitivity of a GC spectrum to a change in age is shown comparing two different populations, a younger (~3 Gyr) and an older one (~13 Gyr). All the spectra are normalised to the Sparkler band with the smaller photometric error (F444W). It is evident how the younger populations can constrain a difference in ages of ±0.5-1.5 Gyr with a considerably higher significance than older populations.

2.3.2 Results

Figure 2.19 summarises the main results. For all 18 sources, we show the posterior distribution of the ages on the left panel, and on the right panels the central value and the 68.4% confidence interval for the age and metallicity. GC candidates are highlighted in bright colours. Remarkably, we find that

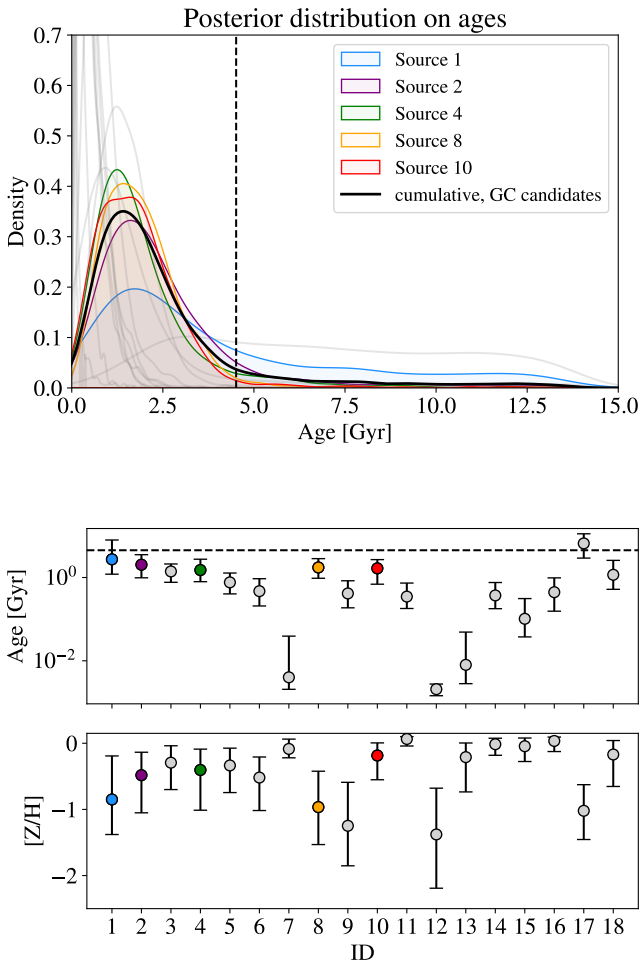

FIGURE 2.19: Top panel: Posterior for the ages of the five GCs in the Sparkler (with the posterior distributions for the other sources shown as thick grey lines). The best fit and 68% credible regions for the ages and metallicities are reported in the bottom panels. For reference, in both panels, the dashed lines indicate the age of the Universe in a vanilla ΛCDM cosmology.

the choice of the upper limit on the prior age does not affect in any significant way the 1– and 2–σ confidence intervals: despite adopting a very wide prior for the ages (uniform between 0 and 15 Gyr) all the recovered ages are compatible with ΛCDM model's predictions.

In Figure 2.20 we show 2D contours for different parameter pairs. Note that the age is always very well constrained and that in general the posterior distributions are not prior dominated. The insets show the derived spectrum from `BAGPIPES` using the six photometric bands used in this study (blue points for the data and orange points for the model).

All the best-fit spectra reproduce very well the observed photometry, except for the filter F150W, where the modelled flux is systematically underestimated. Thus, we tried redoing the analysis masking that photometric point, finding that ages are very stable, just ∼0.2 Gyr younger on average, and metallicities ∼0.2 higher.

The average age of the GC candidates is 1.9 ± 0.4 Gyr, where the error is the standard deviation. We stress that this is the first time that ages for the Sparkler's GC candidates are derived without imposing a

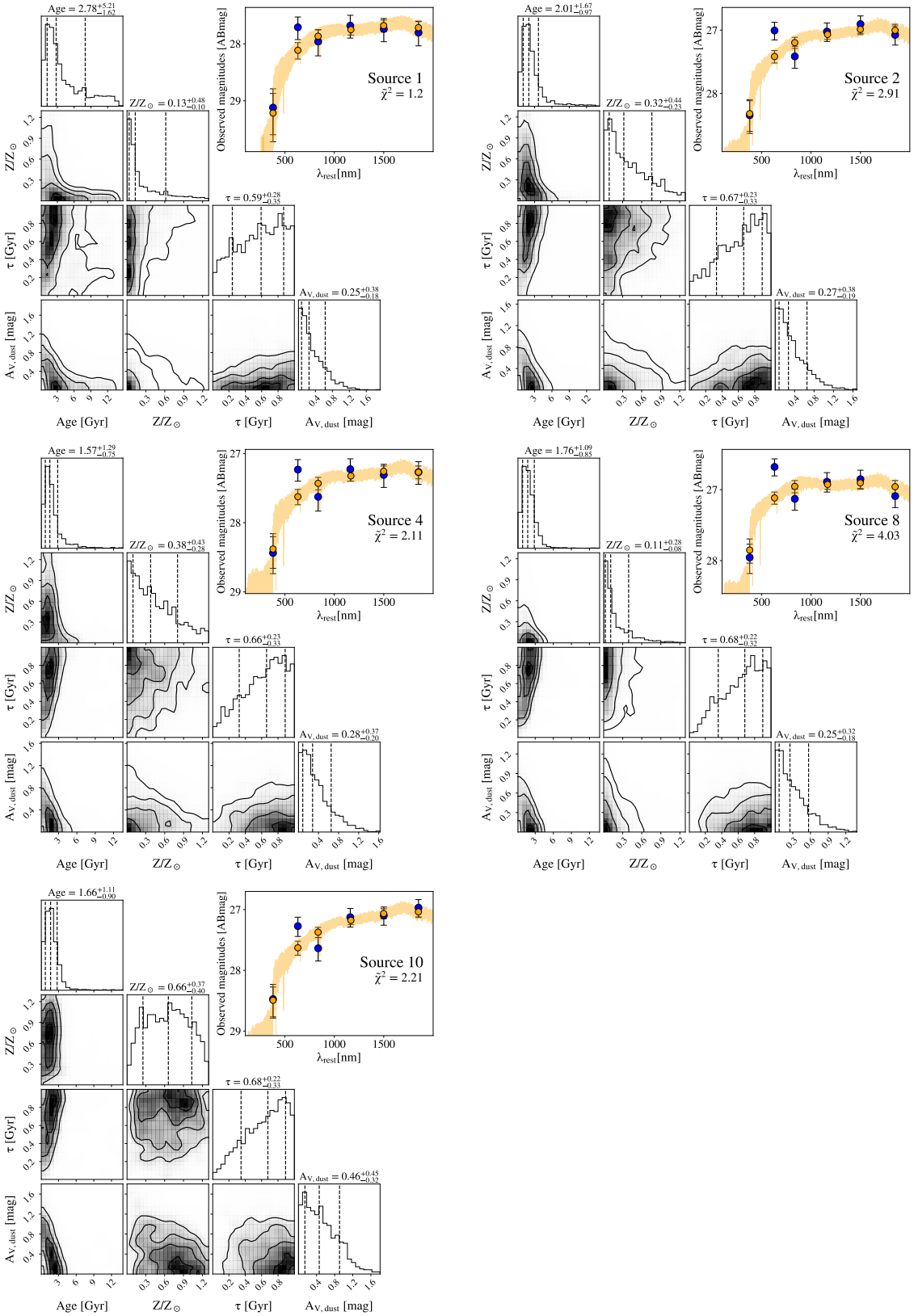

FIGURE 2.20: Joint posteriors for the four parameters studied for the Sparkler. The blue points indicate the data, while the orange points represent the best fit and the corresponding spectrum from `BAGPIPES`.

TABLE 2.2: Results of the SED fitting for the five candidate GCs. The adopted uniform priors are indicated as U(x,y) with x,y the lower and upper limits. The median value and 68.4% confidence interval for age, metallicity, dust reddening, and τ parameter are reported for each source.

ID	Age [Gyr]	$[Z/H]$	$A_{V,dust}$ [mag]	τ [Gyr]
PRIOR	U(0,15)	U(-4,0.1)	U(0,4)	U(0,1)
1	$2.73^{+5.22}_{-1.53}$	$-0.85^{+0.66}_{-0.53}$	$0.22^{+0.40}_{-0.16}$	$0.61^{+0.24}_{-0.37}$
2	$2.03^{+1.50}_{-1.04}$	$-0.48^{+0.35}_{-0.57}$	$0.27^{+0.38}_{-0.18}$	$0.66^{+0.22}_{-0.34}$
4	$1.51^{+1.24}_{-0.71}$	$-0.40^{+0.31}_{-0.61}$	$0.30^{+0.34}_{-0.21}$	$0.64^{+0.24}_{-0.32}$
8	$1.74^{+1.09}_{-0.78}$	$-0.96^{+0.54}_{-0.57}$	$0.26^{+0.31}_{-0.19}$	$0.68^{+0.21}_{-0.32}$
10	$1.66^{+1.03}_{-0.97}$	$-0.18^{+0.19}_{-0.36}$	$0.46^{+0.48}_{-0.34}$	$0.64^{+0.25}_{-0.24}$

cosmological prior, thus allowing for their use in a cosmological context. For reference, the flat ΛCDM Planck18-model inferred age of the Universe at redshift z = 1.378 is ~4.5 Gyr.

For comparison, M22, adopting a non-parametric SED-fitting analysis on fixed-aperture photometry, finds ages for these candidate GCs of approximately 3.9–4.1 Gyr, ~2 Gyr older than the results found here, and converging at the edge of their adopted cosmological prior. C23, instead, after deriving the SEDs with a Gaussian fitting approach and performing SED-fitting analysis based on SSP models, indicates that while two of the five GC candidates have ages of 4 Gyr, aligning with M22's results, the other three show ages around 1 Gyr, compatible with our results. Adamo et al. (2023) reanalysed the photometry for the GC candidates independently published by M22 and C23, using the `MCMAME` code (Usher et al., 2024) to refine the physical properties of the star clusters. They measure ages and metallicities that are qualitatively consistent with those found by C23, but since the ages did not converge, they conclude that these GCs are definitively older than 1 Gyr and could be as old as the Universe.
When comparing our results with those from previous studies, it is important to recognise that the reported age estimates – if constrained by a cosmological prior – could be significantly older if that prior were removed.

In terms of metallicity, the GC candidates show a mean $[Z/H] = -0.6 \pm 0.3$. Our results are consistent with those measured in M22 within the errors, although we find them generally lower by ~ -0.13 dex. C23, instead, finds the lowest χ^2 with the SSP set at $[Z/H] = -1.7$, ~1.1 dex more metal-poor than our results. In their reanalysis of M22 and C23 photometries, Adamo et al. (2023) find on average $[Z/H] \sim -1.7$ and $[Z/H] \sim -1.5$ respectively, both aligning with C23 estimates. The only exception is source 10 when analysed with C23 photometry, with $[Z/H] \sim -0.2$, which is compatible with our findings.

Although beyond the scope of the present paper, the measured ages and metallicities provided here enable the derivation of an age-metallicity relation for the stellar clusters in the Sparkler, making them of broad interest for studies on galaxy formation and chemical enrichment (Forbes & Romanowsky, 2023). In Figure 2.21, the distribution in the age – metallicity plane for the GC candidates obtained in this work is shown in comparison with the results presented in M22 and C23.

The derived dust reddening is fairly low for the GC candidates, $A_V = 0.3 \pm 0.1$ mag on average. Non-isolated sources, instead, often show reddening values above 0.5 mag (e.g., sources 7, 11, 12, 16,

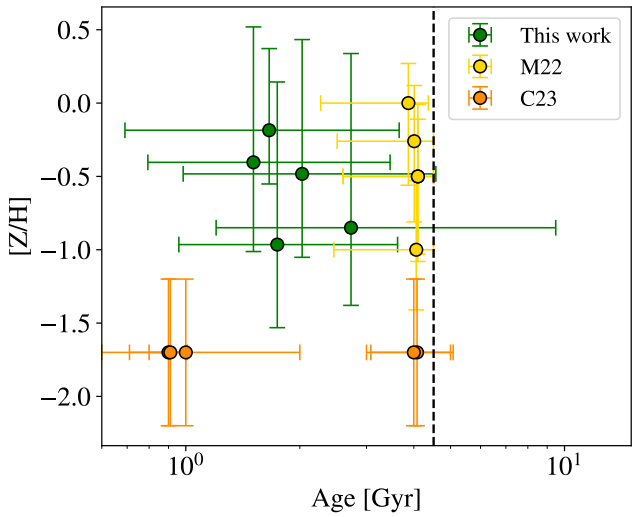

FIGURE 2.21: Overall metallicity versus age for the five GC candidates. The results from this work are shown in green, those from M22 in yellow, and those from C23 in orange. With a dashed line is reported the age of the Universe in vanilla ΛCDM.

and 17). To assess how the inclusion of dust reddening impacts the age and metallicity of the GC candidates, we also performed the analysis excluding it from the modelling. On average, we find an increment of ∼1.1 Gyr in age and ∼0.13 dex in metallicity.

The measured ages, metallicities, dust reddening and SFH width (τ) for the candidate GCs are reported in Table 2.2.

2.3.3 Conclusions and future prospects

Cosmic clocks provide a strictly cosmology-independent constraint on the age of the Universe, and on its expansion history. While this approach was so far limited exclusively to the local Universe, we have explored the possibility of obtaining absolute ages for strongly lensed and magnified GCs at redshift beyond zero in the lensed Sparkler system, using their integrated six-band photometry from space. The wavelet-based deconvolution-photometry algorithm adopted (STARRED) is uniquely suited to isolate the emission from point-like sources from the complex morphology of the lensed arc of the host galaxy.

For all lensed Sparkler objects, using a fully Bayesian pipeline, we estimated key parameters, such as age, metallicity, and dust attenuation. Very broad priors (especially on the age) were adopted so as not to introduce cosmological biases. The simultaneous fit of the physical parameters of the GCs and the broad priors adopted, combined with high-quality deconvolution photometry, are key novel aspects of this work.

GC candidates are point-like and older compared to the other sources. Our main result is that the mean age of the five GC candidates is 1.9 ± 0.4 Gyr, fully consistent with the ΛCDM Planck18-model prediction for the age of the Universe at redshift $z = 1.38$, even 2.6 Gyr younger. This is also interesting from the point of view of GC formation, if we consider that the ages of local GCs are typically comparable to the age of the Universe itself. The difference observed in the Sparkler's candidate GCs may be explained by their higher metallicity, as they lie at the metal-rich end of the distribution ($[Z/H] > -1$). In the local Universe, GCs in this metallicity range generally exhibit younger ages, typically between

10.5 and 11.5 Gyr (see, e.g., VandenBerg et al., 2013; Massari et al., 2019). Adopting the same cosmological model used throughout this work, this corresponds to a delay of approximately 2.5–3.5 Gyr relative to the age of the Universe at $z = 0$ – fully consistent with the age difference we find at $z = 1.38$. The reason for the prevalence of metal-rich GCs in our sample remains not entirely clear. While it is true that metal-rich GCs are generally more luminous in the infrared, it is unlikely that this is a pure selection effect, as metal-poor GCs should still be detectable at these magnitudes. Alternatively, this enrichment could be attributed to a period of very rapid star formation that quickly enhanced the metal content of the gas. However, with the current data, we cannot definitively confirm this scenario.

Our main result, and the fact that the ages of $z \sim 1.4$ GCs could be measured convincingly, opens up the possibility of using GCs at high-z as cosmic clocks to constrain the cosmological model, should more Sparkler-like magnified GCs be observed at different redshifts. Interestingly, the uncertainty in the age determination for these GCs today is comparable to that of the first passively evolving galaxies for which age was obtained at a similar redshift $z = 1.5$ in the mid-90s (Dunlop et al., 1996). New JWST/NIRSpec (IFU) spectroscopic observations of the Sparkler have been acquired (Cycle 2 GO#2969; PI Mowla). These spectra, to which we do not have access at the time of the present study, will represent a strong blind test and validation of our methodology which is based solely on photometry. As photometry is feasible with JWST over large fields of view, these five GC candidates are the tip of the iceberg of a much bigger population of GCs available for cosmic clock studies. JWST multi-band imaging of galaxy clusters shows a plethora not only of lensed GCs but also of GCs in the member galaxies of the clusters themselves, potentially providing GC samples at redshifts typical for galaxy clusters ($0.1 < z < 0.8$) and for lensed sources well beyond $z = 1$. Finally, Euclid images such as the Perseus cluster taken as part of the Early Release Observations data also display numerous (non-lensed) GCs around the very low redshift cluster galaxies (Cuillandre et al., 2025).

A systematic multi-band photometric campaign of GCs in and behind galaxy clusters based on Euclid and JWST can enable the measurement of ages of a sizeable population of GCs spanning a broad range of redshifts, which can then be used as cosmic clocks.

Cosmology with Cosmic Chronometers

In the previous chapter, we have focused on the use of time as an *absolute* tracer of cosmic evolution, by exploiting the ages of the oldest astrophysical objects. We now aim to extend this perspective to higher redshifts, while adopting a complementary strategy: instead of relying on absolute age determinations, we focus on *differential* ageing, which allows one to directly probe the expansion rate of the Universe through the evolution of galaxy populations across cosmic epochs.

Cosmic chronometers have emerged as novel, highly promising probes for obtaining direct measurements of the Hubble parameter, $H(z)$, up to redshifts of $z \sim 2$. This method, first proposed by Jimenez & Loeb (2002), relies on using massive, passively evolving galaxies as tracers of the Universe's ageing, under the minimal assumption of an FLRW metric. While galaxy redshifts can be measured with high precision, dating their stellar ages remains a challenge due to the complex reconstruction of their star formation histories and the degeneracies among key stellar population parameters, such as stellar age, formation timescale, and chemical composition.

In this chapter, we address these challenges by pushing the cosmic chronometer method forward from different perspectives. We define and validate an optimal strategy for selecting a pure sample of CCs, we explore and extend a new method to measure their ages in a cosmology-independent manner, we derive new measurements of the expansion rate of the Universe at low and high redshifts, and assess and evaluate potential systematics involved in the method. While Section 1.2 presents a brief overview of the CC method, this chapter details the original contributions of this Thesis. In particular, we present a first application of the CC method up to $z \sim 1.5$ deriving ages with full spectrum fitting (Section 3.1 and also extend it by employing it to the galaxy cluster environment, opening the way to self-consistent multi-probe combination (Section 3.2).

The main reference articles for the analyses presented in this chapter are:

- **Elena Tomasetti**, Michele Moresco, Nicola Borghi, Kang Jiao, Andrea Cimatti, Lucia Pozzetti, Adam C. Carnall, Ross J. McLure, and Laura Pentericci. *A new measurement of the expansion history of the Universe at $z = 1.26$ with cosmic chronometers in VANDELS*, Astronomy & Astrophysics (2023) [arXiv:2305.16387]

- **Elena Tomasetti**, Michele Moresco, Giovanni Granata, Maurizio D'Addona, Pietro Bergamini, Claudio Grillo, Amata Mercurio, Piero Rosati, and Andrea Cimatti. *Cosmic chronometers with galaxy clusters: a new avenue for multi-probe cosmology*, accepted for publication in Astronomy and Astrophysics [arXiv:2512.02109].

- Eleonora Di Valentino, et al. (incl. **Elena Tomasetti**), *The CosmoVerse White Paper: Addressing observational tensions in cosmology with systematics and fundamental physics*, Phys. Dark Univ. 49 (2025) [arXiv:2504.01669]

3.1 Constraining the expansion history of the Universe at high redshift

In this part of the work, our main goal is to advance the CC method by developing a robust implementation of current FSF techniques at high redshift. Specifically, we aim to test and validate their reliability as cosmology-independent age-dating tools, while critically assessing some of the key sources of systematics currently affecting them, as those related to the SFH modelling.

To this end, we take advantage of the deep VIMOS survey of the CANDELS UDS and CDFS survey fields (VANDELS, McLure et al., 2018), which provides optical spectra and photometry of a wide population of galaxies up to $z \simeq 6.5$. It was designed to provide ultra-deep, medium-resolution spectra, with high enough signal-to-noise ratio (S/N) to perform spectral line studies, both individually on the brighter sources and on stacked spectra for the fainter ones (Garilli et al., 2021). Many works based on VANDELS data have already been published investigating different environments and populations of objects: from the intergalactic medium (IGM; e.g. Thomas et al., 2020, 2021) and active galactic nuclei (AGNs; e.g. Magliocchetti et al., 2020), to Lyα and He II emitters (e.g. Marchi et al., 2019; Hoag et al., 2019; Cullen et al., 2020; Saxena et al., 2020b,a; Guaita et al., 2020) to the physical properties of star-forming (Cullen et al., 2019, 2020; Calabrò et al., 2021, 2022) and quiescent galaxies (Carnall et al., 2019, 2022; Hamadouche et al., 2022). In particular, the last have shown the presence, in VANDELS, of a population of red, massive, and passive galaxies covering the redshift range of $1 \leq z \leq 1.5$, constituting a potential set of chronometers. Moreover, the richness of spectro-photometric information available in VANDELS allows us to adopt a full spectrum fitting approach to estimate ages as well as many other physical properties of the sample, such as metallicity and SFH. For this purpose, we took advantage of the public code `BAGPIPES` (Carnall et al., 2018), which was already tested and validated for VANDELS data, and specifically modified in Jiao et al. (2023) to remove the cosmological prior on ages. All the results obtained in this work are thus independent of any cosmological model.

3.1.1 Data

In this section, we present an overview of the VANDELS survey, the process adopted to select an optimal sample of cosmic chronometers, their spectral features, and physical properties.

The VANDELS survey

The VANDELS survey (McLure et al., 2018; Pentericci et al., 2018; Garilli et al., 2021) is a deep VIMOS spectroscopic survey targeting high-redshift galaxies in the CANDELS UDS and CDFS survey fields, with a footprint of $\simeq 0.2$ deg^2. The observed spectra cover on average the wavelength range $4800 \leq \lambda \leq 9800$ Å with a mean spectral resolution R$\simeq$650. Both in UDS and CDFS, the CANDELS survey (Grogin et al., 2011; Koekemoer et al., 2011) offers deep, optical-near-infrared (nearIR) *HST* imaging, and in CDFS it also offers deep *HST*/ACS optical imaging from the GOODS survey (Giavalisco et al., 2004) and ultra-deep X-ray imaging (Luo et al., 2017). However, about 50% of the VANDELS footprint is not covered by *HST* imaging, which lies only in the central areas, and for those objects in the

wider-field region, the optical-nearIR photometric information is provided by different ground-based telescopes. A complete list of the available photometric data, covering the 3700-45000 Å wavelength range, can be found in Garilli et al. (2021).

We analysed data from the fourth and final data release of VANDELS (DR4, Garilli et al., 2021), which counts 2087 galaxies pre-selected in photometric redshift to lie in the range $1 \leq z \leq 7$, comprising 417 star-forming galaxies (SFG, $2.4 \leq z \leq 5.5$), 1259 Lyman-break galaxies (LBG, $3.0 \leq z \leq 7.0$), and 278 passive galaxies (PASS, $1.0 \leq z \leq 2.5$). The remaining 133 objects are AGNs, *Herschel*-detected galaxies, or secondary objects.

Besides spectra and photometry, DR4 also offers a catalogue including the following: *(i)* spectroscopic redshift measurements ($z_{\rm spec}$) and a relative quality flag ($z_{\rm flag}$); *(ii)* target classification as one of the types listed above, based on photometric criteria (mainly *i*, *z*, *H* magnitudes and *UV* and *VJ* colours) as described in McLure et al. (2018); *(iii)* SED fitting estimates of object properties, including rest-frame *UV* and *VJ* colours, stellar mass, V-band dust attenuation, and star-formation rate (these quantities are derived using the `BAGPIPES` code (Carnall et al., 2018) as described in Garilli et al. (2021)); *(iv)* correction factors for the error spectra, introduced to improve the correlation between the variance in the observed spectra and the associated median error, as described in Talia et al. (2023).

The exposure time for each object (up to 80 hours) is designed to obtain, especially for passive and star-forming galaxies, a *S/N* high enough to perform detailed spectroscopic studies. This consists of a *S/N* higher than ten for star-forming and passive galaxies, and higher than five for the other targets (Garilli et al., 2021).

Selecting a reliable sample of cosmic chronometers

A proper application of the cosmic chronometers method requires the selection of the purest sample of massive and passively evolving galaxies, avoiding contamination by younger star-forming objects that could bias the subsequent cosmological analysis (see Moresco et al., 2022, for more details). Many different criteria have been developed for this purpose, based on rest-frame colours (e.g. *UVJ*,Williams et al. 2009; *NUVrJ*, Ilbert et al. 2013), SED (e.g. Ilbert et al., 2010), star-formation rate (SFR; e.g. Pozzetti et al., 2010), or emission lines (e.g. Mignoli et al., 2009). In this context, several works have also shown that adopting a simple criterion is not enough to identify all the possible star-forming outliers, with possible residual contamination of up to 50% depending on the criterion (Franzetti et al., 2007; Moresco et al., 2013).

For this reason, aiming to maximise the purity of our sample, in this work we combine different and complementary cuts, based on both photometric and spectroscopic information, following this outline:

1) Parent sample: as a starting point, we define a parent sample made of galaxies selected as follows. As a first step, we select galaxies classified as passive targets in VANDELS (278 objects). Among the passive targets, we consider galaxies in the redshift range of $1.0 \leq z \leq 1.5$ (241 objects), with the lower and upper boundaries of the redshift interval excluding, respectively, four and 33 objects. The lower limit is applied because the distribution of the passive sample becomes statistically significant at $z \geq 1$. The upper limit, given the spectra wavelength coverage, is needed to ensure that all spectra include some major spectral features, such as the D4000 break, that are crucial in the following analysis.

Lastly, we require $z_{\rm flag} = 3, 4$. In VANDELS, this flag identifies objects with the most reliable redshift measurements; these are estimated to have a >99% probability of being correct (Garilli et al., 2021).

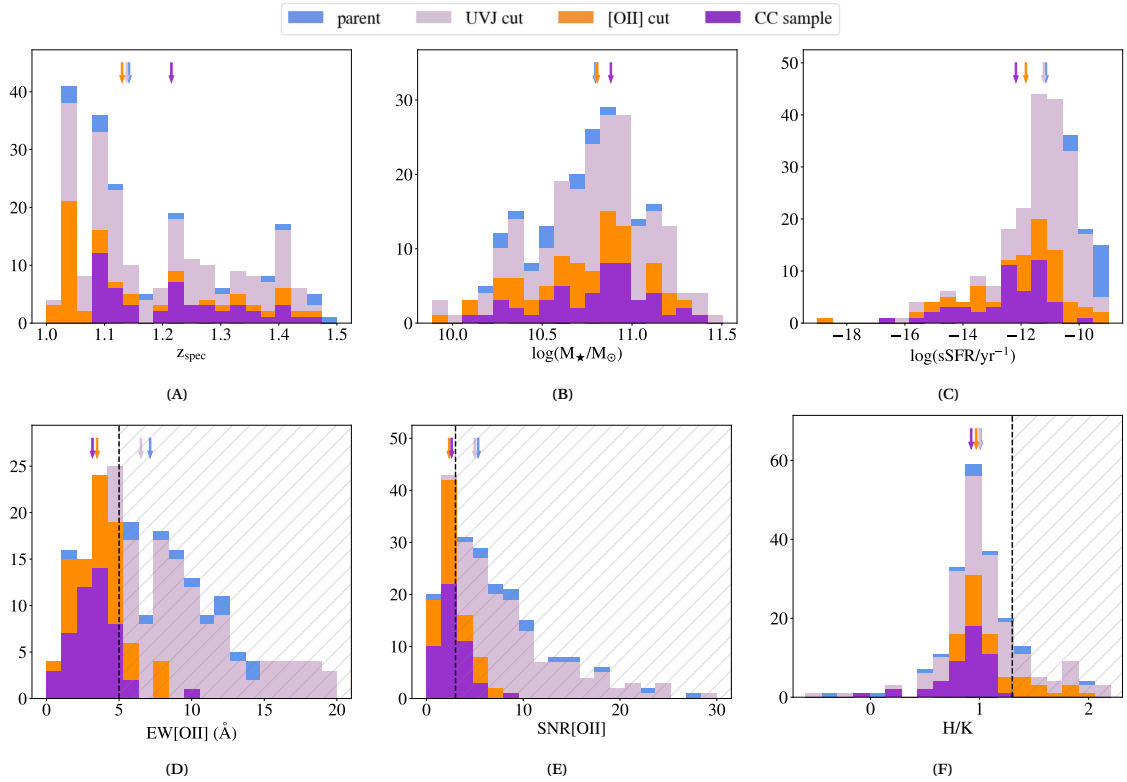

FIGURE 3.1: Histograms for the physical and spectral properties of the samples in each selection step, as shown in the legend and described in Section 3.1.1. Vertical arrows represent the corresponding median values, and, when present, the dashed vertical line indicates the threshold value adopted to select cosmic chronometers according to that quantity (the shaded area showing the discarded range). We note that for the [OII] we adopted a conservative cut, discarding only the objects that showed both EW([OII]) > 5Å and $S/N([OII]) > 3$, aiming to keep objects in which the [OII] line could be due to noise fluctuation.

This requirement, met by 265 passive targets, is particularly relevant for the cosmological analysis. Combining the aforementioned criteria, the parent sample counts 234 galaxies.

2) *UVJ* cut: since the DR4 catalogue provides rest-frame $U - V$ and $V - J$ colours, we apply the photometric criterion based on the colour-colour *UVJ* diagram (Williams et al., 2009) in order to select photometric passive galaxies, adopting the cut in McLure et al. (2018):

$$\begin{cases} U - V > 0.88(V - J) + 0.49 \\ U - V > 1.2 \\ V - J < 1.6 \end{cases} \tag{3.1}$$

As mentioned before, this criterion was already used for the target classification, but the $U - V$ and $V - J$ colours, in that case, were slightly different from those available in the DR4 catalogue. In both cases, they are derived via SED-fitting, but in DR4 this is performed with the additional information of spectroscopic redshifts, an improved photometry, and the `BAGPIPES` code, optimised for this survey. By applying the *UVJ* cut on the parent sample, 25 additional objects are discarded. Most of them were identified as post-starburst galaxies in Carnall et al. (2019). After the *UVJ* selection, our sample

is reduced to 219 galaxies.

3) [OII] cut: we further clean the sample by analysing the [OII]λ3727 emission line, an indicator of ongoing star formation since it is a tracer of photo-ionised gas (Magris C. et al., 2003). A cut on the equivalent width (EW) of the [OII] is often adopted, as in Mignoli et al. (2009), where star-forming objects are identified by EW([OII])>5 Å. In this work, a more conservative choice was preferred, and only galaxies with a significantly detected [OII] line are discarded, namely objects with EW([OII])>5 Å and S/N([OII])>3. This means that spectra with EW([OII])>5 Å but low S/N are not excluded from the sample, with the aim being to keep objects in which the [OII] line could simply be due to noise fluctuation.

The [OII] cut turns out to be the most restrictive selection step, reducing the sample to 96 galaxies (41% of the parent sample), but is fundamental to minimise the contamination by ongoing star formation or younger components, as discussed in Moresco et al. (2022).

4) H/K cut: another stellar population diagnostic is the ratio of two absorption lines, CaII H at 3969 Å and CaII K at 3934 Å, first defined by Rose (1984). In passive galaxies, the CaII K line is generally deeper than the CaII H, but since the CaII H line overlaps with the Hϵ line of the Balmer series at 3970 Å, deeper in the presence of young and hot A and B-type stars, CaII H results more prominent than CaII K if a young component is present in the population. Recent works (Moresco et al., 2018; Borghi et al., 2022a) have proven the effectiveness of this indicator by showing that a 5% contamination by young populations in the flux budget triggers the inversion.

To quantify this behaviour, we evaluate the ratio H/K $\equiv$ (CaII H + Hϵ) / CaII K by measuring the corresponding pseudo-Lick indices with the code `PyLick` (Borghi et al., 2022a). When using integrated quantities, a common requirement to identify non-contaminated objects is H/K < 1.2-1.5 (Borghi et al., 2022a). In this work, we selected galaxies with H/K < 1.3 in order to increase the purity of the sample preserving the statistics, as can be seen in Figure 3.1f. The H/K cut reduces the sample to 78 galaxies.

5) Visual inspection: the remaining spectra are visually checked to search for anomalies such as residual emission lines or calibration issues. We identify four objects showing this kind of issue: CDFS128563, UDS000769, UDS021218, and UDS137225. After this step, the sample counts 74 galaxies.

TABLE 3.1: Median values and associated errors of the most relevant properties describing our sample, according to the different and incremental selection criteria adopted (described in Section 3.1.1). The names of the samples and relative detailed description can be also found in Section 3.1.1.

	parent sample	***UVJ* cut**	**[OII] cut**	**CCs sample**
N° galaxies	234	219	96	49
% parent sample	100%	93%	41%	21%
$z_{\rm spec}$	1.14 ± 0.01	1.14 ± 0.01	1.13 ± 0.01	1.21 ± 0.02
$\log(M_\star/M_\odot)$	10.80 ± 0.02	10.80 ± 0.02	10.81 ± 0.03	10.88 ± 0.05
$\log({\rm sSFR/yr^{-1}})$	-11.1 ± 0.1	-11.2 ± 0.1	-11.8 ± 0.1	-12.2 ± 0.2
S/N[OII]	5.3 ± 0.3	5.0 ± 0.3	2.3 ± 0.2	2.6 ± 0.2
EW[OII] (Å)	7.1 ± 0.3	6.5 ± 0.3	3.5 ± 0.2	3.2 ± 0.2
H/K	1.01 ± 0.02	1.01 ± 0.02	0.97 ± 0.02	0.92 ± 0.02
$S/N_{\rm spec}$	5.44 ± 0.11	5.46 ± 0.11	5.64 ± 0.15	5.69 ± 0.17

6) Redshift cut: on the selected sample, we first perform a study of the spectral features, to which we dedicate the next section. This analysis highlights an anomalous behaviour with redshift of some spectral features, making it necessary to add a further selection step. In particular, we find that all objects below redshift $z < 1.07$ present a 4000 Å break (D4000) weaker than its expected value at those redshifts, with an inconsistent evolutionary trend, which appears to be caused by some systematic effect. Several possible causes for this effect have been explored, like error measurements or calibration issues, however, up to now no clear evidence has been found to account for this anomaly. For this reason, to avoid introducing a potential bias in the subsequent cosmological analysis, we prefer to discard the 23 galaxies below this redshift threshold. We highlight that this does not affect the robustness of the following results since it only reduces the redshift coverage.

Finally, we cross-checked our galaxies with the VANDELS AGN sample (Bongiorno et al. in prep.), removing two objects which are identified as AGNs. We thus obtain a final sample of 49 cosmic chronometers.

In Tab. 3.1, median values for different physical and spectral properties are listed for each step of the selection process. Unless otherwise specified, errors on median values are computed as median absolute deviations (MAD) divided by the square root of the number of objects. The *S/N* for each spectrum is estimated as the median of the *S/N* computed in each pixel in the range $3100 < \lambda < 3500$ Å. In Figure 3.1, the distribution of some of these properties for each passage is shown. Using the same colour-code, in the top panel of Figure 3.2 we show the *UVJ* diagram, and in Figure 3.3 we show the median stacked spectra for each selection step (normalised in the wavelength range of 3320-3850 Å). In the bottom panel of Figure 3.2, we show the EW[OII] against the H/K ratio for the sample obtained after the *UVJ* cut. This highlights how the two selection steps act in clearing the sample. In particular, we can observe that the threshold we adopted in EW[OII] and the one in *S/N*[OII] match very well, meaning that we are discarding galaxies where this emission line is really present and evident.

The selected sample of cosmic chronometers, with a median redshift of $\langle z \rangle = 1.21 \pm 0.02$, populates the tail of the reddest galaxies in the *UVJ* diagram and shows the required properties. In particular, it has a median stellar mass equal to $\langle \log(M_\star/M_\odot) \rangle = 10.88 \pm 0.05$, and about 75% of the sample has $\log(M_\star/M_\odot) > 10.6$, a value often used as a threshold to select CCs (Moresco et al., 2022). The median specific star formation rate (sSFR) is $\langle \log(\mathrm{sSFR/yr^{-1}}) \rangle = -12.2 \pm 0.2$, and more than 90% of the sample has $\log(\mathrm{sSFR/yr^{-1}}) < -11$, a common limit to characterise passive galaxies (Pozzetti et al., 2010). The histograms in Figure 3.1 also show how the selection based on spectral features has been effective in minimising the contamination by young stellar activity, decreasing the sSFR obtained after only the *UVJ* cut by 90%. The distributions in [OII] and H/K are typical of passive populations too, with a typical *S/N*([OII])<3 and a median $\langle \mathrm{H/K} \rangle = 0.92 \pm 0.02$ well below the adopted threshold. In Fig. 3.1d, one can also see the presence of a few objects that, despite having EW[OII]>5 Å, are kept in the CCs sample because of the low *S/N*[OII].

In Figure 3.3, the effect of the selection process is shown on median composite spectra. Top-down, the blue stacked spectrum, relative to the parent sample, has the most prominent [OII] emission and very similar CaII H and CaII K. The lilac one, realised after the *UVJ* cut, is not much different because the sample differs only by 25 objects, mostly post-starburst galaxies (Carnall et al., 2019), but shows a slightly weaker [OII]. Anyway, this confirms again how just adopting a photometric criterion is not enough to remove the contamination by young components, because the [OII] emission line, even if weak, is still present. Only the cut on its EW, which leads to the orange spectrum, is able to clean out this feature. It has a sharp impact on the statistics but is necessary to maximise the purity of the

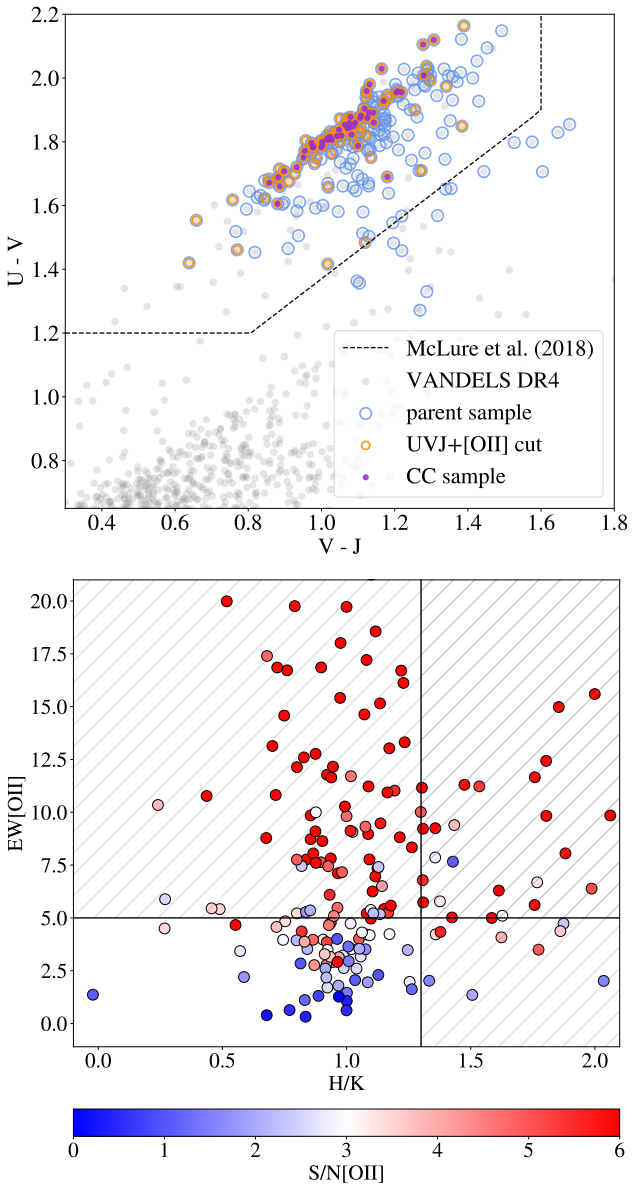

FIGURE 3.2: Photometric and spectroscopic selection criteria. *Top: UVJ* diagram for the main selection steps. Galaxies above the dashed line are qualified as passive following the criterion in McLure et al. (2018). *Bottom*: EW[OII] versus H/K ratio, colour-coded by *S/N*[OII], for the sample after the *UVJ* cut. The shaded areas show the discarded ranges for both quantities.

sample. Finally, the purple spectrum is built with the 49 CCs and, besides showing no [OII] emission, has the minimum H/K ratio.

Spectral properties of the CCs sample

Since the CCs sample falls in the redshift range of $1 < z < 1.5$, the spectral coverage is able to include some interesting spectral features. One of the most relevant is the D4000, a spectral discontinuity at 4000 Å, which is particularly strong in the context of passive galaxies. It is caused by a sudden onset of absorption lines at wavelengths bluer than 4000 Å and is stronger in evolved stellar populations. For

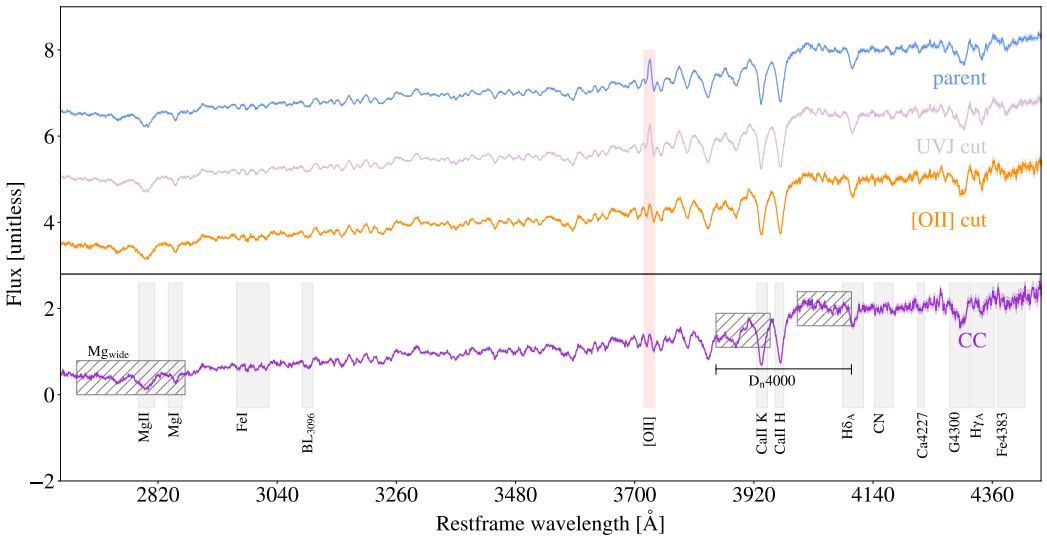

FIGURE 3.3: Median stacked spectra estimated for the different incremental selected samples of our analysis, as described in Section 3.1.1. We underline that the final sample considered is the purple one, on which we also highlight the most characteristic absorption features (grey shaded area) and spectral breaks (dashed area), as well as the position of potential emission lines (red shaded area), showing the absence of emission lines in our final sample.

this reason, at fixed metallicity, it has a tight correlation with the galaxy age – with older galaxies having a stronger D4000 – and a very low dependence on the presence of α-elements (Moresco et al., 2012). The classical definition of the D4000 is given in Bruzual A. (1983), while more recent is the narrow definition (D_n4000) given in Balogh et al. (1999), which is less affected by dust absorption. This last one is shown in the purple spectrum in Figure 3.3.

As with the CaII H and K, we use `PyLick` to measure the D_n4000 for the whole sample of CCs. In order to study its trend with redshift and mass, we separate high-mass (HM) and low-mass (LM) galaxies by the median stellar mass of the sample, $10^{10.88} M_\odot$. We then divide each sub-sample into three redshift bins, such that there is the same number of objects in each bin, obtaining a total of six sub-samples. In each of them, we measure the median D_n4000 value. In Figure 3.4, we show D_n4000 measurements obtained for single galaxies (grey) and median values in each sub-sample: in blue for the LM sample, in red for the HM sample. The D_n4000 shows a clear decreasing trend, both for the HM and the LM samples, providing initial observational evidence that the selected CCs sample ages with cosmic time. We also observe a mass-downsizing trend (Thomas et al., 2010), given that HM galaxies have a stronger median D_n4000 than LM objects at fixed redshift. These results constitute a first observational validation of the core hypotheses of the CC method.

3.1.2 Method and analysis

In this section, we present the method adopted to estimate ages and physical properties of the CCs sample, the code used, its settings, and the results obtained.

Full spectrum fitting in VANDELS

As in the works presented in the previous sections, we retrieved the physical parameters of the CC sample via full spectrum fitting with the `Bagpipes` (Carnall et al., 2018) code, modified as described

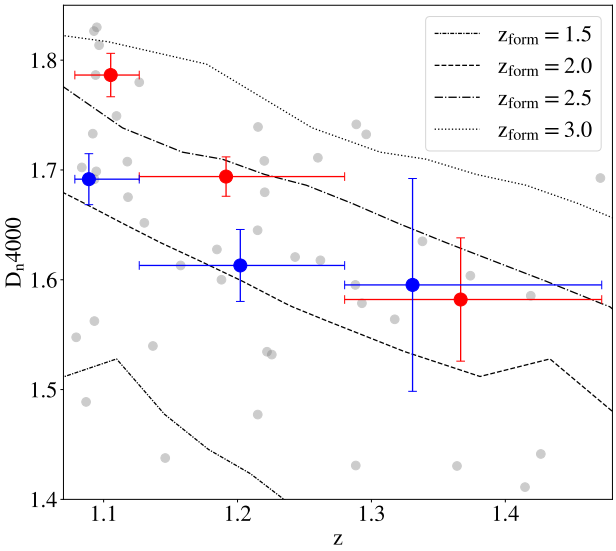

FIGURE 3.4: D_n4000 trend with redshift. The measurements for the single objects of the CCs sample are shown in grey; blue and red dots are median values averaged in two mass bins, $\log(M_\star/M_\odot) \leq 10.88$ (low-mass) and $\log(M_\star/M_\odot) > 10.88$ (high-mass), respectively. The different lines show the $D_n4000 - z$ relation obtained from the 2016 version of the Bruzual & Charlot (2003) models at different formation redshifts and assuming a reference flat ΛCDM cosmology ($\Omega_m = 0.3$, $\Omega_\Lambda = 0.7$ and $H_0 = 70$ km s^{-1} Mpc^{-1}), purely for illustrative purposes. We note that, qualitatively, the observed trends follow the cosmological models quite well, but we defer to Section 3.1.3 the full cosmological analysis.

in 1.3.2 in order to remove the cosmological prior on ages and allow them to span the full range 0 – 20 Gyr.

Before performing the fit on VANDELS data, we checked spectra and photometry to fix possible anomalies. On the one hand, we define a spectroscopic *S/N* by dividing, at each wavelength, the flux for its associated noise, which allowed us to determine the average *S/N* of the spectrum. On the other hand, analysing the photometric *S/N* distribution, we observe that it is up to three orders of magnitude higher ($\max(S/N_{\rm phot}) \sim 10^3$) than the spectroscopic one ($\langle S/N_{\rm spec}\rangle = 5.74 \pm 0.17$) for the same object, especially at the reddest wavelengths. If unaccounted for, this difference can have a significant impact on the fit, forcing it to reproduce the photometry irrespectively of the spectroscopic data. We also observe that the redder photometric points are also the ones with smaller errors, and this could introduce an additional bias in the analysis since the bluer photometric data points have also been proven to be fundamental in reconstructing the physical properties linked to the star-formation activity. To correct for this issue, we assumed a maximum *S/N* for the photometric data points to *S/N*=10, increasing the photometric error to 10% of the flux in case it was smaller. This allowed us to better weight the information coming from spectra and photometry. Nevertheless, their interplay is also managed in the fit through a calibration parameter, as introduced in Section 1.3.2 and explained later in this section.

Once we had performed these corrections, we tested different configurations of parameters and priors, with a particular focus on the impact of the chosen SFH. This is important not only to accurately reproduce the observed data, but also to evaluate how robust the results are when changing the fitting model, which is fundamental to estimate potential biases and systematic effects when performing cosmological analyses. Here, we report parameters and priors of three fit settings: baseline,

configuration 1, and configuration 2, as reported in Tab. 3.2. They mainly differ in two characteristics: the SFH functional form and the data used in the fitting process. The baseline and configuration 1 models both fit spectra and photometry, but with a different SFH: respectively a DED and a DPL; the baseline and configuration 2 models both use a DED SFH, but the second one does not include photometry in the fit. Apart from these differences, all these three models are built on a common set of components, namely: *(i)* a SFH modelled either with a DED or a DPL functional form; *(ii)* a dust attenuation component described in Salim et al. (2018), which consists of a power law as in Calzetti et al. (2000), but with a deviation from the slope parameterised by δ; *(iii)* a nebular component implemented in `BAGPIPES` using the code `Cloudy` (Ferland et al., 2017) and described in more detail in Carnall et al. (2018) (the process of selection should have already excluded objects having this type of emission, but we conservatively decided to include it in the model to verify its absence); *(iv)* redshift fixed, for each galaxy, to the value of the spectroscopic redshift obtained in VANDELS; *(v)* a calibration component, multiplying the spectrum with a second-order Chebyshev polynomial[1]; *(vi)* a noise correction, introduced as white noise. The main parameters and relative priors are listed in Tab. 3.2.

For each configuration, we verified the convergence of the results and that the best-fit model is correctly reproducing the observed spectra and photometry. If these requirements are not met, the results cannot be considered valid, and they are therefore flagged as a bad fit. To perform this operation, we visually examined the best-fit spectra and photometry and the distribution of the posterior probability on the parameters for each galaxy. For the baseline configuration, only 5/49 galaxies are flagged as bad fits. In Figure 3.5, the typical best-fit spectrum and photometry are shown in the case of a good fit for the baseline configuration.

As the name implies, the baseline configuration will be used as a benchmark to perform both the analysis of the physical properties of the population and the cosmological study, which is presented in the next sections. Among the three configurations presented here, it presents the smaller number of bad fits and the best agreement between observed spectrophotometry and the posterior one. The comparison between baseline and configuration 1 results, providing information on how the choice of a more complex SFH impacts the results, also allows us to account for its systematic effect in the cosmological analysis.

[1]This component is fundamental when jointly fitting spectra and photometry, as it allows the spectrum to adjust to the photometric emission, preventing potential calibration issues.

TABLE 3.2: Parameters and priors adopted for each configuration used in the full spectrum fitting. Columns 1-2 indicate wheter spectrum and photometry are considered (✓) or not (✘) in the fit. Columns 3-6 show the type of prior and the range for some main parameters. Columns 7-8 report the type of SFH and relative parameters. The acronyms DED and DPL refer respectively to the delayed exponentially declining and double-power-law SFHs, while the symbol $\mathcal{U}$ indicates a uniform prior with the associated range.

	spectrum (1)	photometry (2)	$\log(\sigma_{\rm vel}/{\rm km\,s^{-1}})$ (3)	age [Gyr] (4)	$\log(M_{\rm formed}/M_\odot)$ (5)	$\log(Z/Z_\odot)$ (6)	SFH (7)	SFH parameters (8)
baseline	✓	✓	$\mathcal{U}(1, 2.7)$	$\mathcal{U}(0, 20)$	$\mathcal{U}(0, 13)$	$\mathcal{U}(-0.85, 0.24)$	DED	$\tau \in \mathcal{U}(0, 1)$ $\tau \in \mathcal{U}(0, 20)$
config. 1	✓	✓	$\mathcal{U}(1, 2.7)$	$\mathcal{U}(0, 20)$	$\mathcal{U}(0, 13)$	$\mathcal{U}(-0.85, 0.24)$	DPL	$\log(\alpha) \in \mathcal{U}(-2, 3)$ $\log(\beta) \in \mathcal{U}(-2, 3)$
config. 2	✓	✘	$\mathcal{U}(1, 2.7)$	$\mathcal{U}(0, 20)$	$\mathcal{U}(0, 13)$	$\mathcal{U}(-0.85, 0.24)$	DED	$\tau \in \mathcal{U}(0, 1)$

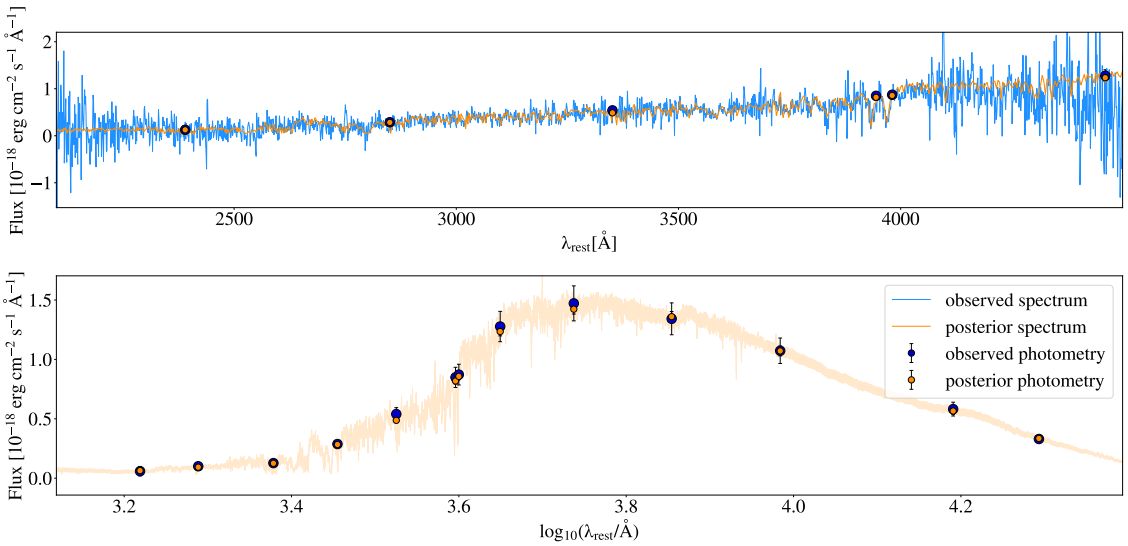

FIGURE 3.5: Example of best-fit spectrum and photometry (in orange) obtained by fitting the observed ones (in blue) with the baseline configuration, as described in Section 3.1.2 (Full spectrum fitting in VANDELS).

Physical properties of the CCs sample

The fitting process with the baseline configuration is successful for 44 CCs (90% of CCs sample), with a median reduced chi-square of $\tilde{\chi}^2$=1.46, considering both spectra and photometry. In order to estimate their physical properties, we computed, for each parameter, the median and 16th-84th percentile ranges of the posterior distribution. The analysis of these quantities shows that our CCs sample, in agreement with our selection process, consists of galaxies with high stellar masses, as commonly occurs in a population of passive galaxies, with a median stellar mass $\langle \log(M_{\rm formed}/M_\odot) \rangle = 11.21 \pm 0.05$; a median metallicity value of $\langle Z/Z_\odot \rangle = 0.44 \pm 0.01$; short SFHs, with a typical timescale for the star formation $\langle \tau \rangle = 0.28 \pm 0.02$ Gyr, which also agrees with a mass-downsizing scenario where more massive galaxies are the first to assemble in very short bursts of formation (Thomas et al., 2010; Citro et al., 2017); and low dust reddening, with a median V-band dust extinction of $\langle A_{\rm V,dust} \rangle = 0.43 \pm 0.02$ mag.

We notice here that in the literature there is quite a large spread in the derived metallicity for passive and massive galaxies at these redshifts, with estimates going from sub-solar values of 0.4-0.7 $Z_\odot$ (e.g., Kriek et al., 2019; Lonoce et al., 2020; Carnall et al., 2022) up to 1.3-1.6 $Z_\odot$ (e.g., Conroy et al., 2014; Onodera et al., 2015). Our results, in particular, are compatible with the ones found in Kriek et al. (2019) and Lonoce et al. (2020), and slightly lower with respect to the metallicities obtained by Carnall et al. (2022), who analysed the stacked spectra from a sample of VANDELS passive galaxies in the range $1 \leq z \leq 1.3$, finding $Z/Z_\odot = 0.74^{+0.15}_{-0.12}$ with `BAGPIPES`.

We also compare our results with the independent analysis of Saracco et al. (2023), who studied a sample of 64 passive galaxies in VANDELS performing non-parametric full spectrum fitting on stacked spectra in six mass ranges, using different combinations of models and fitting codes. The sample was selected following the same requirements adopted in this work to identify the parent sample but with a tighter redshift range ($1 \leq z \leq 1.4$) and adding a lower limit to the S/N (S/N>6 per Å in the range [3400-3600] Å). They find typically over-solar metallicities, different from both the ones in this work and in Carnall et al. (2022). The spread in these results could be due to the models adopted or to the full-spectrum-fitting code used, as also shown in Saracco et al. (2023), where the variation of one or both

of them produces a scatter in the metallicity estimation of up to 0.4 dex.
It is important to underline that, for the cosmological purpose of this work, we expect the impact of this effect to be negligible, given that the CC method relies on the estimation of differential quantities. In particular, given an optimally selected sample of massive and passive galaxies, what is fundamental is ensuring its homogeneity. This condition is met in our sample, which shows homogeneous metallicities in the considered redshift range. Moreover, comparing our age estimates with the ones in Saracco et al. (2023), we find a good agreement with their mass-weighted ages, using both the `STARLIGHT` (Cid Fernandes et al., 2005) and `pPXF` (Cappellari, 2017) codes.

By adopting an archaeological look-back approach, we can study how our measured quantities vary as a function of redshift. In particular, given the cosmological purpose of this work, we are interested in the age-redshift relation, which is discussed in detail in the following (Optimising the selection of cosmic chronometers). In Figure 3.6a, we show the age-redshift for our 44 CCs coloured by stellar mass. From this trend, we can draw three main conclusions. First, for most of the galaxies (95% of CCs), ages are below that of the Universe, as expected in a standard cosmology (flat ΛCDM with $\Omega_m = 0.3$, $\Omega_\Lambda = 0.7$, $H_0 = 70$ km/s/Mpc), even without having imposed a cosmological prior, since they could formally vary between 0 and 20 Gyr across the entire redshift range. This is, *per se,* a significant result since it demonstrates that with enough spectral coverage, a sufficient *S/N*, and adequate photometric data, we can constrain this parameter reliably without any additional cosmological assumption. Second, the ages show a decreasing trend with redshift in agreement with the cosmological expectation, in line with what was already observed for the D_n4000. The third important observation is the existence of a mass-downsizing trend, with more massive galaxies being older than the less massive ones at fixed redshift. In particular, objects with $\log(M_{\rm formed}/M_\odot) \leq 11.1$ show formation redshifts in the $1.5 \lesssim z_F \lesssim 4$ range, while for galaxies with $\log(M_{\rm formed}/M_\odot) > 11.1$ it spans the $2 \lesssim z_F \lesssim 7$ range.

In Figure 3.6, we show the trends with redshift for other relevant physical parameters estimated in the fit (stellar mass, metallicity, and τ parameter), coloured accordingly to the stellar mass. We can notice that for the more massive sample (in red) there are no strong trends with redshift for any of the considered quantities, except the ages, while the lower mass sample (in blue) shows a mild increasing trend with redshift for the stellar mass. This is a well-known effect due to the observational luminosity threshold, which allows us to see only the intrinsically brightest objects when we observe the distant Universe. This effect can be noted in particular for the stellar mass since it correlates with the galaxy luminosity. Given this, it is clear that to obtain a homogeneous sample as a function of redshift for the cosmological analyses, it will be necessary to perform a cut in stellar mass, as we discuss later (Optimising the selection of cosmic chronometers).

Another important observation in this context can be derived for the τ parameter, which is related to the SFH length, and its trend with redshift in Figure 3.6c. Both for the higher and the lower mass galaxies it is stable around 0.3 Gyr, but the high-mass sample seems to have a longer period of star formation, in contrast with what is expected in a mass-downsizing paradigm, in which the more massive a galaxy is, the older it is expected to be, and the shorter its SFH. We trace the origin for this inversion to be the existent degeneracy between τ and age, occurring as a direct correlation between these two parameters. This effect is well known in literature (Gavazzi et al., 2002) when adopting a DED SFH, since age and τ have very similar effects on the spectral shape, and it is difficult to disentangle their contribution. The impact of this effect, however, is negligible on our results since the range of retrieved τ is extremely small and compatible with a very short SFH, and, most importantly, because our cosmological analysis is made on sub-samples with constant mass and where the τ appears very stable as a function of redshift. In this context, it is even more interesting to analyse the impact on the results of

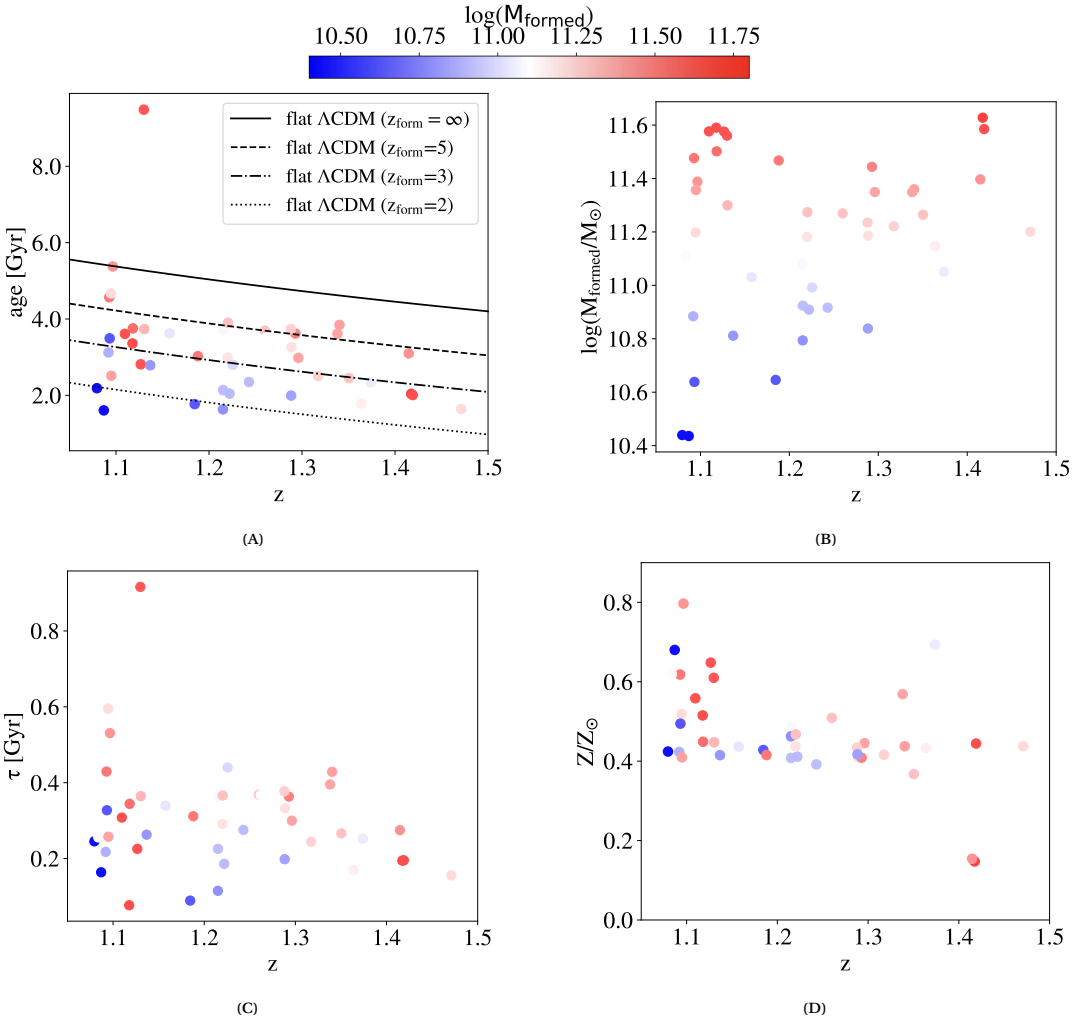

FIGURE 3.6: Trends with redshift of age (a), stellar mass (b), tau parameter (c), and metallicity (d), colour-coded by stellar mass. In the age-redshift the lines in the background represent the theoretical trends in a flat ΛCDM cosmology with $\Omega_m = 0.3$, $\Omega_\Lambda = 0.7$, $H_0 = 70$ km/s/Mpc, and different formation redshifts.

adopting a DPL SFH, in which the decoupling of the rising and falling slope allows more freedom for the SFH shape.

The assumed SFH has been identified in recent literature as a potentially significant source of systematic effects in the estimate of galaxies' physical parameters. For this reason, we extensively tested the dependence of our measurements on the assumed SFH functional form. In particular, we repeated our analysis considering the DPL SFH (configuration 1) and assessed the robustness of our results.

Assessing the impact of the SFH choice

The SFH choice is certainly one of the most significant components when building a fitting model since it describes how the star-formation rate varies as a function of cosmic time and then dictates the chemical enrichment history of the galaxy, as well as its stellar mass. As discussed in Section 1.3.2, the DPL SFH is a valid alternative to the DED SFH that we use as baseline, and it has actually already been adopted while analysing VANDELS data (Carnall et al., 2019, 2022). There are two main differences with respect to a DED SFH: the first is that a DPL has three free parameters instead of two since its shape

is determined separately by the falling (α) and the rising slope (β) of the curve; the second regards the definition of the galaxy age, which is, by default in `BAGPIPES`, the mass-weighted quantity defined in Eq. 1.49 instead of the one in Eq. 1.48 adopted for a DED SFH. For the sake of consistency, in this section we use mass-weighted ages for both DED and DPL SFH assumptions.

As already anticipated, we performed a fit adopting a DPL SFH named configuration 1, with parameters and priors as listed in Tab. 3.2. Once removed the bad fits, we find an exceptional agreement with baseline results for 75% of the galaxy population, as shown in Fig. 3.7, with a median percentage difference in terms of mass-weighted age, stellar mass, metallicity, dust reddening, and velocity dispersion smaller than 1%. The rest of the sample (six objects, after removing bad fits) shows a significant difference with respect to baseline results (purple open dots in Fig. 3.7).
To understand the nature of this difference, we examined all the properties of these six CCs, finding that they show common characteristics, in particular ages over 5 Gyr and β<1. Recalling that β sets the rising slope of the SFH, a value β<1 implies that the first part of the SFH has a concave shape, as in the dark purple curve in Fig. 3.7d, causing an extremely slow rise of the SFR. Solutions of this kind appear highly non-physical because they would require a SFH extremely prolonged over time and without significant episodes of star formation, in contradiction with other indicators available (e.g. the measured sSFR, H/K ratio, etc.) and with all the other results obtained in the literature for these extremely massive and passive systems. For the population whose results agree with baseline ones, instead, the value of β spans from a few tens to hundreds, resulting in a very steep rise of the SFR. It seems that relaxing the cosmological prior on ages and adopting a DPL SFH, which is more flexible than a DED SFH in terms of shape, in some cases allows the fit to find a combination of parameters leading to a non-physical solution.

We ran some tests to understand if a different, physically acceptable solution exists for these objects by increasing the prior on β. In Fig. 3.7d, we show the SFHs obtained for an example object resulting from seven runs where the β prior was gradually raised from 0.001 to 10. We can observe that up to β>5 the resulting SFH still has an anomalous shape and duration, with values for β near the prior limit, suggesting that the fit is still trying to reach the non-physical solution. Starting from $\beta > 6$, however, the fit converges to solutions with β values approximately two orders of magnitude above the prior limit. Further increasing the prior yields the same solution, which is also nearly identical to the one obtained when assuming a DED SFH. This means that a physical solution for these objects does exist, and, if the SFH parameters are properly constrained, the resulting SFH has the same shape if either a DED SFH or a DPL SFH is assumed. It is important to stress that imposing a prior of $\beta > 10$ does not force the SFH to mimic the shape of a DED, which is characterized by a nearly instantaneous rising phase. A value of $\beta = 10$ still corresponds to a rising phase lasting at least ~0.5–1 Gyr, followed by a declining phase of up to 10 Gyr depending on the value of α. The independence of the recovered DPL solution from the specific choice of the prior is further supported by the fact that the same result is already obtained with the less restrictive prior of $\beta > 6$, which would still allow for a rising phase as long as ~2.5 Gyr.

Based on these findings, we repeated the fit on all of our 49 objects using configuration 1 (Tab. 3.2), this time increasing the lower limit on β to 10. In Figs. 3.7a and 3.7b we show the comparison of results for mass-weighted ages and metallicity between baseline (x-axis) and configuration 1 (y-axis), both with the old (open dots) and the new prior (full dots). It is clear that after applying the new prior, the results of the two fits have a one-to-one correlation, with a median percentage difference lower than 2% for both quantities. In terms of stellar mass, velocity dispersion, and dust reddening, the discrepancy is even smaller, reaching a median percent difference lower than 1%. Given the colour-code applied

in these figures, it is also evident how the results of configuration 1 with the old prior are different from the ones obtained with the new prior only when β converges to values lower than 1, while in all the other cases they overlap almost perfectly. The same behaviour is noticeable in the age-redshift relation shown in Fig. 3.7c.

We can conclude that the impact of the SFH choice on the estimation of physical parameters is minimal, under the condition that the SFH parameters are constrained to avoid non-physical solutions. In particular, a lower limit to the rising slope of the DPL SFH β>10 is effective for this purpose. In addition, the fact that the resulting SFH shape is equivalent when adopting a DED or a DPL SFH further validates the robustness of the results obtained with the baseline configuration, despite the existent degeneracy between age and τ in a DEL SFH discussed earlier in this section (Physical properties of the CCs sample).

Optimising the selection of cosmic chronometers

In the previous paragraphs, the discussion of the physical properties of the 44 selected galaxies has provided additional support to the fact that these objects meet the conditions for being CCs, given their high masses ($\langle \log(M_{\rm formed}/M_\odot) \rangle = 11.21 \pm 0.05$) and their very short periods of star formation $\langle \tau \rangle = 0.28 \pm 0.02$ Gyr. At this point, an important aspect to be considered in applying the method is the maximisation of the synchronicity of the sample formation time. In a mass-downsizing scenario, high-mass galaxies (the cut $\log(M_\star/M_\odot) > 10.6$ is often applied; Moresco et al., 2022) are the first to form ($z > 2-3$, Citro et al., 2017; Carnall et al., 2018, 2019) in a short burst of star formation (τ <0.3 Gyr, Thomas et al., 2010; Carnall et al., 2018), so they are the best able to provide a sample of synchronised chronometers. Anyway, it is important not only to select massive galaxies, but also that their properties be consistent in redshift in order to maximise the homogeneity of the sample at different cosmic times and to avoid biases in the cosmological analysis. In the previous section, commenting on Figure 3.6, we note that the sample shows homogeneous metallicity and τ throughout redshift, while the stellar mass for the low-mass sample – in blue in Figure 3.6b – shows an increasing trend with redshift. Then, with the aim of homogenising the sample mass, we apply a further cut $\log(M_{\rm formed}/M_\odot) \geq 10.8$ (discarding 5 galaxies), a threshold that not only makes our CCs homogeneous in mass, but also in redshift of formation, removing all the galaxies with $z_{\rm F}$<2 in Figure 3.6a. The sample of CCs that we adopted for the cosmological analysis thus features 39 galaxies.

With this accurately selected sample, we were then able to build the median age-redshift relation, which is more robust in tracing the ageing trend since it allows us to increase the *S/N* of our measurements. This consists of dividing the sample into redshift bins and eventually into mass bins, and then averaging ages and redshifts in each sub-group. To each median age, we assigned an error computed as MAD/ $\sqrt{N}$. We tested different types of binning: *(i)* equally spaced or equally populated in redshift; *(ii)* two or four redshift bins; *(iii)* sub-dividing (or not) the sample into mass bins according to the median value of the $\log(M_{\rm formed}/M_\odot)$ distribution ($\langle \log(M_{\rm formed}/M_\odot) \rangle = 11.26$). When dividing the sample into mass sub-samples, we decided to split them in redshift bins after the mass separation to obtain more homogeneous sub-samples in mass, and, hence, time of formation.
By combining these three options, eight different binning types can be obtained, but not all of them are effective in tracing the age-redshift trend. For example, using the separation in mass and four redshift intervals at the same time produces a total of eight sub-samples with ≤5 galaxies each, ending with median values that are very sensitive to fluctuations in each bin. On the contrary, adopting two redshift bins and no mass separation would lead to more stable median values, but having just a pair

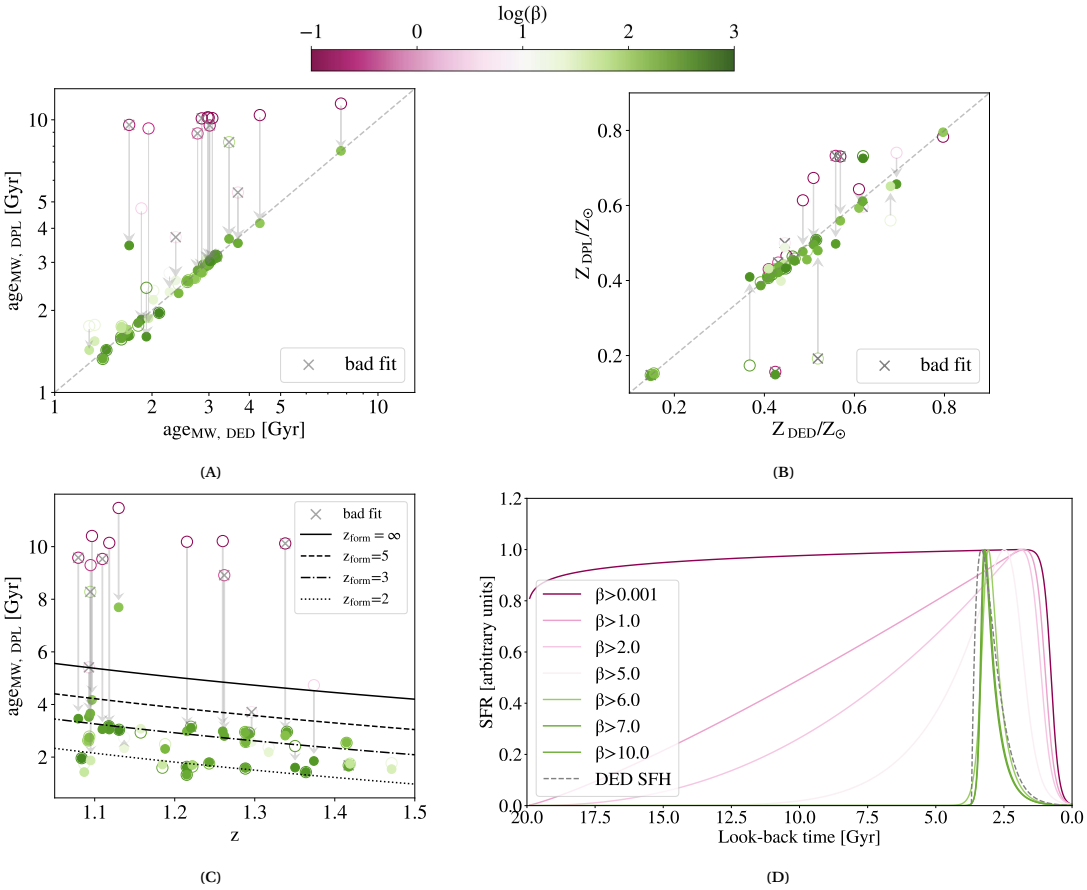

FIGURE 3.7: Comparison of physical parameters obtained with delayed exponentially declining (DED) and double-power-law (DPL) SFH. In panels (a) and (b) we show the comparison of mass-weighted ages and metallicities estimated with the two SFHs. The points are colour-coded according to the parameter β of the DPL model, representing the rising slope of the SFH. We notice that the objects with extremely low β (represented with open circles) are the ones deviating more from the one-to-one relation. For this reason, we fitted those objects again with a more conservative prior on β ($\beta > 10$). The grey arrows show how the results converge to the correct relation with the new prior. In panel (c) we present the age-redshift relation with the same colour-coding as in the previous panels. In panel (d) the star-formation rate is shown as a function of the look-back time normalised to its peak for an object significantly deviating from the one-to-one relation in panel (a). The coloured curves represent how the resulting SFH obtained with the DPL model changes with different priors on β, colour-coded as presented in the legend; the grey dashed line shows the DED SFH, for comparison. We notice that above $\beta > 6$ the DPL model converges almost exactly to the DED model.

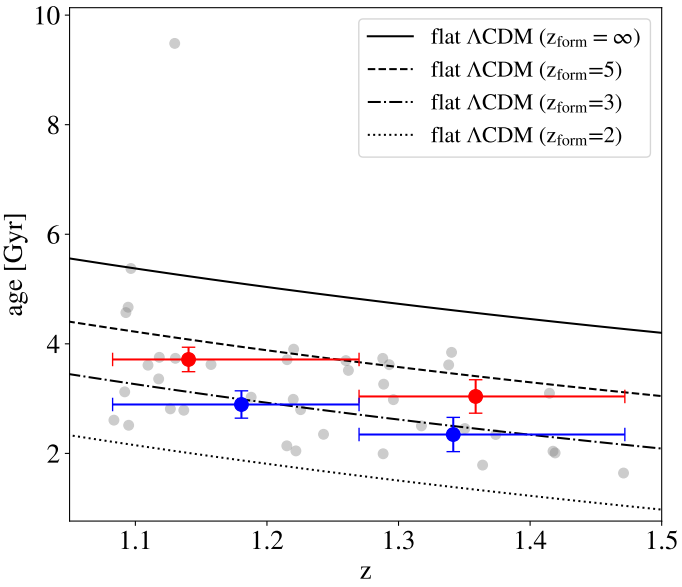

FIGURE 3.8: Median age-redshift trend for the 39 CCs sample, obtained with binning A. Red and blue dots represent median values, respectively, for the high-mass ($\log(M_{\rm formed}/M_\odot) > 11.26$) and the low-mass ($\log(M_{\rm formed}/M_\odot) \leq 11.26$) sample. In the background, grey dots are the 39 single measurements, while lines show, for illustrative purposes only, the theoretical trends with different redshifts of formation, as given by a flat ΛCDM model with $\Omega_m = 0.3$ and $H_0 = 70$ km s^{-1} Mpc^{-1}.

TABLE 3.3: Median ages and properties of the selected CC sample considering the binning A as described in the text. For each sub-sample, we report mean values of redshift, median ages, median stellar mass, and the number of galaxies in each bin.

Binning A	z	age [Gyr]	$\log(M_{\rm formed}/M_\odot)$	N
high mass	1.14	3.7 ± 0.2	11.47 ± 0.04	12
	1.36	3.0 ± 0.3	11.38 ± 0.02	8
low mass	1.18	2.9 ± 0.2	11.01 ± 0.04	12
	1.34	2.3 ± 0.3	11.19 ± 0.02	7

of points is not effective in constraining the age-redshift trend. Additionally, aiming for the maximum synchronicity of the population that we average on, we find it better to always adopt the mass separation, which guarantees a better homogeneity of the sample in each bin.
After these considerations, we can conclude that the best binning types for our sample are two, given by two equally spaced or equally populated redshift bins, divided in mass. We refer to the equally spaced one as *binning A*, which we use as a benchmark, while the equally populated one is referred to as *binning B* and is used as a comparison. This choice was made because the first one guarantees a more homogeneous sampling of the ageing trend also in terms of redshift. The median age-redshift trend for binning A is shown in Figure 3.8 and the relative median values and errors are reported in Tab. 3.3.

3.1.3 Cosmological analysis

In this section, we describe the use of the median age-redshift relation built in Section 3.1.2 to perform the cosmological analysis. In particular, we applied the cosmic chronometers method, directly measuring the Hubble parameter using Eq. 1.11 that does not rely on any cosmological model. In this

way, we obtain a new estimate for $H(z)$ at redshift $z > 1$ that is completely cosmology-independent. As an additional test, we also considered fitting the age-redshift relation directly, assuming instead a cosmological model. This allowed us to derive an estimate of the Hubble constant H_0, which is not, however, cosmology-independent. We note here that it could be also possible to derive a cosmology-independent estimate of H_0 by extrapolating the $H(z)$ relation down to $z = 0$ (Moresco et al., 2022; Moresco, 2023).

Cosmological constraints with the cosmic chronometers approach

Starting from the median age-redshift relation obtained in Section 3.1.2, we were then able to apply the cosmic chronometers method. As already discussed in Section 1.2.2, the Hubble parameter $H(z)$ can be estimated by evaluating the differential age evolution over a small redshift bin $\mathrm{d}z$ of a sample of cosmic chronometers through Eq. 1.11, which means that we can estimate the Hubble parameter at the redshift of the CCs sample by measuring the first derivative of the age-redshift relation. This requires an accurately synchronised sample of CCs; a suitably large redshift interval, such that the differential in age ($\mathrm{d}t$) is larger than its uncertainty; and small age errors, to maximise the accuracy on the measurement of $\mathrm{d}z/\mathrm{d}t$. The selection process presented in Section 3.1.1 and the optimisation of the CCs sample in Section 3.1.2 showed that the 39 selected CCs have the characteristics to satisfy the first requirement. Moreover, the chosen binning type (binning A, described in Section 3.1.2) is optimal for meeting these requisites, representing a good balance between the need for sampling in redshift and the need for statistics in each bin. At the same time, adopting the mass separation allowed us to maximise the synchronicity of each sub-sample given the strong correlation among stellar mass, age, and redshift of formation expected in a mass-downsizing scenario (Thomas et al., 2010).

Computing $H(z)$ with the cosmic chronometers method Starting from the median age-redshift relation obtained with binning A, shown in Figure 3.8 and reported in Tab. 3.3, the Hubble parameter $H(z)$ is computed in two steps: first, Eq. 1.11 is applied separately on the two high- and low-mass data points, where z is computed as the mean redshift of the two points, obtaining two $H(z)$ measurements and relative errors; then we compute the average of these two values, weighted on the associated error. We can obtain this average because, while the median age in the two mass sub-samples is clearly offset due to a different time of formation, and hence needs to be analysed separately, the underlying cosmology has to be the same, and therefore the Hubble parameter estimates can be averaged to increase the accuracy of the measurement. In this way, we obtain an estimate for the Hubble parameter at $z \simeq 1.26$:

$$H(z \simeq 1.26) = 135 \pm 60\,(\mathrm{stat}) \quad [\mathrm{km\,s^{-1}\,Mpc^{-1}}],$$

where the associated error is given here by the only contribution of the statistical uncertainty, resulting from the propagation of the error on median ages, which scales with $\sqrt{N}$, the number of elements in each bin. In the next section, we analyse the impact on the result of two effects, the binning choice, and the SFH choice, aiming to include a systematic component in the uncertainty.

Study of the systematic effects on $H(z)$ In Section 3.1.2 we discussed the different types of fit configurations that have been tested on our CCs sample. We paid particular attention to configuration 1, which differs from the baseline in having a DPL SFH instead of a DED SFH. We found a strong agreement between baseline and configuration 1 results, with a mean percentage difference in ages smaller

TABLE 3.4: Measurements of $H(z)$ obtained applying the CC method to median age-redshift trends obtained with baseline and configuration 1 fits, both using binning A and binning B.

	binning	$\langle z \rangle$	**H(z) [km s^{-1} Mpc^{-1}]**
baseline	A	1.26	135 ± 60
	B	1.24	132 ± 82
config. 1	A	1.25	120 ± 34
	B	1.27	171 ± 109

than 2%. Here, we want to understand how this slight discrepancy in age propagates to the estimation of the Hubble parameter. We should recall that when using a DPL SFH, `BAGPIPES` only provides mass-weighted ages, as defined in Eq. 1.49, while baseline results are built with standard ages, from the definition in Eq. 1.48. As already discussed, this difference does not introduce a change in the slope of the ageing trend, because the results obtained with these two definitions differ by an offset (~ 0.6 Gyr), typically constant in redshift and age.

After performing the fit with configuration 1, we discarded the five objects identified in Section 3.1.2 to have $\log(M_{\rm formed}/M_\odot) < 10.8$, and then we cleared bad fits from the sample, ending up with a sample of 36 CCs. With these, we obtain a new median age-redshift by applying binning A, and then we implemented the CC method by repeating the process explained in Section 3.1.3. The Hubble parameter measurement in this case is $H(z \simeq 1.25) = 156 \pm 51$ km s^{-1} Mpc^{-1}.

To include the effect of the assumed binning in the total error budget, we repeated this process for binning B, both with baseline and configuration 1 results. The four measurements obtained are reported in Tab. 3.4. To estimate the impact of choosing a different SFH, we computed the average difference between baseline and configuration 1 measurement of $H(z)$ for equivalent binnings, which results in a contribution to the error budget of $\Delta H_{\rm SFH} = 27$ km s^{-1} Mpc^{-1}. We note that this large uncertainty is dominated by the $H(z)$ value obtained with configuration 1 and binning B, the less accurate of the four estimates that we derive, as shown in Tab. 3.4. This effect is due to the fact that in this configuration, the number of correctly estimated ages is smaller than in the baseline configuration, and therefore, with the statistics being lower, it is subject to slightly larger fluctuations when varying the binning. In particular, we notice that by choosing the equally populated binning we end up with an uneven redshift sampling that increases the fluctuation in the average ages, resulting in a significantly larger uncertainty on $H(z)$. If we exclude this result, $\Delta H_{\rm SFH}$ would be cut down to 15 km s^{-1} Mpc^{-1}. Lastly, we also included the discrepancy in $H(z)$ between baseline binning A and binning B, $\Delta H_{\rm bin} = 2.4$ km s^{-1} Mpc^{-1}, in the error. Adding these two contributions, we obtain the following:

$$H(z \simeq 1.26) = 135 \pm 60\,(\text{stat}) \pm 27\,(\text{sys}) \pm 2.4\,(\text{bin}) \quad [\text{km s}^{-1}\,\text{Mpc}^{-1}];$$

and, finally, summing the errors in quadrature:

$$H(z \simeq 1.26) = 135 \pm 65 \quad [\text{km s}^{-1}\,\text{Mpc}^{-1}].$$

This measurement, which represents the main result of this work, is also shown in Figure 3.9, where all the $H(z)$ measurements obtained with the CC method are reported as a function of redshift.

It is clear that the statistical uncertainty here dominates the error budget of the final result, as a

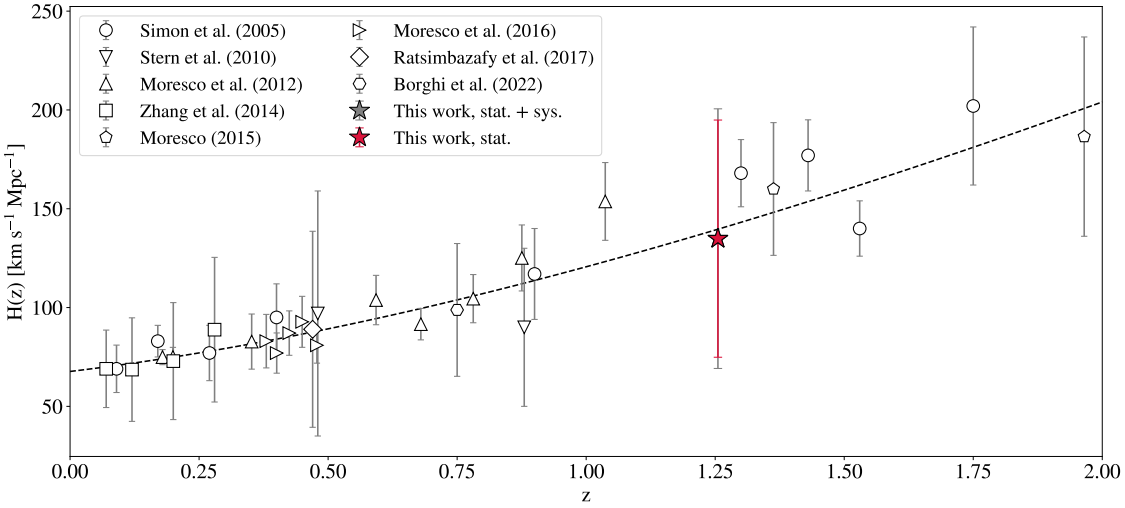

FIGURE 3.9: $H(z)$ measurement obtained in this work in comparison with all the $H(z)$ estimations obtained up to now with the cosmic chronometers method. The dashed line represents the theoretical trend of a flat ΛCDM model as in Planck Collaboration et al. (2020) as a purely illustrative reference.

direct consequence of the low number of CCs in the sample. Recalling that the statistical error on $H(z)$ depends on the uncertainty of median ages, computed as MAD/ $\sqrt{N}$, we would need larger statistics to cut down its contribution. For comparison, in Jiao et al. (2023) an estimate of the Hubble parameter $H(z \simeq 0.80) = 113.1 \pm 15.2$ km s^{-1} Mpc^{-1} (stat) is obtained with a sample of 350 CCs from the LEGA-C survey (Straatman et al., 2018), reaching a statistical error of 13%. Indeed, starting from the statistical error obtained in this work of 44% with a sample of 39 objects and assuming that this scales with $\sqrt{N}$, the expected statistical error for a sample of 350 galaxies is around 15%, very similar to the 13% actually obtained.

This gives an optimistic prospect on the achievable results with future, much larger surveys. The ESA space mission Euclid (Laureijs et al., 2011), for example, is expected to observe up to a few thousand CC candidates in the redshift range of $1.5 < z < 2$, increasing the current statistics by two orders of magnitude. In the context of the $H(z)$ estimate with the CC method, this would mean being able to obtain measurements of the Hubble parameter up to $z = 2$ with a statistical error of the order of 6%, significantly increasing the precision of the estimates at this redshift, which now stands between 10% and 25%. In this way, we could more accurately constrain the $H(z)$ trend and, as a consequence, the expansion history of the Universe.

Analysing the age-redshift relation

As an additional test, we studied the age-redshift relation assuming a cosmological model directly. In particular, we fitted the median age-redshift with a flat ΛCDM model, where the free parameters are the Hubble constant H_0 and the adimensional matter density parameter (Ω_m). Here, we decided to neglect the contribution due to radiation and neutrinos, but we verified that it affects our results by less than 0.2%, which is well below our current error. In this framework, the Hubble parameter $H(z)$ is given by

$$H(z) = H_0 \sqrt{1 - \Omega_m + \Omega_m (1+z)^3}. \tag{3.2}$$

We already saw how, considering an FLRW metric, the age of the Universe at a given redshift $t(z)$ is linked to the Hubble parameter through Eq. 1.12. Before fitting this age-redshift relation to our median data, we needed to pay attention to the fact that $t(z)$ refers to the age of the Universe here, while we obtained ages for a sample of CCs. This means that the two trends are separated by an offset, due to the delay between the Big Bang and the formation of the first galaxies. We parameterised this offset as t_0, representing the age of the Universe at which our CCs formed. Assuming that the objects in the sample are coeval, t_0 can be considered constant in redshift. Its value will instead be left free to vary. Introducing t_0, Eq. 1.12 can be modified to suit the CCs age-redshift trend as follows:

$$t_{\rm cc}(z) = \int_z^\infty \frac{1}{1+z'} \frac{{\rm d}z'}{H_0\sqrt{1-\Omega_m+\Omega_m(1+z')^3}} - t_0. \tag{3.3}$$

Constraining these three parameters at the same time is a non-trivial process, mainly due to their degeneracies; for example, a higher t_0 results in a lower age of the Universe, but this happens with a higher H_0 or a larger Ω_m too. As it is also shown in Borghi et al. (2022b), even if these degeneracies are non-negligible, the three parameters affect the age-redshift slope differently. So, if age errors are small enough and if appropriate priors on the parameters are adopted, we could at least partially mitigate these degeneracies.

We performed the fit of the age-redshift relation obtained with binning A (shown in Figure 3.8 and described in Tab. 3.3) with the theoretical trend in Eq. 3.3 by adopting a Markov chain Monte Carlo (MCMC) technique implemented through the affine-invariant `emcee` sampler (Foreman-Mackey et al., 2013) and considering a Gaussian likelihood function. Uniform uninformative priors were assumed for H_0 and t_0: $H_0 \sim \mathcal{U}(25, 125)$, $t_0 \sim \mathcal{U}(0.5, 5)$. For Ω_m, a Gaussian prior is adopted: $\Omega_m \sim \mathcal{G}(0.3, 0.02)$; this is required to keep degeneracies under control. Its value and uncertainty refer to the ones used in Jimenez et al. (2019), resulting from the combination of different measurements of $\Omega_{\rm m}$, all independent of the cosmic microwave background (CMB).

If the mass-downsizing scenario is valid, lower mass galaxies would have formed later than higher-mass ones. Since the median age-redshift relation is divided into a high-mass and a low-mass sample, to take this effect into account, we introduced a parameter Δt that measures the offset in formation time between the two populations. Differently from t_0, Δt is not considered a free parameter, but its value is assumed constant and is computed as the average age separation between these two subsamples. For binning A we find $\Delta{\rm t} \sim 0.8$ Gyr. To jointly fit all data, therefore, we considered this shift of the lower mass sample in our analysis.

Performing the fit, we obtain $H_0 = 67^{+14}_{-15}$ km s^{-1} Mpc^{-1} and $t_0 = 1.7^{+1.5}_{-0.9}$ Gyr. Values and errors are, respectively, medians and 1σ values of the posterior distribution. Results are shown in Figure 3.10, where grey curves are drawn from the posterior distribution of parameters between the 16$^{\rm th}$ and the 84$^{\rm th}$ percentiles.

Comparing these results with the ones in Riess et al. (2022) and Planck Collaboration et al. (2020), we can say that our errors are not conclusive enough to prefer one or the other, and our measurements agree both with the late- and the early-Universe estimations of H_0. We note here that the large error on H_0 is mostly due to the very low statistics of CCs available in this analysis. However, these results are still promising in view of upcoming large surveys, such as Euclid (Laureijs et al., 2011), where both the redshift coverage and the much lower statistical errors, granted by the much higher statistics, could significantly increase the precision of the cosmological parameters.

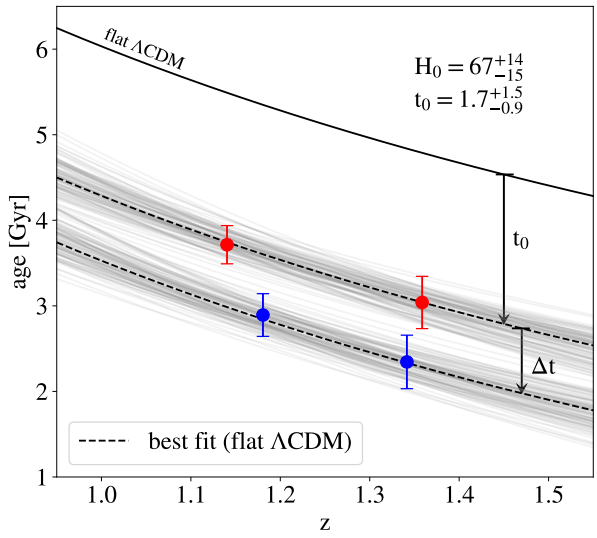

FIGURE 3.10: Fit to median age-redshift trend obtained with binning A. Red and blue dots are median values, respectively, for the high-mass ($\log(M_{\rm formed}/M_\odot) > 11.26$) and the low-mass ($\log(M_{\rm formed}/M_\odot) \leq 11.26$) sample. In grey, we show flat ΛCDM trends with (H_0, Ω_m, t_0) values randomly extracted from the posterior distribution, comprised between the 16$^{\rm th}$ and the 84$^{\rm th}$ percentiles. Dashed black lines represent the best fit.

3.1.4 Conclusions

In this work, we selected and analysed a sample of massive and passively evolving galaxies from data release 4 of the VANDELS spectroscopic survey (McLure et al., 2018), with the purpose of estimating the Hubble parameter $H(z)$ with the cosmic chronometers method. We adopted a full spectrum fitting technique to estimate the physical properties of the sample, to benefit from all the spectral and photometric information available in VANDELS, using the code `BAGPIPES` (Carnall et al., 2018), which was already adopted and optimised within the survey. Differently from the studies already carried out in VANDELS, in this work we adopted a modified version of the code introduced in Jiao et al. (2023), where a non-cosmological prior is assumed on the age of the galaxy population, which is free to vary between 0 and 20 Gyr at all redshifts. This means that the resulting ages are not constrained by a chosen cosmology, but depend only on the adopted stellar population synthesis models and on the component used in the fit to reproduce spectra and photometry.
Our main results are summarised as follows:

1. We selected a sample of 49 purely passive galaxies in the $1 < z < 1.5$ redshift range, adopting multiple and complementary selection criteria: a photometric criterion (UVJ), a cut on the [OII] emission line, a cut on the H/K ratio, a visual inspection, and also a redshift cut. The latter is needed because of an anomaly found in the D4000 trend, for which galaxies at $z < 1.07$ are discarded to avoid biases in the subsequent analysis. The selected galaxies show a red continuum, no emission lines linked to stellar activity, and no H/K inversion. They turn out to have high stellar masses and low sSFR, with median values of $\langle \log(M_\star/M_\odot) \rangle = 10.88 \pm 0.05$ and $\langle \log({\rm sSFR/yr^{-1}}) \rangle = -12.2 \pm 0.2$.

2. Studying the evolution of age-related spectral features, mainly D4000 and D_n4000, we observe a clear decreasing trend with redshift. Since these features are proven to correlate with the galaxy age, this gives initial, purely observational evidence that the population under analysis is ageing

with cosmic time. We also observe that, at fixed redshift, more massive galaxies show a higher D4000 with respect to the lower mass ones, supporting a mass-downsizing scenario.

3. Performing full spectrum fitting, we obtain age estimates below the age of the Universe in a standard flat ΛCDM model ($\Omega_m = 0.3$, $\Omega_\Lambda = 0.7$ and $H_0 = 70$ km s^{-1} Mpc^{-1}) for 95% of the sample, even if they could formally vary between 0 and 20 Gyr. This proves the robustness of our estimates, where the good quality of VANDELS data allows us to determine correct ages, even without imposing the standard cosmological prior on them. Ages also decrease with redshift, in agreement with this cosmological model, and, at fixed redshift, more massive galaxies result older than lower mass ones, confirming the mass-downsizing trend.
   The sample is characterised by high masses, sub-solar metallicities, low dust extinction, and a short period of star formation, with median values of mass, metallicity, dust reddening, and τ parameter equal to $\langle \log(M_{\rm formed}/M_\odot)\rangle = 11.21 \pm 0.05$, $\langle Z/Z_\odot\rangle = 0.44 \pm 0.01$, $\langle A_{\rm V,dust}\rangle = 0.43 \pm 0.02$ mag, and $\langle\tau\rangle = 0.28 \pm 0.02$ Gyr. Metallicity values are compatible with those obtained in Carnall et al. (2022) on a sample of VANDELS passive galaxies.

4. Comparing results obtained by fitting with a delayed SFH or a double-power-law SFH, we find that, despite the different functional forms, the two turn out to be identical if the involved parameters are constrained in a physically reasonable range. In particular, by setting a lower limit to the rising slope of the double-power-law SFH, $\beta > 10$, the median percentage difference in age and metallicity estimates is below 2%, for dust reddening and velocity dispersion is less than 1%, while for stellar mass is of 0.001 dex.

5. We further cleaned the 49 galaxies in the sample by removing bad fits and applying a mass cut ($\log(M_{\rm formed}/M_\odot) \leq 10.8$) to homogenise it, ending with a sample of 39 cosmic chronometers. We built a median age-redshift relation by dividing the sample into two mass bins and two redshift bins. By fitting this median age-redshift relation with a flat ΛCDM model, we obtain an estimate for the Hubble constant $H_0 = 67^{+14}_{-15}$km s^{-1} Mpc^{-1} and for the formation time of high-mass objects of $t_0 = 1.7^{+1.5}_{-0.9}$ Gyr. In doing this, we needed to set a Gaussian prior on $\Omega_{\rm m} = 0.30 \pm 0.02$ in order to keep degeneracies under control.

6. Finally, we obtain a new, cosmology-independent direct measurement of the Hubble parameter at $z \sim 1.26$ equal to $H(z) = 135 \pm 65$ km s^{-1} Mpc^{-1} by applying the cosmic chronometers method. Errors include both statistical and systematic uncertainties, with the first dominating the error budget. In the systematic component, we include the effect on the $H(z)$ estimate by using a more complex SFH and the effect of changing the binning while computing the median age-redshift relation.

In conclusion, this work provides additional evidence supporting the robustness of the CC method up to $z = 1.5$ while proving the effectiveness, even at this redshift, of adopting a full spectrum fitting approach to extract ages and physical parameters of the galaxy population.
At the same time, the positive results obtained in terms of $H(z)$ and H_0, despite the poor statistics, are very promising in view of upcoming large spectroscopic surveys such as *Euclid* (Laureijs et al., 2011), which will dramatically increase the available samples, and of the JWST, which is already opening the possibility to extend these analyses to much higher redshifts and earlier cosmic epochs. Forecasting a number of cosmic-chronometer candidates of two orders of magnitude greater than the ones in this work, we could expect to bring down the statistical error to 6% up to $z \sim 2$.

3.2 A new application: cosmic chronometers in galaxy clusters

In modern cosmology, the robustness of results relies not only on the precision of individual probes, but even more on their combination. Each observable comes with its own assumptions, systematic uncertainties, and range of applicability; combining them helps to break parameter degeneracies and provides independent tests of the concordance model. In recent years, the set of available cosmological probes has significantly expanded, complementing the "traditional" ones with a variety of emerging techniques (for a review, see Moresco et al., 2022).

In the previous section, we discussed in detail the CC method, its application to high-redshift galaxies via FSF, and evaluated their reliability for deriving cosmology-independent galaxy ages. In this section, we want to step toward the possibility of combining this approach with other independent probes. In particular, we will explore the potential synergy between CC and time-delay cosmography (TDC) based on strong gravitational lensing. The latter provides constraints on cosmological distances through the measurement of relative time delays between multiple images of background lensed sources (e.g. Suyu et al., 2017; Grillo et al., 2018), making it highly complementary to the CC approach. The joint use of these probes offers a powerful and independent way to test the cosmological model, overcoming the intrinsic limitations of each single observable.

A particularly promising strategy is to combine CC and TDC within the same observational fields, as first suggested in Bergamini et al. (2024). While CCs provide measurements of the expansion rate $H(z)$, TDC is sensitive to integrated distances, and their complementarity can significantly strengthen cosmological constraints. In this context, galaxy clusters play a dual role: on the one hand, central massive clusters act as lenses suitable for TDC; on the other, clusters at similar redshift host populations of massive, passive galaxies that can serve as CCs. One of the very first applications of the CC method was actually performed using galaxy clusters by Stern et al. (2010), owing to the fact that evolution in dense environments is more rapid and that these structures harbour the most massive and passive galaxy populations.

In this work, we pave the way for a future synergy by applying the CC method probing the member galaxies of MACS J1149.5+2223 (Lotz et al., 2017), the strong-lensing cluster hosting the multiply imaged SN "Refsdal" (Refsdal, 1964), and clusters located in close-by redshift bins. Thanks to the SN Refsdal, MACS J1149.5+2223 enabled the first measurement of H_0 via TDC (Grillo et al., 2018, 2020; Kelly et al., 2023), with a combined statistical and systematic relative uncertainty reaching approximately 6% (Grillo et al., 2024) in a general cosmological model. By deriving independent expansion rate constraints applying the CC approach to the cluster members, we prepare the ground for a future joint CC and TDC analysis. Such a combination holds the potential to mitigate systematic uncertainties and provide a more robust determination of the Hubble constant and the expansion history of the Universe.

3.2.1 Data

In this section, we describe the analysed sample, the specifics of the spectral and photometric observations, and the selection process adopted to identify our CC sample.

Spectra and photometry

We analysed spectra and photometry of the cluster members observed with the VLT/MUSE instrument in MACS J1149.5+2223 ($z = 0.54$, Grillo et al., 2016), SDSS J1029+2623 ($z = 0.59$), and SDSS J2222+2745

($z = 0.49$, Acebron et al., 2022a,b). From here on, we will refer to them as MACS 1149, SDSS 1029, and SDSS 2222, respectively.

For all three clusters, we complemented the spectroscopic information with archival Hubble Space Telescope (HST) multicolour imaging from the Advanced Camera for Surveys (ACS) and the Wide Field Camera 3 (WFC3). Specifically, photometry in F160W, F475W, F814W filters was available for SDSS 1029; in F110W, F160W, F606W and F814W for SDSS 2222; in F105W, F125W, F140W, F160W, F435W, F606W, and F814W for MACS 1149. For each cluster, we extracted a photometric catalogue using Morphofit (Tortorelli & Mercurio, 2023).

We weighted the MUSE cube with the members' surface brightness in the *HST* F814W band image, de-graded and re-binned to the PSF and pixel-scale of our MUSE observations, and extracted the spectra from large circular apertures with a 1.5″ radius, centred on the galaxy centre of light. The spectra resulting from the weighted average are representative of the central regions of the members, which are sampled with a higher weight due to their higher surface brightness. For instance, we found the velocity dispersion value obtained from the weighted spectra to be, on average, equivalent to those measured within the half-light radius of the galaxies Granata et al. (2025). We could thus probe the central regions of the cluster galaxies with high *S/N* and without the need for aperture corrections.
The observed spectra cover a large wavelength range, 4750 – 9350 Å, and offer high spectral resolution (R ∼ 3000) and signal-to-noise. Stellar velocity dispersions, $\sigma_\star$, were measured by fitting the observed spectra with pPXF (Cappellari, 2023). In addition, since for a few objects, the error spectrum derived from the variance data-cube appeared to be overestimated, we treated the residuals between the observed spectrum and the best-fit from pPXF as the actual noise in our spectrum. Accordingly, for each of these spectra, we adopted the standard deviation of the residuals as its 1σ uncertainty.

Lastly, in preparation for performing FSF jointly on spectra and photometry for each galaxy, we applied a preliminary rescaling to align the spectra with the observed photometry. Specifically, we integrated each spectrum over the F814W filter transmission curve (available for all galaxies) and derived a scaling factor as the ratio between the observed F814W photometric flux and this integrated value. This factor was then applied to rescale each spectrum. Figure 3.11 show the spectra and photometry of three selected galaxies, as an illustrative case.

Selection of cosmic chronometers

A critical step in applying the CC approach is the selection of a robust sample of very massive, passive galaxies with no signs of residual star formation. This ensures one can identify a homogeneous population whose star formation ceased well before the epoch of observation. As already discussed in Sections 1.2 and 3.1, different methods can be adopted for selecting passive galaxies, based on different observables.

Concerning the sample considered here, Bergamini et al. (2024) had already identified a sample of CC candidates for each cluster, based on their stellar velocity dispersion values ($\sigma_\star > 180$ km/s) and on their *S/N* (*S/N*>15). Analysing the stacked spectra for each cluster, they observed that these galaxies were indeed showing the characteristics of very passive objects, owing to the red continuum, the absence of emission lines, and the presence of prominent absorption features. Here, we followed this approach by adopting the same cut in *S/N*, but we adopted a less conservative cut in velocity dispersion, selecting objects with $\sigma_\star > 150$ km/s to preserve the statistics. With these criteria, we identified 7, 25, and 8 galaxies for SDSS 2222, MACS 1149, and SDSS 1019, respectively, totalling 40 CC candidates.

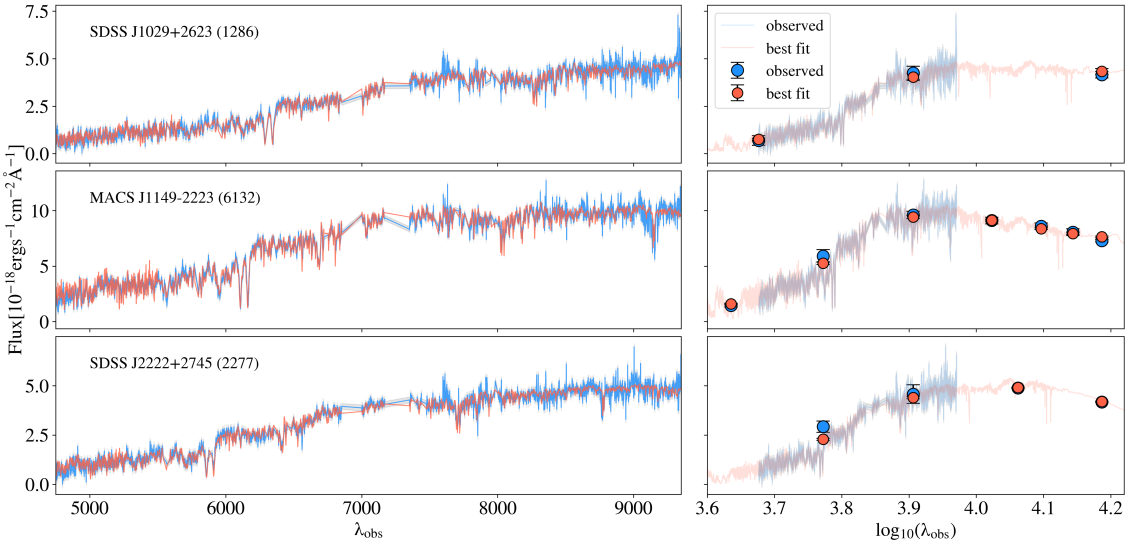

FIGURE 3.11: Fit of the spectrum (left) and photometry (right) of an example galaxy for each cluster. In blue, the observed spectrum and photometry are shown, in red the corresponding best fit. The shaded regions mark potential emission or telluric lines that are masked in the fit.

In addition, we decided to add a further step of selection based on the H/K ratio, already introduced in Section 3.1.1, an excellent diagnostic to identify a possible residual young component in the galaxy. The typical threshold used to select CCs is H/K <1.2–1.5 (Borghi et al., 2022a; Moresco et al., 2018). We evaluated H/K by measuring the involved pseudo-Lick indices via the public code `PyLick` (Borghi et al., 2022a). Here, we opted for a stringent limit on this feature, selecting only galaxies with H/K < 1.2, which excluded just two more objects, thereby demonstrating the very low contamination present in this sample.

In the end, our final CC sample, covering the redshift range 0.49 – 0.59, counted 38 massive and passive galaxies.

3.2.2 Method and analysis

To benefit from the high quality of the spectro-photometric data available for this sample, we measured the physical properties of each object via FSF, jointly fitting spectra and photometry.

Full spectrum fitting

We employed the `Bagpipes` code (Carnall et al., 2018, 2019) which allowed us to perform FSF with a Bayesian approach (see Sect 1.3.2 for a brief description of the code).

We adopted a DED SFH, that has a SFR described by Eq. 1.46, where τ correlates with the SFH length, and T_0 corresponds to the age of the Universe at which the star formation begins. This allows for a more realistic reproduction of the SFH with respect to a single burst, while keeping under control the possible degeneracies arising between the SFH characteristics and the physical parameters involved in the fit. For such passive populations, indeed, it has been shown how more complex parametric SFH converge to the DED shape when a good spectrophotometric coverage is available (Tomasetti et al., 2023, thoroughly discussed in Section 3.1).
For the dust component, we adopted the Calzetti et al. (2000) law, depending only on the reddening in

the V-band, A_V. We also tested the more complex Salim et al. (2018) curve, but given the similarity in the results obtained, we opted for the simpler model.
We also included the noise and calibration components, the first acting as a constant multiplicative factor of the error spectrum, the other represented by a second-order Chebyshev polynomial multiplied to the whole spectrum to better match the photometry.

In summary, the model was built on a set of ten parameters: age, mass ($\log(M_\star/M_\odot)$), metallicity ($Z/Z_\odot$), velocity dispersion ($\sigma_\star$), SFH width (τ), dust reddening (A_V), noise parameter (n), and the three coefficients of the calibration polynomial (C_i, i=0,1,2). The priors adopted for each parameter are presented in Tab. 3.5.

In line with the works presented in the previous sections, no cosmological prior was adopted on the age parameter, allowed to span the range 0 – 15 Gyr independently of redshift. This modification of the code, is fundamental to ensure that the final result is independent of any cosmological model.

Results

After the fit, a visual inspection of the results was performed for each galaxy, to ensure a good convergence of the parameters and an accurate reproduction of the spectra and photometry. Only one object was flagged as a bad fit, owing to the presence of double peaks in the posterior probability distribution. The quality of the fit is also demonstrated by the average reduced chi-square values that, considering both spectrum and photometry, equals $\tilde{\chi}^2 = 1.6$. Accounting for the noise factor introduced in the fit, this further reduces to $\tilde{\chi}^2 = 0.54$. In Figure 3.11, an example of a fit for each cluster is reported.

Figure 3.12 illustrates the redshift dependence of the main physical parameters: age, mass, metallicity, and dust extinction, colour-coded by velocity dispersion ($\sigma_\star$). The CC sample is characterized by high stellar masses, with a mean of $\log(M_\star/M_\odot) = 11.2 \pm 0.3$. As expected, stellar mass and velocity dispersion are positively correlated for the most massive systems, with all objects above $\log(M_\star/M_\odot) \gtrsim 11.2$ exhibiting consistently high $\sigma_\star$. At lower masses, while the majority of galaxies show lower velocity dispersions, the correlation is less tight, with objects spanning a broad range of $\sigma_\star$. The mass distribution is not uniform in redshift: higher-mass galaxies dominate the low-redshift end ($z \leq 0.55$), whereas lower-mass systems become more prevalent at higher redshifts. This must be taken into account in the cosmological analysis of the age–redshift relation to ensure homogeneity across the subsamples used to trace population ageing.

Parameter		Component	Prior type	Prior range
age [Gyr]		SSP	uniform	[0,15]
$Z/Z_\odot$		SSP	uniform	[0.01, 3]
τ [Gyr]		SFH	uniform	[0,0.8]
$\log(M_\star/M_\odot)$		general	uniform	[6, 15]
$\sigma_\star$ [km/s]		general	$\mathcal{G}$(val, err)	[0, 400]
A_V [mag]		dust	uniform	[0, 4]
n		noise	uniform	[1, 10]
C_i	i=0	calibration	$\mathcal{G}$(1,0.1)	[0.75, 1.25]
	i=1,2		$\mathcal{G}$(0,0.1)	[−0.25, 0.25]

TABLE 3.5: List of parameters, priors, and prior ranges. The $\mathcal{G}(x, y)$ stands for a Gaussian prior centred in x with dispersion y. In the case of $\sigma_\star$, the *val* and *err* refer to each galaxy's velocity dispersion and associated error, measured as described in Section 3.2.1.

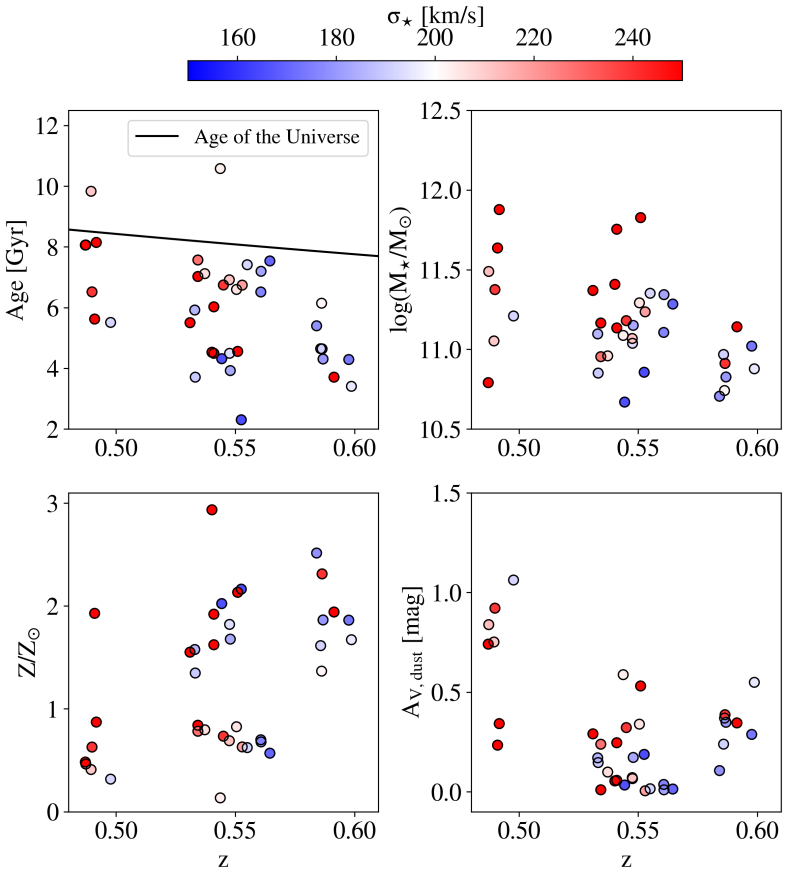

FIGURE 3.12: Trends in redshift for the main physical parameters, colour-coded by the measured velocity dispersion. As visible in the plot in the top-left, despite not imposing any cosmological prior on age, remarkably, almost all the galaxies present ages smaller than the age of the Universe, thanks to the high quality of the spectro-photometric data.

A qualitative inspection of the age–redshift trend already highlights two key results: a clear evidence of mass downsizing (Thomas et al., 2010; Citro et al., 2017), with high-$\sigma_\star$ galaxies appearing systematically older than their low-$\sigma_\star$ counterparts, and an evident overall ageing trend of the CC sample, with stellar ages decreasing steadily towards higher redshift in both the high- and low-$\sigma_\star$ populations. Even though no cosmological prior was adopted in the recovery of the galaxies' ages, 95% of the sample is compatible with the age of the Universe in a flat ΛCDM ($\Omega_m = 0.3$). All objects are also characterized by short bursts of formation, demonstrated by low values of the τ parameter, on average $\tau = 0.6 \pm 0.2$ Gyr. We find typically super-solar metallicities, with a mean value of $Z/Z_\odot = 1.3 \pm 0.7$, but the sample spans the whole range 0–3 $Z_\odot$. Dust reddening is predominantly low, with an average extinction in V-band $A_{V,\mathrm{dust}} = 0.3 \pm 0.3$ mag.

3.2.3 Application to cosmology

Once the age–redshift relation for the sample of chronometers is derived, the CC method allows one to directly measure the Hubble parameter $H(z)$ by evaluating the slope of this trend. In particular, the expansion rate can be expressed as in Eq. 1.11, where dz is the redshift difference between two adjacent bins and dt is the corresponding differential age. In practice, this requires a careful estimate of the CCs' differential ages, and a quantification of the associated statistical and systematic uncertainties.

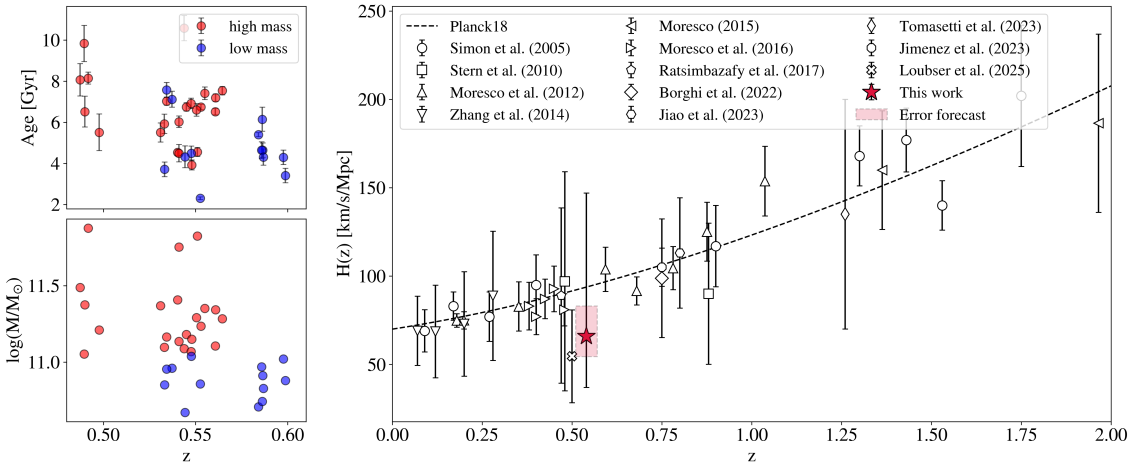

FIGURE 3.13: *Left:* Redshift trends in age (top) and mass (bottom) for the final CC sample, divided into high- (red) and low-mass (blue) subsamples. *Right:* Collection of all $H(z)$ measurements obtained to date, including the result of this work. The red shaded box shows the forecast on the precision achievable with a sample of 100 CCs (see Section 3.2.3 for details).

In this work, analysing three galaxy clusters, we fixed the redshift of each galaxy to that of its parent cluster, namely $z = 0.489$, 0.542, and 0.588 (bins 0, 1, and 2, respectively). To evaluate the ageing of galaxies with comparable stellar masses, we divided the sample into two mass bins. As a threshold, we adopted $\log(M_\star/M_\odot) = 11.05$, which minimises the difference between the mean stellar masses of analogue subsamples. As already noted in the previous section, the mass distribution is not homogeneous: considering bins 0, 1, and 2, the high-mass (HM, $\log(M_\star/M_\odot) > 11.05$) subsample contains 5, 17, and 1 CCs, while the low-mass (LM, $\log(M_\star/M_\odot) \leq 11.05$) subsample includes 1, 6, and 7 galaxies, respectively. Counting only one galaxy, both the last HM bin (HM2) and the first LM bin (LM0) had to be discarded. For this reason, we could evaluate the ageing of only two pairs of subsamples, HM0–HM1 and LM1–LM2, represented in the left panels of Figure 3.13, to be combined into a single $H(z)$ measurement.

To this end, we decided to adopt a bootstrap approach, for which a visual representation is provided in Figure 3.14. We generated N=1000 perturbed realisations of the galaxy ages by sampling each object from its best-fit Gaussian distribution. For each realization, we performed K=1000 bootstrap resamplings, computed the median ages in each mass–redshift bin, and derived age differences dt between adjacent bins. Converting those into $H(z)$ via Eq. 1.11 and averaging HM and LM results, we obtained N bootstrap realizations of $H(z)$. The final value of $H(z)$ and its statistical uncertainty are represented by the median, 16$^{\text{th}}$ and 84$^{\text{th}}$ percentiles of this distribution:

$$H(z = 0.542) = 63^{+82}_{-32}\,(\text{stat})\ \text{km s}^{-1}\ \text{Mpc}^{-1}.$$

Systematic effects

With only 35 CCs, the statistical uncertainties are inevitably large and strongly dominate over systematics. Nevertheless, we want to include an estimate of systematic effects, following what was found in Section 3.1.3, where the CC method was applied with the same FSF approach and a comparable sample size (39 CCs). In particular, the impact of the SFH was considered, and found to affect $H(z)$ at the ∼20% level. We stress, however, that this value likely overestimates this systematic contribution,

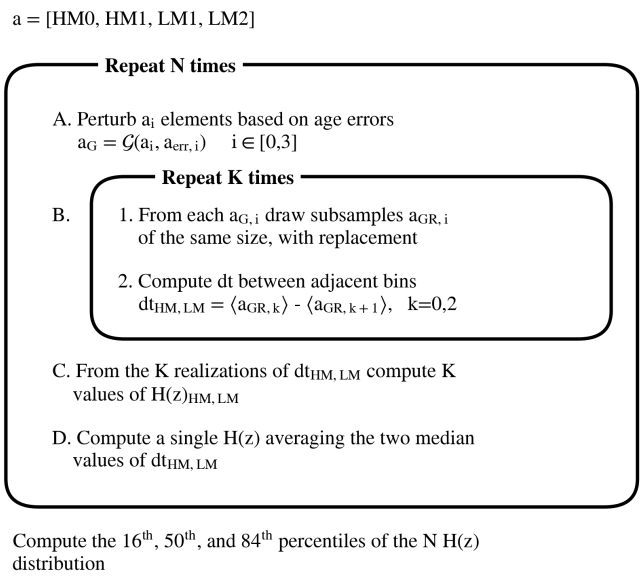

FIGURE 3.14: Visual diagram of the bootstrap algorithm. The CC sample was divided into three redshift bins (0, 1, 2) and into two mass bins, high-mass (HM) and low-mass (LM), but only bins HM0, HM1, LM1, and LM2 have enough statistics to be used.

as the effect of SFH fluctuations would be significantly reduced in larger samples. Considering this 20% as a conservative estimate of the systematics at play, and adding it in quadrature to the statistical component, we find:

$$H(z = 0.542) = 66^{+81}_{-29}\ (\text{stat}) \pm 13\ (\text{syst}) = \\ = 66^{+82}_{-32}\ (\text{stat+syst})\ \text{km s}^{-1}\ \text{Mpc}^{-1}.$$

This final result, comprising both statistical and systematic error, is reported in Figure 3.13, together with all other CC measurements obtained to date.

Future perspectives

As current and future facilities (e.g., Euclid, Laureijs et al. 2011; WST, Bacon et al. 2024) will deliver spectroscopic data for vast galaxy samples, it is timely to explore the potential gains from larger statistics. To this end, we estimated the precision achievable on $H(z)$ with samples of different sizes, or different distributions, drawing synthetic age samples based on a flat ΛCDM cosmology, and applied the same bootstrap procedure described at the beginning of this section to retrieve the $H(z)$ measurement. In order to compare the results to this work, we considered the same division into two HM and two LM bins, four in total.

We performed various types of simulations, varying the distribution in redshift, the redshift coverage, and the statistics of the CC sample, to forecast the kind of statistical uncertainty achievable in future works. These simulations followed the bootstrap procedure described in Figure 3.14, with one modification: at step A of the algorithm, we generated random samples drawn from a Gaussian distribution centered on the age predicted by a flat ΛCDM cosmology for an object formed at redshift $z_F = 3$ (for the HM sample) and $z_F = 1.5$ (for the LM sample), with a dispersion of 0.5 Gyr.

In this work, we analysed a sample of 35 CCs, unevenly distributed in four bins (with 5, 17, 6, and 7 galaxies respectively), covering a redshift interval $dz = 0.1$. In these simulations, we tested three variations to this baseline: A) homogenizing the sample in redshift, so that each bin has the same number (10) of CCs, B) enlarging the redshift interval from $dz = 0.1$ to $dz = 0.2$, and C) increasing the sample size to 100 CCs. In Figure 3.15, we show the results of some of the tests performed, including different combinations of the three modifications listed above.

Interestingly, extending the redshift interval alone yielded the largest gain, with an error on $H(z)$, compared to the one found in this work, reduced by ~30%. Increasing the sample size also had a significant, though smaller, effect, reducing the error by ~20%. Homogenizing the distribution across bins had little impact on its own, but in combination with a wider redshift interval, it reduced the error by nearly 50%. As expected, combining all three improvements provided the strongest result, lowering the uncertainty on $H(z)$ by approximately a factor of 4.

3.2.4 Conclusions

We applied the CC method to measure the expansion history of the Universe, analysing VLT/MUSE data for the most massive, passively evolving galaxies in three galaxy clusters: SDSS 2222 ($z = 0.49$), MACS 1149 ($z = 0.54$), and SDSS 1029 ($z = 0.59$). Since MACS 1149 also hosts the multiply imaged SN Refsdal, previously used to infer H_0 via TDC, our measurement of $H(z)$ from the ageing of its member galaxies enables a direct combination of complementary probes, thereby strengthening constraints on cosmological parameters.

We first selected the CC sample by combining a cut in stellar velocity dispersion, on their *S/N*, and on the H/K ratio, to isolate the most massive and passive cluster members, ending up with a sample of 38 CCs. We then performed FSF with the `Bagpipes` code, specifically modified to remove the cosmological prior on ages, so that they could vary up to 15 Gyr. Despite this, 95% of the sample results compatible with the age of the Universe in a flat ΛCDM model, and shows an ageing trend with redshift. Concerning the other physical parameters, the CC sample shows the characteristics of a passive population, with high stellar mass ($\log(M_\star/M_\odot) = 11.2 \pm 0.3$), low dust extinction ($A_{V,\mathrm{dust}} = 0.3 \pm 0.3$ mag), and short timescale of formation ($\tau = 0.6 \pm 0.2$ Gyr). The metallicity is on average super-solar, with a mean of $Z/Z_\odot = 1.3 \pm 0.7$.

From the age–redshift relation, separating the high- and the low-mass galaxies (with $\log(M_\star/M_\odot) = 11.05$ as a threshold to ensure maximum homogeneity among subsamples), we measured $H(z)$ applying the CC method through a bootstrap approach, obtaining: $H(z = 0.542) = 66^{+81}_{-29}$ (stat) ±13 (syst). The error budget is currently dominated by the statistical component, but simulations showed that with ~100 CCs and an extended redshift interval of $dz = 0.2$, the statistical uncertainty could be reduced by up to 75%.

Future and upcoming surveys (e.g., Euclid, WST, MOONS) will provide large samples of galaxies and galaxy clusters, offering unprecedented opportunities to apply the TDC method to strong lensing galaxy clusters, and the CC method to those cluster members with the required spectroscopic quality (or the necessary follow-up observations). Euclid (Laureijs et al., 2011), in particular, is expected to increase the census of strong gravitational lenses by orders of magnitude (Euclid Collaboration: Bergamini et al., 2025), opening the door to a systematic exploitation of this synergy.

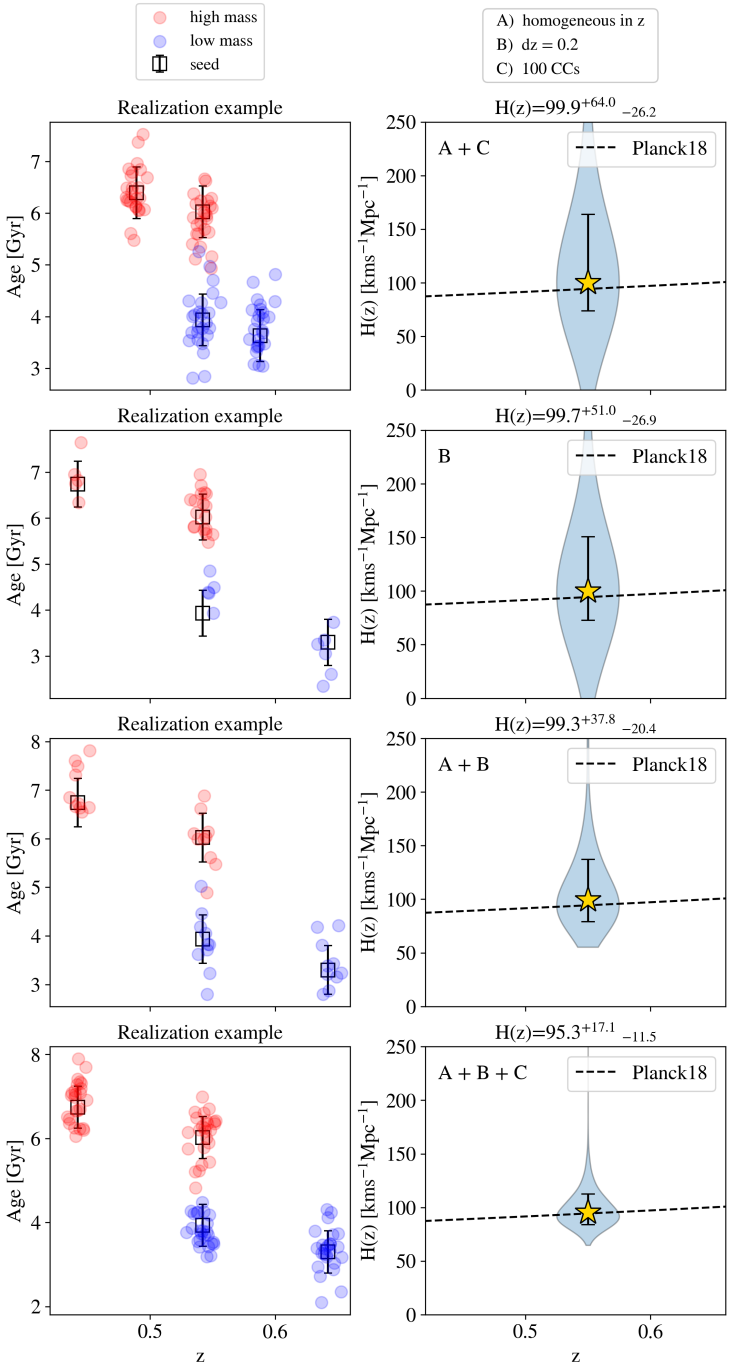

FIGURE 3.15: Results of the simulations. The left column shows, for each setting, an example of age–redshift both for the HM (red) and LM (blue) samples, randomly extracted from a Gaussian distribution centred on the *seed*, in black. The right column shows the resulting H(z) distribution and the derived measurement (yellow star, also reported in the title), in comparison with the assumed cosmology (Planck Collaboration et al., 2020).

3.3 Cosmic chronometers: an eye to the future

So far, we have seen two applications of the CC approach, both successfully mapping the ageing evolution with cosmic time of massive and passively evolving galaxies to provide new estimates of the Hubble parameter in two different redshift ranges. Still, both results are strongly limited in precision by the limited statistical size of the CC samples, due to intrinsic limitations of the corresponding surveys. To ensure the homogeneity of the sample, indeed, a detailed process of selection, combining both spectroscopic and photometric criteria, is required, dramatically reducing the sample size. On the other hand, the numerosity of the sample mapping the age-redshift is fundamental to reconstruct its slope (dz/dt).

To date, the CC technique has robustly mapped the expansion history of the Universe with uncertainties of the order of $\lesssim$10% up to $z \sim 0.6$ (Moresco et al., 2012, 2016), mainly thanks to the Sloan Digital Sky Survey (SDSS). Beyond this range, the lack of wide, homogeneous, high-quality spectroscopic datasets leads to a sparse and noisier $H(z)$ reconstruction, with typical uncertainties still above the 20% level.

This clearly highlights one of the current bottlenecks of the CC method: statistics. This is mainly due to the absence of a dedicated survey to identify and characterize a large sample of massive and passive galaxies at high redshifts. The next generation of spectroscopic facilities will play a transformative role. In particular, the Wide-field Spectroscopic Telescope (WST, Bacon et al., 2024) will provide a combination of statistics, resolution, and signal-to-noise required to unlock the full potential of cosmic chronometers.

Among the different classes of targets that WST will observe, the CC approach will specifically benefit from the abundant sample of luminous red galaxies (LRGs). According to the current survey design (see, e.g., Mainieri et al., 2024), these will be observed up to redshift $z \sim 1.2$ (peaking in the interval 0.8–1.2), with a spectral coverage spanning 370–970 nm and a resolution of $R \sim 4000$ in the low-resolution multi-object spectroscopy configuration (MOS-LR). This means that for the whole LRG sample, the rest-frame range 280–450 nm will be covered, providing crucial information: on ages, encoded in the D4000 feature and in the Balmer series; on metallicities, thanks to the numerous *Fe* and *Mg* lines; on the potential contamination from starforming outliers, covering the region of the H/K diagnostic and the [OII] emission line.

In terms of statistical power, WST will be truly transformative. Over its first five years of operations, WST is expected to collect the spectra of nearly 250 million galaxies. Even under a conservative assumption that only ~10 million of these will be classified as LRGs, the resulting sample would still represent an unprecedented breakthrough for cosmic chronometers. This can be appreciated from simple qualitative considerations.

Let us assume that the initial sample of 10^7 LRGs is divided into two subsamples: 20% covering the redshift range 0.3–0.8, and the remaining 80% populating the 0.8–1.2 interval. A stringent selection process to isolate a clean CC sample could reduce the effective number of galaxies to roughly one-fifth of the original size. This would yield approximately 4×10^5 CCs in the low-z bin, and about 1.6×10^6 CCs in the high-z bin. To date, a density of roughly 10^4 CCs per $\Delta z = 0.1$ has typically yielded a precision of about 10% on $H(z)$ (see, e.g., Moresco et al., 2016; Jimenez et al., 2023). With an order-of-magnitude increase in statistics, reaching $\sim 10^5$ CCs per redshift bin (as in Moresco et al., 2012), the expected uncertainty can be reduced to approximately 5%. Translating these assumptions into the forecast sample sizes derived above, we can expect to obtain approximately four independent $H(z)$ measurements in the 0.3–0.8 redshift range with a precision of $\sim$ 5%, and about eight $H(z)$ constraints in the 0.8–1.2

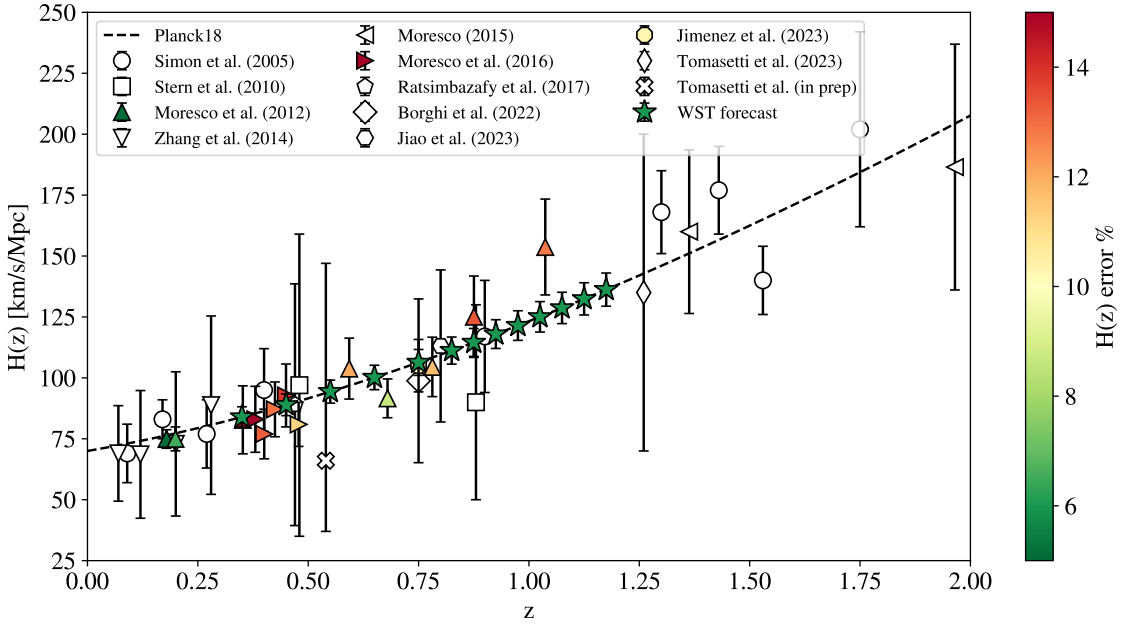

FIGURE 3.16: Forecast of the $H(z)$ measurements attainable with WST observations in the redshift range 0.3–1.2, compared to all CC measurements obtained to date. Only the measurements with an error budget smaller than 15% are coloured-coded by their precision. For reference, the dashed line corresponds to a flat ΛCDM cosmology with $\Omega_m = 0.3$.

interval with even higher precision, as each redshift bin would host $\sim 2 \times 10^5$ CCs. A visual representation of such improvement is provided in Figure 3.16, where all $H(z)$ measurements obtained to date are shown, but only the ones with an error budget lower than 15% are coloured, according to their precision. The green stars show the distribution of the WST forecast just mentioned, assuming that they are precisely reconstructing a flat ΛCDM with $\Omega_m = 0.3$.

Such constraints would be pivotal for exploring a redshift regime that could prove transformative in testing the curvature of the Universe and in probing possible deviations from a constant dark energy equation of state. Moreover, obtaining an accurate and densely sampled redshift mapping of the $H(z)$ trend would also enable a more precise determination of H_0, as demonstrated by Moresco (2023). Specifically, with future high-quality measurements and a refined treatment of systematics, it showed that the CC method could reach a precision of the order of 1% on H_0.

Conclusions

The main goal of this Thesis is to explore the potential of using *cosmic time as cosmological probe*, considering cosmic clocks and cosmic chronometers as independent and complementary tracers of the expansion history of the Universe. Together, these two approaches – absolute age estimates for cosmic clocks and differential age-dating for cosmic chronometers – probe different redshift regimes and rely on distinct observational diagnostics. Their combination strengthens the overall constraints by minimising systematics and enabling internal consistency checks across cosmic epochs, from the earliest phases of star formation to the present day. A key advantage of this framework lies in its independence from any global cosmological assumptions: the inferred quantities are entirely based on stellar and population synthesis modelling, offering a genuinely model-independent perspective on cosmic expansion.

This work is also motivated by the persistent tension between early- and late-Universe determinations of the Hubble constant, H_0, and by the need for cosmological model-independent tests of the standard ΛCDM framework. Current results also hint at the possibility of an evolving dark energy scenario, which could manifest as deviations of $H(z)$ from the standard prediction at different cosmic epochs. Mapping the expansion rate across a wide range of redshifts using independent tracers such as cosmic clocks and cosmic chronometers can therefore provide crucial insights, offering both an independent cross-check of H_0 measurements and potential evidence for new physics beyond the standard cosmological model.

In this chapter, we summarize the main results of this Thesis, emphasizing the principal strengths and current limitations of the adopted methodology. We also discuss future perspectives and potential directions for further research.

4.1 From stars to galaxies: constraining cosmic history with clocks and chronometers

Four classes of tracers were analysed – Milky Way stars, galactic and lensed globular clusters, and passively evolving galaxies – each probing different redshift regimes and levels of stellar population complexity. By applying different age-dating techniques tailored to each system, this study provides a coherent picture of the expansion history of the Universe across a wide range of cosmic epochs, while bridging complementary expertise from stellar evolution, cluster formation, and galaxy evolution.

As a general remark, it is worth emphasising that in all our constraints, ages have been derived without imposing any cosmological prior, unlike standard procedures typically adopted in stellar or

extragalactic studies. This approach ensures that the derived ages are fully independent of any assumed cosmological model. Our results demonstrate that the combination of high-quality data and a careful and robust analysis framework allows us to obtain reliable and sensitive age estimates even in the absence of such priors, achieving, in many cases, *truly cosmology-independent age determinations* for the first time in the literature. This step is also essential for our analysis, since ages are later used as cosmological probes; otherwise, adopting cosmology-dependent priors would have led to a circular argument.
In the following, we briefly summarize the key findings.

Milky Way stars In Section 2.1, we applied the *cosmic clocks* approach to a carefully selected sample of old Milky Way field stars. Stellar ages were determined via isochrone fitting exploiting high-quality *Gaia*-DR3 data, prior knowledge on the metal content extracted from RVS spectra, and photometry in various bands; in this procedure, no age prior has been applied, with maximum ages allowed up to 20 Gyr. After carefully selecting a sample of 160 stars with very precise and robust age measurements, we derived a lower limit to the age of the Universe of 13.8 ± 1.0 (stat) ± 1.3 (syst) Gyr. Considerations on potential $[\alpha/Fe]$ variations, alternative isochrone prescriptions, and the treatment of diffusion were included to assess a comprehensive systematic error budget. Assuming a flat ΛCDM model, this could be translated into an upper limit on the Hubble constant of:

$$H_0 \leq 68.3^{+5.4}_{-4.7}\ (\text{stat})\ ^{+7.2}_{-5.9}\ (\text{syst})\ \text{km s}^{-1}\ \text{Mpc}^{-1}.$$

Galactic GCs In Section 2.2, we extended the analysis to galactic GCs, which trace the earliest star formation episodes in the MW. Using integrated-light spectra from the WAGGS project, we performed full spectrum fitting and identified a tail of 24 old GCs with an average age of 13.4 ± 1.1 Gyr, consistent with literature values from isochrone fitting in 92% of the cases, and on average 0.67 Gyr older. Converted into H_0 (assuming a flat ΛCDM with $\Omega_m = 0.3 \pm 0.02$), we obtained:

$$H_0 = 70.5^{+7.7}_{-6.3}\ \text{km s}^{-1}\ \text{Mpc}^{-1}\ (\text{stat} + \text{syst}).$$

Lensed GC candidates at high redshift Section 2.3 explored a more novel application: age dating lensed GCs and compact stellar systems at redshifts $z > 1$, recently revealed by JWST observations in the Hubble Frontier Field. Performing SED fitting on accurate deconvolution photometry provided well-constrained formation ages for the five GC candidates in the *Sparkler* system ($z = 1.38$): 1.9±0.4 Gyr on average. This proved that multi-band photometric campaigns with JWST and Euclid can expand cosmic clock measurements to distant systems.

Cosmic Chronometers Massive and passively evolving galaxies, which formed rapidly at high redshift and have evolved quiescently since, can be used as *cosmic chronometers* (CCs), allowing direct measurements of $H(z)$ at intermediate redshifts. In Sections 3.1 and 3.2 we focused on these systems in two different datasets. In the first, we benefited from the richness of the spectrophotometric information in the VANDELS survey, selecting 39 CCs at $z \sim 1.25$, pushing modern full spectrum fitting techniques to the higher redshift. In the second, we exploited the high quality of VLT/MUSE data for 35 members of three galaxy clusters at redshift $z \sim 0.5$, assessing the potential of this method in the galaxy clusters' environment. In both cases, after reconstructing the ageing trend in redshift via full

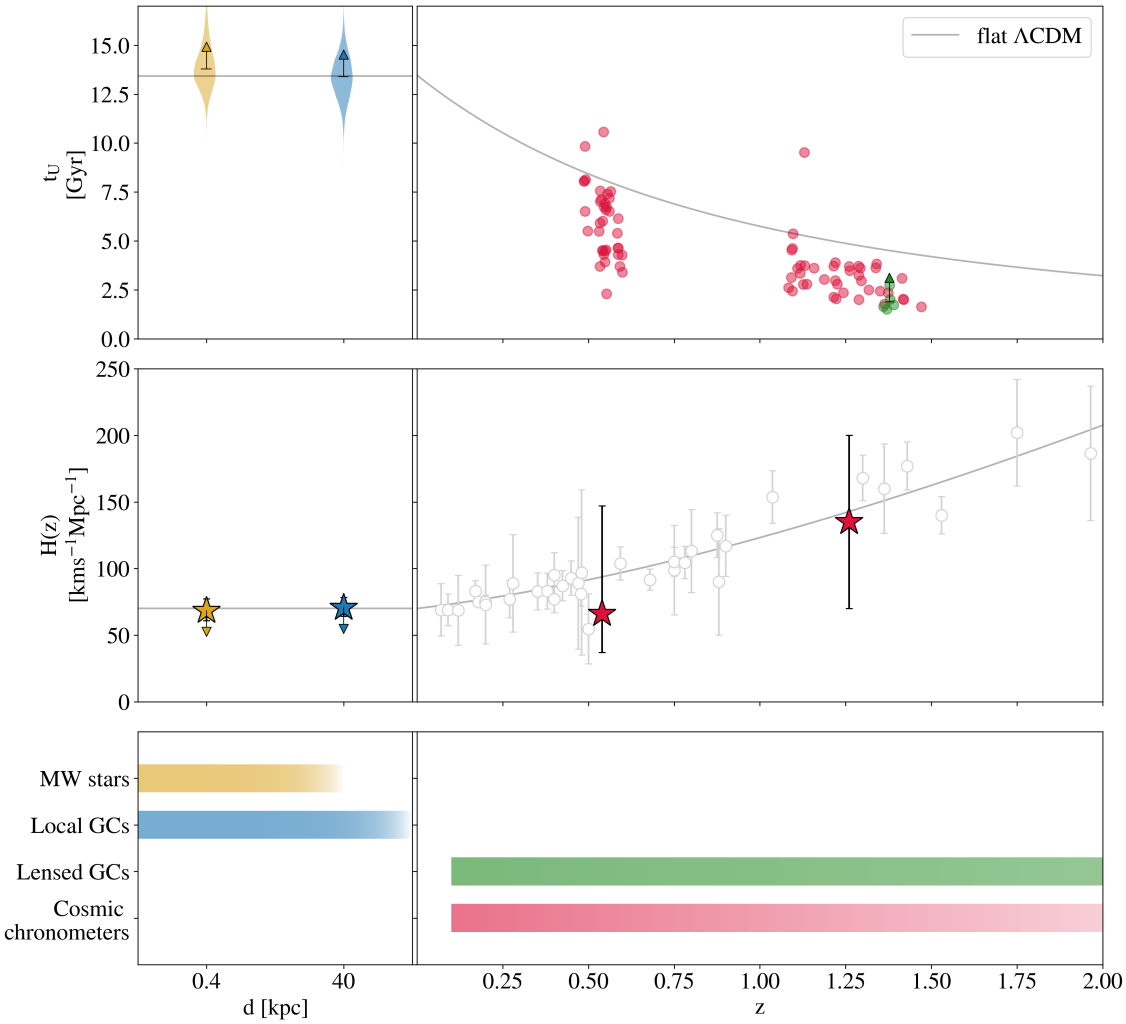

FIGURE 4.1: Summary of the main results obtained in this Thesis. *Top:* Constraints on the age of the Universe at different redshift coming from the MW oldest stars sample (gold, see Section 2.1), the local GCs sample (blue, see Section 2.2), the lensed GCs (green, Section 2.3), while red points refer to the age of the cosmic chronometers samples presented in Sections 3.1 and 3.2. *Center:* With corresponding colours, the constraints obtained in terms of $H(z)$ are shown for each probe, with all measurements obtained so far with the CC method in the background. The solid line shows the age of the Universe (top) and Hubble parameter (center) trends with redshift in a flat ΛCDM with $\Omega_m = 0.3$. The lower panel shows the typical ranges of applicability of the methods depending on the astrophysical object.

spectrum fitting for samples of around 40 galaxies, we obtained two new, independent values of $H(z)$:

$$H(z = 0.54) = 66^{+82}_{-32}\ \mathrm{km\,s^{-1}\,Mpc^{-1}}(\mathrm{stat} + \mathrm{syst}) \qquad (\mathrm{VLT/MUSE})$$
$$H(z = 1.26) = 135 \pm 65\ \mathrm{km\,s^{-1}\,Mpc^{-1}}(\mathrm{stat} + \mathrm{syst}) \qquad (\mathrm{VANDELS})$$

The main results obtained in this Thesis are summarised in Figure 4.1, which replicates Figure 1.12, this time populating the age–redshift and $H(z)$ relations with the new measurements obtained in all these works.

At high redshift, the constraints from cosmic chronometers we obtained are still affected by large statistical uncertainties, yet they show the potential of the method in constraining the expansion of the Universe up to $z \sim 2$. Moreover, the application of the cosmic clocks method to lensed GC progenitors represents the first cosmology–independent determination of the age of these high-z structures, providing a compelling proof-of-concept for extending time-based probes deep into the early Universe. Although precision remains limited, these results demonstrate the feasibility and strong potential of age dating at high-z.

In the local Universe, the constraints derived from the cosmic clocks approach are becoming increasingly competitive. The inferred values of H_0 lie between the two measurements currently defining the Hubble tension (Planck Collaboration et al., 2020; Riess et al., 2022), and remain statistically consistent with both. This further highlights the relevance of independent, astrophysically-grounded, direct constraints in the ongoing effort to clarify the present-day expansion rate.

4.2 Leveraging multiple tracers for robust cosmic age estimates

A major strength of this work lies in the combined use of distinct tracers, which allows the coverage of a broad redshift range while simultaneously providing cross-validation between independent age-dating methods. Despite their different physical basis, the consistency among results from Milky Way stars, globular clusters, and cosmic chronometers reinforces the robustness of the overall framework and provides a valuable consistency check across widely separated redshift regimes, thereby mitigating model-dependent systematics. Such a multi-tracer strategy is particularly powerful in the current era of precision cosmology, as it exploits complementary datasets and reduces dependence on any single modelling assumption.

Ultimately, this approach lays the groundwork for a robust implementation of cosmic time as a cosmological probe. This also opens the door to self-consistent combination with complementary observables, yielding more stringent and internally consistent constraints on $H(z)$ and H_0.

4.2.1 Some current limitations

The results presented in this manuscript rely on a combination of stellar and galactic age-dating techniques, each with its own strengths and limitations. To ensure that cosmological conclusions are robust against assumptions in stellar modelling, it is essential to carefully quantify and propagate all sources of uncertainty. In the following, we briefly review the main sources of uncertainty that affect our conclusions.

The cosmic clock approach is conceptually simple yet powerful: stellar ages, when properly calibrated, depend only on stellar structure and evolution, with minimal assumptions about the cosmological model. However, stellar age determinations remain affected by several systematic uncertainties. Isochrone-based ages depend on model ingredients such as opacities, convection efficiency, helium content, and the treatment of microscopic diffusion (e.g., VandenBerg et al., 2013; Choi et al., 2016; Hidalgo et al., 2018), which can translate into differences of the order of ~1 Gyr for the oldest stars. Uncertainties in metallicity and α-enhancement further propagate into the derived ages (Serenelli et al., 2013; Lebreton & Goupil, 2014). While Gaia has dramatically improved distance accuracy, residual systematics in the parallax zero point can still impact luminosity estimates and therefore age determinations (Riello et al., 2021). For globular clusters, as discussed in Section 2.2.7, additional complications arise from the presence of multiple stellar populations and internal abundance spreads

(Piotto et al., 2015; Bastian & Lardo, 2018; Gratton et al., 2019). While modern isochrones can model these effects (Dotter et al., 2017; VandenBerg et al., 2022), the precise age of a GC often depends on the adopted distance modulus and reddening correction. These remain key areas for refinement, particularly when aiming to significantly reduce uncertainty in the inferred ages.

The cosmic chronometer method, based on the differential age evolution of passively evolving galaxies, provides one of the few direct measurements of the Hubble parameter at intermediate redshift (Jimenez & Loeb, 2002; Moresco et al., 2012, 2016). Nevertheless, this technique is sensitive to several astrophysical assumptions. Age estimates for composite stellar populations depend on the adopted SPS models, which are subject to uncertainties in stellar libraries, isochrone calibration, the treatment of thermally pulsating AGB stars, and the inclusion of varying $[\alpha/Fe]$ abundance (Conroy et al., 2009; Conroy et al., 2010; Vazdekis et al., 2016; Moresco et al., 2020; Park et al., 2024). Furthermore, metallicity and age are partially degenerate in spectral fitting, which introduces additional covariance between the derived ages and inferred $H(z)$ values. These aspects still require a thorough assessment, which will become feasible once larger statistical samples allow us to disentangle stochastic fluctuations from true systematic uncertainties. In any case, a key strength of the CC approach is that any effect impacting absolute age estimates becomes significantly reduced when relying on differential age measurements, as required for the determination of $H(z)$.

4.2.2 Outlook and future directions

The picture emerging from cosmic clocks and chronometers confirms that the *time-based* reconstruction of cosmic history has now reached a level of maturity that fully justifies a greater observational effort and the development of dedicated surveys, to test the standard cosmological model with competitive precision. Future advancements in astrometry, spectroscopy, and stellar modelling are expected to further consolidate the role of these methods in cosmology, overcoming the current limitations listed above, and strengthening the link between local stellar physics and the large-scale evolution of the Universe.

The coming decade promises transformative progress in stellar and galactic chronometry, driven by synergistic developments in both observations and theory. Below, we briefly outline some of the most promising directions for future research.

1. **Asteroseismology as a cornerstone for future stellar age determinations –** Over the last decades, the CoRoT (Baglin et al., 2009) and Kepler (Borucki et al., 2008) space-missions have demonstrated the power of asteroseismology (the study of a star's internal structure through its intrinsic global oscillations) as a precise tool for testing stellar physics and accurately characterizing stellar properties, including ages. Upcoming and ongoing missions such as TESS (Ricker et al., 2015) and PLATO (Rauer et al., 2014) are expected to deliver seismic ages for thousands of subgiants and red giants across the Galaxy.

   The proposed HAYDN mission (Miglio et al., 2021a), an ESA M-class candidate, would be specifically dedicated to obtaining long photometric time series for large samples of coeval and initially chemically homogeneous stars in open and globular clusters. By transforming these stars into astrophysical laboratories, HAYDN would enable stringent tests of stellar physics and drive the development of next-generation stellar models. Such data are expected to provide absolute stellar ages with precisions better than 10%, offering robust constraints on the ages of the oldest stellar populations and, consequently, on the lower bound of the cosmic age.

2. **Advancements in stellar models –** In recent years, significant progress has been made in various aspects of stellar physics, including radiative opacities and the equation of state, leading to continuous improvements in both solar and stellar evolution models (Cassisi et al., 1998). These advancements have resulted in non-negligible revisions of quantitative predictions, such as the inferred ages of galactic globular clusters (Salaris et al., 1997). Despite these achievements, the predictive power of current stellar models remains limited by the simplified treatment of several internal processes that govern the transport of chemical elements throughout the stellar interior. In particular, uncertainties in the modelling of convection, atomic diffusion, rotation, thermohaline mixing, and gravity-wave-induced mixing still affect evolutionary timescales, surface temperatures, luminosities, internal structures, and surface abundances (Salaris, 2016; Hidalgo et al., 2018; Pietrinferni et al., 2021).

   The growing influx of high-precision, large-volume data from both ground-based and space-based facilities demands a corresponding increase in the physical realism of stellar models, incorporating (magneto-)hydrodynamic simulations and multi-dimensional approaches. On the other hand, observations play a crucial role in calibrating and validating these models: asteroseismology offers direct constraints on stellar interiors (e.g., Miglio et al., 2021b), while field stars with precise Gaia parallaxes and metallicities, as well as star clusters with accurate photometry and distance determinations, provide robust benchmarks. By coupling increasingly sophisticated models with high-quality observations, systematic uncertainties can be significantly reduced.

3. **The potential of nucleocosmochronology for stellar age determination –** As discussed in this Thesis, stellar ages are typically inferred either through empirical methods or model-dependent approaches, both of which rely on underlying assumptions and can be affected by observational biases (Soderblom, 2010). In contrast, the only semi-fundamental approach for determining stellar ages, where the relevant physics is largely well understood, is nucleocosmochronology. This method leverages the radioactive decay of long-lived actinides, specifically uranium (^{238}U, $t_{1/2} = 4.47$ Gyr) and thorium (^{232}Th, $t_{1/2} = 14.05$ Gyr), to infer stellar ages (Cowan et al., 1991; Shah et al., 2023). The only key assumption concerns the initial abundances of these elements, typically scaled from other *r*-process elements. Future high-resolution, high-multiplex spectrographs[1] will enable precise and independent age determinations of the oldest stellar populations in the Galaxy through measurements of the Th/U ratio in surveys of Galactic halo stars (Magrini et al., 2023). Furthermore, extending this technique to multiple members of a GC will allow for the calibration of complementary age-dating methods, such as isochrone fitting and asteroseismology, yielding significantly more precise ages than those obtainable from individual field stars.

4. **Globular clusters as cosmic clocks in the JWST era –** The advent of the JWST has opened a new observational window into the early Universe (see, e.g., Adamo et al., 2025). Its capability to detect compact stellar systems at high redshift allows for the direct photometric and spectroscopic study of bound stellar systems, such as proto-globular clusters (Mowla et al., 2022; Claeyssens et al., 2023; Adamo et al., 2024). Modelling their light provides insights into the earliest phases of star cluster formation and evolution. Current JWST multi-band imaging of galaxy clusters already reveals a wealth of GCs in the member galaxies, potentially yielding GC samples at cluster redshifts ($0.1 < z < 0.8$) and for lensed sources well beyond $z = 1$ that can eventually be followed

[1] Such as the High-Resolution Multi-Object Spectrograph (HRMOS) proposed for the Very Large Telescope (VLT) as part of the VLT2030 roadmap.

up spectroscopically. Future systematic multi-band photometric campaigns targeting GCs in and behind galaxy clusters, leveraging Euclid (Cuillandre et al., 2025) and JWST, will enable age determinations for large populations of GCs across a wide redshift range, establishing them as robust cosmic clocks. Finally, facilities like the Roman Space Telescope (Spergel et al., 2015) and the Extremely Large Telescope (Gilmozzi & Spyromilio, 2007), will play a key role in expanding high-redshift samples and refining age estimates across cosmic time.

5. **Prospects from upcoming large spectroscopic surveys –** Upcoming data releases from Gaia, combined with extensive ground-based spectroscopic surveys such as 4MOST (de Jong et al., 2019), WEAVE (Jin et al., 2024), MOONS (Cirasuolo et al., 2011, 2020), WST (Bacon et al., 2024), and DESI (DESI Collaboration et al., 2016), will significantly expand the samples of well-characterised stars and galaxies. Improved measurements of distances, metallicities, and kinematics will reduce systematic uncertainties in both stellar and galactic age determinations, allowing for more precise and reliable age estimates. The unprecedented statistical power, on the other hand, will allow very precise constraints both for the cosmic clocks and the cosmic chronometers approaches, making their results fully comparable in precision to those of the standard cosmological probes.

6. **Exploring new synergies** The combination of the cosmic clocks and chronometers approaches with other innovative cosmological probes (as the TDC example, presented in this work, or gravitational waves as standard sirens), independent from the standard ones, offers a fresh perspective on the H_0 tension through independent measurements (see, e.g. Moresco et al., 2022). In addition, it lays the foundation for a self-consistent and comprehensive mapping of the Universe's expansion history, in a synergy that could provide stringent tests of the standard cosmological model.

Bibliography

Abdalla E., et al., 2022, "Cosmology intertwined: A review of the particle physics, astrophysics, and cosmology associated with the cosmological tensions and anomalies" Journal of High Energy Astrophysics, 34, 49

Acebron A., et al., 2022a, "New strong lensing modelling of SDSS J2222+2745 enhanced with VLT/-MUSE spectroscopy" A&A, 668, A142 (arXiv:2208.13788)

Acebron A., et al., 2022b, "VLT/MUSE Observations of SDSS J1029+2623: Toward a High-precision Strong Lensing Model" ApJ, 926, 86 (arXiv:2111.05871)

Adamo A., Usher C., Pfeffer J., Claeyssens A., 2023, "The ages and metallicities of the globular clusters in the Sparkler" MNRAS, 525, L6 (arXiv:2306.11814)

Adamo A., et al., 2024, "Bound star clusters observed in a lensed galaxy 460 Myr after the Big Bang" Nature, 632, 513

Adamo A., et al., 2025, "The first billion years according to JWST" Nature Astronomy, 9, 1134

Amard L., Palacios A., Charbonnel C., Gallet F., Georgy C., Lagarde N., Siess L., 2019, "First grids of low-mass stellar models and isochrones with self-consistent treatment of rotation. From 0.2 to 1.5 $M_{\odot}$ at seven metallicities from PMS to TAMS" A&A, 631, A77 (arXiv:1905.08516)

Amati L., Guidorzi C., Frontera F., Della Valle M., Finelli F., Landi R., Montanari E., 2008, "Measuring the cosmological parameters with the Ep,i-Eiso correlation of gamma-ray bursts" MNRAS, 391, 577

Anders F., Chiappini C., Santiago B. X., Matijevič G., Queiroz A. B., Steinmetz M., Guiglion G., 2018, "Dissecting stellar chemical abundance space with t-SNE" A&A, 619, A125

Anders F., et al., 2022, "Photo-astrometric distances, extinctions, and astrophysical parameters for Gaia EDR3 stars brighter than G = 18.5" A&A, 658, A91 (arXiv:2111.01860)

Annibali F., et al., 2018, "LBT/MODS spectroscopy of globular clusters in the irregular galaxy NGC 4449" MNRAS, 476, 1942 (arXiv:1802.02338)

Arnouts S., et al., 2013, "Encoding of the infrared excess in the NUVrK color diagram for star-forming galaxies" A&A, 558, A67

Bacon R., et al., 2024, WST – Widefield Spectroscopic Telescope: Motivation, science drivers and top-level requirements for a new dedicated facility, doi:10.48550/arXiv.2405.12518, https://ui.adsabs.harvard.edu/abs/2024arXiv240512518B

Baglin A., Auvergne M., Barge P., Deleuil M., Michel E., CoRoT Exoplanet Science Team 2009. pp 71–81, doi:10.1017/S1743921308026252, https://ui.adsabs.harvard.edu/abs/2009IAUS..253...71B

Balogh M. L., Morris S. L., Yee H. K. C., Carlberg R. G., Ellingson E., 1999, "Differential Galaxy Evolution in Cluster and Field Galaxies at z˜0.3" ApJ, 527, 54 (arXiv:astro-ph/9906470)

Bastian N., Lardo C., 2015, "Globular cluster mass-loss in the context of multiple populations" MNRAS, 453, 357

Bastian N., Lardo C., 2018, "Multiple Stellar Populations in Globular Clusters" ARA&A, 56, 83 (arXiv:1712.01286)

Bastian N., Covey K. R., Meyer M. R., 2010, "A Universal Stellar Initial Mass Function? A Critical Look at Variations" ARA&A, 48, 339 (arXiv:1001.2965)

Baumgardt H., Sollima A., Hilker M., 2020, "Absolute V-band magnitudes and mass-to-light ratios of Galactic globular clusters" PASA, 37, e046 (arXiv:2009.09611)

Baumgardt H., Hénault-Brunet V., Dickson N., Sollima A., 2023, "Evidence for a bottom-light initial mass function in massive star clusters" MNRAS, 521, 3991 (arXiv:2303.01636)

Beccari G., Dalessandro E., Lanzoni B., Ferraro F. R., Bellazzini M., Sollima A., 2015, "Deep Multi-telescope Photometry of NGC 5466. II. The Radial Behavior of the Mass Function Slope" ApJ, 814, 144 (arXiv:1511.00829)

Bekki K., Jeřábková T., Kroupa P., 2017, "The origin of discrete multiple stellar populations in globular clusters" MNRAS, 471, 2242

Belli S., et al., 2017, "KMOS^{3D} Reveals Low-level Star Formation Activity in Massive Quiescent Galaxies at 0.7 < z < 2.7" ApJ, 841, L6 (arXiv:1703.07778)

Bensby T., Feltzing S., Oey M. S., 2014, "Exploring the Milky Way stellar disk. A detailed elemental abundance study of 714 F and G dwarf stars in the solar neighbourhood" A&A, 562, A71

Bergamini P., et al., 2024, "Augmenting the power of time-delay cosmography in lens galaxy clusters by probing their member galaxies. II. Cosmic chronometers" A&A, 682, L2 (arXiv:2401.04767)

Borbolato L., et al., 2025, "Early Co-formation of the Milky Way's Thin and Thick Disks at Redshift z > 2" arXiv e-prints, p. arXiv:2504.00135 (arXiv:2504.00135)

Borghi N., Moresco M., Cimatti A., Huchet A., Quai S., Pozzetti L., 2022a, "Toward a Better Understanding of Cosmic Chronometers: Stellar Population Properties of Passive Galaxies at Intermediate Redshift" ApJ, 927, 164 (arXiv:2106.14894)

Borghi N., Moresco M., Cimatti A., 2022b, "Toward a Better Understanding of Cosmic Chronometers: A New Measurement of H(z) at z 0.7" ApJ, 928, L4 (arXiv:2110.04304)

Borucki W., et al., 2008. pp 17–24, doi:10.1017/S174392130801630X, https://ui.adsabs.harvard.edu/abs/2008IAUS..249...17B

Boylan-Kolchin M., Weisz D. R., 2021, "Uncertain times: the redshift-time relation from cosmology and stars" MNRAS, 505, 2764 (arXiv:2103.15825)

Brammer G., Matharu J., 2021, gbrammer/grizli: Release 2021, Zenodo, doi:10.5281/zenodo.5012699

Bressan A., Marigo P., Girardi L., Salasnich B., Dal Cero C., Rubele S., Nanni A., 2012, "PARSEC: stellar tracks and isochrones with the PAdova and TRieste Stellar Evolution Code" MNRAS, 427, 127

Breuval L., et al., 2024, "Small Magellanic Cloud Cepheids Observed with the Hubble Space Telescope Provide a New Anchor for the SH0ES Distance Ladder" ApJ, 973, 30

Bromm V., Yoshida N., 2011, "The First Galaxies" ARA&A, 49, 373 (arXiv:1102.4638)

Brout D., et al., 2022, "The Pantheon+ Analysis: Cosmological Constraints" ApJ, 938, 110 (arXiv:2202.04077)

Brown T. M., Casertano S., Strader J., Riess A., VandenBerg D. A., Soderblom D. R., Kalirai J., Salinas R., 2018, "A High-precision Trigonometric Parallax to an Ancient Metal-poor Globular Cluster" ApJ, 856, L6 (arXiv:1803.02927)

Bruzual G., Charlot S., 2003, "Stellar population synthesis at the resolution of 2003" MNRAS, 344, 1000

Bruzual A. G., 1983, "Spectral evolution of galaxies. I. Early-type systems." ApJ, 273, 105

Buchner J., 2016, "A statistical test for Nested Sampling algorithms" Statistics and Computing, 26, 383

Buder S., et al., 2021, "The GALAH+ survey: Third data release" MNRAS, 506, 150 (arXiv:2011.02505)

Burstein D., Faber S. M., Gaskell C. M., Krumm N., 1984, "Old stellar populations. I. A spectroscopic comparison of galactic globular clusters, M 31 globular clusters, and elliptical galaxies." ApJ, 287, 586

Cabrera-Ziri I., Conroy C., 2022, "Deriving ages and horizontal branch properties of integrated stellar populations" MNRAS, 511, 341 (arXiv:2112.07562)

Cabrera-Ziri I., Lardo C., Mucciarelli A., 2019, "Constant light element abundances suggest that the extended P1 in NGC 2808 is not a consequence of CNO-cycle nucleosynthesis" MNRAS, 485, 4128

Calabrò A., et al., 2021, "The VANDELS survey: The relation between the UV continuum slope and stellar metallicity in star-forming galaxies at z ~ 3" A&A, 646, A39 (arXiv:2011.06615)

Calabrò A., et al., 2022, "Properties of the interstellar medium in star-forming galaxies at redshifts 2 ≤ z ≤ 5 from the VANDELS survey" A&A, 667, A117 (arXiv:2206.14918)

Calzetti D., Armus L., Bohlin R. C., Kinney A. L., Koornneef J., Storchi-Bergmann T., 2000, "The Dust Content and Opacity of Actively Star-forming Galaxies" ApJ, 533, 682 (arXiv:astro-ph/9911459)

Caminha G. B., Suyu S. H., Mercurio A., Brammer G., Bergamini P., Acebron A., Vanzella E., 2022, "First JWST observations of a gravitational lens. Mass model from new multiple images with near-infrared observations of SMACS J0723.3−7327" A&A, 666, L9 (arXiv:2207.07567)

Cappellari M., 2017, "Improving the full spectrum fitting method: accurate convolution with Gauss-Hermite functions" MNRAS, 466, 798 (arXiv:1607.08538)

Cappellari M., 2023, "Full spectrum fitting with photometry in PPXF: stellar population versus dynamical masses, non-parametric star formation history and metallicity for 3200 LEGA-C galaxies at redshift z ≈ 0.8" MNRAS, 526, 3273

Cardelli J. A., Clayton G. C., Mathis J. S., 1989, "The Relationship between Infrared, Optical, and Ultraviolet Extinction" ApJ, 345, 245

Cargile P. A., Conroy C., Johnson B. D., Ting Y.-S., Bonaca A., Dotter A., Speagle J. S., 2020, "MINESweeper: Spectrophotometric Modeling of Stars in the Gaia Era" ApJ, 900, 28

Carnall A. C., McLure R. J., Dunlop J. S., Davé R., 2018, "Inferring the star formation histories of massive quiescent galaxies with BAGPIPES: evidence for multiple quenching mechanisms" MNRAS, 480, 4379 (arXiv:1712.04452)

Carnall A. C., et al., 2019, "The VANDELS survey: the star-formation histories of massive quiescent galaxies at 1.0 < z < 1.3" MNRAS, 490, 417 (arXiv:1903.11082)

Carnall A. C., et al., 2022, "The Stellar Metallicities of Massive Quiescent Galaxies at 1.0 < z < 1.3 from KMOS + VANDELS" ApJ, 929, 131 (arXiv:2108.13430)

Carnall A. C., et al., 2023, "A massive quiescent galaxy at redshift 4.658" Nature, 619, 716

Carnall A. C., et al., 2024, "The JWST EXCELS survey: too much, too young, too fast? Ultra-massive quiescent galaxies at 3 < z < 5" MNRAS, 534, 325

Carniani S., et al., 2024, "Spectroscopic confirmation of two luminous galaxies at a redshift of 14" Nature, 633, 318 (arXiv:2405.18485)

Cassisi S., Salaris M., 2013, Old Stellar Populations: How to Study the Fossil Record of Galaxy Formation. https://ui.adsabs.harvard.edu/abs/2013osp..book.....C

Cassisi S., Castellani V., degl'Innocenti S., Weiss A., 1998, "An updated theoretical scenario for globular cluster stars" A&AS, 129, 267 (arXiv:astro-ph/9707180)

Cezario E., Coelho P. R. T., Alves-Brito A., Forbes D. A., Brodie J. P., 2013, "Full spectral fitting of Milky Way and M 31 globular clusters: ages and metallicities" A&A, 549, A60 (arXiv:1211.1216)

Chabrier G., 2003, "Galactic Stellar and Substellar Initial Mass Function" PASP, 115, 763 (arXiv:astro-ph/0304382)

Charlot S., Fall S. M., 2000, "A Simple Model for the Absorption of Starlight by Dust in Galaxies" ApJ, 539, 718 (arXiv:astro-ph/0003128)

Charlot S., Longhetti M., 2001, "Nebular emission from star-forming galaxies" MNRAS, 323, 887 (arXiv:astro-ph/0101097)

Chevallard J., Charlot S., 2016, "Modelling and interpreting spectral energy distributions of galaxies with BEAGLE" MNRAS, 462, 1415 (arXiv:1603.03037)

Chevallier M., Polarski D., 2001, "Accelerating Universes with Scaling Dark Matter" International Journal of Modern Physics D, 10, 213 (arXiv:gr-qc/0009008)

Chilingarian I., Prugniel P., Sil'chenko O., Koleva M., 2007, in Vazdekis A., Peletier R., eds, IAU Symposium Vol. 241, Stellar Populations as Building Blocks of Galaxies. pp 175–176 (arXiv:0709.3047), doi:10.1017/S1743921307007752, https://ui.adsabs.harvard.edu/abs/2007IAUS..241..175C

Choi J., Dotter A., Conroy C., Cantiello M., Paxton B., Johnson B. D., 2016, "Mesa Isochrones and Stellar Tracks (MIST). I. Solar-scaled Models" ApJ, 823, 102

Cid Fernandes R., Mateus A., Sodré L., Stasińska G., Gomes J. M., 2005, "Semi-empirical analysis of Sloan Digital Sky Survey galaxies - I. Spectral synthesis method" MNRAS, 358, 363 (arXiv:astro-ph/0412481)

Cimatti A., Moresco M., 2023, "Revisiting the Oldest Stars as Cosmological Probes: New Constraints on the Hubble Constant" ApJ, 953, 149 (arXiv:2302.07899)

Cimatti A., Daddi E., Renzini A., 2006, "Mass downsizing and "top-down" assembly of early-type galaxies" A&A, 453, L29

Cirasuolo M., Afonso J., Bender R., Bonifacio P., Evans C., Kaper L., Oliva E., Vanzi L., 2011, "MOONS: The Multi-Object Optical and Near-infrared Spectrograph" The Messenger, 145, 11

Cirasuolo M., et al., 2020, "MOONS: The New Multi-Object Spectrograph for the VLT" The Messenger, 180, 10

Citro A., Pozzetti L., Quai S., Moresco M., Vallini L., Cimatti A., 2017, "A methodology to select galaxies just after the quenching of star formation" MNRAS, 469, 3108 (arXiv:1704.05462)

Claeyssens A., Adamo A., Richard J., Mahler G., Messa M., Dessauges-Zavadsky M., 2023, "Star formation at the smallest scales: a JWST study of the clump populations in SMACS0723" MNRAS, 520, 2180 (arXiv:2208.10450)

Coelho P. R. T., 2014, "A new library of theoretical stellar spectra with scaled-solar and α-enhanced mixtures" MNRAS, 440, 1027 (arXiv:1404.3243)

Cole S., et al., 2005, "The 2dF Galaxy Redshift Survey: power-spectrum analysis of the final data set and cosmological implications" MNRAS, 362, 505 (arXiv:astro-ph/0501174)

Colucci J. E., Bernstein R. A., McWilliam A., 2017, "Globular Cluster Abundances from High-resolution, Integrated-light Spectroscopy. II. Expanding the Metallicity Range for Old Clusters and Updated Analysis Techniques" ApJ, 834, 105 (arXiv:1611.02734)

Conroy C., 2013, "Modeling the Panchromatic Spectral Energy Distributions of Galaxies" ARA&A, 51, 393 (arXiv:1301.7095)

Conroy C., Spergel D. N., 2011, "On the Formation of Multiple Stellar Populations in Globular Clusters" ApJ, 726, 36

Conroy C., van Dokkum P., 2012, "Counting Low-mass Stars in Integrated Light" ApJ, 747, 69 (arXiv:1109.0007)

Conroy C., Gunn J. E., White M., 2009, "The Propagation of Uncertainties in Stellar Population Synthesis Modeling. I. The Relevance of Uncertain Aspects of Stellar Evolution and the Initial Mass Function

to the Derived Physical Properties of Galaxies" ApJ, 699, 486

Conroy C., White M., Gunn J. E., 2010, "The Propagation of Uncertainties in Stellar Population Synthesis Modeling. II. The Challenge of Comparing Galaxy Evolution Models to Observations" ApJ, 708, 58 (arXiv:0904.0002)

Conroy C., Graves G. J., van Dokkum P. G., 2014, "Early-type Galaxy Archeology: Ages, Abundance Ratios, and Effective Temperatures from Full-spectrum Fitting" ApJ, 780, 33 (arXiv:1303.6629)

Cowan J. J., Thielemann F.-K., Truran J. W., 1991, "The R-process and nucleochronology" Physics Reports, 208, 267

Cowie L. L., Songaila A., Hu E. M., Cohen J. G., 1996, "New Insight on Galaxy Formation and Evolution From Keck Spectroscopy of the Hawaii Deep Fields" AJ, 112, 839

Cuillandre J. C., et al., 2025, "Euclid: Early Release Observations – Overview of the Perseus cluster and analysis of its luminosity and stellar mass functions" A&A, 697, A11 (arXiv:2405.13501)

Cullen F., et al., 2019, "The VANDELS survey: the stellar metallicities of star-forming galaxies at 2.5 < z < 5.0" MNRAS, 487, 2038 (arXiv:1903.11081)

Cullen F., et al., 2020, "The VANDELS survey: a strong correlation between Ly α equivalent width and stellar metallicity at $3 \leq z \leq 5$" MNRAS, 495, 1501 (arXiv:2001.11063)

Curtis-Lake E., et al., 2023, "Spectroscopic confirmation of four metal-poor galaxies at z = 10.3-13.2" Nature Astronomy, 7, 622 (arXiv:2212.04568)

DESI Collaboration et al., 2016, The DESI Experiment Part I: Science,Targeting, and Survey Design, doi:10.48550/arXiv.1611.00036, https://ui.adsabs.harvard.edu/abs/2016arXiv161100036D

D'Ercole A., Vesperini E., D'Antona F., McMillan S. L. W., Recchi S., 2008, "Formation and dynamical evolution of multiple stellar generations in globular clusters" MNRAS, 391, 825

Dawson K., Palanque-Delabrouille N., 2025, "DESI2024: Dark Energy Spectroscopic Instrument (DESI) survey, presentation of Year 1 results" J. Cosmology Astropart. Phys., 2025, 123

Deepak S., Howk J. C., Lehner N., Péroux C., 2025, "A Global Census of Metals in the Universe" ApJ, 987, 199

Denissenkov P. A., Hartwick F. D. A., 2014, "Supermassive stars as a source of abundance anomalies of proton-capture elements in globular clusters" MNRAS, 437, L21

Di Valentino E., et al., 2021a, "In the realm of the Hubble tension-a review of solutions" Classical and Quantum Gravity, 38, 153001

Di Valentino E., et al., 2021b, "Cosmology Intertwined III: fσ8 and S8" Astroparticle Physics, 131, 102604

Di Valentino E., et al., 2021c, "Cosmology Intertwined IV: The age of the universe and its curvature" Astroparticle Physics, 131, 102607 (arXiv:2008.11286)

Di Valentino E., et al., 2025, "The CosmoVerse White Paper: Addressing observational tensions in cosmology with systematics and fundamental physics" Physics of the Dark Universe, 49, 101965

Dotter A., Chaboyer B., Jevremović D., Kostov V., Baron E., Ferguson J. W., 2008, "The Dartmouth Stellar Evolution Database" ApJS, 178, 89

Dotter A., Conroy C., Cargile P., Asplund M., 2017, "The Influence of Atomic Diffusion on Stellar Ages and Chemical Tagging" ApJ, 840, 99 (arXiv:1704.03465)

Draine B. T., 2003, "Interstellar Dust Grains" ARA&A, 41, 241

Dunlop J., Peacock J., Spinrad H., Dey A., Jimenez R., Stern D., Windhorst R., 1996, "A 3.5-Gyr-old galaxy at redshift 1.55" Nature, 381, 581

Dux F., et al., 2025, "J1721+8842: The first Einstein zigzag lens" A&A, 694, A300 (arXiv:2411.04177)

Einstein A., 1915, "Zur allgemeinen Relativitätstheorie" Sitzungsberichte der Königlich Preussischen Akademie der Wissenschaften, pp 778–786

Einstein A., 1916, "The Foundation of the General Theory of Relativity" Annalen Phys., 49, 769

Einstein A., 1917, "Kosmologische Betrachtungen zur allgemeinen Relativitätstheorie" Sitzungsberichte der Königlich Preussischen Akademie der Wissenschaften, pp 142–152

Eisenstein D. J., et al., 2005, "Detection of the Baryon Acoustic Peak in the Large-Scale Correlation Function of SDSS Luminous Red Galaxies" ApJ, 633, 560 (arXiv:astro-ph/0501171)

Estrada-Carpenter V., et al., 2019, "CLEAR. I. Ages and Metallicities of Quiescent Galaxies at 1.0 < z < 1.8 Derived from Deep Hubble Space Telescope Grism Data" ApJ, 870, 133 (arXiv:1810.02824)

Euclid Collaboration: Bergamini P., et al., 2025, Euclid Quick Data Release (Q1). The first catalogue of strong-lensing galaxy clusters, doi:10.48550/arXiv.2503.15330, https://ui.adsabs.harvard.edu/abs/2025arXiv250315330E

Faber S. M., Friel E. D., Burstein D., Gaskell C. M., 1985, "Old stellar populations. II. an analysis of K-giant spectra." ApJS, 57, 711

Falcón-Barroso J., Sánchez-Blázquez P., Vazdekis A., Ricciardelli E., Cardiel N., Cenarro A. J., Gorgas J., Peletier R. F., 2011, "An updated MILES stellar library and stellar population models" A&A, 532, A95 (arXiv:1107.2303)

Ferland G. J., et al., 2017, "The 2017 Release Cloudy" Rev. Mexicana Astron. Astrofis., 53, 385 (arXiv:1705.10877)

Forbes D. A., Romanowsky A. J., 2023, "Reconstructing the genesis of a globular cluster system at a look-back time of 9.1 Gyr with the JWST" MNRAS, 520, L58 (arXiv:2212.05078)

Foreman-Mackey D., Hogg D. W., Lang D., Goodman J., 2013, "emcee: The MCMC Hammer" PASP, 125, 306 (arXiv:1202.3665)

Franzetti P., et al., 2007, "The VIMOS-VLT deep survey. Color bimodality and the mix of galaxy populations up to z ~2" A&A, 465, 711 (arXiv:astro-ph/0607075)

Friedmann A., 1922, "Über die Krümmung des Raumes" Zeitschrift fur Physik, 10, 377

Fuhrmann K., Chini R., 2021, "On ancient solar-type stars - II" MNRAS, 501, 4903

Gaia Collaboration et al., 2016, "The Gaia mission" A&A, 595, A1

Gaia Collaboration et al., 2023, "Gaia Data Release 3. Summary of the content and survey properties" A&A, 674, A1

Galli D., Palla F., 2013, "The Dawn of Chemistry" ARA&A, 51, 163 (arXiv:1211.3319)

Garilli B., et al., 2021, "The VANDELS ESO public spectroscopic survey. Final data release of 2087 spectra and spectroscopic measurements" A&A, 647, A150 (arXiv:2101.07645)

Gavazzi G., Bonfanti C., Sanvito G., Boselli A., Scodeggio M., 2002, "Spectrophotometry of Galaxies in the Virgo Cluster. I. The Star Formation History" ApJ, 576, 135

Giavalisco M., et al., 2004, "The Great Observatories Origins Deep Survey: Initial Results from Optical and Near-Infrared Imaging" ApJ, 600, L93 (arXiv:astro-ph/0309105)

Gibson B. K., Madgwick D. S., Jones L. A., Da Costa G. S., Norris J. E., 1999, "The Spectroscopic Age of 47 Tucanae" AJ, 118, 1268 (arXiv:astro-ph/9906095)

Gieles M., et al., 2018, "Concurrent formation of supermassive stars and globular clusters: implications for early self-enrichment" MNRAS, 478, 2461

Gilmozzi R., Spyromilio J., 2007, "The European Extremely Large Telescope (E-ELT)" The Messenger, 127, 11

Goncalves G., Coelho P., Schiavon R., Usher C., 2023, "VizieR Online Data Catalog: Ages and abundances from spectral fitting (Goncalves+, 2020)" VizieR Online Data Catalog, p. J/MNRAS/499/2327

Gonçalves G., Coelho P., Schiavon R., Usher C., 2020, "How well can we determine ages and chemical abundances from spectral fitting of integrated light spectra?" MNRAS, 499, 2327

(arXiv:2010.02940)

Granata G., et al., 2025, "Cosmology with supernova Encore in the strong lensing cluster MACS J0138-2155: Spectroscopy with MUSE" A&A, 697, A94 (arXiv:2412.13250)

Gratton R., Bragaglia A., Carretta E., D'Orazi V., Lucatello S., Sollima A., 2019, "What is a globular cluster? An observational perspective" A&A Rev., 27, 8 (arXiv:1911.02835)

Gray D. F., 2008, The Observation and Analysis of Stellar Photospheres. https://ui.adsabs.harvard.edu/abs/2008oasp.book.....G

Grillo C., et al., 2016, "The Story of Supernova "Refsdal" Told by Muse" ApJ, 822, 78 (arXiv:1511.04093)

Grillo C., et al., 2018, "Measuring the Value of the Hubble Constant "à la Refsdal"" ApJ, 860, 94

Grillo C., Rosati P., Suyu S. H., Caminha G. B., Mercurio A., Halkola A., 2020, "On the Accuracy of Time-delay Cosmography in the Frontier Fields Cluster MACS J1149.5+2223 with Supernova Refsdal" ApJ, 898, 87

Grillo C., Pagano L., Rosati P., Suyu S. H., 2024, "Cosmography with supernova Refsdal through time-delay cluster lensing: Independent measurements of the Hubble constant and geometry of the Universe" A&A, 684, L23 (arXiv:2401.10980)

Grogin N. A., et al., 2011, "CANDELS: The Cosmic Assembly Near-infrared Deep Extragalactic Legacy Survey" ApJS, 197, 35 (arXiv:1105.3753)

Guaita L., et al., 2020, "The VANDELS survey: Discovery of massive overdensities of galaxies at z > 2. Location of Lyα-emitting galaxies with respect to environment" A&A, 640, A107 (arXiv:2007.12314)

Guiglion G., et al., 2020, "The RAdial Velocity Experiment (RAVE): Parameterisation of RAVE spectra based on convolutional neural networks" A&A, 644, A168

Guiglion G., et al., 2024, "Beyond Gaia DR3: Tracing the [\ensuremath\alpha/M] - [M/H] bimodality from the inner to the outer Milky Way disc with Gaia-RVS and convolutional neural networks" A&A, 682, A9

Guy J., Astier P., Nobili S., Regnault N., Pain R., 2005, "SALT: a spectral adaptive light curve template for type Ia supernovae" A&A, 443, 781

Hamadouche M. L., et al., 2022, "A combined VANDELS and LEGA-C study: the evolution of quiescent galaxy size, stellar mass, and age from z = 0.6 to z = 1.3" MNRAS, 512, 1262 (arXiv:2201.10576)

Harris W. E., 1996, "A Catalog of Parameters for Globular Clusters in the Milky Way" AJ, 112, 1487

Harris W. E., 2010, "A New Catalog of Globular Clusters in the Milky Way" arXiv e-prints, p. arXiv:1012.3224 (arXiv:1012.3224)

Hénault-Brunet V., Gieles M., Sollima A., Watkins L. L., Zocchi A., Claydon I., Pancino E., Baumgardt H., 2019, "Mass modelling globular clusters in the Gaiaera: a method comparison using mock data from an N-body simulation of M 4" MNRAS, 483, 1400 (arXiv:1810.05167)

Hidalgo S. L., et al., 2018, "The Updated BaSTI Stellar Evolution Models and Isochrones. I. Solar-scaled Calculations" ApJ, 856, 125

Hoag A., et al., 2019, "Constraining Lyman-alpha spatial offsets at 3 < z < 5.5 from VANDELS slit spectroscopy" MNRAS, 488, 706 (arXiv:1905.09467)

Hubble E., 1929, "A Relation between Distance and Radial Velocity among Extra-Galactic Nebulae" Proceedings of the National Academy of Science, 15, 168

Husser T. O., Wende-von Berg S., Dreizler S., Homeier D., Reiners A., Barman T., Hauschildt P. H., 2013, "A new extensive library of PHOENIX stellar atmospheres and synthetic spectra" A&A, 553, A6 (arXiv:1303.5632)

Huterer D., Shafer D. L., 2018, "Dark energy two decades after: observables, probes, consistency tests" Reports on Progress in Physics, 81, 016901 (arXiv:1709.01091)

Huyan J., Kulkarni V. P., Poudel S., Tejos N., Peroux C., Lopez S., 2025, "The Diversity of Metal-Enrichment and Abundance Patterns at High Redshift: A Magellan Survey of Gas-rich Galaxies Traced by Damped Lyman-alpha Absorbers at z~5" arXiv e-prints, p. arXiv:2508.02940 (arXiv:2508.02940)

Iben Jr. I., 1967, "Stellar Evolution Within and off the Main Sequence" ARA&A, 5, 571

Ilbert O., et al., 2010, "Galaxy Stellar Mass Assembly Between 0.2 < z < 2 from the S-COSMOS Survey" ApJ, 709, 644 (arXiv:0903.0102)

Ilbert O., et al., 2013, "Mass assembly in quiescent and star-forming galaxies since z = 4 from UltraVISTA" A&A, 556, A55 (arXiv:1301.3157)

Iyer K., Gawiser E., 2017, "Reconstruction of Galaxy Star Formation Histories through SED Fitting:The Dense Basis Approach" ApJ, 838, 127 (arXiv:1702.04371)

Jiao K., Borghi N., Moresco M., Zhang T.-J., 2023, "New Observational H(z) Data from Full-spectrum Fitting of Cosmic Chronometers in the LEGA-C Survey" ApJS, 265, 48 (arXiv:2205.05701)

Jimenez R., Loeb A., 2002, "Constraining Cosmological Parameters Based on Relative Galaxy Ages" ApJ, 573, 37 (arXiv:astro-ph/0106145)

Jimenez R., MacDonald J., Dunlop J. S., Padoan P., Peacock J. A., 2004, "Synthetic stellar populations: single stellar populations, stellar interior models and primordial protogalaxies" MNRAS, 349, 240 (arXiv:astro-ph/0402271)

Jimenez R., Cimatti A., Verde L., Moresco M., Wandelt B., 2019, "The local and distant Universe: stellar ages and H0" J. Cosmology Astropart. Phys., 2019, 043

Jimenez R., Moresco M., Verde L., Wandelt B. D., 2023, "Cosmic chronometers with photometry: a new path to H(z)" J. Cosmology Astropart. Phys., 2023, 047 (arXiv:2306.11425)

Jin S., et al., 2024, "The wide-field, multiplexed, spectroscopic facility WEAVE: Survey design, overview, and simulated implementation" MNRAS, 530, 2688

Johnson B. D., Leja J., Conroy C., Speagle J. S., 2021, "Stellar Population Inference with Prospector" ApJS, 254, 22 (arXiv:2012.01426)

Joyce M., Johnson C. I., Marchetti T., Rich R. M., Simion I., Bourke J., 2023, "The Ages of Galactic Bulge Stars with Realistic Uncertainties" ApJ, 946, 28 (arXiv:2205.07964)

Kelly P. L., et al., 2023, "The Magnificent Five Images of Supernova Refsdal: Time Delay and Magnification Measurements" ApJ, 948, 93

Koekemoer A. M., et al., 2011, "CANDELS: The Cosmic Assembly Near-infrared Deep Extragalactic Legacy Survey—The Hubble Space Telescope Observations, Imaging Data Products, and Mosaics" ApJS, 197, 36 (arXiv:1105.3754)

Koleva M., Prugniel P., Ocvirk P., Le Borgne D., Soubiran C., 2008, "Spectroscopic ages and metallicities of stellar populations: validation of full spectrum fitting" MNRAS, 385, 1998 (arXiv:0801.0871)

Koleva M., Prugniel P., Bouchard A., Wu Y., 2009, "ULySS: a full spectrum fitting package" A&A, 501, 1269 (arXiv:0903.2979)

Kordopatis G., Recio-Blanco A., de Laverny P., Bijaoui A., Hill V., Gilmore G., Wyse R. F. G., Ordenovic C., 2011, "Automatic stellar spectra parameterisation in the IR Ca ii triplet region" A&A, 535, A106

Kordopatis G., et al., 2013, "The Radial Velocity Experiment (RAVE): Fourth Data Release" AJ, 146, 134

Korn A. J., Grundahl F., Richard O., Mashonkina L., Barklem P. S., Collet R., Gustafsson B., Piskunov N., 2007, "Atomic Diffusion and Mixing in Old Stars. I. Very Large Telescope FLAMES-UVES Observations of Stars in NGC 6397" ApJ, 671, 402 (arXiv:0709.0639)

Kriek M., et al., 2019, "Stellar Metallicities and Elemental Abundance Ratios of z ~ 1.4 Massive Quiescent Galaxies" ApJ, 880, L31 (arXiv:1907.04327)

Kroupa P., 2001, "On the variation of the initial mass function" MNRAS, 322, 231 (arXiv:astro-ph/0009005)

Kroupa P., Boily C. M., 2002, "On the mass function of star clusters" MNRAS, 336, 1188 (arXiv:astro-ph/0207514)

Kruijssen J. M. D., 2015, "Globular clusters as the relics of regular star formation in 'normal' high-redshift galaxies" MNRAS, 454, 1658

Laureijs R., et al., 2011, "Euclid Definition Study Report" doi:10.48550/ARXIV.1110.3193 (arXiv:1110.3193)

Le Borgne J. F., et al., 2003, "STELIB: A library of stellar spectra at R ~ 2000" A&A, 402, 433

Lebreton Y., Goupil M. J., 2014, "Asteroseismology for "à la carte" stellar age-dating and weighing. Age and mass of the CoRoT exoplanet host HD 52265" A&A, 569, A21

Lebreton Y., Goupil M. J., Montalbán J., 2014. eprint: arXiv:1410.5336, pp 99–176, doi:10.1051/eas/1465004, https://ui.adsabs.harvard.edu/abs/2014EAS....65...99L

Lee Y.-W., 1989, PhD thesis, Yale University, Connecticut, https://ui.adsabs.harvard.edu/abs/1989PhDT.....7L

Lee H.-c., Worthey G., 2005, "α-Enhanced Integrated Lick/IDS Spectral Indices and Milky Way and M31 Globular Clusters and Early-Type Galaxies" ApJS, 160, 176 (arXiv:astro-ph/0504509)

Lee Y.-W., Demarque P., Zinn R., 1994, "The Horizontal-Branch Stars in Globular Clusters. II. The Second Parameter Phenomenon" ApJ, 423, 248

Lee H.-c., Yoon S.-J., Lee Y.-W., 2000, "The Hβ Index as an Age Indicator of Old Stellar Systems: The Effects of Horizontal-Branch Stars" AJ, 120, 998 (arXiv:astro-ph/0004247)

Leja J., Carnall A. C., Johnson B. D., Conroy C., Speagle J. S., 2019a, "How to Measure Galaxy Star Formation Histories. II. Nonparametric Models" ApJ, 876, 3

Leja J., Tacchella S., Conroy C., 2019b, "Beyond UVJ: More Efficient Selection of Quiescent Galaxies with Ultraviolet/Mid-infrared Fluxes" ApJ, 880, L9

Lejeune T., Cuisinier F., Buser R., 1997, "Standard stellar library for evolutionary synthesis. I. Calibration of theoretical spectra" A&AS, 125, 229

Lejeune T., Cuisinier F., Buser R., 1998, "A standard stellar library for evolutionary synthesis. II. The M dwarf extension" A&AS, 130, 65

Lemaître G., 1927, "Un Univers homogène de masse constante et de rayon croissant rendant compte de la vitesse radiale des nébuleuses extra-galactiques" Annales de la Société Scientifique de Bruxelles, 47, 49

Linder E. V., 2003, "Exploring the Expansion History of the Universe" Phys. Rev. Lett., 90, 091301 (arXiv:astro-ph/0208512)

Lodha K., et al., 2025a, "DESI 2024: Constraints on physics-focused aspects of dark energy using DESI DR1 BAO data" Physical Review D, 111, 023532

Lodha K., et al., 2025b, "Extended dark energy analysis using DESI DR2 BAO measurements" Physical Review D, 112, 083511

Lonoce I., Maraston C., Thomas D., Longhetti M., Parikh T., Guarnieri P., Comparat J., 2020, "Stellar population properties of individual massive early-type galaxies at 1.4 < z < 2" MNRAS, 492, 326 (arXiv:1912.00084)

Lotz J. M., et al., 2017, "The Frontier Fields: Survey Design and Initial Results" ApJ, 837, 97 (arXiv:1605.06567)

Luo B., et al., 2017, "The Chandra Deep Field-South Survey: 7 Ms Source Catalogs" ApJS, 228, 2 (arXiv:1611.03501)

Magain P., Courbin F., Sohy S., 1998, "Deconvolution with Correct Sampling" ApJ, 494, 472 (arXiv:astro-ph/9704059)

Magliocchetti M., et al., 2020, "The role of galaxy mass on AGN emission: a view from the VANDELS survey" MNRAS, 493, 3838 (arXiv:2002.02980)

Magrini L., et al., 2023, HRMOS White Paper: Science Motivation, doi:10.48550/arXiv.2312.08270, https://ui.adsabs.harvard.edu/abs/2023arXiv231208270M

Magris C. G., Binette L., Bruzual A. G., 2003, "ADEMIS: A Library of Evolutionary Models for Emission-Line Galaxies. I. Dust-free Models" ApJS, 149, 313 (arXiv:astro-ph/0311233)

Mahler G., et al., 2023, "Precision Modeling of JWST's First Cluster Lens SMACS J0723.3-7327" ApJ, 945, 49 (arXiv:2207.07101)

Mainieri V., et al., 2024, The Wide-field Spectroscopic Telescope (WST) Science White Paper, doi:10.48550/arXiv.2403.05398, https://ui.adsabs.harvard.edu/abs/2024arXiv240305398M

Maraston C., Strömbäck G., 2011, "Stellar population models at high spectral resolution" MNRAS, 418, 2785 (arXiv:1109.0543)

Marchi F., et al., 2019, "The VANDELS survey: the role of ISM and galaxy physical properties in the escape of Lyα emission in z ~ 3.5 star-forming galaxies" A&A, 631, A19 (arXiv:1903.08593)

Massari D., Koppelman H. H., Helmi A., 2019, "Origin of the system of globular clusters in the Milky Way" A&A, 630, L4 (arXiv:1906.08271)

Massari D., et al., 2023, "Cluster Ages to Reconstruct the Milky Way Assembly (CARMA). I. The final word on the origin of NGC 6388 and NGC 6441" A&A, 680, A20 (arXiv:2310.01495)

Matteucci F., Recchi S., 2001, "On the Typical Timescale for the Chemical Enrichment from Type Ia Supernovae in Galaxies" ApJ, 558, 351

McLure R. J., et al., 2018, "The VANDELS ESO public spectroscopic survey" MNRAS, 479, 25 (arXiv:1803.07414)

Mendel J. T., Proctor R. N., Forbes D. A., 2007, "The age, metallicity and α-element abundance of Galactic globular clusters from single stellar population models" MNRAS, 379, 1618 (arXiv:0705.4511)

Messa M., Adamo A., Östlin G., Melinder J., Hayes M., Bridge J. S., Cannon J., 2019, "Star-forming clumps in the Lyman Alpha Reference Sample of galaxies - I. Photometric analysis and clumpiness" MNRAS, 487, 4238 (arXiv:1906.04751)

Messa M., Dessauges-Zavadsky M., Richard J., Adamo A., Nagy D., Combes F., Mayer L., Ebeling H., 2022, "Multiply lensed star forming clumps in the A521-sys1 galaxy at redshift 1" MNRAS, 516, 2420 (arXiv:2208.02863)

Michalewicz K., Millon M., Dux F., Courbin F., 2023, "STARRED: a two-channel deconvolution method with Starlet regularization" The Journal of Open Source Software, 8, 5340 (arXiv:2305.18526)

Miglio A., et al., 2021a, "Haydn" Experimental Astronomy, 51, 963

Miglio A., et al., 2021b, "Age dissection of the Milky Way discs: Red giants in the Kepler field" A&A, 645, A85 (arXiv:2004.14806)

Mignoli M., et al., 2009, "The zCOSMOS redshift survey: the three-dimensional classification cube and bimodality in galaxy physical properties" A&A, 493, 39 (arXiv:0810.2245)

Millon M., Michalewicz K., Dux F., Courbin F., Marshall P. J., 2024, "Image Deconvolution and Point-spread Function Reconstruction with STARRED: A Wavelet-based Two-channel Method Optimized for Light-curve Extraction" AJ, 168, 55 (arXiv:2402.08725)

Milone A. P., Marino A. F., 2022, "Multiple Populations in Star Clusters" Universe, 8, 359 (arXiv:2206.10564)

Morel T., Miglio A., 2012, "Assessing the accuracy of the surface gravity determination in late-type stars with solar-like pulsators" MNRAS, 419, L34

Moresco M., 2015, "Raising the bar: new constraints on the Hubble parameter with cosmic chronometers at z ~2." MNRAS, 450, L16 (arXiv:1503.01116)

Moresco M., 2023, "Addressing the Hubble tension with cosmic chronometers" arXiv e-prints, p. arXiv:2307.09501 (arXiv:2307.09501)

Moresco M., et al., 2012, "Improved constraints on the expansion rate of the Universe up to z ~1.1 from the spectroscopic evolution of cosmic chronometers" J. Cosmology Astropart. Phys., 2012, 006 (arXiv:1201.3609)

Moresco M., et al., 2013, "Spot the difference. Impact of different selection criteria on observed properties of passive galaxies in zCOSMOS-20k sample" A&A, 558, A61 (arXiv:1305.1308)

Moresco M., et al., 2016, "A 6% measurement of the Hubble parameter at z~0.45: direct evidence of the epoch of cosmic re-acceleration" J. Cosmology Astropart. Phys., 2016, 014 (arXiv:1601.01701)

Moresco M., Jimenez R., Verde L., Pozzetti L., Cimatti A., Citro A., 2018, "Setting the Stage for Cosmic Chronometers. I. Assessing the Impact of Young Stellar Populations on Hubble Parameter Measurements" ApJ, 868, 84 (arXiv:1804.05864)

Moresco M., Jimenez R., Verde L., Cimatti A., Pozzetti L., 2020, "Setting the Stage for Cosmic Chronometers. II. Impact of Stellar Population Synthesis Models Systematics and Full Covariance Matrix" ApJ, 898, 82

Moresco M., et al., 2022, "Unveiling the Universe with emerging cosmological probes" Living Reviews in Relativity, 25, 6 (arXiv:2201.07241)

Mowla L., et al., 2022, "The Sparkler: Evolved High-redshift Globular Cluster Candidates Captured by JWST" ApJ, 937, L35 (arXiv:2208.02233)

Mowla L., et al., 2024, "The Firefly Sparkle: The Earliest Stages of the Assembly of A Milky Way-type Galaxy in a 600 Myr Old Universe" arXiv e-prints, p. arXiv:2402.08696 (arXiv:2402.08696)

Nepal S., Chiappini C., Queiroz A. B., Guiglion G., Montalbán J., Steinmetz M., Miglio A., Khalatyan A., 2024, "Discovery of the local counterpart of disc galaxies at z > 4: The oldest thin disc of the Milky Way using Gaia-RVS" A&A, 688, A167

Niederhofer F., et al., 2025, Cluster Ages to Reconstruct the Milky Way Assembly (CARMA) IV. Chrono-dynamics of seven old star clusters in the Large Magellanic Cloud and the peculiar origin of NGC 1841, doi:10.48550/arXiv.2509.10144, https://ui.adsabs.harvard.edu/abs/2025arXiv250910144N

Noirot G., et al., 2023, "The first large catalogue of spectroscopic redshifts in Webb's first deep field, SMACS J0723.3-7327" MNRAS, 525, 1867 (arXiv:2212.07366)

Nsamba B., et al., 2021, "Asteroseismic modelling of solar-type stars: a deeper look at the treatment of initial helium abundance" MNRAS, 500, 54

O'Malley E. M., Gilligan C., Chaboyer B., 2017, "Absolute Ages and Distances of 22 GCs Using Monte Carlo Main-sequence Fitting" ApJ, 838, 162 (arXiv:1703.01915)

Ocvirk P., Pichon C., Lançon A., Thiébaut E., 2006, "STECKMAP: STEllar Content and Kinematics from high resolution galactic spectra via Maximum A Posteriori" MNRAS, 365, 74 (arXiv:astro-ph/0507002)

Oliveira R. A. P., et al., 2020, "The Hubble Space Telescope UV Legacy Survey of Galactic Globular Clusters. XX. Ages of Single and Multiple Stellar Populations in Seven Bulge Globular Clusters" ApJ, 891,

37 (arXiv:2001.08611)

Onodera M., et al., 2015, "The Ages, Metallicities, and Element Abundance Ratios of Massive Quenched Galaxies at z ≈ 1.6" ApJ, 808, 161 (arXiv:1411.5023)

Oser L., Ostriker J. P., Naab T., Johansson P. H., Burkert A., 2010, "The Two Phases of Galaxy Formation" ApJ, 725, 2312

Pagel B. E. J., Tautvaisiene G., 1995, "Chemical evolution of primary elements in the Galactic disc: an analytical model" MNRAS, 276, 505

Pancino E., et al., 2017, "The Gaia-ESO Survey. Mg-Al anti-correlation in iDR4 globular clusters" A&A, 601, A112 (arXiv:1702.06083)

Park M., Conroy C., Johnson B. D., Leja J., Dotter A., Cargile P. A., 2024, α-MC: Self-consistent α-enhanced stellar population models covering a wide range of age, metallicity, and wavelength, doi:10.48550/arXiv.2410.21375, https://ui.adsabs.harvard.edu/abs/2024arXiv241021375P

Park M., Conroy C., Johnson B. D., Leja J., Dotter A., Cargile P. A., 2025, "α-MC: Self-consistent α-enhanced Stellar Population Models Covering a Wide Range of Age, Metallicity, and Wavelength" ApJ, 994, 165

Pentericci L., et al., 2018, "The VANDELS ESO public spectroscopic survey: Observations and first data release" A&A, 616, A174 (arXiv:1803.07373)

Penzias A. A., Wilson R. W., 1965, "A Measurement of Excess Antenna Temperature at 4080 Mc/s." ApJ, 142, 419

Percival S. M., Salaris M., 2011, "Modelling realistic horizontal branch morphologies and their impact on spectroscopic ages of unresolved stellar systems" MNRAS, 412, 2445 (arXiv:1012.0004)

Percival W. J., Cole S., Eisenstein D. J., Nichol R. C., Peacock J. A., Pope A. C., Szalay A. S., 2007, "Measuring the Baryon Acoustic Oscillation scale using the Sloan Digital Sky Survey and 2dF Galaxy Redshift Survey" MNRAS, 381, 1053 (arXiv:0705.3323)

Perlmutter S., et al., 1999, "Measurements of Ω and Λ from 42 High-Redshift Supernovae" ApJ, 517, 565 (arXiv:astro-ph/9812133)

Pietrinferni A., et al., 2021, "Updated BaSTI Stellar Evolution Models and Isochrones. II. α-enhanced Calculations" ApJ, 908, 102

Piotto G., et al., 2015, "The Hubble Space Telescope UV Legacy Survey of Galactic Globular Clusters. I. Overview of the Project and Detection of Multiple Stellar Populations" AJ, 149, 91

Planck Collaboration et al., 2020, "Planck 2018 results. VI. Cosmological parameters" A&A, 641, A6 (arXiv:1807.06209)

Pontoppidan K. M., et al., 2022, "The JWST Early Release Observations" ApJ, 936, L14 (arXiv:2207.13067)

Pozzetti L., et al., 2010, "zCOSMOS - 10k-bright spectroscopic sample. The bimodality in the galaxy stellar mass function: exploring its evolution with redshift" A&A, 523, A13 (arXiv:0907.5416)

Price-Whelan A. M., et al., 2020, "Close Binary Companions to APOGEE DR16 Stars: 20,000 Binary-star Systems Across the Color-Magnitude Diagram" ApJ, 895, 2 (arXiv:2002.00014)

Pritzl B. J., Venn K. A., Irwin M., 2005, "A Comparison of Elemental Abundance Ratios in Globular Clusters, Field Stars, and Dwarf Spheroidal Galaxies" AJ, 130, 2140 (arXiv:astro-ph/0506238)

Proctor R. N., Forbes D. A., Beasley M. A., 2004, "A robust method for the analysis of integrated spectra from globular clusters using Lick indices" MNRAS, 355, 1327 (arXiv:astro-ph/0409526)

Prugniel P., Soubiran C., 2004, "New release of the ELODIE library" arXiv e-prints, pp astro–ph/0409214 (arXiv:astro-ph/0409214)

Queiroz A. B. A., et al., 2018, "StarHorse: a Bayesian tool for determining stellar masses, ages, distances, and extinctions for field stars" MNRAS, 476, 2556

Queiroz A. B. A., et al., 2023, "StarHorse results for spectroscopic surveys and Gaia DR3: Chrono-chemical populations in the solar vicinity, the genuine thick disk, and young alpha-rich stars" A&A, 673, A155

Rauer H., et al., 2014, "The PLATO 2.0 mission" Experimental Astronomy, 38, 249

Refsdal S., 1964, "On the possibility of determining Hubble's parameter and the masses of galaxies from the gravitational lens effect" MNRAS, 128, 307

Renzini A., Marino A. F., Milone A. P., 2022, "The formation of globular clusters as a case of overcooling" MNRAS, 513, 2111

Ricker G. R., et al., 2015, "Transiting Exoplanet Survey Satellite (TESS)" Journal of Astronomical Telescopes, Instruments, and Systems, 1, 014003

Riello M., et al., 2021, "Gaia Early Data Release 3. Photometric content and validation" A&A, 649, A3

Riess A. G., et al., 1998, "Observational Evidence from Supernovae for an Accelerating Universe and a Cosmological Constant" AJ, 116, 1009 (arXiv:astro-ph/9805201)

Riess A. G., et al., 2022, "A Comprehensive Measurement of the Local Value of the Hubble Constant with 1 km s^{-1} Mpc^{-1} Uncertainty from the Hubble Space Telescope and the SH0ES Team" ApJ, 934, L7 (arXiv:2112.04510)

Risaliti G., Lusso E., 2015, "A Hubble Diagram for Quasars" ApJ, 815, 33

Risaliti G., Lusso E., 2019, "Cosmological Constraints from the Hubble Diagram of Quasars at High Redshifts" Nature Astronomy, 3, 272

Roediger J. C., Courteau S., Graves G., Schiavon R. P., 2014, "Constraining Stellar Population Models. I. Age, Metallicity and Abundance Pattern Compilation for Galactic Globular Clusters" ApJS, 210, 10 (arXiv:1310.3275)

Rose J. A., 1984, "Spectral anomalies in the Hyades and Pleiades and in field stars with active chromospheres." AJ, 89, 1238

Rubin V. C., Ford W. Kent J., 1970, "Rotation of the Andromeda Nebula from a Spectroscopic Survey of Emission Regions" ApJ, 159, 379

Ruiz-Lara T., et al., 2018, "Integrated-light analyses vs. colour-magnitude diagrams. II. Leo A: an extremely young dwarf in the Local Group" A&A, 617, A18 (arXiv:1805.04323)

Salaris M., 2016, "Age dating of old field stars: Challenges from the uncertain efficiency of atomic diffusion" Astronomische Nachrichten, 337, 805

Salaris M., Cassisi S., 2005, Evolution of Stars and Stellar Populations. https://ui.adsabs.harvard.edu/abs/2005essp.book.....S

Salaris M., Degl'Innocenti S., Weiss A., 1997, "The Age of the Oldest Globular Clusters" ApJ, 479, 665

Salaris M., Groenewegen M. A. T., Weiss A., 2000, "Atomic diffusion in metal poor stars. The influence on the Main Sequence fitting distance scale, subdwarfs ages and the value of Delta Y/ Delta Z" A&A, 355, 299 (arXiv:astro-ph/0001386)

Salasnich B., Girardi L., Weiss A., Chiosi C., 2000, "Evolutionary tracks and isochrones for alpha - enhanced stars" A&A, 361, 1023 (arXiv:astro-ph/0007388)

Salim S., Boquien M., Lee J. C., 2018, "Dust Attenuation Curves in the Local Universe: Demographics and New Laws for Star-forming Galaxies and High-redshift Analogs" ApJ, 859, 11 (arXiv:1804.05850)

Salpeter E. E., 1955, "The Luminosity Function and Stellar Evolution." ApJ, 121, 161

Sánchez-Blázquez P., et al., 2006, "Medium-resolution Isaac Newton Telescope library of empirical spectra" MNRAS, 371, 703 (arXiv:astro-ph/0607009)

Santiago B. X., et al., 2016, "Spectro-photometric distances to stars: A general purpose Bayesian approach" A&A, 585, A42

Saracco P., et al., 2023, "The star formation history and the nature of the mass-metallicity relation of passive galaxies at 1.0 < z < 1.4 from VANDELS" MNRAS, 520, 3027 (arXiv:2301.09653)

Saxena A., et al., 2020a, "X-ray properties of He II λ 1640 emitting galaxies in VANDELS" MNRAS, 496, 3796 (arXiv:2003.13800)

Saxena A., et al., 2020b, "The properties of He IIλ1640 emitters at z ∼ 2.5-5 from the VANDELS survey" A&A, 636, A47 (arXiv:1911.09999)

Schiavon R. P., Rose J. A., Courteau S., MacArthur L. A., 2004, "The Identification of Blue Horizontal-Branch Stars in the Integrated Spectra of Globular Clusters" ApJ, 608, L33 (arXiv:astro-ph/0404592)

Schiavon R. P., Rose J. A., Courteau S., MacArthur L. A., 2005, "A Library of Integrated Spectra of Galactic Globular Clusters" ApJS, 160, 163 (arXiv:astro-ph/0504313)

Scott N., et al., 2017, "The SAMI Galaxy Survey: global stellar populations on the size-mass plane" MNRAS, 472, 2833 (arXiv:1708.06849)

Serenelli A. M., Bergemann M., Ruchti G., Casagrande L., 2013, "Bayesian analysis of ages, masses and distances to cool stars with non-LTE spectroscopic parameters" MNRAS, 429, 3645

Shah S. P., et al., 2023, "Uranium Abundances and Ages of r-process Enhanced Stars with Novel U II Lines" ApJ, 948, 122

Skilling J., 2006, in Mohammad-Djafari A., ed., American Institute of Physics Conference Series Vol. 872, Bayesian Inference and Maximum Entropy Methods In Science and Engineering. pp 321–330, doi:10.1063/1.2423290, https://ui.adsabs.harvard.edu/abs/2006AIPC..872..321S

Skrutskie M. F., et al., 2006, "The Two Micron All Sky Survey (2MASS)" AJ, 131, 1163

Smoot G. F., et al., 1992, "Structure in the COBE Differential Microwave Radiometer First-Year Maps" ApJ, 396, L1

Soderblom D. R., 2010, "The Ages of Stars" ARA&A, 48, 581 (arXiv:1003.6074)

Souza S. O., et al., 2024, "Combined Gemini-South and HST photometric analysis of the globular cluster NGC 6558: The age of the metal-poor population of the Galactic bulge" A&A, 690, A37 (arXiv:2407.15918)

Spergel D., et al., 2015, Wide-Field InfrarRed Survey Telescope-Astrophysics Focused Telescope Assets WFIRST-AFTA 2015 Report, doi:10.48550/arXiv.1503.03757, https://ui.adsabs.harvard.edu/abs/2015arXiv150303757S

Stern D., Jimenez R., Verde L., Stanford S. A., Kamionkowski M., 2010, "Cosmic Chronometers: Constraining the Equation of State of Dark Energy. II. A Spectroscopic Catalog of Red Galaxies in Galaxy Clusters" ApJS, 188, 280

Straatman C. M. S., et al., 2018, "The Large Early Galaxy Astrophysics Census (LEGA-C) Data Release 2: Dynamical and Stellar Population Properties of z ≲ 1 Galaxies in the COSMOS Field" ApJS, 239, 27 (arXiv:1809.08236)

Strader J., Brodie J. P., 2004, "A Principal Components Analysis of the Lick Indices of Galactic Globular Clusters" AJ, 128, 1671 (arXiv:astro-ph/0407001)

Suyu S. H., et al., 2017, "H0LiCOW - I. H0 Lenses in COSMOGRAIL's Wellspring: program overview" MNRAS, 468, 2590

Talia M., et al., 2023, "The VANDELS ESO public spectroscopic survey: The spectroscopic measurements catalogue" A&A, 678, A25 (arXiv:2309.14436)

Thomas D., Maraston C., 2003, "The impact of alpha /Fe enhanced stellar evolutionary tracks on the ages of elliptical galaxies" A&A, 401, 429 (arXiv:astro-ph/0302063)

Thomas D., Maraston C., Bender R., 2003, "Stellar population models of Lick indices with variable element abundance ratios" MNRAS, 339, 897 (arXiv:astro-ph/0209250)

Thomas D., Maraston C., Korn A., 2004, "Higher-order Balmer line indices in α/Fe-enhanced stellar population models" MNRAS, 351, L19 (arXiv:astro-ph/0404511)

Thomas D., Maraston C., Schawinski K., Sarzi M., Silk J., 2010, "Environment and self-regulation in galaxy formation" MNRAS, 404, 1775 (arXiv:0912.0259)

Thomas D., Maraston C., Johansson J., 2011, "Flux-calibrated stellar population models of Lick absorption-line indices with variable element abundance ratios" MNRAS, 412, 2183 (arXiv:1010.4569)

Thomas R., et al., 2020, "The intergalactic medium transmission towards z $\gtrsim$ 4 galaxies with VANDELS and the impact of dust attenuation" A&A, 634, A110 (arXiv:1911.12532)

Thomas R., et al., 2021, "Less and more IGM-transmitted galaxies from z $\sim$ 2.7 to z $\sim$ 6 from VANDELS and VUDS" A&A, 650, A63 (arXiv:2103.02946)

Tomasetti E., et al., 2023, "A new measurement of the expansion history of the Universe at z = 1.26 with cosmic chronometers in VANDELS" A&A, 679, A96

Tomasetti E., et al., 2025b, Cosmic chronometers with galaxy clusters: a new avenue for multi-probe cosmology, doi:10.48550/arXiv.2512.02109, https://ui.adsabs.harvard.edu/abs/2025arXiv251202109T

Tomasetti E., et al., 2025a, The oldest Milky Way stars: New constraints on the age of the Universe and the Hubble constant, doi:10.48550/arXiv.2509.02692, https://ui.adsabs.harvard.edu/abs/2025arXiv250902692T

Tomasetti E., Moresco M., Lardo C., Cimatti A., Jimenez R., 2025c, "Globular clusters as cosmic clocks: New cosmological hints from their integrated light" A&A, 696, A98

Tomasetti E., Moresco M., Lardo C., Courbin F., Jimenez R., Verde L., Millon M., Cimatti A., 2025d, "Time to Sparkler: Accurate ages of lensed globular clusters at z = 1.4 with JWST photometry" A&A, 699, A240

Tortorelli L., Mercurio A., 2023, "MORPHOFIT: An automated galaxy structural parameters fitting package" Frontiers in Astronomy and Space Sciences, 10, 51 (arXiv:2302.07890)

Trevisan M., Barbuy B., Eriksson K., Gustafsson B., Grenon M., Pompéia L., 2011, "Analysis of old very metal rich stars in the solar neighbourhood" A&A, 535, A42

Tripp R., 1998, "A two-parameter luminosity correction for Type IA supernovae" A&A, 331, 815

Usher C., et al., 2017, "The WAGGS project - I. The WiFeS Atlas of Galactic Globular cluster Spectra" MNRAS, 468, 3828 (arXiv:1703.07397)

Usher C., et al., 2019a, "The WAGGS project - II. The reliability of the calcium triplet as a metallicity indicator in integrated stellar light" MNRAS, 482, 1275 (arXiv:1809.07650)

Usher C., Brodie J. P., Forbes D. A., Romanowsky A. J., Strader J., Pfeffer J., Bastian N., 2019b, "The SLUGGS survey: measuring globular cluster ages using both photometry and spectroscopy" MNRAS, 490, 491 (arXiv:1909.05753)

Usher C., Caldwell N., Cabrera-Ziri I., 2024, "Measuring M31 globular cluster ages and metallicities using both photometry and spectroscopy" MNRAS, 528, 6010 (arXiv:2401.13918)

Vagnozzi S., Pacucci F., Loeb A., 2022, "Implications for the Hubble tension from the ages of the oldest astrophysical objects" Journal of High Energy Astrophysics, 36, 27 (arXiv:2105.10421)

Valcin D., Bernal J. L., Jimenez R., Verde L., Wandelt B. D., 2020, "Inferring the age of the universe with globular clusters" J. Cosmology Astropart. Phys., 2020, 002 (arXiv:2007.06594)

Valcin D., Jimenez R., Verde L., Bernal J. L., Wandelt B. D., 2021, "The age of the Universe with globular clusters: reducing systematic uncertainties" J. Cosmology Astropart. Phys., 2021, 017 (arXiv:2102.04486)

Valcin D., Jimenez R., Seljak U., Verde L., 2025, "The Age of the Universe with Globular Clusters III: Gaia distances and hierarchical modeling" arXiv e-prints, p. arXiv:2503.19481 (arXiv:2503.19481)

VandenBerg D. A., Bolte M., Stetson P. B., 1996, "THE AGE OF THE GALACTIC GLOBULAR CLUSTER SYSTEM" ARA&A, 34, 461

VandenBerg D. A., Brogaard K., Leaman R., Casagrande L., 2013, "The Ages of 55 Globular Clusters as Determined Using an Improved ΔV_{TO}^{HB} Method along with Color-Magnitude Diagram Constraints, and Their Implications for Broader Issues" ApJ, 775, 134 (arXiv:1308.2257)

VandenBerg D. A., Casagrande L., Edvardsson B., 2022, "Models for metal-poor stars with different initial abundances of C, N, O, Mg, and Si. II. Application to the colour-magnitude diagrams of the globular clusters 47 Tuc, NGC 6362, M 5, M 3, M 55, and M92" MNRAS, 509, 4208

Vazdekis A., Sánchez-Blázquez P., Falcón-Barroso J., Cenarro A. J., Beasley M. A., Cardiel N., Gorgas J., Peletier R. F., 2010, "Evolutionary stellar population synthesis with MILES - I. The base models and a new line index system" MNRAS, 404, 1639 (arXiv:1004.4439)

Vazdekis A., et al., 2015, "Evolutionary stellar population synthesis with MILES - II. Scaled-solar and α-enhanced models" MNRAS, 449, 1177 (arXiv:1504.08032)

Vazdekis A., Koleva M., Ricciardelli E., Röck B., Falcón-Barroso J., 2016, "UV-extended E-MILES stellar population models: young components in massive early-type galaxies" MNRAS, 463, 3409 (arXiv:1612.01187)

Walcher C. J., Coelho P., Gallazzi A., Charlot S., 2009, "Differential stellar population models: how to reliably measure [Fe/H] and [α/Fe] in galaxies" MNRAS, 398, L44 (arXiv:0906.5000)

Williams R. J., Quadri R. F., Franx M., van Dokkum P., Labbé I., 2009, "Detection of Quiescent Galaxies in a Bicolor Sequence from Z = 0-2" ApJ, 691, 1879 (arXiv:0806.0625)

Woody T., et al., 2025, "The Rapid Formation of the Metal-poor Milky Way" ApJ, 978, 152 (arXiv:2409.04529)

Worley C. C., et al., 2020, "The Gaia-ESO Survey: Spectroscopic-asteroseismic analysis of K2 stars in Gaia-ESO. The K2 Galactic Caps Project" A&A, 643, A83

Zackrisson E., Rydberg C.-E., Schaerer D., Östlin G., Tuli M., 2011, "The Spectral Evolution of the First Galaxies. I. James Webb Space Telescope Detection Limits and Color Criteria for Population III Galaxies" ApJ, 740, 13 (arXiv:1105.0921)

Zwicky F., 1933, "Die Rotverschiebung von extragalaktischen Nebeln" Helvetica Physica Acta, 6, 110

da Silva L., et al., 2006, "Basic physical parameters of a selected sample of evolved stars" A&A, 458, 609

de Jong R. S., et al., 2019, "4MOST: Project overview and information for the First Call for Proposals" The Messenger, 175, 3

van den Bergh S., 1969, "Photometric and Spectroscopic Observations of Globular Clusters in the Andromeda Nebula" ApJS, 19, 145

van den Bergh S., 1981, "UBV observations of globular clusters in the Magellanic Clouds." A&AS, 46, 79